FRONTIERS IN PHYSICS - RISING STARS ASIA

EDITED BY: Wenxiang Xu, Jinjin Li, Gang Zhang, Xinming Li, Rajarshi Chakrabarti, Kimiko Sekiguchi and Liang Hong

PUBLISHED IN: Frontiers in Physics

frontiers Research Topics

frontiers

ISSN 1664-8714
ISBN 978-2-88974-598-2
DOI 10.3389/978-2-88974-598-2

About Frontiers

Frontiers is more than just an open-access publisher of scholarly articles: it is a pioneering approach to the world of academia, radically improving the way scholarly research is managed. The grand vision of Frontiers is a world where all people have an equal opportunity to seek, share and generate knowledge. Frontiers provides immediate and permanent online open access to all its publications, but this alone is not enough to realize our grand goals.

Frontiers Journal Series

The Frontiers Journal Series is a multi-tier and interdisciplinary set of open-access, online journals, promising a paradigm shift from the current review, selection and dissemination processes in academic publishing. All Frontiers journals are driven by researchers for researchers; therefore, they constitute a service to the scholarly community. At the same time, the Frontiers Journal Series operates on a revolutionary invention, the tiered publishing system, initially addressing specific communities of scholars, and gradually climbing up to broader public understanding, thus serving the interests of the lay society, too.

Dedication to Quality

Each Frontiers article is a landmark of the highest quality, thanks to genuinely collaborative interactions between authors and review editors, who include some of the world's best academicians. Research must be certified by peers before entering a stream of knowledge that may eventually reach the public - and shape society; therefore, Frontiers only applies the most rigorous and unbiased reviews.
Frontiers revolutionizes research publishing by freely delivering the most outstanding research, evaluated with no bias from both the academic and social point of view. By applying the most advanced information technologies, Frontiers is catapulting scholarly publishing into a new generation.

What are Frontiers Research Topics?

Frontiers Research Topics are very popular trademarks of the Frontiers Journals Series: they are collections of at least ten articles, all centered on a particular subject. With their unique mix of varied contributions from Original Research to Review Articles, Frontiers Research Topics unify the most influential researchers, the latest key findings and historical advances in a hot research area! Find out more on how to host your own Frontiers Research Topic or contribute to one as an author by contacting the Frontiers Editorial Office: frontiersin.org/about/contact

FRONTIERS IN PHYSICS - RISING STARS ASIA

Topic Editors:
Wenxiang Xu, Hohai University, China
Jinjin Li, Shanghai Jiao Tong University, China
Gang Zhang, Technology and Research (A*STAR), Singapore
Xinming Li, South China Normal University, China
Rajarshi Chakrabarti, Indian Institute of Technology Bombay, India
Kimiko Sekiguchi, Tohoku University, Japan
Liang Hong, Shanghai Jiao Tong University, China

Citation: Xu, W., Li, J., Zhang, G., Li, X., Chakrabarti, R., Sekiguchi, K., Hong, L., eds. (2022). Frontiers in Physics - Rising Stars Asia. Lausanne: Frontiers Media SA. doi: 10.3389/978-2-88974-598-2

Table of Contents

frontiers in Physics

MINI REVIEW
published: 01 April 2021
doi: 10.3389/fphy.2021.669736

Electron and Ion Transport of Tin Dioxide in Secondary Batteries: Enhancement Approaches, Mechanisms, and Performance

Tianli Han[1†], Mingqiang Qi[1†], Shanshan Yang[1†], Xinya Diao[1], Jiawei Long[1], Mengfei Zhu[1], Xiaoyong Xu[2], Chaoquan Hu[3,4] and Jinyun Liu[1*]*

[1] Anhui Provincial Engineering Laboratory for New-Energy Vehicle Battery Energy-Storage Materials, College of Chemistry and Materials Science, Anhui Normal University, Wuhu, China, [2] College of Chemistry and Material Engineering, Chaohu University, Hefei, China, [3] Nanjing IPE Institute of Green Manufacturing Industry, Nanjing, China, [4] State Key Laboratory of Multiphase Complex Systems, Institute of Process Engineering, Chinese Academy of Sciences, Beijing, China

OPEN ACCESS

Edited by:
Jinjin Li,
Shanghai Jiao Tong University, China

Reviewed by:
Kaisheng Zhang,
Hefei Institutes of Physical Science (CAS), China
Bai Sun,
Anhui Jianzhu University, China

***Correspondence:**
Jinyun Liu
jyliu@ahnu.edu.cn
Chaoquan Hu
cqhu@ipe.ac.cn

[†] These authors have contributed equally to this work

Specialty section:
This article was submitted to Interdisciplinary Physics, a section of the journal Frontiers in Physics

Received: 19 February 2021
Accepted: 08 March 2021
Published: 01 April 2021

Citation:
Han T, Qi M, Yang S, Diao X, Long J, Zhu M, Xu X, Hu C and Liu J (2021) Electron and Ion Transport of Tin Dioxide in Secondary Batteries: Enhancement Approaches, Mechanisms, and Performance. Front. Phys. 9:669736. doi: 10.3389/fphy.2021.669736

Secondary batteries have been important across several aspects of daily life and industrial manufacture. The electron and ion transport of electrodes significantly affects the energy-storage performance of batteries. Among many fascinating materials, transition metal oxides have been considered promising as candidate electrode materials of high-performance batteries owing to their high theoretical capacity and good stability. Herein, tin dioxide is chosen as a representative transition metal oxide to show the specific electron and ion transport in some types of secondary batteries including lithium-ion, lithium-sulfur, potassium-ion batteries, etc. The way to optimize the structure and the strategies to enhance electron and ion transport have been summarized. Recently, tin dioxide doping and the preparation of tin dioxide-based composites have been reported. In addition, the main challenges and possible prospects are also proposed, which provide important suggestions for researchers to develop high-performance energy-storage materials and to explore new physical science.

Keywords: electron transfer, ion diffusion, transition metal oxide, composite, doping

INTRODUCTION

Depending on the rapid development of modern society, the production of clean, renewable energy has become an important direction [1–3] that is necessary to the development of energy storage systems. Secondary batteries have been considered the best choice. In the past few decades, apart from lithium-ion (Li-ion) batteries, some new types of batteries, such as lithium-sulfur (Li-S), sodium (Na)-ion, and potassium (K)-ion batteries, have been developed [4–7]. The energy-storage performance relies on the property of the electrode materials, and this is especially relevant when it comes to large theoretical capacity and good stability.

As a transition metal oxide, tin oxide (SnO_2) has a high theoretical capacity, good safety, and a low cost of production, which has attracted much attention [8–11]. However, SnO_2, as a semiconductor, has poor conductivity and ion diffusivity, which highly restricts its electrochemical performance [12, 13]. After many cycles, the electrode structure changes greatly, which results in capacity decay [14, 15]. It is important to improve the electron and ion transport of the SnO_2 electrodes, which is mainly achieved by constructing composites and doping [16–18]. In this

review, we focus on the main strategies to improve the electron transfer and ion diffusion of SnO_2 in batteries, which will be important for the broad researchers who are working on energy storage and related physical sciences.

CHALLENGES FOR ELECTRON AND ION TRANSPORT

Even though SnO_2 has been widely studied for secondary batteries, it has several disadvantages that restrict its electrochemical performance and practical applications, such as low electronic conductivity and the poor ability of ion transport. For example, the conductivity of SnO_2 at room temperature reported by Park et al. was only 1.242×10^{-8} S cm^{-1} [12]. In addition, Xie et al. reported that the Li-ion diffusion coefficient of amorphous SnO_2 thin film was 10^{-15}-10^{-13} cm^2 s^{-1} [13]. It greatly limits the overall capacity and rate-performance of SnO_2-based secondary batteries. Moreover, the SnO_2 exhibits a large volume change during the lithiation–delithiation, which makes the electrode gradually pulverize, resulting in a rapid capacity decay.

Recently, it was reported the physical properties of SnO_2 can be adjusted by controlling the morphology [2]. Many researchers have selectively focused on the adjustment of the morphology of nanostructured SnO_2 in secondary battery systems. It was reported the conductivity of a single SnO_2 nanowire was 0.1–0.9 S cm^{-1}[19]. Park et al. employed SnO_2 nanowires as anode materials for Li-ion batteries and compared the electrochemical performance with SnO_2 powders. SnO_2 nanowires showed a high lithium-storage performance [20]. The improvement of the electrochemical performance of SnO_2 nanowires was ascribed to the large surface area. Yin et al. indicated the electrochemical performance of SnO_2 nanosheets for Li-ion batteries was improved because the nanostructure increased the surface area, enhanced the structural stability, and shortened the diffusion distance of ions and electrons [21].

Compared to some morphologies such as 1D nanowires [22, 23], nanorods [24, 25], nanotubes [26], and two-dimensional (2D) nanosheets [27, 28], three-dimensional (3D) porous structures provide sufficient voids to buffer volume expansion. Since then, it has attracted great attention [29]. In 2017, Li et al. prepared a dumbbell hollow porous SnO_2 anode for a Li-ion battery, and it exhibited a high capacity [10]. There were nanopores in the porous shell, which promoted electrolyte transport and Li-ion diffusion; and the hollow porous structure provided space for buffer volume expansion. Zhang et al. prepared uniform multi-shell SnO_2 hollow microspheres through a continuous hard template method, which was used as the anode of the Li-ion battery [30]. Each shell of the multi-shell hollow structure could form parallel resistance to improve the conductivity.

Nanostructured SnO_2 can not only improve the electronic conductivity but also shorten the Li-ion diffusion pathway by improving the electrode–electrolyte interface properties [3, 31]. However, the electrochemical performance of the nanostructured SnO_2 hinders the application in large-scale secondary batteries. In some studies, it was found that surface coating and elemental doping improved the performance [3, 9, 32]. Researchers have developed several strategies to improve the electron and ion transport of SnO_2 to enhance the energy-storage performance, and these have potential for large-scale application.

ELECTRON AND ION TRANSPORT OF SnO_2 COMPOSITES

SnO_2@C Composites in Li-Ion Batteries

Carbonaceous materials have good electrical conductivity, exhibiting a synergistic effect with SnO_2 to improve the overall electronic conductivity [33]. Guo et al. prepared porous carbon-coated SnO_2 nanoparticles (SnO_2@PC) by using glucose as the carbon source [34]. Porous carbon provided a fast electron/ion transport pathway, which prevents the crushing and aggregation of SnO_2 nanoparticles and promotes the formation of stable solid electrolyte interface (SEI) films. Moreover, the highly specific surface area provided more active centers for Li storage and promoted ion/electron transport. When the carbon content was 14.1%, the discharge capacity was 1130.1 mAh g^{-1} after 100 cycles at 0.2 A g^{-1}.

Since graphene was discovered by Andre and Konstantin Novoselov in 2004, it has attracted wide attention in many fields. Owing to its excellent mechanical properties and electrical conductivity, graphene has been used for energy storage [35]. Many studies have focused on combining graphene with a transition metal oxide like SnO_2. Chen et al. reported a SnO_2/graphene composite, which was beneficial to improve the electrochemical performance [36]. The green approach to prepare the SnO_2/graphene composites directly anchored SnO_2 nanoparticles on graphene nanosheets via Sn-O-C bonds. The prepared SnO_2/graphene composite exhibited a capacity of 1420 mAh g^{-1} at 0.1 A g^{-1} after 90 cycles and good cycling retention of 97% at 1 A g^{-1} after 230 cycles.

Some investigations have indicated that the composites of SnO_2 with carbon materials often suffered from material loss during long-term cycles, which leads to the increase of resistance and the rapid decay of electrochemical performance. Therefore, researchers have prepared some multi-dimensional materials with a topological structure. A double-carbon confinement strategy was presented by Wu et al. to prepare double-carbon to confine SnO_2 hollow nanospheres (denoted as G@C@SnO_2), as shown in **Figure 1** [33]. The G@C@SnO_2 showed a highly reversible performance in Li-ion batteries. The enhancement was ascribed to the following advantages: (i) a 3D structure based on graphene increased the conductivity, avoided the aggregation of nanoparticles, and provided an open framework for the transmission of electrons and ions; (ii) hollow SnO_2 nanospheres shortened ion diffusion distance and buffered volume change; and (iii) a nitrogen-doped carbon shell can further accommodate volume change, ensuring structural integrity and improved conductivity.

SnO_2@C Composites in Li-S Batteries

Li-S battery is considered an excellent candidate for energy-storage systems because of its high energy density. However, the sulfur cathode has the problem of low conductivity (5×10^{-30} S

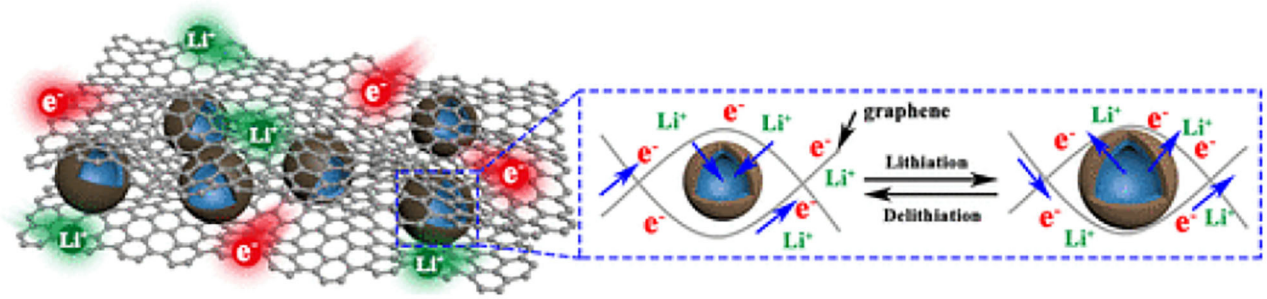

FIGURE 1 | Illustration of the reversible Li-ion storage in G@C@SnO_2. Reproduced from Wu et al. [33].

cm^{-1}) and the huge volume-change during cycling, resulting in a rapid capacity decay [7, 37]. In addition, polysulfide is easily soluble in electrolytes, leading to a shuttle effect [38]. Surface modification of sulfur cathodes and coating with conductive materials are common strategies to solve the problems [39]. Liu's group prepared a ternary composite of S/C@SnO_2, which could improve the conductivity of sulfur, adapt to the volume-change, and adsorb polysulfide [40]. Porous carbon could improve the conductivity, and the porous structure reserved space for the volume change of sulfur. In addition, the SnO_2 shell improved the mechanical strength of the whole structure, displayed strong adsorption toward polysulfide, and further reduced the shuttle effect.

Moreover, SnO_2/carbon composites, as functional interlayer materials used in Li-S batteries, weaken the shuttle effect by chemical adsorption. In the meantime, carbon materials in SnO_2/carbon composite can improve the overall conductivity of the composite. Hu et al. prepared a SnO_2/reduced graphene oxide (rGO) composite as dual-function interlayer cathode material for Li-S batteries [41]. The close interaction between rGO and SnO_2 nanoparticles not only reduced the resistance of the sulfur cathode but also averted the deformation of the electrode.

SnO_2@TMO Composites in Secondary Batteries

Typical transition metal oxides (TMOs), including SnO_2, TiO_2, MoO_2, Co_3O_4, V_2O_5, NiO, CuO, ZnO, and Fe_2O_3, etc., commonly possess a high capacity compared to the graphite anode in Li-ion batteries [42, 43]. Researchers found that TMO composites are beneficial to the improvement of cycle stability, and they are attributed to the synergistic effect [44–46]. Recently, many studies have been conducted in developing composites of SnO_2 and TMOs. SnO_2@TMO composites are often used as anodes of Li-ion batteries, and they show good electrochemical performances. For example, SnO_2 is n-typed semiconductor with a wide band gap (3.6 eV), while α-Fe_2O_3 is a p-type semiconductor with a narrow band gap (2.2 eV). Electron transfer from the conduction band of SnO_2 to the conduction band of α-Fe_2O_3, crosses the heterojunction interface, and finally their Fermi levels reach an equilibrium. **Figure 2** schematically shows the energy band of lithium storage of a SnO_2/α-Fe_2O_3 heterostructure. The synergistic effect of SnO_2 and α-Fe_2O_3 effectively improved the conductivity, and the diffusion rate of lithium ion thus improved the rate performance of the battery [47].

SnO_2@TMO has been used in many secondary batteries, such as Li-ion and Li-S batteries, exhibiting good performance. Liu et al. indicated that the low conductivity of pure sulfur and shuttle effect seriously hindered the commercial development of Li-S batteries [48]. The results showed the resistance of the S@SnO_2@MnO_2 composite was 6.4×10^7 Ω, which was one order of magnitude lower than pure sulfur (5.8×10^8 Ω). According to the first-principal calculation, SnO_2 and MnO_2 had a compact band gap structure and a good density of states (DOS), which are helpful to the reduction of the electron transfer barrier. It was indicated that SnO_2 and MnO_2 improve the electrical conductivity and accelerate the electron transfer of S@SnO_2@MnO_2 composite. The capacity of the Li-S battery with a S@SnO_2@MnO_2 composite as the cathode was 1,323 mAh g^{-1} at 0.1 C, and the low capacity decay rate was 0.03% after 500 cycles, indicating great confinement of the shuttle effect. In addition, the battery also showed good rate-performance.

ELECTRON TRANSFER AND ION DIFFUSION OF DOPED-SnO_2 FOR ENERGY-STORAGE

Doping technology is an economical, simple, and effective modification strategy that has been used broadly to improve the electronic properties of SnO_2 in secondary batteries. Several materials have been chosen as dopants, including the group IIIA element (Al, Ga, and In), the group VA elements Sb, and so on [49, 50]. It has been reported that doping transition metals can not only increase the conductivity of SnO_2 but also reduce the volume change in the process of circulation [51, 52]. Lübke et al. reported two categories of transition metal dopants in SnO_2 [53]. The first one are the elements without redox activity, including Zr [53], Ti [54], Nb [55], W [56], and Pb [57]. The doping of these elements will not change the capacity of SnO_2, but it can significantly increase the cycling life and rate performance [53]. Dominic et al. indicated that the improvement of the performance of doped SnO_2 depending on the increase

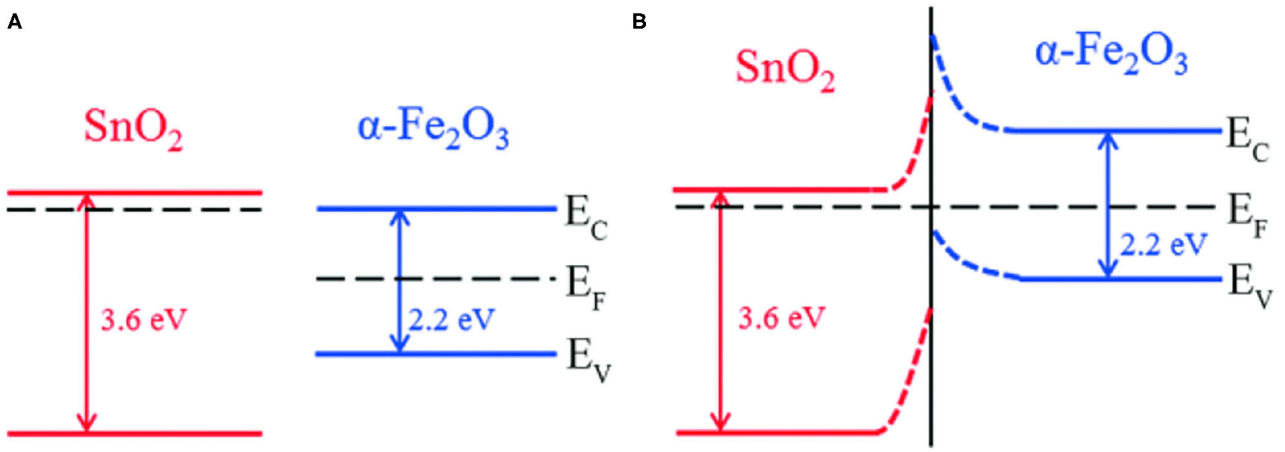

FIGURE 2 | (A) Schematic diagram of the energy band structures for SnO_2 and α-Fe_2O_3. **(B)** The energy band of SnO_2@α-Fe_2O_3 heterostructures. E_C, E_F, and E_V stand for conduction band energy, Fermi energy, and valence band energy, respectively. Reproduced from Cui et al. [47].

of the electrical conductivity caused by the additional charge percolation path. Belonging to the second group elements of Cu [53], Mn [58], Fe [59], Co [60], Ni [61], Zn [62], Mo [63], and Sb [64], which showed redox activity, can ensure participation in the conversion reaction, leading to the increase of theoretical capacity. Among them, Mo is an interesting dopant, as it increased the concentration of free electrons in SnO_2. Chen et al. prepared ultrafine Mo-doped SnO_2 in which Mo uniformly distributed and banded to a SnO_2 lattice in the form of Mo^{6+} [63]. The initial capacity was as high as 2751.4 mAh g^{-1}. Even at 0.5 A g^{-1}, the initial capacity was 1121.8 mAh g^{-1}, and the high capacity of 670.5 mAh g^{-1} can be maintained after 700 cycles. Moreover, Sb-doped SnO_2 has also been studied widely. Wang et al. reported a Sb-doped SnO_2 hollow nanosphere that showed the capacity of 709 mAh g^{-1} at 0.1 A g^{-1} after 100 cycles [65].

In addition, doping and co-doping strategies by non-metallic elements are also reported, such as F [66–68], N [69], P [70], S/F [71], and Co/F [52]. It was reported that doping fluorine atoms in SnO_2 could increase the electrical conductivity to about 5×10^3 S cm^{-1} [72]. In order to improve the Li-storage performance, Luo et al. chose active fluorine and sulfur atoms as dopants to prepare S and F co-doped SnO_2@graphene oxide binary composites [71]. On the one hand, fluorine atoms replaced O^{2-} in SnO_2 to improve the electrical conductivity; on the other hand, S-doping enhanced Li-ion diffusion efficiency in the binary structure. The improvement of electronic conductivity can also be verified through the impedance spectra. Furthermore, the material can effectively reduce the volume expansion of electrode materials, thus reducing the capacity loss in the cycling process. It can be ascribed to the formation of the SnS_x protective layer and C–F bond on the surface of SnO_2 and graphite oxide [71]. In addition, Ma et al. demonstrated the effect of doping ratio by comparing pure SnO_2 and cobalt-doped SnO_2 with the content of 5, 10, and 15%, respectively [73]. They found the size of the synthesized particles decreased with the increase in dopant concentration. Electrochemical tests showed a doping ratio of 10% ($Sn_{0.9}Co_{0.10}O_2$) possessed the best stability among the four samples.

ELECTRON AND ION TRANSPORT IN Na- AND K-ION BATTERIES

SnO_2 in Na-Ion Batteries

Because of the larger diameters of Na- and Li-ions than Li-ions ($K^+ > Na^+ > Li^+$, 1.38 Å>1.02 Å>0.76 Å), the problems caused by volume change during the cycling are extremely critical, resulting in rapid capacity decay. In order to solve this problem, researchers have developed many strategies, such as nanostructures, making composites with carbon, etc. For example, Chen et al. used the synergistic-induced ultra-fine SnO_2/graphene nanocomposite as the cathode for a K/Na-ion battery, which showed a highly reversible capacity [36]. Xu et al. prepared a sandwich structure (MWNTs@SnO_2@C) in which MWNTs were coated with thick SnO_2, SnO_2, thin SnO_2, and the carbon layer [74]. After removing the thick and thin SnO_2, the larger internal space could alleviate the problems caused by SnO_2 volume transformation, and the 1D MWNTs and carbon layer also improved the conductivity, which made the composite material have a better performance.

Ma et al. demonstrated the failure mechanism of the SnO_2 electrode in Na- and K-ion batteries and indicated that OVs could manipulate the energy band structure and carrier migration, thus adjusting the intrinsic properties of oxide semiconductors [75]. In addition, Wang et al. used layer-by-layer-assembled porphyrin derivatives as an interface linker to uniformly attach SnO_2 crystals to N and S co-doped graphene, achieving a high capacity and optimizing the electrochemical performance effectively [76].

SnO_2 in K-Ion Batteries

Owing to the significant advantages, such as fast interface diffusion rate, low price, and wide distribution, K-ion batteries have become a possible candidate to replace Li-ion batteries.

Since 2015, research on K-ion batteries has become a hot spot. Some studies indicated that the use of SnO_2 in K-ion batteries can significantly alleviate the large volume change and the capacity decay.

Recently, Huang et al. reported the K-storage performance of SnO_2/carbon nanofibers [18]. Graphene was introduced through the electrospinning process, and the synergistic effect between SnO_2, rGO, and carbon was generated to improve the conductivity of the composites. Huang et al. doped SnO_2/rGO/C with phosphoric acid. The prepared composite showed an improved diffusion of K^+ ions after the modification by H_3PO_4 and an increased conductivity by rGO, which further improves the electrochemical performance [77]. Suo et al. prepared SnS_2/SnO_2 heterostructures to enhance the K-storage performance through a facile two-step hydrothermal method to fix SnS_2/SnO_2 heterostructures onto stainless steel mesh (SnS_2/SnO_2/SSM). The SnS_2/SnO_2/SSM anode displayed an enhanced electrochemical performance [78]. Li et al. used amorphous carbon to coat SnO_2 nanosheets, which exhibited good K-ion storage performance. The HCHS, as a stable carrier skeleton for SnO_2 nanosheets, is good at providing high electrical conductivity. Amorphous carbon wrapping solved the problems of volume expansion and provided surface-induced capacitance [79].

CONCLUSION

In summary, the challenges for enhancing the electronic and ionic properties of SnO_2 electrodes reported recently have been introduced. The conductivity and ion diffusion of SnO_2 strongly depends on the structure and composition. Moreover, we indicated that the SnO_2 exhibited great potential as the electrode material with good volumetric and gravimetric capacities in many secondary batteries, including Li-ion, Li-S, Na-ion, and K-ion batteries, as displayed in **Supplementary Tables 1–6**. However, electrons and ions transport both require significant improvement. In order to address the issues and enable the application of SnO_2-based secondary batteries, some approaches have been demonstrated. It is expected that possible investigations in the future will be focused on the optimization of the SnO_2 structure, modifying this with some other functional dopants to seek ideal SnO_2-based composites through both theoretical modeling and experimental preparation.

AUTHOR CONTRIBUTIONS

JL and CH supervised the mini-review. All authors prepared and approved the manuscript.

FUNDING

This work was supported by the Science and Technology Major Project of Anhui Province (18030901093), Key Research and Development Program of Wuhu (2019YF07), Natural Science Research Project for Universities in Anhui Province (KJ2018ZD034 and KJ2019A0502), and Foundation of Anhui Laboratory of Molecule-Based Materials (FZJ19014).

SUPPLEMENTARY MATERIAL

The Supplementary Material for this article can be found online at: https://www.frontiersin.org/articles/10.3389/fphy.2021.669736/full#supplementary-material

REFERENCES

1. Baidya S, Nandi C. Advances in greener energy technologies green energy and technology. *Int J Green Energy*. (2020) 16:259–76. doi: 10.1007/978-981-15-4246-6_16
2. Periyasamy M, Kar A. Modulating the properties of SnO_2 nanocrystals: morphological effects on structural, photoluminescence, photocatalytic, electrochemical and gas sensing properties. *J Mater Chem C*. (2020) 8:4604–35. doi: 10.1039/C9TC06469A
3. Zoller F, Bohm D, Bein T, Fattakhova-Rohlfing, D. Tin oxide based nanomaterials and their application as anodes in lithium-ion batteries and beyond. *ChemSusChem*. (2019) 12:4140–59. doi: 10.1002/cssc.201901487
4. Fang R, Chen K, Yin L, Sun Z, Li F, Cheng HM. The regulating role of carbon nanotubes and graphene in lithium-ion and lithium-sulfur batteries. *Adv Mater*. (2019) 31:e1800863. doi: 10.1002/adma.201800863
5. Hosaka T, Kubota K, Hameed AS, Komaba S. Research development on K-ion batteries. *Chem Rev*. (2020) 120:6358–466. doi: 10.1021/acs.chemrev.9b00463
6. Kim T, Song WT, Son DY, Ono LK, Qi YB. Lithium-ion batteries: outlook on present, future, and hybridized technologies. *J Mater Chem A*. (2019) 7:2942–64. doi: 10.1039/C8TA10513H
7. Kumar R, Liu J, Hwang JY, Sun YK. Recent research trends in Li–S batteries. *J Mater Chem A*. (2018) 6:11582–605. doi: 10.1039/C8TA01483C
8. Liu Q, Hu Z, Chen M, Zou C, Jin H, Wang S, et al. Recent progress of layered transition metal oxide cathodes for sodium-ion batteries. *Small*. (2019) 15:e1805381. doi: 10.1002/smll.201805381
9. Li F, Liu Q, Hu J, Yang J, Ma J. Recent progresses on SnO_2 anode materials for sodium storage. *J Phys D Appl Phys*. (2020) 53:353001. doi: 10.1088/1361-6463/ab8e79
10. Li HJ, Su QM, Kang J, Huang M, Feng M, Feng H, et al. Porous SnO_2 hollow microspheres as anodes for high-performance lithium ion battery. *Mater Lett*. (2018) 217:276–80. doi: 10.1016/j.matlet.2018.01.015
11. Yoshio IT, Kubota AM, Yukio M, Miyasaka T. Tin-based amorphous oxide: a high-capacity lithium-ion–storage material. *Science*. (1997) 276:1395–7. doi: 10.1126/science.276.5317.1395
12. Park MS, Kang YM, Wang GX, Dou SX, Liu HK. The effect of morphological modification on the electrochemical properties of SnO_2 nanomaterials. *Adv Funct Mater*. (2008) 18:455–61. doi: 10.1002/adfm.200700407
13. Xie J, Imanishi N, Hirano A, Takeda Y, Yamamoto O, Zhao XB, et al. Li-ion diffusion behavior in Sn SnO and SnO_2 thin films studied by galvanostatic intermittent titration technique. *Solid State Ionics*. (2010) 181:1611–5. doi: 10.1016/j.ssi.2010.09.006
14. Han TL, Wu Y, Ding YY, Zhong Y, Zhou P, Liu JY. Encapsulating tin nanoflowers into microcapsules for high-rate-performance secondary battery anodes through in situ polymerizing oil-in-water interface. *Energy Technol*. (2020) 8:1901404. doi: 10.1002/ente.201901404
15. Wu Y, Han TL, Zhou T, Qiao X, Chen X, Zhou P, et al. A novel silicon nanoparticles-infilled capsule prepared by an oil-in-water emulsion strategy for high-performance Li-ion battery anodes. *Nanotechnology*. (2020) 31:335403. doi: 10.1088/1361-6528/ab90b9
16. Liu JY, Cheng MY, Han TL, Lu QQ, Zhang HK, Zhou P, et al. A novel mechanically robust leaf-shaped tin dioxide Li-ion battery anode and its

dynamic structural transformation and electron-transfer simulation. *Energy Technol.* (2020) 8:1901149. doi: 10.1002/ente.201901149
17. Kebede, Mesfin A. Tin oxide–based anodes for both lithium-ion and sodium-ion batteries. *Curr Opin Electroche.* (2020) 21:182–7. doi: 10.1016/j.coelec.2020.02.003
18. Huang Z, Chen Z, Ding SS, Chen CM, Zhang M. Enhanced conductivity and properties of SnO_2-graphene-carbon nanofibers for potassium-ion batteries by graphene modification. *Mater Lett.* (2018) 219:19–22. doi: 10.1016/j.matlet.2018.02.053
19. Hernandez-Ramirez F, Tarancon A, Casals O, Pellicer E, Rodriguez J, Romano-Rodriguez A, et al. Electrical properties of individual tin oxide nanowires contacted to platinum electrodes. *Phys Rev B.* (2007) 76:085429. doi: 10.1103/PhysRevB.76.085429
20. Park MS, Wang GX, Kang YM, Wexler D, Dou SX, Liu HK. Preparation and electrochemical properties of SnO_2 nanowires for application in lithium-ion batteries. *Angew Chem Int edit.* (2007) 46:750–753. doi: 10.1002/anie.200603309
21. Yin XM, Li CC, Zhang M, Hao QY, Liu S, Chen LB, et al. One-step synthesis of hierarchical SnO_2 hollow nanostructures via self-assembly for high power lithium ion batteries. *J Phys Chem C.* (2010) 114:8084–8. doi: 10.1021/jp100224x
22. Lee SH, Kim WB. Stripe- or square-patterned arrays of tin dioxide nanowires for use in lithium-ion battery electrodes. *J Power Sources.* (2016) 307:38–44. doi: 10.1016/j.jpowsour.2015.12.075
23. Wu S, Wang M, Li C, Zhu Y, Wang H. Single crystalline SnO_2 nanowires obtained from heat-treated SnO_2 and C mixture and their electrochemical properties. *Mater Chem Phys.* (2014) 147:184–90. doi: 10.1016/j.matchemphys.2014.04.028
24. Sennu P, Aravindan V, Lee YS. Marine algae inspired pre-treated SnO_2 nanorods bundle as negative electrode for Li-ion capacitor and battery: an approach beyond intercalation. *Chem Eng J.* (2017) 324:26–34. doi: 10.1016/j.cej.2017.05.003
25. Teng XL, Zhang FL, Li Q, Wang X, Ye WN, Li HS, et al. Interfacial engineering of self-supported SnO_2 nanorod arrays as anode for flexible lithium-ion batteries. *J Electrochem Soc.* (2020) 167:120515. doi: 10.1149/1945-7111/abac86
26. Man J, Liu K, Du YH, Sun JC. Self-assemble SnO_2 porous nanotubes as high-performance anodes for lithium-ion batteries. *Mater Chem Phys.* (2020) 256:123669. doi: 10.1016/j.matchemphys.2020.123669
27. Mei J, Liao T, Sun Z. Two-dimensional metal oxide nanosheets for rechargeable batteries. *J Energy Chem.* (2018) 27:117–7, doi: 10.1016/j.jechem.2017.10.012
28. Zhang L, Wu HB, Lou X. Growth of SnO_2 nanosheet arrays on various conductive substrates as integrated electrodes for lithium-ion batteries. *Mater Horiz.* (2014) 1:133–8. doi: 10.1039/C3MH00077J
29. Liu JY, Zhang M, Han TL, Si T, Zhang HG, Hu CQ. A general template-induced sulfuration approach for preparing bifunctional hollow sulfides for high-performance Al- and Li-ion batteries. *Energy Technol.* (2020) 9:2000900. doi: 10.1002/ente.202000900
30. Zhang J, Ren H, Wang JY, Qi J, Yu Rb, Wang D, et al. Engineering of multi-shelled SnO_2 hollow microspheres for highly stable lithium-ion batteries. *J Mater Chem A.* (2016) 4:17673–7. doi: 10.1039/C6TA07717J
31. Long JW, Zhang HK, Ren JH, Li JJ, Zhu MF, Han TL, et al. A metal organic foam-derived multi-layered and porous copper sulfide scaffold as sulfur host with multiple shields for preventing shuttle effect in lithium-sulfur batteries. *Electrochim Acta.* (2020) 356:136853. doi: 10.1016/j.electacta.2020.136853
32. Cheng MY, Han TL, Zhang M, Zhang HK, Sun B, Zhu SG, et al. Hydrogel and sulfur co-coating on semispherical TiO_2 as polysulfides-immobilized cathodes for high capacity and stable rate performance lithium-sulfur batteries. *Appl Surf Sci.* (2020) 513:145887. doi: 10.1016/j.apsusc.2020.145887
33. Wu Q, Shao Q, Li Q, Duan Q, Li Y, Wang HG. Dual carbon-confined SnO_2 hollow nanospheres enabling high performance for the reversible storage of alkali metal ions. *ACS Appl Mater Inter.* (2018) 10:15642–51. doi: 10.1021/acsami.8b00605
34. Guo J, Li P, Chai LY, Su Y, Diao JX, Guo XH. Silica template-assisted synthesis of SnO_2@porous carbon composites as anode materials with excellent rate capability and cycling stability for lithium-ion batteries. *RSC Adv.* (2017) 7:30070–30079. doi: 10.1039/C7RA03594B
35. Gao CW, Jiang ZJ, Wang PX, Jensen LR, Zhang YF, Yue YZ. Optimized assembling of MOF/SnO_2/Graphene leads to superior anode for lithium ion batteries. *Nano Energy.* (2020) 74:104868. doi: 10.1016/j.nanoen.2020.104868
36. Chen WH, Song KM, Mi LW, Feng XM, Zhang JM, Cui SZ, et al. Synergistic effect induced ultrafine SnO_2/graphene nanocomposite as an advanced lithium/sodium-ion batteries anode. *J Mater Chem A.* (2017) 5:10027–38. doi: 10.1039/C7TA01634D
37. Balach J, Linnemann J, Jaumann T, Giebeler L. Metal-based nanostructured materials for advanced lithium–sulfur batteries. *J Mater Chem A.* (2018) 6:23127–68. doi: 10.1039/C8TA07220E
38. Zhang M, Zhu MF, Zhong Y, Han TL, Sun B, Zhu S, et al. A novel sulfur@void@hydrogel yolk-shell particle with a high sulfur content for volume-accommodable and poly-sulfide adsorptive lithium-sulfur battery cathodes. *Nanotechnology.* (2020) 31:455402. doi: 10.1088/1361-6528/abaa72
39. Chen L, Yu H, Li WX, Dirican M, Liu Y, Zhang XW. Interlayer design based on carbon materials for lithium–sulfur batteries: a review. *J Mater Chem A.* (2020) 8:10709–35. doi: 10.1039/D0TA03028G
40. Wu Y, Zhang W, Han TL, Shen Z, Cheng D, Zhang HK, et al. A novel ternary sulfur/carbon@tin dioxide composite with polysulfides-adsorptive shell and conductive core as high-performance lithium-sulfur battery cathodes. *Appl Surf Sci.* (2019) 489:462–9. doi: 10.1016/j.apsusc.2019.06.052
41. Hu N, Lv X, Dai Y, Fan L, Xiong D, Li X. SnO_2/reduced graphene oxide interlayer mitigating the shuttle effect of Li-S batteries. *ACS Appl Mater Inter.* (2018) 10:18665–74. doi: 10.1021/acsami.8b03255
42. Liu JY, Ding YY, Han TL, Long JW, Pei X, Luo Y, et al. An oriented laterally-growing $NiCo_2O_4$ nanowire array on a Fe_2O_3 microdisc as a high-capacity and excellent rate-performance secondary battery anode. *Chem Commun.* (2020) 56:2618–21. doi: 10.1039/D0CC00553C
43. Han TL, Ding YY, Chen Y, Cheng D, Zhou P, Liu JY. A novel spring-structured coaxial hierarchical SiO_2@Co_3O_4 nanowire as a lithium-ion battery anode and its in situ real-time lithiation. *Nanotechnology.* (2020) 31:035401. doi: 10.1088/1361-6528/ab4848
44. Choi J, Kim WS, Hong SH. Highly stable SnO_2-Fe_2O_3-C hollow spheres for reversible lithium storage with extremely long cycle life. *Nanoscale.* (2018) 10:4370–6. doi: 10.1039/C7NR07208B
45. Zeng W, Zheng F, Li R, Zhan Y, Li Y, Liu J. Template synthesis of SnO_2/alpha-Fe_2O_3 nanotube array for 3D lithium ion battery anode with large areal capacity. *Nanoscale.* (2012) 4:2760–5. doi: 10.1039/c2nr30089c
46. Zhu XS, Shi HM, Yin JW, Zhu HM, Zhou YM, Tang YW, et al. Facile preparation of CuO@SnO_2 nanobelts as a high-capacity and long-life anode for lithium-ion batteries. *RSC Adv.* (2014) 4:34417–20. doi: 10.1039/C4RA04373A
47. Cui ZP, Sun M, Liu HQ, Li SJ, Zhang QY, Yang CP, et al. Double-shell SnO_2@Fe_2O_3 hollow spheres as a high-performance anode material for lithium-ion batteries. *Crystengcomm.* (2020) 22:1197–208. doi: 10.1039/C9CE01621J
48. Zhou P, Han TL, Gu CP, Li JJ, Shen ZH, Zhang HG, et al. A novel wheel-confined composite as cathode in Li-S batteries with high capacity retention. *J Alloy Compd.* (2019) 776:504–10. doi: 10.1016/j.jallcom.2018.10.172
49. Skoromets V, Němec H, Kopeček J, KuŽel P, Peters K, Fattakhova-Rohlfing D, et al. Conductivity mechanisms in Sb-doped SnO_2 nanoparticle assemblies: DC and terahertz regime. *J Phys Chem C.* (2015) 119:19485–95. doi: 10.1021/acs.jpcc.5b05091
50. Zoller F, Peter K, Zehetmaier PM, Zeller P, Döblinger M, Bein T, et al. Making ultrafast high-capacity anodes for lithium-ion batteries via antimony doping of nanosized tin oxide/graphene composites. *Adv Funct Mater.* (2018) 28:1706529. doi: 10.1002/adfm.201706529
51. Nithyadharseni P, Abhilash, KP, Petnikota S, Anilkumar MR, Jose R, Ozoemena, KI, et al. Synthesis and lithium storage properties of Zn Co and Mg doped SnO_2 nano materials. *Electrochim Acta.* (2017) 247:358–370. doi: 10.1016/j.electacta.2017.06.170
52. Pan D, Wan N, Ren Y, Zhang W, Lu X, Wang Y, et al. Enhanced structural and electrochemical stability of self-similar rice-shaped SnO_2 nanoparticles. *ACS Appl Mater Inter.* (2017) 9:9747–55. doi: 10.1021/acsami.7b00232
53. Lübke M, Ning D, Armer Ceilidh F, Howard DB, Dan JL, Liu ZL, et al. Evaluating the potential benefits of metal ion doping in SnO_2 negative electrodes for lithium-ion batteries. *Electrochim Acta.* (2017) 242:400–7. doi: 10.1016/j.electacta.2017.05.029

54. Ba CQ, Shi LY, Wang ZY, Chen GR, Wang S, Zhao Y, et al. Fabrication of Ti-doped SnO_2/rGO composites as anode materials with high stability for lithium-ion batteries. *Res Chem Intermediat.* (2017) 43:5857–69. doi: 10.1007/s11164-017-2967-7
55. Zhang SL, Zhang JH, Cao GQ, Wang Q, Hu JH, Zhang P, et al. Strong interplay between dopant and SnO_2 in amorphous transparent (Sn, Nb)O_2 anode with high conductivity in electrochemical cycling. *J Alloy Compd.* (2018) 735:2401–9. doi: 10.1016/j.jallcom.2017.12.021
56. Wang S, Shi LY, Chen GR, Ba CQ, Wang ZY, Zhu JF, et al. In situ synthesis of tungsten-doped SnO_2 and graphene nanocomposites for high-performance anode materials of lithium-ion batteries. *ACS Appl Mater Inter.* (2017) 9:17163–71. doi: 10.1021/acsami.7b03705
57. Zhao P, Yue WB, Yuan X, Bao HY. Exceptional lithium anodic performance of Pd-doped graphene-based SnO_2 nanocomposite. *Electrochim Acta.* (2017) 225:322–9. doi: 10.1016/j.electacta.2016.12.124
58. Ma YJ, Ma Y, Guili G, Diemant T, Behm RJ, Geiger D, et al. Conversion/alloying lithium-ion anodes-enhancing the energy density by transition metal doping. *Sustain Energ Fuels.* (2018) 2:2601–8. doi: 10.1039/C8SE00424B
59. Yan Y, Du FH, Shen XP, Ji ZY, Sheng XX, Zhou H, et al. Large-scale facile synthesis of Fe-doped SnO_2 porous hierarchical nanostructures and their enhanced lithium storage properties. *J Mater Chem A.* (2014) 2:15875–82. doi: 10.1039/C4TA02077D
60. Liang BR, Wang JJ, Zhang SY, Liang XQ, Huang HF, Huang D, et al. Hybrid of Co-doped SnO_2 and graphene sheets as anode material with enhanced lithium storage properties. *Appl Surf Sci.* (2020) 533:147447. doi: 10.1016/j.apsusc.2020.147447
61. Ye XM, Zhang WJ, Liu QJ, Wang SP, Yang YZ, Wei HY. One-step synthesis of Ni-doped SnO_2 nanospheres with enhanced lithium ion storage performance. *New J Chem.* (2015) 39:130–5. doi: 10.1039/C4NJ00989D
62. Jia TK, Chen J, Deng Z, Fu F, Zhao JW, Wang XF, et al. Facile synthesis of Zn-doped SnO_2 dendrite-built hierarchical cube-like architectures and their application in lithium storage. *Mat Sci Eng B.* (2014) 189:32–7. doi: 10.1016/j.mseb.2014.07.006
63. Chen YL, Ge DT, Zhang J, Chu RX, Zheng J, Wu CQ, et al. Ultrafine Mo-doped SnO_2 nanostructure and derivative Mo-doped Sn/C nanofibers for high-performance lithium-ion batteries. *Nanoscale.* (2018) 10:17378–87. doi: 10.1039/C8NR01195H
64. An GH, Lee DY, Lee YJ, Ahn HJ. Ultrafast lithium storage using antimony-doped tin oxide nanoparticles sandwiched between carbon nanofibers and a carbon skin. *ACS Appl Mater Inter.* (2016) 8:30264–70. doi: 10.1021/acsami.6b10868
65. Wang S, Liu JX, Yu XH, Zhang YJ, Liu JM, Zhong ZR, et al. Antimony-doped SnO_2 hollow nanospheres as negative materials for high-performance lithium-ion batteries. *Int J Electrochem Soc.* (2019) 14:9112–21. doi: 10.20964/2019.09.78
66. Cui DM, Zheng Z, Peng X, Li T, Sun TT, Yuan LJ. Fluorine-doped SnO_2 nanoparticles anchored on reduced graphene oxide as a high-performance lithium ion battery anode. *J Power Sources.* (2017) 362:20–6. doi: 10.1016/j.jpowsour.2017.07.024
67. Sun JH, Xiao LH, Jiang SD, Li GX, Huang Y, Geng JX. Fluorine-doped SnO_2@Graphene porous composite for high capacity lithium-ion batteries. *Chem Mater.* (2015) 27:4594–603. doi: 10.1021/acs.chemmater.5b00885
68. Zhang YC, Wang RZ, Zheng Z, Li T, Tong ZQ, Ai CC. Fluorine-doped SnO_2/reduced graphene oxide-artificial graphite hybrids as lithium-ion battery anodes with stable capacity. *Ionics.* (2020) 26:2835–43. doi: 10.1007/s11581-020-03493-w
69. Wang LP, Leconte Y, Feng ZX, Wei C, Zhao Y, Ma Q, et al. Novel preparation of N-doped SnO_2 nanoparticles via laser-assisted pyrolysis: demonstration of exceptional lithium storage properties. *Adv Mater.* (2017) 29:1603286. doi: 10.1002/adma.201603286
70. Liu XW, Teng DH, Li T, Yu YH, Shao XH, Yang XP. Phosphorus-doped tin oxides/carbon nanofibers webs as lithium-ion battery anodes with enhanced reversible capacity. *J Power Sources.* (2014) 272:614–21. doi: 10.1016/j.jpowsour.2014.08.084
71. Luo Y, Yuan DD, Balogun MS, Yang H, Qiu WT, Liu JC, et al. Dual doping strategy enhanced the lithium storage properties of graphene oxide binary composites. *J Mater Chem A.* (2016) 4:13431–38. doi: 10.1039/C6TA05511G
72. Russo B, Cao GZ. Fabrication and characterization of fluorine-doped thin oxide thin films and nanorod arrays via spray pyrolysis. *Appl Phys A Mater.* (2007) 90:311–5. doi: 10.1007/s00339-007-4274-4
73. Ma YJ, Ma Y, Ulissi U, Ji YC, Streb C, Bresser D, et al. Influence of the doping ratio and the carbon coating content on the electrochemical performance of Co-doped SnO_2 for lithium-ion anodes. *Electrochim Acta.* (2018) 277:100–9. doi: 10.1016/j.electacta.2018.04.209
74. Zhao Y, Wei C, Sun SN, Wang LP, Xu ZJ. Reserving interior void space for volume change accommodation: an example of cable-like MWNTs@SnO_2@C composite for superior lithium and sodium storage. *Adv Sci.* (2015) 2:1500097. doi: 10.1002/advs.201500097
75. Ma DT, Li YL, Zhang PX, Lin ZQ. Oxygen vacancy engineering in tin(IV) oxide based anode materials toward advanced sodium-Ion batteries. *ChemSusChem.* (2018) 11:3693–703. doi: 10.1002/cssc.201801694
76. Wang HG, Wu Q, Wang YH, Wang X, Wu LL, Song SY, et al. Molecular engineering of monodisperse SnO_2 nanocrystals anchored on doped graphene with high-performance lithium/sodium-storage properties in half/full cells. *Adv Energy Mater.* (2019) 9:1802993. doi: 10.1002/aenm.201802993
77. Huang Z, Chen Z, Ding SS, Chen CM, Zhang M. Enhanced electrochemical properties of SnO_2-graphene–carbon nanofibers tuned by phosphoric acid for potassium storage. *Nanotechnology.* (2018) 29:19–22. doi: 10.1088/1361-6528/aace25
78. Suo GQ, Li D, Feng L, Hou XJ, Ye XH, Zhang L, et al. Construction of SnS_2/SnO_2 heterostructures with enhanced potassium storage performance. *J Mater Sci Technol.* (2020) 55:167–72. doi: 10.1016/j.jmst.2019.05.074
79. Li D, Zhang JQ, Ahmed SM, Suo GQ, Wang W, Feng L, et al. Amorphous carbon coated SnO_2 nanosheets on hard carbon hollow spheres to boost potassium storage with high surface capacitive contributions. *J Colloid Interf Sci.* (2020) 574:174–81. doi: 10.1016/j.jcis.2020.04.045

Conflict of Interest: The authors declare that the research was conducted in the absence of any commercial or financial relationships that could be construed as a potential conflict of interest.

frontiers in Physics

ORIGINAL RESEARCH
published: 14 April 2021
doi: 10.3389/fphy.2021.669707

A Dual-Band Non-destructive Dielectric Measurement Sensor Based on Complementary Split-Ring Resonator

Chen Wang[1], *Xiaoming Liu*[1,2*], *Lu Gan*[1,2] *and Qing Cai*[3]

[1] School of Physics and Electronic Engineering, Anhui Normal University, Wuhu, China, [2] Anhui Provincial Engineering Laboratory on Information Fusion and Control of Intelligent Robot, Wuhu, China, [3] Shanghai Institute of Measurement and Testing Technology, Shanghai, China

A dual-band non-destructive dielectric constant sensor based on the complementary split ring resonators is presented. The resonators for both bands use the complementary split ring structure of different sizes. Numerical simulation demonstrates that the resonating frequency and quality factor is dependent on the variation of dielectric constant and loss tangent, making it a potential structure for dielectric measurement. To search for the optimal thickness for measurement, parametric study is conducted and the retrieval expressions are obtained for both bands. The measured results indicate an accuracy of 1.5% in comparison with the data in the literature. In addition, the effect of air gap has been analyzed, showing that it is an important error source and eliminating such effect can improve the measurement accuracy.

Keywords: dielectric constant, dual band, loss tangent, resonate frequency, quality factor, complementary split ring resonator

OPEN ACCESS

Edited by:
Jinjin Li,
Shanghai Jiao Tong University, China

Reviewed by:
Lingtao Kong,
Hefei Institutes of Physical Science (CAS), China
Zhen Peng,
Chaohu University, China

***Correspondence:**
Xiaoming Liu
xiaoming.liu@ahnu.edu.cn

Specialty section:
This article was submitted to Interdisciplinary Physics, a section of the journal Frontiers in Physics

Received: *19 February 2021*
Accepted: *18 March 2021*
Published: *14 April 2021*

Citation:
Wang C, Liu X, Gan L and Cai Q (2021) A Dual-Band Non-destructive Dielectric Measurement Sensor Based on Complementary Split-Ring Resonator. Front. Phys. 9:669707. doi: 10.3389/fphy.2021.669707

INTRODUCTION

Dielectric constant is fundamental physical property for dielectric or insulating materials [1]. It is also a critical parameter in many engineering areas. For instance, in the design of microwave and millimeter wave planar circuits, the dielectric constant of the substrate material has to be known as a priori. With the fast evolving of electronic technologies, materials are involved in many areas such as manufacturing processing, antenna design, and aerospace technology [2–5]. Therefore, precision measurement of the dielectric constant is becoming more and more critical.

Many methods for dielectric constant measurement have been developed, such as the free space method, the transmission line method, and the resonant cavity method. The free space method uses free space as transmission medium, and is suitable for dielectric measurement in the millimeter wave range [6, 7]. In addition, this method requires a slab of large area planar sample for measurement. The transmission line method requires the material to be placed inside a part of the enclosed transmission line during measurement [8]. The dielectric constant of the material is calculated from the reflected coefficients (S_{11}) and the transmission coefficients (S_{21}). However, the transmission line method requires the sample precisely fabricated to be fitted in the transmission line [9]. In addition, it is not good enough for measurement of low loss materials.

The resonant cavity method is a precision method for low loss material measurement. The dielectric constant is extracted from the resonant frequencies and quality factors [10–12]. The traditional resonating method requires sample placed inside the chamber of a cavity, which inevitably makes the operation less convenient [13, 14].

In recent years, micro strip line based planar resonator sensors have been developed [15–17]. One of the resonators is so called the complementary split ring resonator (CSRR) sensor. It can measure the dielectric constant of a material with high sensitivity [18]. An improved circular CSRR structure is reported in Ref. [19], where higher quality factor and sensitivity has been reached than the single slit CSRR structure. These sensors, however, are still working in a single band. Nowadays, the communication system with dual-band or multiband operation has been widely deployed. In this connection, multi-band measurement of dielectric property is preferred.

This paper investigated the feasibility of dual-band CSRR structure for dielectric constant measurement. Theoretically, the resonant frequency of a CSRR structure is proportional to its size. Being inspired by this property, two CSRR structures of different dimensions are built on a single substrate aiming at creating two resonating frequencies. In order to verify this design, theoretical model is built and extensive simulation analysis is conducted. Based on the analysis, the circuit model is built, the optimal thickness for measurement is obtained numerically, and retrieval expressions are also reached. Finally, the air gap effect is discussed.

In order to convey the concept as well as demonstrate the feasibility of this work. The following parts of this paper are organized as follows: Section II introduces the fundamental theories of resonator sensor and the CSRR sensor; Section III is devoted to the methods covering simulation, modeling and dielectric retrieve; Section IV presents the measurements and error analysis; and Section V concludes this work.

FUNDAMENTAL THEORIES FOR RESONATOR AND CSRR

Dielectric Measurement Based on Resonator

For a conventional resonator sensor, the relationship between the change of resonant frequency $\Delta f_r/f_r$ and the dielectric constant and permeability of the sample can generally be expressed by [20].

$$\frac{\Delta f_r}{f_r} = \frac{\int_{V_c} (\Delta\varepsilon E_1 \cdot E_0 + \Delta\mu H_1 \cdot H_0)\, dV}{\int_{V_c} (\varepsilon_0 |E_0|^2 + \mu_0 |H_0|^2) dV} \quad (1)$$

where, V_c is the cavity volume, $\Delta\varepsilon$ is the change in complex permittivity, $\Delta\mu$ is the change in complex permeability, ε_0 and μ_0 are the free space permittivity and permeability, respectively. The electric and the magnetic fields of the empty cavity are denoted asE_0 and H_0, while E_1 andH_1 represent the electric and the magnetic fields under loaded condition, respectively. For electrically small samples, the electric and the magnetic fields inside the resonator, before and after loading the sample, are assumed to be unchanged. For dielectric materials, the change in complex permeability μ may be assumed to be zero. Also, the electric energy must be equal to the magnetic field energy stored in the resonant structure at the resonant frequency. Under these conditions, the frequency shift can be simplified as

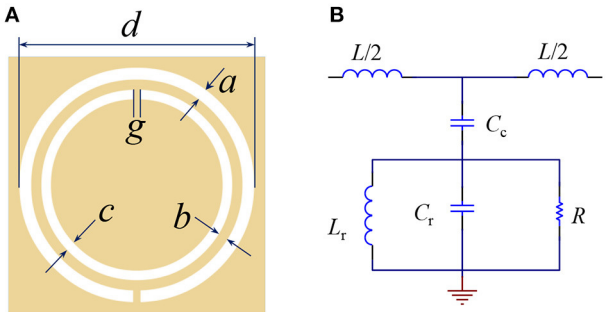

FIGURE 1 | Structure and equivalent model of the CSRR sensor. **(A)** The schematic structure; **(B)** Equivalent circuit model.

$$\frac{\Delta f_r}{f_r} = \frac{\int_{V_s} \Delta\varepsilon E_1 \cdot E_0 dV}{2\int_{V_c} \varepsilon_0 |E_0|^2 dV} \quad (2)$$

where, V_s is the sample volume.

This is a general description of resonator for dielectric measurement. Such a method, however, is in practice only suitable for well-defined structure and field distribution (or mode). For a structure of a bit more complicated, closed form for frequency shift is usually difficult to find. With the rapid development of numerical techniques, simulation methods have been widely used in the calculation of complicated structures. In addition, more details can be derived from the simulation results.

Dielectric Measurement Based on CSRR Resonator

Several geometries based on the CSRR structure have been proposed in the Literature [21–24]. In material characterization, the sensitivity of the planar sensor is of the primary concern, which is further associated with the electric and the magnetic field intensity present across the planar architecture. It has been recognized that circular resonator may provide better accuracy [25].

The CSRR structure is illustrated in **Figure 1A**. The quasi-static electrically small resonators are usually designed with a loop and a gap separating the loop into two parts. The electrically small structure resonates due to inductance induced by circulating current in the loop and the effective capacitance developed across the gap between the loops. The change in capacitance of CSRR usually depends on the change in the permittivity of the material under test (MUT), whereas the inductance of the CSRR is considered to be unchanged in case of dielectric materials.

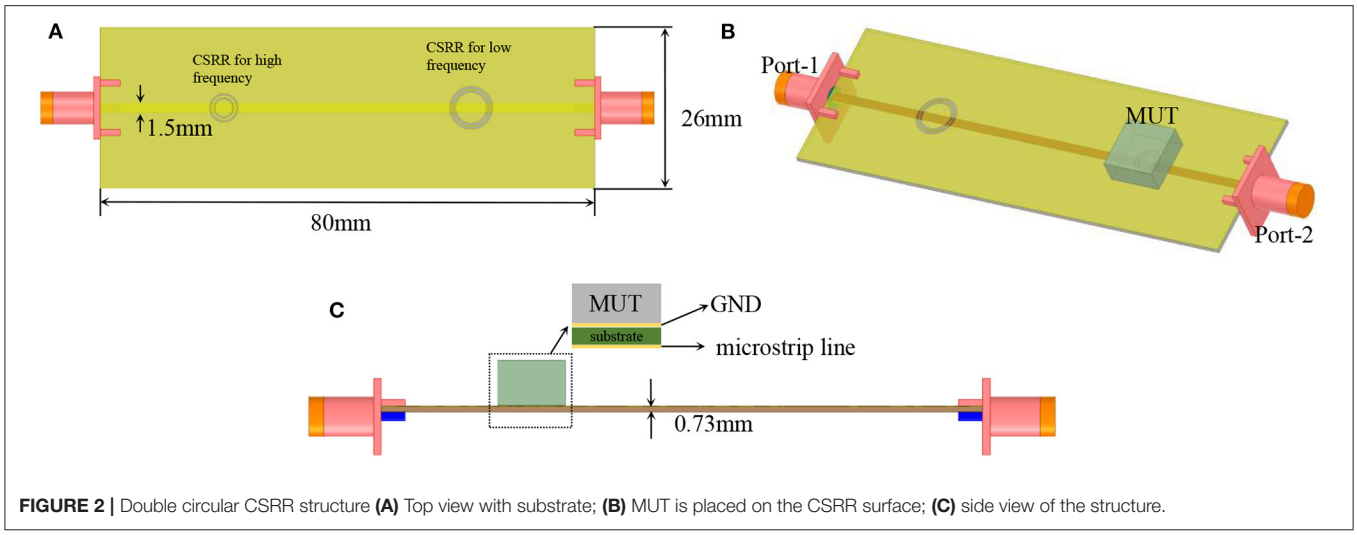

FIGURE 2 | Double circular CSRR structure **(A)** Top view with substrate; **(B)** MUT is placed on the CSRR surface; **(C)** side view of the structure.

This structure can be modeled using an equivalent circuit, as shown in **Figure 1B**, where, L_r, $C_r$represent the inductance and capacitance of CSRR, respectively, $L$is the line inductance, C_c is the coupling capacitance between micro strip line and CSRR. To extract the exact values of these components, full wave simulation using HFSS in couple with ADS simulation has to be conducted [26].

After these parameters are determined, it can be drawn from **Figure 2** that the relationship between the resonant frequency can be written as

$$f_r = \frac{1}{2\pi\sqrt{L_r(C_c + C_r)}} \tag{3}$$

This is a fast way to estimate the resonating frequency and the dimension. In the previous publications, only one operation band was achieved. In order to obtain dual-band operation, two identical CSRR structures of difference sizes are used, as shown in **Figure 2A**. The larger CSRR structure works in lower frequency band, and the smaller one in higher frequency band. These two structures are separated by a certain distance in order to reduce mutual coupling.

Two circular CSRR structures are etched out from the GND layer. MUT is placed on top of the CSRR and covers it completely. Field will be coupled to the sample though the circular slots, therefore, it is expected that such field-matter interaction will be reflected in the transmission coefficient of this structure.

The Simulation Results for Unloaded Dual-Band CSRR

Before any measurement can be conducted, the dual-band CSRR has to be designed. In this work, we choose 1.8GHz-2.8GHz and 3.5GHz-5GHz as two separate working bands for measurement. By placing two CSRRs on the same sensor, and through optimization, the following parameters as shown in **Table 1** are reached. In this design, the substrate is FR4 with the dielectric constant being 4.9. The extracted lumped parameters for each component in **Figure 1B** are presented in **Table 2**.

TABLE 1 | The main parameters for the two operation bands.

Parameters (mm)	a	b	c	g	d
Band-1:1.8GHz-2.8GHz	0.39	0.22	0.38	0.22	7
Band-2:3.5GHz-5GHz	0.2	0.11	0.19	0.11	3.5

TABLE 2 | The lumped parameters for the equivalent circuits.

Lumped parameters	Band-1	Band-2
L	4.214	1.214
C_c	0.7,737	0.4,737
C_r	1.2,817	0.7,221
L_r	1.7,547	0.8,672

In this work, the full wave simulation was conducted using HFSS. And the circuit simulation was done using ADS. The full wave simulation is to precisely predict the response of the design and the ADS simulation is to fast pinpoint the resonating frequencies. The simulated results for unloaded situation are plotted in **Figure 3**. The reason for using S_{21} as representative data is that S_{21} is closely related to the resonating frequency and the quality factor. It is clearly seen that the simulated results using HFSS and ADS demonstrated very good agreement in terms of resonating frequencies. The discrepancy in the transmission coefficient outside the resonating frequencies is due to the fact that the circuit theory only reflects the resonating frequency. More complicated modeling has to be built to fully model the structure.

After mounting the sample to the top of each CSRR resonator, the resonating frequency undergoes shift, and the quality factor will also show variation with the loss tangent. It is seen

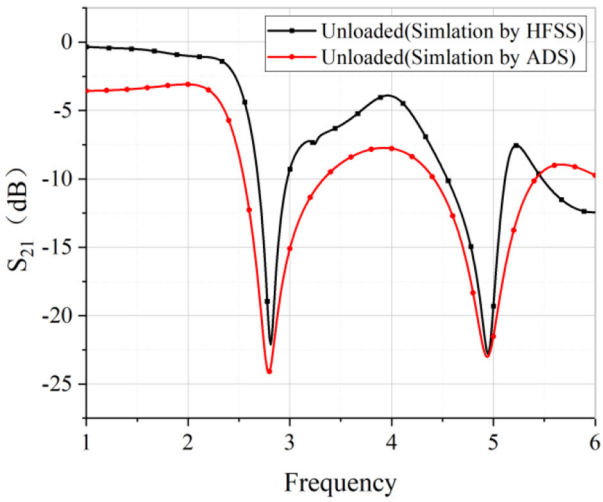

FIGURE 3 | The transmission coefficient on unloaded cases.

from **Figures 4A,B**, when the sample is placed at the low-frequency CSRR, the first resonance changes accordingly with ε_r, while the position of the second resonance remains unchanged. Keep$\varepsilon_r$unchanged, varying the loss tangent will not change the resonating frequencies of either band, however, the quality factor (the depth of the resonance) will be changed noticeably. Placing the sample at the second CSRR, the same observations can be made, as shown in **Figures 4C,D**. It is also noticed that the quality factor is also dependent on the dielectric constant. Such phenomenon is evident by that the Resonate depth is varying with the dielectric constant. In summary, such properties can be made for use of dielectric constant measurement as single value functions can be derived, as shown in **Figure 5**.

METHODS

Up to now, we have demonstrated that the transmission coefficient S_{21} does reflect the changing of dielectric constant and loss tangent. To extract the parameter from S_{21}, a method has to be developed. Also, some practical aspects, such as the optimal thickness of the sample has to be considered. In next section, quantitative analysis on the variation of the resonating frequency and quality factor with the dielectric property will be analyzed, aiming to reach a reliable expression for dielectric constant extract.

Variation of Resonating Frequency and Quality Factor With Dielectric Constant

The resonating frequency at each ε'_r is recorded, and Δf_r is calculated using $\Delta f_r = f_0 - f_r$. As the dielectric constant changes, the resonant frequency also gradually increases in a nonlinear manner. This indicates that the variation of the frequency is a single value function of the permittivity and loss tangent.

It is found during the analysis that the sample thickness will affect the measurement results. To search for the optimal thickness for measurement, parametric study over a range of thickness is conducted. The analysis results are plotted in **Figure 6**.

It is seen from **Figures 6A,B**, for the lower frequency band, both the dielectric constant and the loss tangent present good linearity when the sample thickness is 6 mm. Therefore, it is best to prepare 6 mm thick sample for measurement in the low frequency band. And one has

$$\varepsilon'_{r\_low} = \frac{f_{r\_low}^{-2} - 0.11529}{0.01677} \tag{4}$$

Similar, the optimal sample thickness for the higher frequency band is 4 mm, and one has

$$\varepsilon'_{r\_high} = \frac{f_{r\_high}^{-2} - 0.0343}{0.00545} \tag{5}$$

It is reasonable that the lower frequency requires larger sample and the higher frequency needs smaller one. This is closely related to the electrical size of each resonator.

Theoretically, the dielectric constant of the MUT in two different frequency bands can be calculated separately by Equations (4) and (5), which are very close to relationship of $f_r \propto 1/\sqrt{\varepsilon'_{r\_high}}$.

It can be seen from **Figures 6C,D** that the relationship between Q_{MUT}^{-1} and $\tan\delta$ is a linear function for the tested sample of selected thickness. The specific calculation method of Q_{MUT}^{-1} is related to its Q_U at unloaded and the S_{21} parameter coefficient after adding load [27].

$$Q_{MUT} = Q_U\left[1 - 10^{\frac{S_{21}(dB)}{20}}\right] \tag{6}$$

Q_U is the quality factor of the sensor at unload. It is calculated from the center frequency and the frequency at−3dB. The loaded quality factor will be used for retrieval of the loss tangent. However, Equation (6) does not take into account the mutual effect of involving dielectric constant and loss tangent. In this regard, new fitting formulae will be derived in later section to retrieve the loss tangent more accurately.

Building the Permittivity Retrieval Function of Resonating Frequency and Quality Factor

The samples with dielectric constants and loss tangents are simulated in two Frequency bands, and two sets of curves are obtained, as shown in **Figure 6**. It is seen from **Figure 6**, the numerical models in the two frequency bands can be fitted separately. In many cases, the permittivity is also expressed using dielectric constant and imaginary part. The imaginary part of the complex permittivity of the MUT can be expressed by the loss tangent value, and the loss tangent value can be calculated by the Q_{MUT} and ε'_r. The formula can be written as [28].

$$Q_{MUT} = \frac{1}{\tan\delta} = \frac{\varepsilon'_r}{\varepsilon''_r} \tag{7}$$

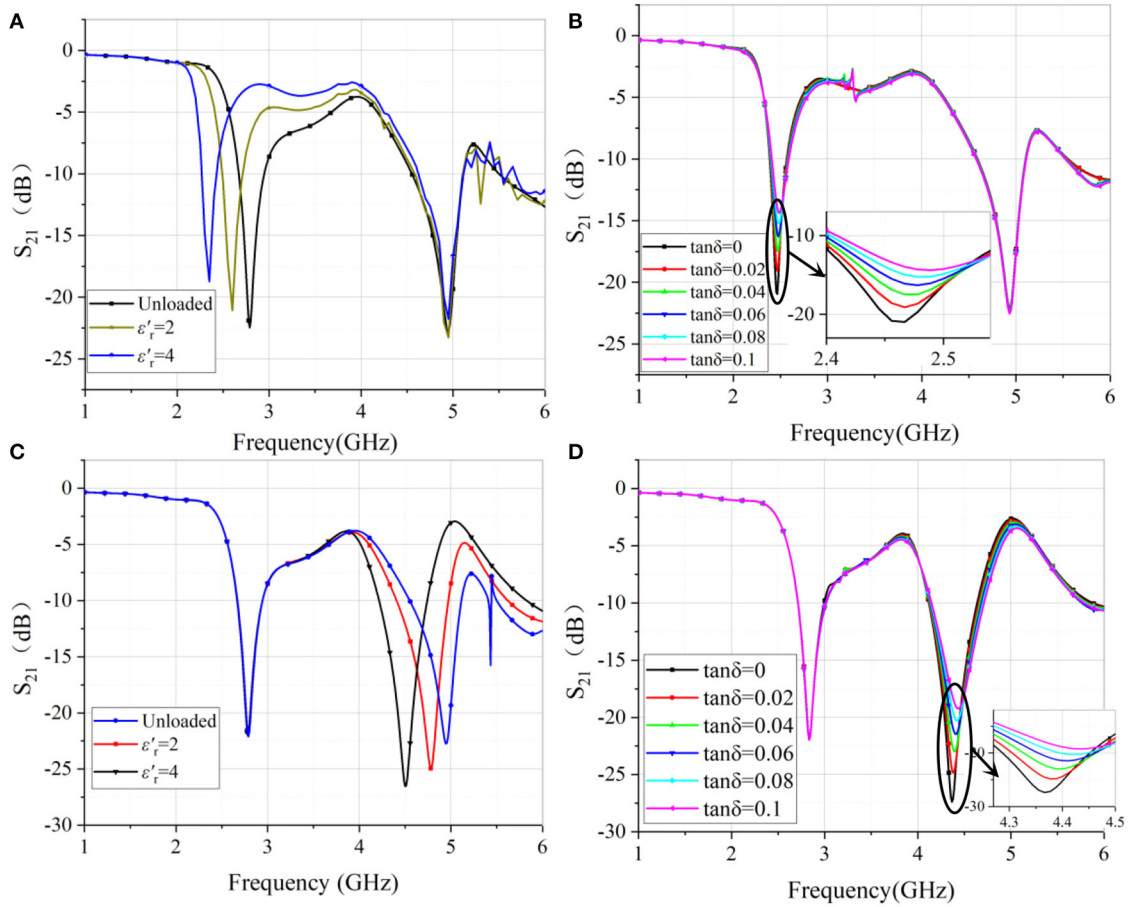

FIGURE 4 | S_{21} parameters of samples **(A)** with different dielectric constants at 1.8GHz-2.8GHz; **(B)** with different loss tangent when the $\varepsilon'_r = 3$ at 1.8GHz-2.8GHz (sample thickness = 6mm); **(C)** with different dielectric constants at 3.5GHz-5GHz; **(D)** with different loss tangent when the $\varepsilon'_r = 3$ at 3.5GHz-5GHz (sample thickness = 4 mm).

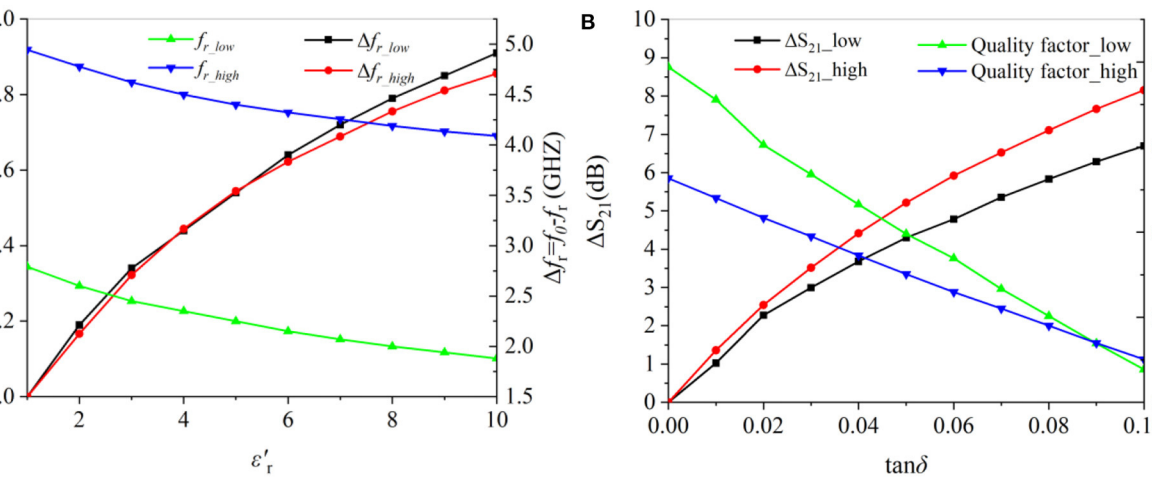

FIGURE 5 | S_{21} parameters of samples **(A)** with different dielectric constants1.8GHz-2.8GHz; **(B)** with different loss tangent 3.5GHz-5GHz.

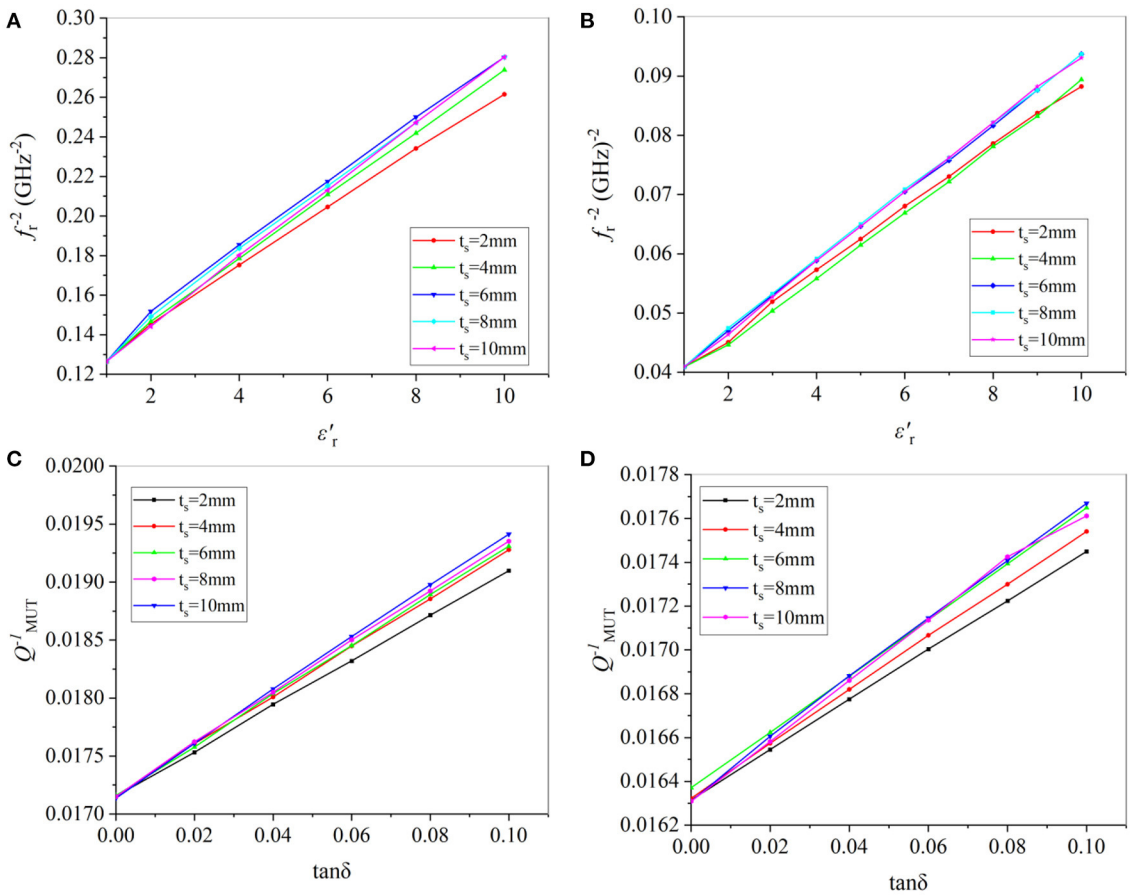

FIGURE 6 | Thickness effects. **(A)** f_r^{-2}vs. ε'_r for different thickness at 1.8GHz-2.8GHz; **(B)** f_r^{-2} vs. ε'_r for different thickness at 3.5GHz-5GHz; **(C)** Q^{-1}_{MUT} vs. tan δ for different thickness at 1.8GHz-2.8 GHz; **(D)** Q^{-1}_{MUT} vs. tan δ for different thickness at 3.5GHz-5GHz.

Two models of Rational Taylor [29] and Extreme Cum [30] are used to fit the functions corresponding to the two frequency bands. In the Rational Talor model, both nominator and denominator are polynomial of the dielectric constant and the quality factor. For the Extreme Cum model, the fitting Function are exponential polynomial. The Goodness of fitting of a statistical model describes how well it fits simulation data [31], and is denoted by R^2. It is equal to the ratio of the regression sum of squares to the total sum of squares. The closer the R^2 of the function model is to 1, the better the fit of the function established by the model. Fitting the data in **Figure 7** using the two models, the following equations can be obtained for low and high frequency bands, respectively. For the low-frequency band, the imaginary part can be calculated using

$$\varepsilon''_{r\_Low} = \varepsilon'_{r\_Low} \cdot \frac{F\left(Q^{-1}_{MUT\_low}, \varepsilon'_{r\_Low}\right)}{G\left(Q^{-1}_{MUT\_low}, \varepsilon'_{r\_Low}\right)} \tag{8}$$

where

$$\begin{cases} F\left(Q^{-1}_{MUT\_low}, \varepsilon'_{r\_Low}\right) = 1 - 66.650Q^{-1}_{MUT\_low} \\ +2013.247Q^{-2}_{MUT\_low} \\ -11.100\varepsilon'_{r\_Low} \cdot Q^{-1}_{MUT\_low} - 0.167\varepsilon'_{r\_Low} + 0.163\left(\varepsilon'_{r\_Low}\right)^2 \\ G\left(Q^{-1}_{MUT\_low}, \varepsilon'_{r\_Low}\right) = -0.642 - Q^{-1}_{MUT\_low} \\ +13.649\varepsilon'_{r\_Low} \cdot Q^{-1}_{MUT\_low} - 0.212\varepsilon'_{r\_Low} - 0.004\left(\varepsilon'_{r\_Low}\right)^2 \end{cases} \tag{9}$$

And for the high-frequency band

$$\varepsilon''_{r\_high} = \frac{\varepsilon'_{r\_high}}{H(Q^{-1}_{MUT\_high}, \varepsilon'_{r\_high})} \tag{10}$$

where

$$H(Q^{-1}_{MUT\_high}, \varepsilon'_{r\_high}) = 0.444 - 32.158e^{D(Q^{-1}_{MUT\_high})} \\ -12.623e^{E(\varepsilon'_{r\_high})} + 848.631e^{D(Q^{-1}_{MUT\_high})+E(\varepsilon'_{r\_high})} \tag{11}$$

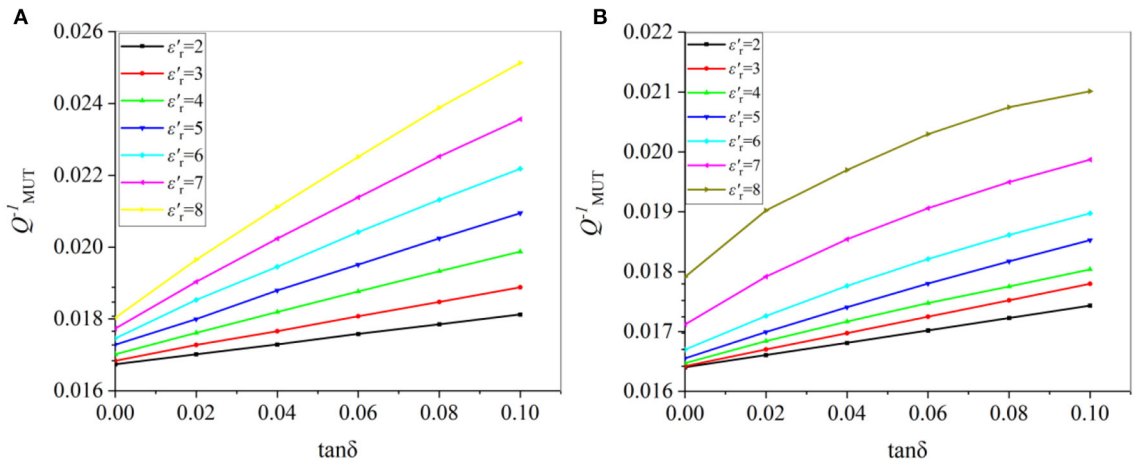

FIGURE 7 | The linear relationship between the reciprocal of the Q^{-1}_{MUT} factor and tan δ under different ε_r' values in the band of **(A)** 1.8GHz-2.8GHz; **(B)** 3.5GHz-5GHz.

and

$$\begin{cases} D(Q^{-1}_{MUT\_high}) = -e^{\frac{-Q^{-1}_{MUT\_high}+0.0366}{0.014}} \\ E(\varepsilon'_{r\_high}) = -e^{\frac{\varepsilon'_{r\_high}+63.224}{61.564}} \end{cases} \quad (12)$$

Putting Q^{-1}_{MUT} and ε'_r into these equations, the loss tangent under the two frequency bands can be calculated. Here, the R^2 of Rational Taylor and Extreme Cum is 0.9977 and 0.9752, respectively. They are sufficiently good for data retrieve.

MEASUREMENTS AND RESULTS

Measurements

The sensor is manufactured using planar PCB technology, as shown in **Figure 8**. The substrate is 0.8 mm thick FR4 substrate with 4.9 dielectric constant. A pair of 50 Ω SMA connectors are soldered onto both ends of the sensor. Measurement was done using a vector network analyzer (VNA) *Ceyear* AV3672D. The VNA is calibrated using a standard short-load-open-thru (SLOT) method with a 3211-3.5mm calibration kit. The measurement frequency was 1 GHz - 6 GHz.

After calibrating the system, the S_{21} of unloaded situation was first measured. Then, several samples were measured by placing these samples at the two CSRRs consecutively. The transmission coefficients S_{21} are plotted in **Figure 9**. From the measured data, the resonating frequency and the quality fact can be deduced. And therefore, the dielectric constant and loss tangent can be calculated by using the simulated results. The retrieved results are tabulated in **Table 3**, with comparison with the data in the literature [32, 33].

It is seen from the results that the agreement between the simulation and measurement is pretty good. For most samples, the accuracy of the dielectric constant is smaller than 1.5%. The only exception is Polycarbonate,

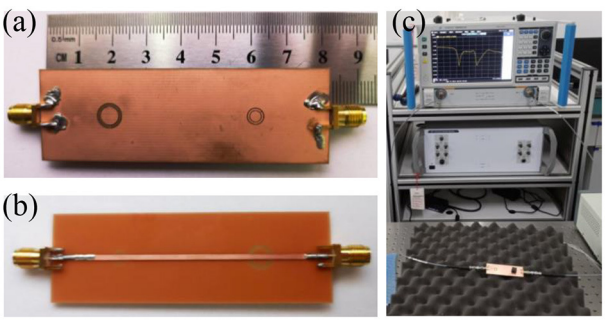

FIGURE 8 | Experimental verification. **(a)** Top view of the CSCR; **(b)** Bottom view of the CSRR; **(c)** Experiment set up.

the discrepancy is 5%. The loss factor is also very close to the provided value in the literature. For the polycarbonate, the discrepancy is very much dependent on the difference in the sample since polycarbonate has very broad range of permittivity.

The Effects of Air Gap

When using a sensor with a CSRR structure to accurately measure the complex permittivity, the air gap between the GND layer and the sample surface is an important factor affecting the measurement results. In this paper, an approximate model of the air gap is set up through HFSS. The thickness of the air gap is set to be 0 to 80μm, and various dielectric constants in the range of 1 to 10 are simulated. The material is polypropylene. The relationship between f_r^{-2} and ε'_r in different frequency bands is shown in **Figure 10**. It is clearly seen that the slope of the curve decreases as the thickness of the air gap increases. This is reasonable since with the increase of the air gap, more energy will be stored in the air gap so that the effective dielectric constant is reduced. This will in turn reduce the frequency shift. The air gap effect is a challenge for micro strip based dielectric measurement.

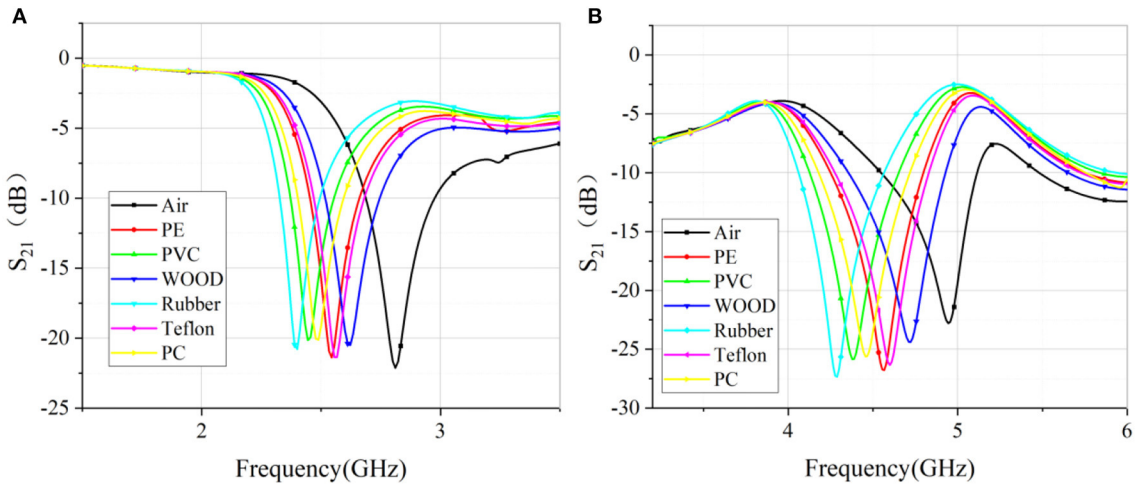

FIGURE 9 | (A) Measured S_{21} (dB) for various dielectric samples at 1.8GHz-2.8GHz. **(B)**. Measured S_{21} (dB) for various dielectric samples at 3.5GHz-5GHz.

TABLE 3 | Comparison between measured results of this work and data in the literature.

	Reference Value		Measured data(1.8GHz-2.8GHz)		Measured data(3.5GHz-5GHz)	
MUT	ε'_r	ε''_r	ε'_r	ε''_r	ε'_r	ε''_r
PE	2.26	0.0007	2.25	0.00072	2.25	0.00066
PVC	3	0.027	2.98	0.028	2.97	0.032
WOOD	2	0.034	1.97	0.032	1.97	0.029
Rubber	3.4	/	3.37	/	3.36	/
Teflon	2.1	0.006	2.12	0.0058	2.12	0.006
Polycarbonate	2.8	0.003	2.78	0.0032	2.72	0.0035

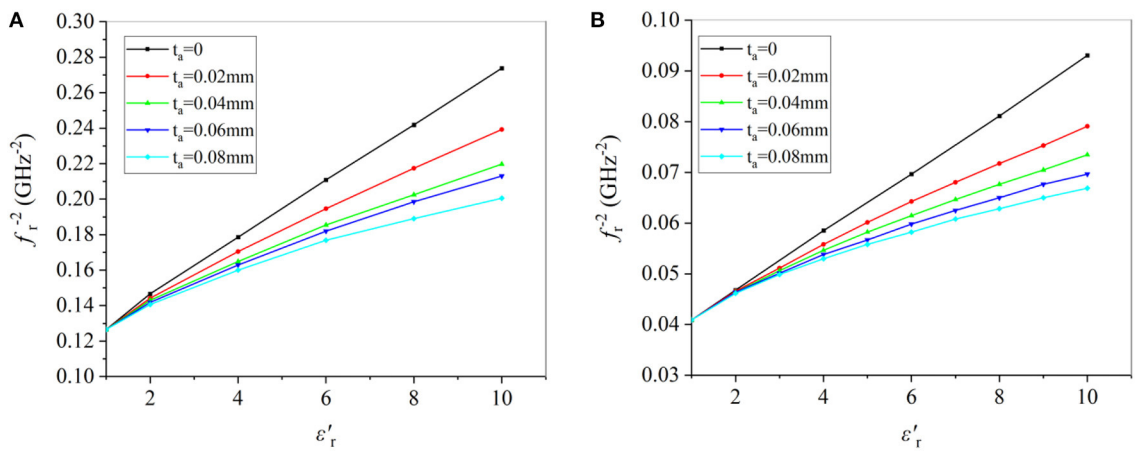

FIGURE 10 | Plot of $f_r^{-2}$with real permittivity at different air gap ranging from 0 to 80μm at **(A)** 1.8GHz-2.8GHz; **(B)** 3.5GHz-5GHz.

To account for this effect, a realistic way is to consider the air gap as part of the structure. By so doing, more precise value can be obtained.

Fitting the data in **Figure 10**, the relationship between the dielectric constant and the air gap can be obtained.

$$\varepsilon'_{\text{r\_low}} = -3.065 - 106.874t_{\text{a}} - 115.880t_{\text{a}}^2 + 17.847f_{\text{r}}^{-2} + 115.712f_{\text{r}}^{-4} + 847.953t_{\text{a}} \cdot f_{\text{r}}^{-2} \quad (13)$$

$$\varepsilon'_{\text{r\_high}} = -2.720 - 107.945t_{\text{a}} - 161.583t_{\text{a}}^2 + 54.595f_{\text{r}}^{-2} + 969.123f_{\text{r}}^{-4} + 2613.400t_{\text{a}} \cdot f_{\text{r}}^{-2} \quad (14)$$

Both Equations (13) and (14) are fitted with Poly2D models [30], and their R^2 are 0.9916 and 0.9895 respectively.

To apply these formulae, the air gap has to be precisely measured. And the frequency shift has to be measured using either a VNA or a spectrum analyzer. This method can be used separately, but they are not general ones that can be used to other structures. However, this method can be instructive to dielectric measurement.

Taking the wood in **Table 3** as an example. Measure the degree of adhesion between the wood and the CSRR surface by microscope micrometer, the air gap is 3um. Corrected by Equations (13) and (14), the dielectric constants are 2 and 1.99 in the two frequency bands respectively. The corrected values are much closer to the values in the literature.

CONCLUSION

A dual-band non-destructive dielectric measurement sensor based on complementary split-ring resonator has been studied and experimentally verified. By pacing two complementary split-ring resonators with a proper separation distance on the same sensor, dual-band operation has been realized with excellent isolation. The measured results demonstrated very good agreement with the data in the literature. In addition, the air-gap effects have been analyzed and better agreement can be obtained.

DATA AVAILABILITY STATEMENT

The raw data supporting the conclusions of this article will be made available by the authors, without undue reservation.

AUTHOR CONTRIBUTIONS

CW did the simulation and measurement. XL proposed the idea and designed the measurement and finalized the edition. CW and XL prepared the draft. LG and QC did investigation. All authors contributed to the article and approved the submitted version.

FUNDING

This work was supported by the National Natural Science Foundation of China under Contract 61871003, and the open project of the State Key Laboratory of complex electromagnetic environment effects on electronics and information system under Grant CEMEE2021Z0201B, and the open-ended Foundation of National Radar Signal Processing Laboratory under Grant 61424100105.

REFERENCES

1. Kirichek A, Chassagne C, Ghose R. Predicting the dielectric response of saturated sandstones using a 2-electrode measuring system. *Front Phys.* (2019) 6:148. doi: 10.3389/fphy.2018.00148
2. Adamietz R, Desmulliez MPY, Pavuluri SK, Tilford T, Bailey C, Schreier-Alt T, et al. Reliability testing and stress measurement of QFN packages encapsulated by an open-ended microwave curing system. ieee transactions on components, packaging and manufacturing technology. *IEEE Transcations on components, packaging and manufacturing technology*. (2019) 9:173. doi: 10.1109/TCPMT.2018.2859031
3. Zhou Z, Feng W, Chen Y, Ge N. Adaptive scheduling for millimeter wave multi-beam satellite communication systems. *J Commun Inf Netw.* (2016) 1:42. doi: 10.1007/BF03391569
4. Liu X, Yu S, Gan L, Yu J. Broadband quasi-optical dielectric spectroscopy for solid and liquid samples. *Int J Inf Mill Ter Waves.* (2020) 41:810. doi: 10.1007/s10762-020-00710-5
5. Gowrish B, Mansour RR. A novel bandwidth reconfigurable waveguide filter for aerospace applications. *IEEE Mic Wir Comp Lett.* (2020) 30:577. doi: 10.1109/LMWC.2020.2989283
6. Tosaka T, Fujii K, Fukunaga K, Kasamatsu A. Development of complex relative permittivity measurement system based on free-space in 220–330-ghz range. *IEEE Trans Ter Sci Tech.* (2014) 5:102 doi: 10.1109/TTHZ.2014.2362013
7. Rashidian A, Shafai L, Klymyshyn D, Shafai C. A fast and efficient free-space dielectric measurement technique at mm-wave frequencies. *IEEE Ant Wir Pro Lett.* (2017) 16:2630. doi: 10.1109/LAWP.2017.2737632
8. Fontana N, Canicattì E, Monorchio A. *An Application of the Virtual Transmission Line Model of an Open-Ended Coaxial Probe for Dielectric Properties Characterization of Biological Tissues*. Atlanta, GA: 2019 IEEE International Symposium on Antennas and Propagation and USNC-URSI Radio Science Meeting (2019). p. 341.
9. Szostak K, Słobodzian P. Broadband dielectric measurement of PCB and substrate materials by means of a microstrip line of adjustable width. *IEEE Mic Wir Comp Lett.* (2018) 28:945. doi: 10.1109/LMWC.2018.2864196
10. Jha AK, Akhtar MJ. A generalized rectangular cavity approach for determination of complex permittivity of materials. *IEEE Trans Inst Meas.* (2014) 63:2632. doi: 10.1109/TIM.2014.2313415
11. Tiwari NK, Jha AK, Singh SP, Akhter Z, Varshney PK, Akhtar MJ. Generalized multimode SIW cavity-based sensor for retrieval of complex permittivity of materials. *IEEE Tran Micro The Tech*. (2018) 66:3063. doi: 10.1109/TMTT.2018.2830332
12. Boybay MS, Ramahi OM. Material characterization using complementary split-ring resonators. *IEEE Tran Ins Meas*. (2012) 61:3039. doi: 10.1109/TIM.2012.2203450
13. Muqaibel AH, Safaai-Jazi A, Riad SM. Fork-coupled resonators for high-frequency characterization of dielectric substrate materials. *IEEE Trans Ins Meas.* (2006) 55:2216. doi: 10.1109/TIM.2006.884390
14. Waldron I, Makarov SN, Biederman S, Ludwig R. Suspended ring resonator for dielectric constant measurement of foams. IEEE Micro Wir Comp Lett. (2006) 16:496. doi: 10.1109/LMWC.2006.880708
15. Mohd Bahar AA, Zakaria Z, Ab Rashid SR, Isa AAM, Alahnomi AR. High-Efficiency microwave planar resonator sensor based on bridge split ring topology. *IEEE Micro Wir Comp Lett*. (2017) 27:545. doi: 10.1109/LMWC.2017.2701338

16. Zarifi MH, Daneshmand M. Monitoring solid particle deposition in lossy medium using planar resonator sensor. *IEEE Sens J.* (2017) 17:7981. doi: 10.1109/JSEN.2017.2757027
17. Lim S, Kim C, Hong S. Simultaneous measurement of thickness and permittivity by means of the resonant frequency fitting of a microstrip line ring resonator. *IEEE Micro Wir Comp Lett.* (2018) 28:539. doi: 10.1109/LMWC.2018.2833202
18. Ansari MAH, Jha AK, Akhtar MJ. Design and application of the CSRR-based planar sensor for noninvasive measurement of complex permittivity. *IEEE Sens J.* (2015) 15:7181. doi: 10.1109/JSEN.2015.2469683
19. Tiwari NK, Tiwari Y, Akhtar MJ. Design of CSRR-based electronically tunable compact RF sensor for material testing. *IEEE Sens J.* (2018) 18:7450. doi: 10.1109/JSEN.2018.2861365
20. Chen LF, Ong CK, Neo CP, Varadan VV, Varadan VK. *Microwave Electronics: Measurement and Materials Characterization.* New Jersey: John Wiley & Sons (2004).
21. Duran Sindreu M, Naqui J, Bonache J, Martin F. Split rings for metamaterial and microwave circuit design: a review of recent developments. *Int J RF Micr Comp Aided Eng.* (2012). 22:439 doi: 10.1002/mmce.20635
22. Gan HY, Zhao WS, He L, Yu Y, Xu K, Wen F, et al. A CSRR-loaded planar sensor for simultaneously measuring permittivity and permeability. *IEEE Micro Wir Comp Lett.* (2020) 30:219 doi: 10.1109/LMWC.2019.2957657
23. Saadat-Safa M, Nayyeri V, Khanjarian M, Soleimani M, Ramahi M. A CSRR-based sensor for full characterization of magneto-dielectric materials. *IEEE Trans Micro Theory Tech.* (2019) 67:806. doi: 10.1109/TMTT.2018.2882826
24. Oliveira João GD, Pinto EN, Silva Neto VP, D'Assunção AG. CSRR-based microwave sensor for dielectric materials characterization applied to soil water content determination. *Sensors.* (2020) 20:255. doi: 10.3390/s20010255
25. Govind G, Tiwari NK, Agrawal KK, Akhtar MJ. Microwave subsurface imaging of composite structures using complementary split ring resonators. *IEEE Sens J.* (2018) 18:7442. doi: 10.1109/JSEN.2018.2859228
26. Ebrahimi A, Withayachumnankul W, Al-Sarawi SF, Abbott D. Dual-mode behavior of the complementary electric-LC resonators loaded on transmission line: analysis and applications. *J Appl Phys.* (2014) 116:439. doi: 10.1063/1.4893751
27. Kai C, Hsieh L. Microwave ring circuits and related structures second edition. *Cir Dev Mag IEEE.* (2004) 22:36. doi: 10.1109/MCD.2006.1708387
28. Pozar David M. *Microwave Engineering.* John wiley & sons (2011).
29. Hazewinkel M. *Rational Function*, *Encyclopedia of mathematics.* Berlin: EMS Press (2001).
30. Yongjiu S, Wei S, Yuanqing W, Yi L, Yue X. *The Pressure Distribution of Insulating Glass Unites Under Thermal Gradient*. Lushan: 2011 International Conference on Electric Technology and Civil Engineering (2011). p. 862.
31. Liu Q, Lee JD, Jordan MI. A kernelized stein discrepancy for goodness-of-fit tests. International conference on machine learning. *Pro Mach Lear Res. arXiv:1602.03253* (2016) 276.
32. *Ansys HFSS Material Library*. (2020) Available online at: https://www.ansys.com/products/electronics/ansys-hfss (accessed March 28).
33. The Engineering Tool Box. *Relative Permittivity-Dielectric Constant.* (2015). Available online at: http://www.engineeringtoolbox.com/relative-permittivity-d_1660.html (accessed March 28).

Conflict of Interest: The authors declare that the research was conducted in the absence of any commercial or financial relationships that could be construed as a potential conflict of interest.

frontiers in Physics

ORIGINAL RESEARCH
published: 13 May 2021
doi: 10.3389/fphy.2021.678777

Self-Calibrated Measurement of Frequency Response for Broadband Photodetectors Based on Two-Tone Photonic Sampling

Mengke Wang, Ying Xu, Yutong He, Zhao Liu, Yali Zhang, Zhiyao Zhang, Heping Li, Shangjian Zhang and Yong Liu*

State Key Laboratory of Electronic Thin Films and Integrated Devices, School of Optoelectronic Science and Engineering, University of Electronic Science and Technology of China, Chengdu, China

A self-calibrated method to measuring the frequency responses of broadband photodetectors (PDs) is proposed based on photonic pulse sampling of two-tone microwave signal, with the help of a mode-locked laser diode (MLLD) and a Mach-Zehnder modulator (MZM). Firstly, the repetition frequency of the optical comb from the MLLD divides the whole measuring frequency range into several segments. Then, a close-spaced two-tone signal modulates every comb tooth through the MZM and generates the sum- and difference-frequency products, working as the probing signal to extract the frequency response of the PD in every segment. Hyper-fine frequency response of the PD at any frequency point can be obtained in every segment by subtly varying the center frequency of the two-tone signal while keeping the difference frequency fixed. Finally, the whole frequency response of the PD in ultra-wide frequency range is obtained by seamlessly stitching the segmental frequency responses. In our experiment, measurement of a commercial PD is demonstrated up to 49.765 GHz with an optical comb at the repetition frequency of 9.953 GHz and a two-tone modulation up to 4.9765 GHz. The measured results are compared with those by using the traditional methods to check accuracy. Moreover, the uneven responses of the MLLD and the MZM are fully subtracted, verifying the ultra-wideband, hyperfine and self-calibrated measurement of PDs based on the two-tone photonic sampling.

Keywords: frequency response, photodetectors, photonic sampling, optical fiber communication, microwave photonics

OPEN ACCESS

Edited by:
Jinjin Li,
Shanghai Jiao Tong University, China

Reviewed by:
Xie Liang,
Institute of Semiconductors (CAS), China
Zizheng Cao,
Eindhoven University of Technology, Netherlands

****Correspondence:***
Shangjian Zhang
sjzhang@uestc.edu.cn

Specialty section:
This article was submitted to Interdisciplinary Physics, a section of the journal Frontiers in Physics

Received: *10 March 2021*
Accepted: *14 April 2021*
Published: *13 May 2021*

Citation:
Wang M, Xu Y, He Y, Liu Z, Zhang Y, Zhang Z, Li H, Zhang S and Liu Y (2021) Self-Calibrated Measurement of Frequency Response for Broadband Photodetectors Based on Two-Tone Photonic Sampling. Front. Phys. 9:678777. doi: 10.3389/fphy.2021.678777

INTRODUCTION

Broadband photodetectors (PDs) are essential optical receiver components in optical fiber communication systems and microwave photonic links [1–3], and the frequency response measurement with high-resolution and high-accuracy is very critical to supporting the device characterization and link evaluation for high-spectral-efficiency optical communication systems and hyper-fine microwave photonic links [4–6].

There are numerous methods reported for characterizing frequency responses of PDs by employing all-optical or electro-optical stimulus. The all-optical methods can achieve ultra-wideband measurements of PDs based on the ultra-wideband optical stimulus. However, the

optical wavelength-beating method requires to control the optical wavelength drifting and power fluctuation with extremely high accuracy [7–10], and the optical noise-beating method is subject to the poor signal-to-noise ratio and insufficient frequency resolution [11–14]. By contrast, the electro-optical methods make the best use of electro-optical modulation to improve the frequency resolution. However, the widely used electro-optical swept frequency method needs intense calibration to subtract the effect of the assisted modulator [15–17]. In order to alleviate the electro-optical calibration, the improved swept frequency method was proposed with the help of an electro-absorption modulator used as a modulator and a PD, provided that the frequency responses of the modulator and the PD are identical [18, 19]. The twice modulation method requires active bias control of two intensity modulators [20]. For the calibration-free and bias-drifting-free measurement, we proposed a frequency-shifted heterodyne scheme for extracting frequency responses of PDs [21–24]. Recently, we also presented a low-speed photonic sampling method for the frequency response measurement within ultra-wide frequency range based on a mode-locked laser diode (MLLD), which is also free of the uneven frequency responses of other components in the setup [25]. Nevertheless, the major difficulty of this method lies in that hyper-fine measurement of PD at any frequency point cannot be obtained, since the frequency resolution is limited to be tens of MHz by the repetition frequency of the MLLD.

In this work, we demonstrate a two-tone photonic sampling method, featuring hyper-fine frequency resolution and ultra-wide frequency range, for self-calibrated frequency response measurement of broadband PDs. As is shown in **Figure 1**, the optical pulses from a MLLD are sent to a Mach-Zehnder modulator (MZM) for two-tone modulation, and then are detected by the PD under test. Firstly, the whole frequency range is equally divided into several segments by the repetition frequency of the optical comb from the MLLD. The comb tooth in every segment mixes with the two-tone signal and generates the sum- and difference-frequency products, working as the probing signal to measure the frequency response of the PD, and then the hyper-fine frequency response of the PD at any frequency point is obtained in every segment by subtly varying the center frequency of the two-tone signal. Finally, the whole frequency response of the PD in ultra-wide frequency range can be obtained by stitching the multiple segments. It is noteworthy that the uneven response of the MLLD and the MZM are subtracted by carefully setting the two-tone photonic sampling. Theoretical basis and experimental results are elaborated in detail, where the experimental results agree well-with those obtained by employing the low-speed photonic sampling method.

Theoretical Basis

The schematic diagram of the proposed two-tone photonic sampling is shown in **Figure 1**. The ultrashort pulses with a repetition frequency of f_r from the MLLD is modulated by the two-tone signal at the frequencies of f_1 and f_2 *via* the MZM. After two-tone electro-optical modulation, upper- and lower-optical sidebands will be generated at both sides of the optical comb teeth of the MLLD. The two-tone sampling optical signals are then detected by the PD under test, and analyzed by an electrical spectrum analyzer (ESA). After photodetection, the two-tone upper- and lower-optical sidebands will mix with each other and generate sum- and difference-frequency products at the offset frequency of $f_1 \pm f_2$ ($f_1 > f_2$) of the comb tooth at the frequency of nf_r. As we know, each pair of optical upper- and lower-sidebands will keep equalized in the optical domain, and their amplitude difference in the electrical domain only depends on the frequency response of PD. In our method, the two-tone frequencies f_1 and f_2 are carefully chosen so that the lower frequency of Δf ($= f_1$-f_2) is fixed and close to DC, and the frequency response of the PD at the frequency of $nf_r + f_1 + f_2$ with respect to the frequency of $nf_r + \Delta f$ can be calculated through the amplitude ratio between these two frequency components, which is shown in **Figure 1(I)**. Then, through subtly varying $f_1 + f_2$ from 0 to f_r while keeping f_1–f_2 constant, the relative frequency response of the PD at any frequency point between $nf_r + \Delta f$ ($\approx nf_r$) and $nf_r + f_1 + f_2$ ($\approx (n+1)f_r$) can be extracted in the n-th segment. As is presented in **Figure 1(II)**, the frequency response at the frequency of $nf_r + f_1 + f_2$ is normalized to that at the frequency of $nf_r + \Delta f$ in every segment. In order to obtain the whole frequency response of PD in ultra-wide frequency range, in our case, a specific two-tone frequency is carefully chosen to be $f_1' = f_r/4$ and $f_2' = f_r/4$-Δf to ensure all the frequency responses at the frequencies of $nf_r + \Delta f$ are referenced to the same fixed low-frequency of Δf as illustrated in **Figure 1(III)**. Therefore, the segmental frequency responses are seamlessly stitched, as shown in **Figure 1(IV)**, allowing for the self-calibrated measurement of frequency response of PDs within ultra-wide frequency range of $(n+1)f_r$.

Mathematically, the ultrashort optical pulses from the MLLD can be expressed in the optical domain as

$$E_{MLLD}(t) = \sum_{l=-N}^{N} q_l e^{j2\pi (f_0 + lf_r)t} \tag{1}$$

Thereinto, f_0 and q_l are the central frequency of the amplitude of the optical comb from the MLLD, respectively. N represents the effective order of the optical comb tooth. The ultrashort optical pulses are injected into the MZM onto which two closely spaced tones $v_1(t) = v_1 \sin 2\pi f_1 t$ and $v_2(t) = v_2 \sin 2\pi f_2 t$ ($f_1 > f_2, f_1 \approx f_2$, and $0 < f_1, f_2 \leq f_r/2$) are applied. The output optical field from the MZM can be written by [26].

$$E_{MZM}(t) = E_{MLLD}(t) \cdot \left[1 + \gamma e^{jm_1 \sin 2\pi f_1 t + jm_2 \sin 2\pi f_2 t + j\varphi_b}\right] \tag{2}$$

with the asymmetric factor γ and the phase bias φ_b of the MZM. m_1 and m_2 are the modulation indices at the modulation frequencies of f_1 and f_2, respectively. Then, the photonic sampling signal is sent into the PD under test, and is then

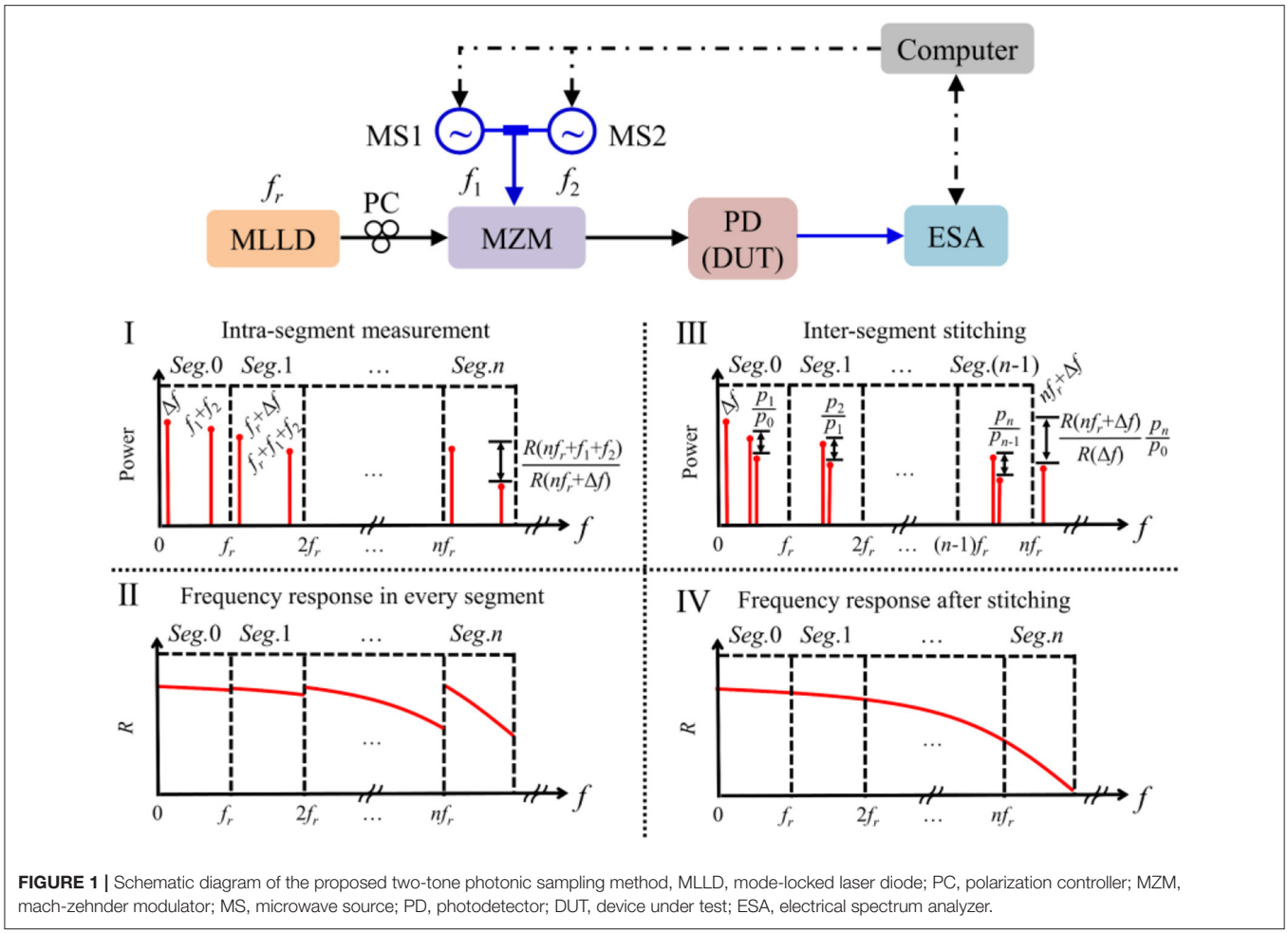

FIGURE 1 | Schematic diagram of the proposed two-tone photonic sampling method, MLLD, mode-locked laser diode; PC, polarization controller; MZM, mach-zehnder modulator; MS, microwave source; PD, photodetector; DUT, device under test; ESA, electrical spectrum analyzer.

converted into electrical domain, which can be written as

$$\begin{aligned} i_{PD}(t) &= R\cdot|E_{MZM}(t)|^2 = R\Big\{2\left(1+\gamma^2\right)\sum_{n=0}^{2N}p_n\cos\left(2\pi nf_rt\right) \\ &-p_0\left(1+\gamma^2\right)-2\gamma p_0\sum_{p=-\infty}^{+\infty}\sum_{q=-\infty}^{+\infty}J_p(m_1)J_q(m_2) \\ &\cdot\cos\left[2\pi\left(pf_1+qf_2\right)t+\varphi_b\right]+2\gamma\sum_{n=0}^{2N}p_n\sum_{p=-\infty}^{+\infty}\sum_{q=-\infty}^{+\infty}J_p(m_1) \\ &J_q(m_2)\cos[2\pi\left(nf_r\pm pf_1\pm qf_2\right)t\pm\varphi_b]\Big\} \end{aligned} \tag{3}$$

where R is the responsivity of PD, $J_p(\cdot)$ and $J_q(\cdot)$ are the pth and qth-order Bessel function of the first kind, respectively. The coefficient p_n represents the intensity of the comb tooth from the MLLD, expressed by

$$\sum_{l=-N}^{N-n}q_lq_{l+n}=p_n,\ (n=0,1,...,2N)$$

The two-tone signal will mix with each comb tooth and generate frequency up- and down-conversion components quantified as

$$\begin{aligned} &A\left(nf_r+f_1-f_2\right) \\ &\quad=4\gamma p_nR\left(nf_r+f_1-f_2\right)J_1(m_1)J_1(m_2)\cos\varphi_b \end{aligned} \tag{4a}$$

$$\begin{aligned} &A\left[nf_r\pm\left(f_1+f_2\right)\right] \\ &\quad=4\gamma p_nR\left[nf_r\pm\left(f_1+f_2\right)\right]J_1(m_1)J_1(m_2)\cos\varphi_b \end{aligned} \tag{4b}$$

where the bias status of the MZM is the same for these desired frequency components.

In our method, the whole measuring frequency range are divided into several segments by the repetition frequency f_r of the MLLD. The frequency component at $nf_r+f_1+f_2$ is served as the probe signal to extract the high frequency response of PD under test, meanwhile the frequency component at $nf_r+\Delta f$ ($\Delta f=f_1-f_2$) is taken as the reference signal. Therefore, the frequency response of PD at the frequency of $nf_r+f_1+f_2$ relative to the frequency of $nf_r+\Delta f$ can be obtained in the n-th intra-segment measurement by

$$\frac{R\left(nf_r+f_1+f_2\right)}{R\left(nf_r+\Delta f\right)}=\frac{A\left(nf_r+f_1+f_2\right)}{A\left(nf_r+\Delta f\right)} \tag{5}$$

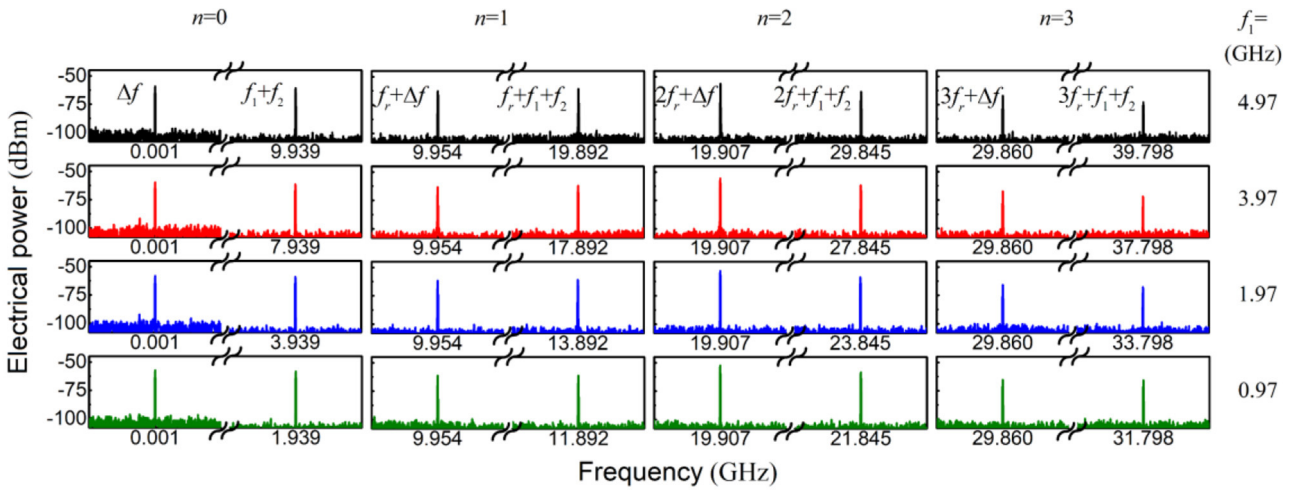

FIGURE 2 | Measured electrical spectra around $nf_r + f_1 + f_2$ and $nf_r + \Delta f$ in the initial ($n = 0$), first ($n = 1$), second ($n = 2$) and third ($n = 3$) segment under different two-tone modulations.

It is easily seen from Eqs. (4) and (5) that phase bias and the uneven response of the MZM is totally canceled out through the amplitude ratios of these frequency components, indicating the intra-segment measurement can be self-calibrated.

To characterize the PD in the whole frequency range, the frequency responses of PD at the frequency of $nf_r + \Delta f$ are required to be referenced to that at the same low-frequency of Δf ($n = 0$) so that all the segmental frequency responses can be seamlessly stitched. According to Eq. (4a), the frequency response of PD at the frequency of $nf_r + \Delta f$ ($= nf_r + f_1$'$-f_2$') relative to the frequency of Δf ($= f_1$'$-f_2$') is written by

$$\frac{R\left(nf_r + \Delta f\right)}{R\left(\Delta f\right)} = \frac{A\left(nf_r + \Delta f\right)}{A\left(\Delta f\right)} \cdot \frac{p_0}{p_n} \tag{6}$$

where the term p_0/p_n represents the uneven comb intensity of the MLLD. For the inter-segment stitching, the two-tone frequencies are carefully set to be $f_1' = f_r/4$ and $f_2' = f_r/4\text{-}\Delta f$, to have the assumptions of $if_r + f_1' + f_2' \approx (i+1)f_r - f_1' - f_2'$ and $R(if_r + f_1' + f_2') \approx R[(i+1)f_r - f_1' - f_2']$ ($i = 0 \sim n-1$) stand. In this case, the uneven comb intensity of the MLLD can be obtained by comparing these two frequencies, given by

$$\frac{p_0}{p_n} = \prod_{i=0}^{n-1} \frac{p_i}{p_{i+1}} = \prod_{i=0}^{n-1} \frac{A\left(if_r + f_1' + f_2'\right)}{A\left[(i+1)f_r - f_1' - f_2'\right]} \tag{7}$$

Through substituting Eq. (7) into Eq. (6), any frequency response of PD at the frequency of $nf_r + \Delta f$ can be uniformly referenced to the same low-frequency of Δf. It is easily seen from Eqs. (4–6) that the uneven comb intensity of the MLLD is totally subtracted, indicating the inter-segment stitching can be self-referenced. Moreover, through slightly sweeping the two-tone frequencies from 0 to $f_r/2$, the relative frequency response of PD at any frequency can be extracted within the measuring frequency range of $(n+1)f_r$.

RESULTS AND ANALYSIS

In our experiment, the ultrashort optical pulses come from a MLLD with the repetition frequency of 9.953 GHz (f_r) and the output power of 0.58 dBm. The two-tone signal provided by two microwave sources (MSs, R&S SMB100A) is loaded onto a MZM (EOSPACE AX-0MSS-10) through a microwave combiner. The optical sampling signal after the MZM is detected by the PD under test (DSC 10H), and the output electrical spectrum is acquired and analyzed by an ESA (R&S FSU50). In the measurement, the whole measuring frequency range of 49.765 GHz is divided into five segments ($= 5 \times f_r$, $n = 0 \sim 4$) by the repetition frequency of 9.953 GHz (f_r). The two-tone frequency is chosen to be f_1–f_2 $= 1$ MHz ($\Delta f = 1$ MHz), where Δf can be taken other smaller values as long as the desired frequency component can be distinguished by the employed ESA, and it will not affect the measurement results. In this case, the frequency response of PD at the frequency of $nf_r + f_1 + f_2$ with respect to the frequency of $nf_r + \Delta f$ can be calculated in the intra-segment measurement. **Figure 2** shows typical electrical spectra around $nf_r + f_1 + f_2$ and $nf_r + \Delta f$ in the initial ($n = 0$), first ($n = 1$), second ($n = 2$) and third ($n = 3$) segment under different two-tone modulations, where the resolution bandwidth (RBW) of the ESA is set as 500 Hz. For example, when the two-tone frequencies of f_1 and f_2 are set to be 4.97 GHz and 4.969 GHz, the electrical powers at the frequencies of 1 MHz (Δf) and 9.939 GHz ($f_1 + f_2$) are measured to be −59.07 dBm and −60.63 dBm in the initial segment ($n = 0$). According to Eq. (5), the frequency response of PD at the frequency of 9.939 GHz ($f_1 + f_2$) with respect to the frequency of 1 MHz (Δf) is calculated as−1.56 dB ($= -60.63 + 59.07$). Under the same condition, the electrical powers at the frequencies of 9.954 GHz ($f_r + \Delta f$) and 19.892 GHz ($f_r + f_1 + f_2$) are measured to be −62.99 dBm and −60.65 dBm in the first segment ($n = 1$). Thus, the frequency response of PD at the frequency of 19.892 GHz ($f_r + f_1 + f_2$) with respect to the frequency of 9.954 GHz ($f_r + \Delta f$) is solved to be 2.34 dB

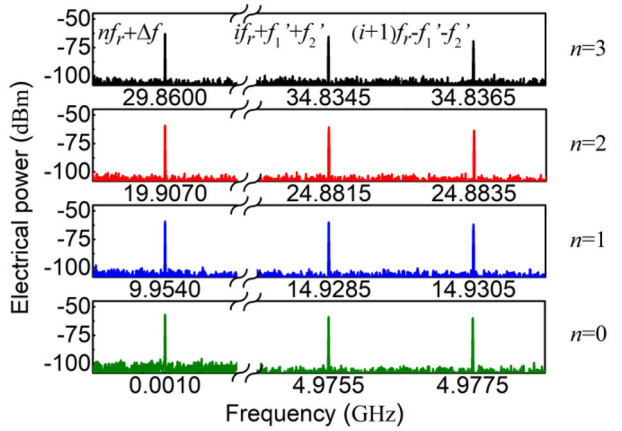

FIGURE 3 | Measured electrical spectra around $nf_r + \Delta f$, $if_r + f_1' + f_2'$ and $(i + 1)f_r - f_1' - f_2'$ for different segments.

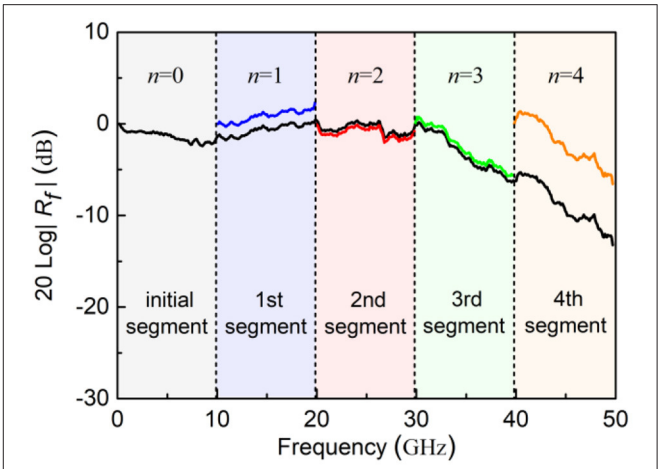

FIGURE 4 | Measured frequency response of PD before and after inter-segment stitching.

(= −60.65+62.99) in the first segment ($n = 1$). Similarly, the frequency response of PD at the frequency of $nf_r + f_1 + f_2$ with respect to the frequency of $nf_r + \Delta f$ can be obtained for other segments ($n = 2, 3, 4$). In addition, through slightly sweeping the two-tone frequencies from 0 to 4.9765 GHz ($f_r/2$), the frequency response of PD at any frequency with respect to the reference frequency in each segment can be obtained, as displayed in **Figure 4**.

To stitch the five segments, the two-tone frequencies are carefully set to be $f_1' = 2.48825$ GHz ($f_r/4$) and $f_2' = 2.48725$ GHz ($f_r/4$-Δf), and the measured electrical spectra around $nf_r + \Delta f$, $if_r + f_1' + f_2'$ and $(i + 1)f_r - f_1' - f_2'$ are illustrated in **Figure 3** for different segments. For example, the desired frequency components are measured to be −56.70 dBm at 1 MHz (Δf),−59.21 dBm at 9.954 GHz ($f_r + \Delta f$),−58.79 dBm at 4.9755 GHz ($f_1' + f_2'$) and −59.82 dBm at 4.9775 GHz ($f_r - f_1' - f_2'$), respectively. According to Eqs. (6) and (7), the uneven comb intensity p_0/p_1 of the MLLD can be determined to be 1.03 dB, and then the frequency response of PD at the frequency of 9.954 GHz ($f_r + \Delta f$) relative to the low-frequency of 1 MHz (Δf) can be solved to be −1.48 dB in the initial segment ($n = 0$). Therefore, the frequency response of PD at the frequency of 19.892 GHz ($f_r + f_1 + f_2$) in the first segment ($n = 1$) can be referenced to that at the low-frequency of 1 MHz (Δf) in the initial segment ($n = 0$), and is calculated as 0.86 dB (2.34–1.48). Similarly, the uneven comb intensity p_0/p_2 of the MLLD can be solved to be 2.85 dB, and the frequency response of PD at the frequency of 19.907 GHz ($2f_r + \Delta f$) in the second segment ($n = 2$) relative to the frequency of 1 MHz (Δf) in the initial segment ($n = 0$) can be determined to be 0.46 dB. In this case, the frequency response of PD at any frequency of $nf_r + f_1 + f_2$ relative to the same low-frequency of Δf can be extracted, and the frequency responses of all five segments can be stitched together, as shown in **Figure 4**.

Figure 5 shows the measured results with the proposed method and the method in [23] as well as the manufacturer data. The good consistency between these results verifies the

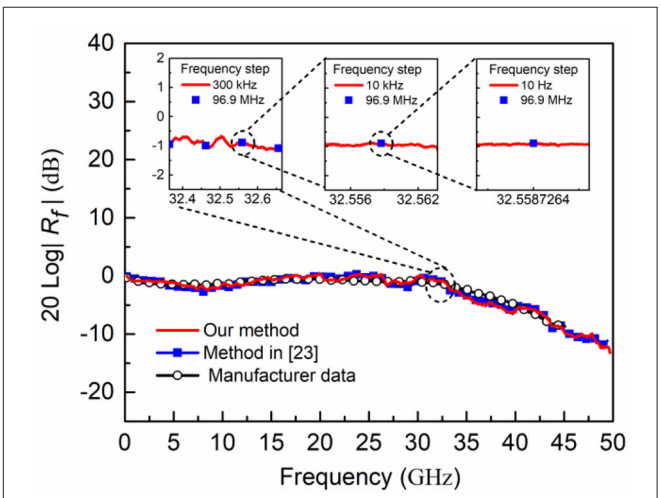

FIGURE 5 | Measured frequency response of PD with different methods and resolutions.

effectiveness of the proposed method. To further demonstrate hyperfine measurement, the frequency response of PD has been finely measured at around 32.51 GHz, as shown in the **Figure 5**. It can be seen that there are only four data points in the frequency range of 300 MHz based on the method in [23], which is limited by the repetition frequency of 96.9 MHz of the employed MLLD. In contrast, our method enables hyperfine measurement with different frequency steps, such as 300 kHz, 10 kHz and 10 Hz, which is mainly limited by the coherence characteristics of the ultrashort optical pulses, the tuning step of the MS and the RBW of the ESA. As displayed in **Figure 2**, the output electrical spectra from PD show extremely narrow spectral lines, indicating the inherent coherence of the ultrashort optical pulse source. The tuning step of the MS is 1 Hz, and the minimum RBW of the ESA is 10 Hz. Therefore, our method can be qualified by the hyperfine measurement of 10 Hz level.

Measurement Uncertainty

For the accuracy, the measurement uncertainty of the proposed method is investigated. In the intra-segment measurement, the uncertainty of the relative frequency response of PD in the n-th segment can be derived by the total derivative of Eq. (5)

$$\frac{\delta R\left(nf_r+f_1+f_2\right)}{R\left(nf_r+f_1+f_2\right)}=\frac{\delta A\left(nf_r+f_1+f_2\right)}{A\left(nf_r+f_1+f_2\right)}+\frac{\delta A\left(nf_r+\Delta f\right)}{A\left(nf_r+\Delta f\right)} \quad (8)$$

According to the specification of ESA, the measurement uncertainty of amplitude is 0.05 dB when the range of RBW is from 10 Hz to 100 kHz. Therefore, the relative frequency response of PD in the n-th segment would have an uncertainty of <0.1 dB (= 0.05 × 2). It means that the uncertainty of the relative frequency response of PD in the initial segment (n = 0) is 0.1 dB, corresponding to a relative error of 1.16% [= ($10^{0.1/20}$-1) × 100%].

In the inter-segment stitching, the uncertainty of the frequency response of PD at the frequency of $nf_r + \Delta f$ relative to the frequency of Δf can also be obtained by the total derivative of Eq. (6)

$$\frac{\delta R\left(nf_r+\Delta f\right)}{R\left(nf_r+\Delta f\right)}=\frac{\delta A\left(nf_r+\Delta f\right)}{A\left(nf_r+\Delta f\right)}+\frac{\delta A\left(\Delta f\right)}{A\left(\Delta f\right)}+\frac{\delta\left(p_0/p_n\right)}{p_0/p_n} \quad (9)$$

Thereinto, the uncertainty of the uneven response p_0/p_n induced by the MLLD is mainly determined by the assumption of PD responsivity, that is $R(if_r + f_1' + f_2') \approx R[(i+1)f_r - f_1' - f_2']$ (i = 0∼n−1). In the experiment, the frequency difference of these two components is set to be 2 MHz (= 2 × Δf), and an uncertainty of the PD responsivity fluctuation introduced by the frequency difference is 0.05 dB based on the PD's specification. Thus, the uncertainty of the uneven response p_0/p_n from the MLLD would be 0.05 × n dB. This uncertainty can be reduced by further reducing the frequency difference. Meanwhile, the measurement amplitude uncertainty of ESA is 0.05 dB. Therefore, the frequency response of PD at the frequency of $nf_r + \Delta f$ relative to the frequency of Δf will have an uncertainty of <0.05 × (n + 2) dB based on Eq. (9).

Finally, the frequency response of PD at the frequency of $nf_r + f_1 + f_2$ relative to the fixed low frequency of Δf has a total uncertainty of no more than 0.05 × (n + 4) dB (n = 1, 2, 3, 4), which is directly related to the number of the frequency segments. t means that the maximum uncertainty in the experiment is 0.4 dB (= 0.05 × 8), and the corresponding relative error is 4.71% [= ($10^{0.4/20}$-1) × 100%].

DISCUSSION AND CONCLUSIONS

In the proposed method, the measuring frequency range of PD is related to the repetition frequency and the effective tooth number of the ultrashort optical pulses from the MLLD, which can be theoretically extended up to (2n + 1)f_r. In the proof-of-concept experiment, the measurement of PD is only performed up to 49.765 GHz (= 5 × f_r, f_r = 9.953 GHz), which is mainly limited by the operation bandwidth of the ESA (20 Hz∼50 GHz). In addition, the method is also applicable for the MLLD with low or higher repetition frequency. If a MLLD with lower repetition frequency is used as the ultrashort optical pulse source, the sweeping frequency range of the two-tone signal can be further reduced, which is only half of the repetition frequency. However, a lower repetition frequency of MLLD will result in more frequency segments and larger measurement uncertainty, so in practical applications, the repetition frequency of MLLD should be compromised in terms of the sweeping frequency range of MS and the measurement uncertainty. If the measurement uncertainty is to be reduced and a higher sweeping frequency range of the two-tone signal can be acceptable, a higher repetition frequency MLLD is better for measurement. In addition, the influence introduced by the phase bias of the MZM can be canceled out by the relative amplitudes of the desired frequency components. However, for a better signal-to-noise ratio (SNR), it is recommended to adjust the phase bias φ_b of MZM to make $|\cos\varphi_b|$ as large as possible.

In conclusion, we have demonstrated a self-calibrated method for measuring frequency response of broadband PDs through two-tone photonic sampling. The two-tone microwave signal mixes with the optical comb of MLLD, and generates the sum- and difference-frequency products, working as the probing signal to extract the frequency response of PDs. Hyper-fine frequency response of PDs at any frequency point in intra-segment measurement is obtained by subtly varying the center frequency of the two-tone signal. Moreover, the frequency response of the PD can be obtained in ultra-wide frequency range by inter-segment stitching. In our method, the uneven responses of the MLLD and the MZM are completely eliminated through carefully setting the two-tone photonic sampling, enabling ultra-wideband, hyperfine and self-calibrated measurement for high-speed PDs.

DATA AVAILABILITY STATEMENT

The raw data supporting the conclusions of this article will be made available by the authors, without undue reservation.

AUTHOR CONTRIBUTIONS

MW discussed with YZ, ZZ, HL, and YL, and drafted the content of the manuscript. MW and YX completed the experiment. YH and ZL participated in the analysis and discussion of the experimental results. SZ guided and revised the manuscript. All authors contributed to the article and approved the submitted version.

FUNDING

This work was supported by the National Key Research and Development Program of China (2019YFB2203500), the National Natural Science Foundation of China (NSFC) (61927821), the Joint Research Fund of Ministry of Education of China (6141A02022436), and the Fundamental Research Funds for the Central Universities (ZYGX2019Z011).

REFERENCES

1. Yao JP. Microwave photonics. *J Lightwave Technol.* (2009) 27:314–35. doi: 10.1109/JLT.2008.2009551
2. Minasian RA, Chan EHW, Yi X. Microwave photonic signal processing. *Opt Express.* (2013) 21:22918–36. doi: 10.1364/OE.21.022918
3. Capmany J, Li GF, Lim C, Yao JP. Microwave photonics: current challenges towards widespread application. *Opt Express.* (2013) 21:22862–7. doi: 10.1364/OE.21.022862
4. Winzer PJ. High-spectral-efficiency optical modulation formats. *J Lightwave Technol.* (2012) 30:3824–35. doi: 10.1109/JLT.2012.2212180
5. Li Q, Li K, Fu Y, Xie X, Yang Z, Beling A, et al. High-power flip-chip bonded photodiode with 110 GHz bandwidth. *J Lightwave Technol.* (2016) 34:2139–44. doi: 10.1109/JLT.2016.2520826
6. Baumgartner Y, Caimi D, Sousa M, Hopstaken M, Salamin Y, Baeuerle B, et al. High-speed CMOS-compatible III-V on Si membrane photodetectors. *Opt Express.* (2021) 29:509–16. doi: 10.1364/OE.414013
7. Tan TS, Jungerman RL, Elliott SS. Optical receiver and modulator frequency response measurement with a Nd:YAG ring laser heterodyn technique. *IEEE T Microw Theory.* (1989) 37:1217–22. doi: 10.1109/22.31081
8. Wang LX, Zhu NH, Ke JH, Li W, Chen SF, Xie L. Improved peak power method for measuring frequency responses of photodetectors in a self-heterodyne system. *Microw Opt Technol Lett.* (2010) 52:2199–203. doi: 10.1002/mop.25448
9. Feng XJ, Yang P, He LB, Niu F, Zhong B, Xu H. Heterodyne system for measuring frequency response of photodetectors in ultrasonic applications. *IEEE Photon Technol Lett.* (2016) 28:1360–2. doi: 10.1109/LPT.2016.2542839
10. Feng XJ, Yang P, He LB, Xing GZ, Wang M, Ke W. Improved heterodyne system using double-passed acousto-optic frequency shifters for measuring the frequency response of photodetectors in ultrasonic applications. *Opt Express.* (2020) 28:4387–97. doi: 10.1364/OE.381107
11. Eichen E, Schlafer J, Rideout W, Mccabe J. Wide-bandwidth receiver photodetector frequency response measurements using amplified spontaneous emission from a semiconductor optical amplifier. *J Lightwave Technol.* (1990) 8:912–6. doi: 10.1109/50.54509
12. Baney DM, Sorin WV. Broadband frequency characterization of optical receivers using intensity noise. *Hewlett Packard J.* (1995) 46:6–12.
13. Baney DM, Sorin WV, Newton SA. High-frequency photodiode characterization using a filtered intensity noise technique. *IEEE Photon Technol Lett.* (1994) 6:1258–60. doi: 10.1109/68.329656
14. Xie FZ, Kuhl D, Bottcher EH, Ren SY, Bimberg D. Wide-band frequency response measurements of photodetectors using low-level photocurrent noise detection. *J Appl Phys.* (1993) 73:8641–6. doi: 10.1063/1.353397
15. Uehara S. Calibration of optical modulator frequency response with application to signal level control. *Appl Opt.* (1978) 17:68–71. doi: 10.1364/AO.17.000068
16. Humphreys DA, Harper MR, Smith AJA, Smith IM. Vector calibration of optical reference receivers using a frequency-domain method. *IEEE Trans Instrum Meas.* (2005) 54:894–7. doi: 10.1109/TIM.2004.843325
17. Ye Q, Yang C, Chong Y. Measuring the frequency response of photodiode using phase-modulated interferometric detection. *IEEE Photon Technol Lett.* (2014) 26:29–32. doi: 10.1109/LPT.2013.2280767
18. Wu XM, Man JW, Xie L, Liu JG, Liu Y, Zhu NH. A new method for measuring the frequency response of broadband optoelectronic devices. *IEEE Photonics J.* (2012) 4:1679–85. doi: 10.1109/JPHOT.2012.2213297
19. Wu XM, Man JW, Xie L, Liu Y, Qi XQ, Wang LX, et al. Novel method for frequency response measurement of optoelectronic devices. *IEEE Photon Technol Lett.* (2012) 24:575–7. doi: 10.1109/LPT.2012.2183122
20. Yoshioka M, Sato S, Kikuchi T. A method for measuring the frequency response of photodetector modules using twice-modulated light. *J Lightwave Technol.* (2005) 23:2112–7. doi: 10.1109/JLT.2005.846905
21. Zhang SJ, Wang H, Zou XH, Zhang YL, Lu RG, Li HP, et al. Optical frequency-detuned heterodyne for self-referenced measurement of photodetectors. *IEEE Photon Technol Lett.* (2015) 27:1014–7. doi: 10.1109/LPT.2015.2405253
22. Wang H, Zhang SJ, Zou XH, Zhang YL, Lu RG, Zhang ZY, et al. Two-tone intensity-modulated optical stimulus for self-referencing microwave characterization of high-speed photodetectors. *Opt Commun.* (2016) 373:110–3. doi: 10.1016/j.optcom.2015.08.028
23. Zhang SJ, Zhang C, Wang H, Zou XH, Zhang YL, Liu Y, et al. Self-calibrated microwave characterization of high-speed optoelectronic devices by heterodyne spectrum mapping. *J Lightwave Technol.* (2017) 35:1952–61. doi: 10.1109/JLT.2017.2678978
24. Zhang SJ, Wang H, Zou XH, Zhang C, Zhang YL, Zhang ZY, et al. Electrical probing test for characterizing wideband optical transceiving devices with self-reference and on-chip capability. *J Lightwave Technol.* (2018) 36:4326–36. doi: 10.1109/JLT.2018.2822944
25. Wang MK, Zhang SJ, He YT, Liu Z, Zhang XY, Wang H, et al. Self-referenced frequency response measurement of high-speed photodetectors through segmental up-conversion based on low-speed photonic sampling. *Opt Express.* (2019) 27:38250–8. doi: 10.1364/OE.382798
26. Zhang SJ, Li W, Chen W, Zhang YL, Zhu NH. Accurate calibration and measurement of optoelectronic devices. *J Lightwave Technol.* (2020). doi: 10.1109/JLT.2020.3010065

Conflict of Interest: The authors declare that the research was conducted in the absence of any commercial or financial relationships that could be construed as a potential conflict of interest.

frontiers in Physics

ORIGINAL RESEARCH
published: 21 May 2021
doi: 10.3389/fphy.2021.673764

Multi-Scale Simulation of Two-Dimensional Chloride Transport Under the Effect of Bending Load in Concrete

Lijuan Zhang[1], *Jianjian Zhang*[2], *Guowen Sun*[3] *and Zhiyong Liu*[4]*

[1]Foundational Subjects Department, Shijiazhuang TieDao University SiFang College, Shijiazhuang, China, [2]School of Civil Engineering, Harbin Institute of Technology, Harbin, China, [3]School of Materials Science and Engineering, Shijiazhuang Tiedao University, Shijiazhuang, China, [4]Jiangsu Key Laboratory for Construction Materials, Southeast University, Nanjing, China

Chloride transport in marine concrete under loading is the main cause of its structural deterioration. The traditional numerical simulation assumes that the coefficient of chloride transport is constant, resulting in a large deviation in the prediction results. Based on the porous medium theory, micromechanics theory, and the idea of equivalent homogenization, a multi-scale model of the effective diffusion variable coefficient of chloride transport under bending load was established, which was calculated and programmed by the numerical analysis. The results show that the prediction values of the two-dimensional variable coefficient model are basically consistent with those in the literature, and the prediction accuracy is significantly improved. In addition, the theoretical simulation proves that the bending load affects the porosity of the cement matrix, and then the diffusion coefficient of chloride is changed in concrete. The compression zone can slow down the chloride transport process, while tension zone will accelerate it. The chloride concentration under tension zone is 42.1% higher than that under compression zone when the diffusion time is 200 days and the concrete depth is 15 mm.

Keywords: concrete, chloride transport, variable coefficient, bending load, numerical simulation

OPEN ACCESS

Edited by:
Wenxiang Xu,
Hohai University, China

Reviewed by:
Zhigang Zhu,
Jiangsu University, China
Katerina Ioannidou,
UMR5508 Laboratoire de mécanique et génie civil (LMGC), France

***Correspondence:**
Zhiyong Liu
liuzhiyong0728@163.com

Specialty section:
This article was submitted to Soft Matter Physics, a section of the journal Frontiers in Physics

Received: *28 February 2021*
Accepted: *28 April 2021*
Published: *21 May 2021*

Citation:
Zhang L, Zhang J, Sun G and Liu Z (2021) Multi-Scale Simulation of Two-Dimensional Chloride Transport Under the Effect of Bending Load in Concrete. Front. Phys. 9:673764. doi: 10.3389/fphy.2021.673764

INTRODUCTION

Traditionally, it is mainly through soak test or sampling the samples, and then testing the distribution of chloride concentration for regression test [1, 2]. Researchers have been exploring to combine the coefficient of chloride transport with the microstructure characteristics of the concrete composite [3] so that the accuracy of prediction results is significantly improved. Tegguer et al. [4] considered the damage variable of specimens showed relationship with gas permeability and chloride diffusion of concrete. Wang et al. [5] indicated that the chloride concentration and apparent chloride diffusion coefficient decreased with the increase of the compressive stress, up to 55% of the compressive strength, and they increased with the increase of the flexural stress. Gowripalan et al. [6] considered the crack width/cover ratio (W_{cr}/C) can be a suitable parameter to study in relation to the durability performance of a cracked reinforced concrete.

Xi et al. [7] established a mathematical model of chloride transport in saturated concrete, which regarded concrete materials as a mortar phase and an aggregate phase. Liu et al. [8] presented a mesoscale model by various parameters to examine the effects of aggregates of shapes and volume fractions on chloride transport. In comparison, Cao et al. [9] established a more systematic model considering the changes of the water-to-binder ratio (w/c), the hydration degree, the tortuosity of the transport path caused by the cement matrix, and aggregate morphology. In fact, the concrete has typical porous, multiphase, and multi-scale characteristics, with each phase and each scale having different transport and mechanical properties. Garboczi and Bentz [10] used the multi-scale scheme and the theory to link the ion diffusion with the concrete microstructure, where the model mainly considered the ITZ volume fraction. Zhang et al. [11] achieved the diffusion coefficient of the low-density and high-density C-S-H gel based on a multi-scale scheme. Based on the theory of porous medium and micromechanics, Sun et al. [12] systematically established a model to predict the effective diffusion coefficient of chloride in concrete, starting from the C-S-H gel, the smallest scale unit of concrete, and ranging from the nanoscale to the microscale, mesoscale, and macroscale. This result has a very good guidance for the prediction of concrete transport performance and is also the study idea of this article.

In fact, the concrete is subjected to dual or multiple effects of mechanical and environmental loading in the service environment. Bending load is one of the loading types of large-scale infrastructure, and it is also the focus of the study [9, 13–15]. In the normal service environment, the loading is generally not enough to cause the deterioration of concrete performance [16], but with the passage of time, the loading will change the distribution of pores and microcracks in concrete.

Xu and Li [13–16] indicated that the diffusion coefficient of chloride and current porosity of concrete decreased with the increase in compressive stress and increased with the increase in tensile stress at low deformation levels. Li and Guo [16] developed a coupled mechanical-diffusive model to simulate chloride diffusion under various loading in saturated concrete.

In the above model, the diffusion coefficient of chloride predicted under loading and without loading is regarded as constant [5, 6]. In fact, under the action of loading, the internal pores, microcracks, and even macrocracks in the structural concrete are constantly changing, and the corresponding chloride transport coefficient is also constantly changing.

Aiming at the chloride transport under loading in saturated concrete, this article established the diffusion model of chloride transport predicted under without loading in concrete. On this basis, the two-dimensional (2D) diffusion model of chloride with variation coefficient under loading was established based on the three-phase sphere model of concrete and elastic mechanics theory. It should be noted that the study objective of this article is that the structural marine concrete is still in the normal service environment, so the bending load stress is relatively small, and there are no obvious macrocracks on its internal structure.

REPRESENTATION OF MULTI-SCALE MICROSTRUCTURE IN CONCRETE UNDER LOAD

Compared with single material, concrete material has more complex mechanical properties and size effect, and its internal structure presents high heterogeneity [17]. From the main hydration product C-S-H of cement to aggregate, their size from nanometer to centimeter, the size span is relatively large, and its internal pore size can also be from nanometer to millimeter. The concrete has typical porous, multiphase, and multi-scale characteristics, and each phase has independent mechanical properties and diffusion properties [12], so the study of concrete performance also needs to use the multi-scale method.

On the mesoscale, concrete is regarded as a three-phase composite material made up of ellipsoidal aggregate, cement matrix, and ITZ between them, as shown in **Figure 1A**. The hardened cement matrix is considered as a two-phase composite material made up of the hydration product solid phase (various hydration products and unhydration particles) and the pore phase (capillary pores and microcracks), as shown in **Figure 1B**. It needs to be indicated that chloride is mainly diffused in the capillary pores, and only a small amount are transported in gel pores with larger pore sizes [12]. Considering the percolation threshold of pores, which will be given in the next section, the gel pores of C-S-H are also basically contained. In the corresponding theoretical simulation, the solid phase can be regarded as an isotropic medium, as shown in **Figure 1D**. The ITZ composition is essentially the same as that of the cement matrix, but the porosity of the interface zone is relatively high, so it is also considered to be composed of the solid phase of the cement production and the pores (the scale reaches to the capillary pores and cracks), as shown in **Figure 1C**. The theoretical simulation is similar to that of **Figure 1D**, except that the ITZ volume fraction and its corresponding diffusion performance need to be calculated separately. On the microscale, the cement matrix is composed of hydrated products, pore water, pore, and unhydrated cement particles [18, 19].

In the theoretical simulation of concrete diffusion performance, the concept of equivalent diameter (D_{eq}) is introduced to deal with the size distribution of aspheric aggregate particle [20]. In this way, the concrete composed of ellipsoidal aggregate adopts the three-phase sphere model, as shown in **Figure 1E**. According to the mean-field theory of micromechanics, the homogenized equivalent medium is shown in **Figure 1F**. The diffusion performance of equivalent medium is the macroscopic diffusion performance of the concrete [21].

When the concrete is under loading (tensile as shown in **Figure 1G**), the main deformation occurs in the cement matrix

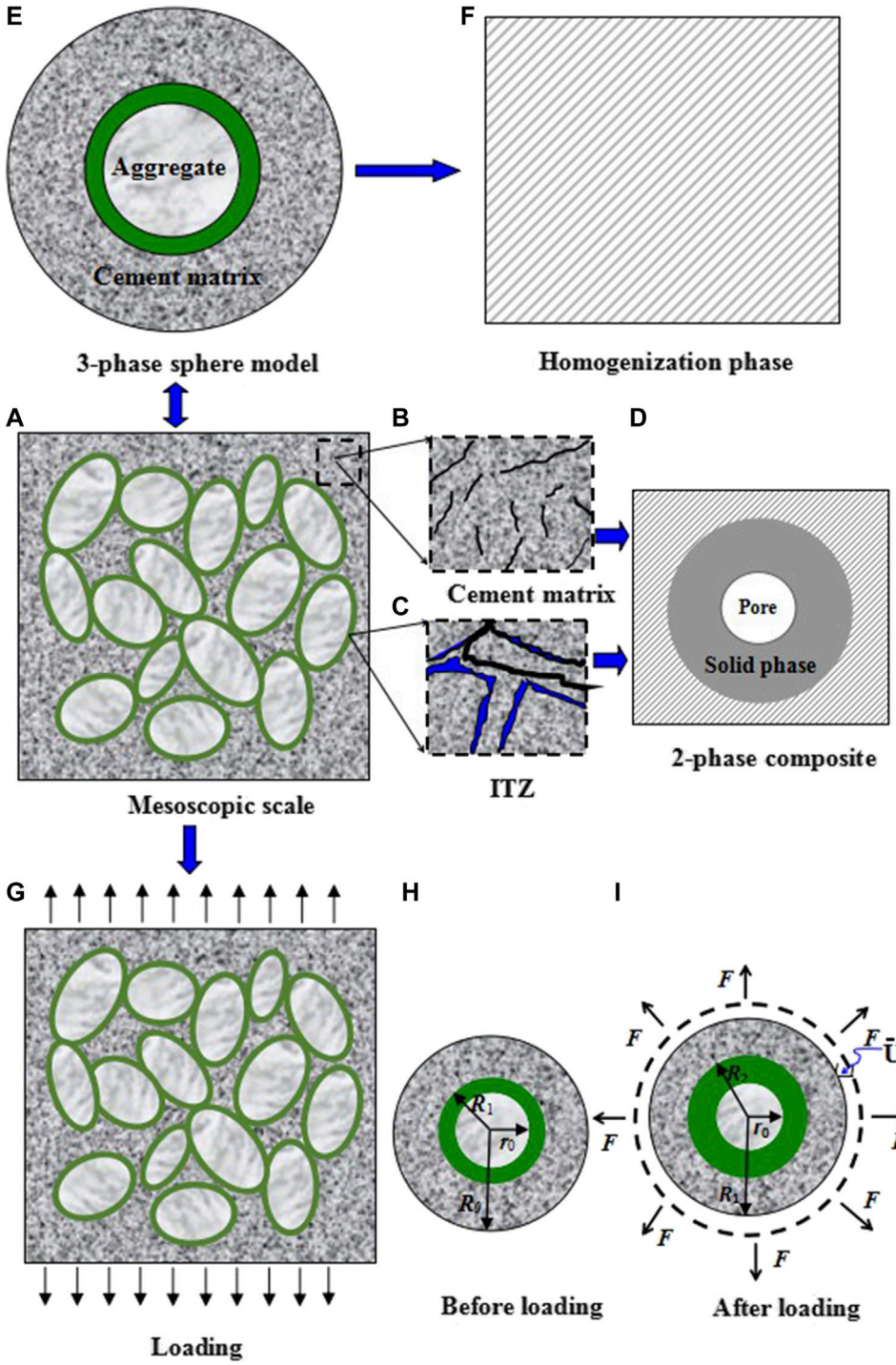

FIGURE 1 | Diagram of multi-scale in concrete under load.

and ITZ. Due to the relatively large elastic modulus of the aggregate, the self-deformation is very small, which can be ignored. Under tensile loading, the volume unit of the concrete is selected, as shown in **Figure 1H**, and its volume changes after being subjected to the external loading (indicated by the radial forced displacement u) as shown in **Figure 1I**. It should be pointed out that there are no obvious macrocracks in the concrete after it is loaded, so the difference between the total volume strain of the concrete before and after deformation is used to represent the change of the total pore of the concrete.

The relationship between the change process of the specific total strain and the porosity is given in *Diffusion Coefficient Model of Chloride in Concrete Under Bending Load*.

MULTI-SCALE PREDICTION OF THE DIFFUSION COEFFICIENT OF CHLORIDE IN CONCRETE UNDER BENDING LOAD

Diffusion Coefficient Model of Chloride in Concrete Without Loading

Aggregate is an important part of structural concrete, which accounts for more than 70% of the unit volume of concrete. In addition, the random distribution of aggregate and the overlapping phenomenon of the ITZ around aggregate make the diffusion prediction of chloride in structural concrete have certain complexity [22]. Based on the micromechanics theory and the idea of equivalent homogenization, Sun et al. [12] proposed a Mori–Tanaka scheme to predict the effective diffusion coefficient of chloride in concrete, considering the morphology characteristics of ellipsoidal aggregate. It can be expressed as

$$D_{eff} = D_{cp}\frac{2D_{cp} + D_e + 2V_e\left(D_e - D_{cp}\right)}{2D_{cp} + D_e - V_e\left(D_e - D_{cp}\right)}, \tag{1a}$$

$$D_e = D_{ITZ}\frac{2D_{ITZ} + D_a + 2V_a\left(D_a - D_{ITZ}\right)}{2D_{ITZ} + D_a - V_a\left(D_a - D_{ITZ}\right)}, \tag{1b}$$

$$V_e = V_a + V_{ITZ}, \tag{1c}$$

where D_a, D_{ITZ}, D_{cp}, and D_e are the diffusion coefficients of aggregate, ITZ, cement matrix, and equivalent spherical particles composed of aggregate and ITZ, respectively. V_{ITZ} and V_a are the volume fractions of the ITZ and aggregate, respectively.

The aggregate is dense and has very low porosity. It is assumed that the aggregate has no permeability; that is, the diffusion coefficient of chloride is zero ($D_a = 0$) in the aggregate, modifying **Eq. 1b** to obtain the following result:

$$D_e = D_{ITZ}\frac{2D_{ITZ} - 2V_aD_{ITZ}}{2D_{ITZ} + V_aD_{ITZ}} \tag{2}$$

The following gives the determination of the parameters in **Eq. 2**.

Diffusion Coefficient of Chloride in Cement Matrix Pore Solution (D_{cp})

As mentioned above, the process of chloride diffusion in concrete is essentially the migration of charged particles or molecules in the pore solution of the porous medium. In the hardened cement paste, the channels of chloride diffusion are mainly capillary pores, followed by a small amount of gel pores with slightly larger pore sizes [12]. The size and quantity of these two types of pores are related to the w/c and hydration degree of the cement. The relationship between the porosity and diffusion coefficient (D_{cp}) can be expressed as [23]

$$D_{cp} = \frac{2p_{cp}^{2.75}D_p}{p_{cp}^{1.75}\left(3 - p_{cp}\right) + n\left(1 - p_{cp}\right)^{2.75}}, \tag{3a}$$

$$p_{0\ cp} = \frac{w/c - 0.17\alpha}{w/c + 0.32}, \tag{3b}$$

$$\alpha = 1 - 0.5\left[(1 + 1.67t)^{-0.6} + (1 + 0.29t)^{-0.48}\right], \tag{3c}$$

where $p_{0\ cp}$ and p_{cp} are the initial porosity and current porosity of cement matrix, respectively, including capillary pores and gel pores. When the concrete is predicted without loading, $p_{cp} = p_{0\ cp}$, n is 14.44. α is the hydration degree of cement, t is the cement hydration time (s), and D_p is the diffusion coefficient of chloride ions in the pore solution (m^2/s), which is given separately below.

It should be emphasized that the chloride diffusion in cement paste pore solution is also affected by the types and concentrations of ions in the pore solution. Considering the factor, Zuo et al. [24] established the model of chloride diffusion in the pore solution based on the theory of electrolyte solution in concrete, which can be expressed as

$$D_p = \frac{RT_0}{F^2}\left\{1 - \left[\frac{1}{4\sqrt{I}\left(1 + \alpha_{cl^-}B\sqrt{I}\right)^2} - \frac{0.1 - 4.17\times10^{-5}I}{\sqrt{1000}}\right]Ac_{cl^-}\right\}\Lambda_{cl^-}, \tag{4}$$

where R is the universal gas constant ($R = 8.314$ J/Kmol), T_0 is the ambient temperature ($T = 298.15$ K), F is the Faraday constant ($F = 9.648\times10^4$ C/mol), I is the ionic strength (mol/m^3), c_{cl}^- is the chloride concentration in the pore solution (mol/L), α_{cl}^- is the atomic radius of chloride ions ($\alpha_{cl}^- = 1.81\times10^{-10}$ m), and Λ_{cl}^- is the molar conductivity of chloride ions in the electrolyte solution (Sm^2/mol); the detailed calculation process is shown in reference [25].

By substituting the results of **Eq. 4** into **Eq. 3**, the diffusion coefficient of chloride ions in the pore solution of cement matrix (D_{cp}) can be determined. This prediction model comprehensively considers the influence of w/c, hydration age, hydration degree, and ion type, and concentration in pore solution.

Diffusion Coefficient of Chloride in ITZ (D_{ITZ})

Based on the study of Garboczi and Bentz [26], Sun et al. [25] gave the diffusion coefficient of the ITZ, which can be expressed as

$$D_{ITZ} = D_0\left(0.001 + 0.07p_{ITZ} + 1.8H\left(p_{ITZ} - \varphi_{cri}\right)\cdot\left(p_{ITZ} - \varphi_{cri}\right)^2\right), \tag{5a}$$

$$p_{0\ ITZ} = \frac{\int_0^{t_{ITZ}} p\,(x)dx}{t_{ITZ}}, \tag{5b}$$

where D_0 is the diffusion coefficient of chloride in free water and $D_0 = 2.032\times10^{-9}$ m^2/s at 25°C; $p_{0\ ITZ}$ and p_{ITZ} are the initial porosity and current porosity of ITZ, respectively; when the prediction in concrete is without loading, $p_{ITZ} = p_{0\ ITZ}$. H is the Heaviside function; when $p(x) > \phi_{cri}$, H $(p(x)\text{-}\phi_{cri}) = 1$; otherwise, it is 0; ϕ_{cri} is the percolation threshold of capillary pores, which is 0.18; t_{ITZ} represents the ITZ thickness; x is the distance from the aggregate surface, and dx is the infinitesimal interval of the distance from the aggregate surface; $p(x)$ represents the porosity at the distance x from the aggregate surface, and its derivation and numerical calculation are shown in reference [25].

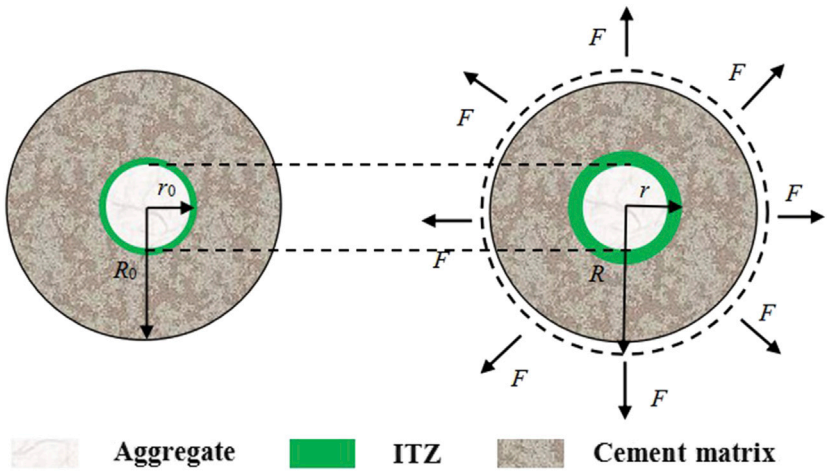

FIGURE 2 | implified spherical mechanical model of three-phase concrete.

Volume Fraction of ITZ (V_{ITZ})

Based on the study of ITZ around the spherical aggregate of Garboczi and Bentz [27], Zhang et al. [20] gave the numerical model of volume fraction of ITZ around the ellipsoid aggregate, where they assumed that a certain thickness of the interface layer is uniformly distributed around the aggregate. Comprehensively, considering the random distribution of the aggregate in concrete and the overlapping phenomenon between the interfaces, the expression of volume fraction of ITZ around the ellipsoid aggregate is as follows:

$$V_{ITZ}^{S} = 1 - (1 - V_a)\exp\left[- \pi N_V^S \left(c^S t_{ITZ} + d^S t_{ITZ}^2 + g^S t_{ITZ}^3\right)\right], \quad (6a)$$

$$c^S = \frac{\langle D_{eq}^2 \rangle}{1 - V_a}, \quad (6b)$$

$$d^S = \frac{2\langle D_{eq} \rangle}{1 - V_a} + \frac{\pi N_V^S \langle D_{eq}^2 \rangle^2}{2(1 - V_a)^2}, \quad (6c)$$

$$g^S = \frac{2\langle D_{eq} \rangle}{3(1 - V_a)} + \frac{\pi N_V^S \langle D_{eq}^2 \rangle \langle D_{eq} \rangle}{6(1 - V_a)^2} + \frac{A\pi^2 \left(N_V^S\right)^2 \langle D_{eq}^2 \rangle^3}{27(1 - V_a)^3}, \quad (6d)$$

$$N_V^S = \frac{6V_a}{\pi \langle D_{eq}^3 \rangle}, \quad (6e)$$

where N_V^S and V_a are the total aggregate number and the volume fraction of aggregate particles per unit volume, respectively, t_{ITZ} represents the ITZ thickness, and $<D_{eq}>$ indicates the equivalent diameter of the aggregate size, that is, c^s, d^s, and g^s, including the volume fraction V_a and equivalent diameter $< D_{eq}>$ of aggregate particles. A is a constant parameter with a value of 0. The detailed calculation process is shown in reference [20].

Diffusion Coefficient Model of Chloride in Concrete Under Bending Load

It is assumed that under external loading, the concrete is still under loading in service, and the main internal cracks are microcracks without obvious macrocracks. The microcracks under loading are equivalent to the change of the internal porosity of the concrete caused by the loading [28]; that is, the change of the porosity is an important link between the changes of the concrete before and after the loading. Generally, the aggregate is relatively dense, and the channel of chloride diffusion in the concrete is located in the cement matrix and ITZ. In this way, under the saturated state, the concrete composed of three-phase composite materials can be further simplified as a two-phase composite material composed of solid matrix phase (including coarse and fine aggregates and cement particles, the porosity of which is zero) and pore water phase. The main difference between the cement matrix and ITZ is its high porosity. As shown in **Figure 2A**, the pore water phase in this representative unit is the water content of the gel pores, capillary pores, microcracks, and bubble pores. This mechanical model is the widely used Hansen model [17].

In the above three-phase sphere model, before the external loading is applied, that is, before deformation, the radius of the ITZ sphere is r_0, and the radius of the mortar phase sphere is R_0. After the loading is applied, that is, after deformation, the radius of the ITZ sphere is r, and the radius of the solid matrix phase sphere is R. Based on the theory of elasticity and material mechanics, Jin and Du [17] deduced the quantitative relationship between the current porosity p and the initial porosity p_0, and the volume strain ε_V in concrete under the action of external loading. The results are as follows:

$$p = \frac{p_0}{1 - \varepsilon_V} \cdot \left[1 - \frac{(3\lambda + \phi) \cdot H}{\phi + 3\lambda \cdot p_0}\right]^3, \quad (7a)$$

$$H = 1 - \sqrt[3]{1 - \varepsilon_V}, \quad (7b)$$

$$\lambda = K_m - K_w, \quad (7c)$$

$$\phi = 3K_w + 4\mu_m, \quad (7d)$$

$$p_0 = p_{0\,cp} + p_{0\,ITZ}, \quad (7e)$$

where K_m is the bulk modulus (GPa) of the solid phase, u_m is the shear modulus (GPa) of the solid phase, and K_w is the bulk modulus of pore water in the liquid phase (GPa).

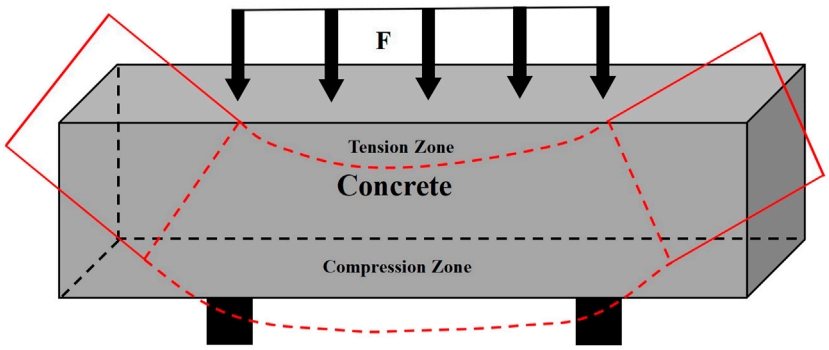

FIGURE 3 | Concrete structure under the blending load.

When the structural concrete is subjected to the bending load, it is divided into compression zone and tension zone, as shown in **Figure 3**. The change of concrete under loading is usually characterized by the total volume strain of concrete (ε_V). The loading is also commonly used to express the effect of stress on concrete. If the concrete is considered to be isotropic macroscopically, the relationship among compressive stress, tensile stress, and strain is [29]

$$\sigma = f_c \cdot \left[2\frac{\varepsilon}{\varepsilon_0} - \left(\frac{\varepsilon}{\varepsilon_0}\right)^2 \right] \qquad (\varepsilon \le \varepsilon_0), \tag{8}$$

$$\sigma = f_t \cdot \left[1.2\frac{\varepsilon}{\varepsilon_0} - 0.2\left(\frac{\varepsilon}{\varepsilon_0}\right)^6 \right] \qquad (\varepsilon \le \varepsilon_0), \tag{9}$$

where σ is the stress of concrete under the external loading (MPa), f_c is the uniaxial compressive strength of the concrete (MPa), f_t is the uniaxial tensile strength of the concrete (MPa), ε is the strain under stress, and ε_0 is the strain, which is 0.002, corresponding to the peak stress of the concrete.

According to **Eqs. 8Eqs. 9**, the strains ε_x, ε_y, and ε_z of each point of concrete material can be obtained, and the volume strain ε_v of concrete structure under loading is as follows:

$$\varepsilon_v = \varepsilon_x + \varepsilon_y + \varepsilon_z + \varepsilon_x\varepsilon_y + \varepsilon_y\varepsilon_z + \varepsilon_z\varepsilon_x + \varepsilon_x\varepsilon_y\varepsilon_z, \tag{10}$$

The above constitutive relation requires that the external loading should be less than the uniaxial compressive or tensile strength; that is, the concrete does not appear to have macrocracks when it is under loading. Through **Eqs. 7–10**, the quantitative relationship among p, p_0, and σ is established in concrete.

Loading will also affect the current porosity of cement matrix and ITZ in concrete, but how to quantify this effect? Based on the study of Jin and Du [17], the relationship between σ and p of the cement matrix and ITZ can be obtained, as shown in **Eq. (11)**.

$$p_X = \frac{p_{0X}}{1-\varepsilon_{VX}} \cdot \left[1 - \frac{(3\lambda_X + \phi_X)\cdot H_X}{\phi_X + 3\lambda_X \cdot p_{0X}} \right]^3, \tag{11a}$$

$$H_X = 1 - \sqrt[3]{1-\varepsilon_{VX}}, \tag{11b}$$

$$\lambda_X = k_X - k_w, \tag{11c}$$

$$\phi_X = 3K_w + 4\mu_X, \tag{11d}$$

where X means the cement matrix or ITZ, and K and u are the bulk modulus (GPa) and shear modulus (GPa) of cement matrix and ITZ, respectively. K_w is the bulk modulus of pore water in the liquid phase (GPa).

The initial porosity $p_{0\ cp}$ and $p_{0\ ITZ}$ of the ITZ and cement matrix can be calculated by **Eq. 3b** and **Eq. 5b**, respectively. Based on **Eq. 7a** and **Eq. 11a**, the current porosity p, p_{cp}, and p_{ITZ} of concrete, cement matrix, and ITZ, respectively, can be calculated. When the above parameters are substituted into **Eq. 3a** and **Eq. 5a** under loading, the diffusion coefficients of chloride $D_{L\ cp}$ and $D_{L\ ITZ}$ can be obtained in cement matrix and ITZ under loading, and then the effective diffusion coefficient $D_{L\ eff}$ of chloride can be obtained from **Eq. 2** in concrete under loading.

The mechanical parameters of materials required for the calculation model are shown in **Table 1** and **Table 2**.

It should be noted that the above theoretical derivation is a diffusion model of chloride variation coefficient in concrete under loading based on elastic deformation conditions; that is, the external loading has not reached its strength limit, and no new cracks have occurred in the concrete.

Therefore, the calculation flowchart of chloride diffusion coefficient is as shown in **Figure 4**.

By inputting different parameters and bringing them into the corresponding calculation equation, the chloride diffusion coefficient is obtained in cement paste and ITZ. Finally, combined with the ITZ content, the chloride diffusion coefficient is obtained. Red and blue represent the effective chloride diffusion coefficient predicted under without loading and loading, respectively.

PREDICTION OF CHLORIDE CONCENTRATION DISTRIBUTION WITH VARIABLE DIFFUSION COEFFICIENT IN CONCRETE UNDER 2D EROSION

The diffusion flux of chloride is a function that changes with time and space, and its diffusion process is called the unsteady

TABLE 1 | Mechanical parameters of materials.

Materials	Bulk modulus *K*/GPa	Shear modulus *μ*/GPa	Elastic modulus *E*/GPa	Poisson's ratio *v*
Nonporous matrix	30.3	22.1	35.2	0.27
Porous water	3.5	—	—	—

TABLE 2 | Mechanical parameters of concrete micro-component materials.

Materials	Tensile strength f_t/MPa	Compressive strength f_c/MPa	Elastic modulus *E*/GPa	Poisson's ratio *v*
Aggregate	—	—	70	0.16
Mortar matrix	1.43	14.3	30	0.2
Interface	1.2	12.0	25	0.22

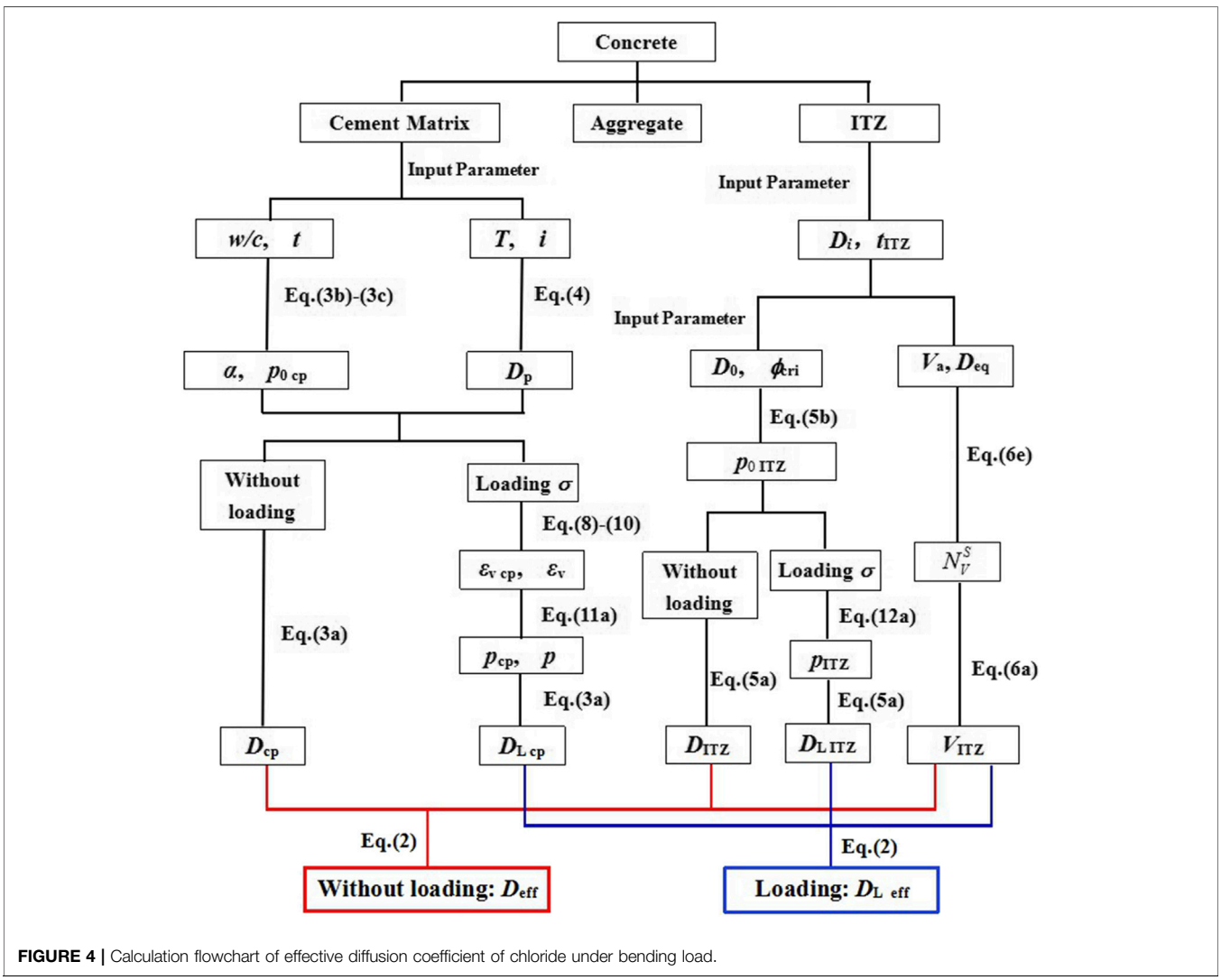

FIGURE 4 | Calculation flowchart of effective diffusion coefficient of chloride under bending load.

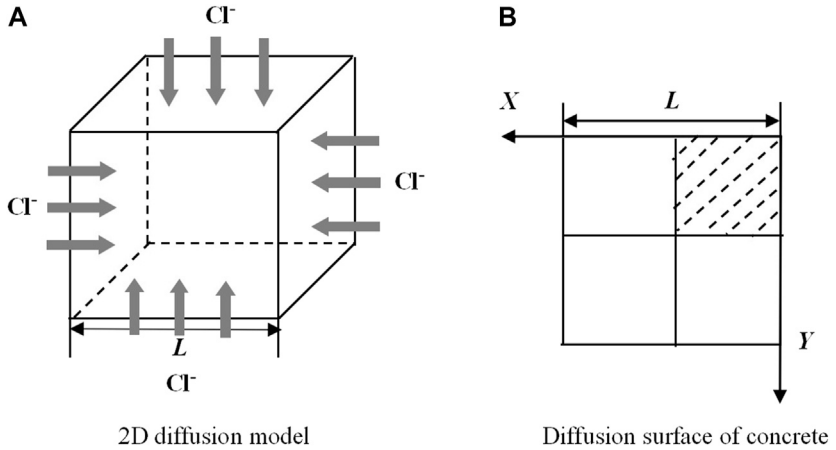

FIGURE 5 | 2D diffusion model of chloride.

diffusion process. When the structure is eroded, its 2D diffusion model is as shown in **Figure 5**.

Therefore, modified Fick's second law is often employed to describe the distribution of Cl^- concentration in the 2D direction. The specific 2D diffusion variable coefficient equation and boundary conditions are as follows:

$$\frac{\partial C}{\partial t} = \frac{\partial\left[D_x(x,y,t)\frac{\partial C}{\partial x}\right]}{\partial x} + \frac{\partial\left[D_y(x,y,t)\frac{\partial C}{\partial y}\right]}{\partial y}, \tag{12a}$$

$$C(x,y,0) = 0, \quad [x \in (0, L/2), \quad y \in (0, L/2)], \tag{12b}$$

$$C(x,0,t) = C_S, \; C(0,y,t) = C_S \quad [0 < t \le T], \tag{12c}$$

$$D(x,0,t) = D(0,y,t) = D_{eff} \quad [0 < t \le T], \tag{12d}$$

where C and D are the Cl^- concentration (C=$C(x,y,t)$ mol/m^3) and diffusion coefficient of chloride ($D = D(x,y,t)$ m^2/s) at the point (x,y) in concrete at the time of t, respectively. C_S is the Cl^- concentration on the surface in concrete (mol/m^3), x is the distance from a point in concrete along the X direction to the concrete surface (m), y is the distance from a point in concrete along the Y direction to the concrete surface (m), t is the diffusion time of chloride (s), L is the sample thickness, and D_{eff} determined by **Figure 4** is the diffusion initial coefficient of chloride in concrete (m^2/s).

It is relatively difficult to solve the variable coefficient in **Eq. 12**, where the numerical analysis is used to calculate, and the alternating direction implicit format (ADI) is adopted, which is not only unconditionally stable but also can be solved by the catch-up method. First, $\partial^2C/\partial x^2$ is placed on the k+1/2 layer, and $\partial^2C/\partial y^2$ is superseded by the second-order central difference quotient on the k layer. Second, $\partial^2C/\partial y^2$ is placed on the k+1 layer, and $\partial^2C/\partial x^2$ is superseded by the second-order central difference quotient on the k+1/2 layer. The two steps belong to the implicit format in one dimension; the implicit format is used in the X or Y direction. Through the above steps, the solution of a time layer from k to k+1 can be completed by using the two-time catch-up method.

As shown in **Figure 6**, the parallel line cluster formula of grid division is expressed as follows:

$$x_i = ih \quad y_j = jh \quad (i,j = 0,1,2,\ldots,M), \tag{13}$$

$$t_k = k\Delta t \quad (k = 0,1,2,\ldots,K), \tag{14}$$

where h and Δt can be calculated from M, K, L, and T assumed by the model. The grid nodes are (x_i, y_i, t_k). The solution of the differential equation $(C^k_{i,j})$ represents the Cl^- concentration of a point (x, y) in space at time t. D_x and D_y are dependent on the normal strain components of the X and Y direction, respectively.

The solution process is divided into two steps.

First, the implicit format and explicit format are used in the X direction and the Y direction from the k to k+1/2 layer, respectively, as follows:

$$\frac{\partial C^k_{i,j}}{\partial t} = \frac{C^{k+\frac{1}{2}}_{i,j} - C^k_{i,j}}{\Delta t/2}, \tag{15}$$

$$\frac{\partial\left(D_x\frac{\partial C^{k+\frac{1}{2}}_{i,j}}{\partial x}\right)}{\partial x} = \frac{1}{h^2}\left[D^{k+\frac{1}{2}}_{x_{i+\frac{1}{2},j}}\left(C^{k+\frac{1}{2}}_{i+1,j} - C^{k+\frac{1}{2}}_{i,j}\right) - D^{k+\frac{1}{2}}_{x_{i-\frac{1}{2},j}}\left(C^{k+\frac{1}{2}}_{i,j} - C^{k+\frac{1}{2}}_{i-1,j}\right)\right] \tag{16}$$

$$\frac{\partial\left(D_y\frac{\partial C^k_{i,j}}{\partial y}\right)}{\partial y} = \frac{1}{h^2}\left[D^k_{y_{i,j+\frac{1}{2}}}\left(C^k_{i,j+1} - C^k_{i,j}\right) - D^k_{y_{i,j-\frac{1}{2}}}\left(C^k_{i,j} - C^k_{i,j-1}\right)\right] \tag{17}$$

Substitution of **Eqs. 15–17** into **Eq. 12** yields

$$\frac{C^{k+\frac{1}{2}}_{i,j} - C^k_{i,j}}{\Delta t/2} = \frac{1}{h^2}\left[\begin{array}{l} D^{k+\frac{1}{2}}_{x_{i+\frac{1}{2},j}}\left(C^{k+\frac{1}{2}}_{i+1,j} - C^{k+\frac{1}{2}}_{i,j}\right) - D^{k+\frac{1}{2}}_{x_{i-\frac{1}{2},j}}\left(C^{k+\frac{1}{2}}_{i,j} - C^{k+\frac{1}{2}}_{i-1,j}\right) + \\ D^k_{y_{i,j+\frac{1}{2}}}\left(C^k_{i,j+1} - C^k_{i,j}\right) - D^k_{y_{i,j-\frac{1}{2}}}\left(C^k_{i,j} - C^k_{i,j-1}\right) \end{array}\right] \tag{18}$$

In **Eq. 16**, the diffusion coefficient of the k+1/2 layer is half of the sum of the diffusion coefficients of the two points in the same direction, and the implicit format is used for the difference

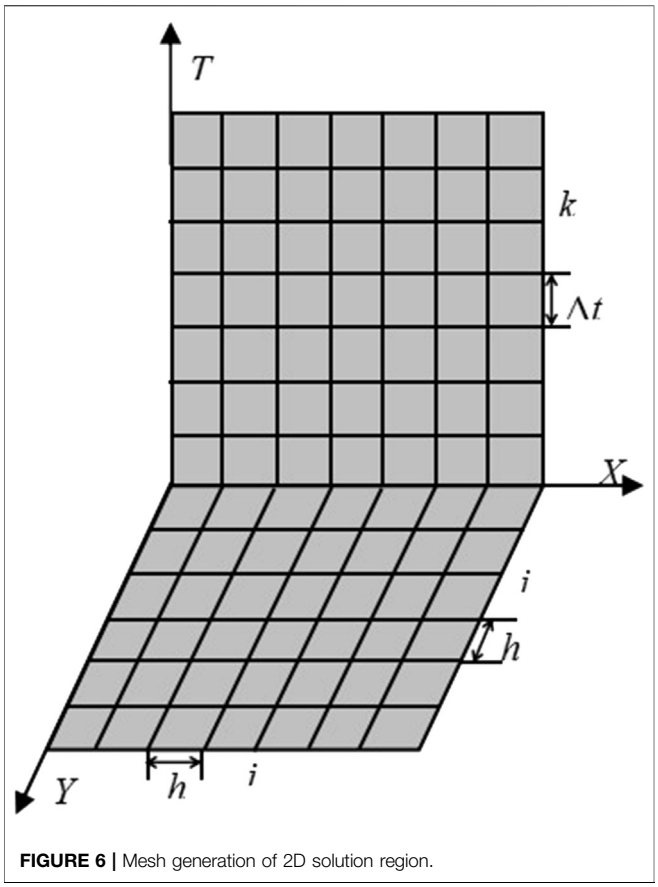

FIGURE 6 | Mesh generation of 2D solution region.

quotient. **Eq. 17** represents the diffusion coefficient of the k+1/2 layer in the X direction, and **Eq. 18** represents the diffusion coefficient of the k+1/2 layer in the Y direction.

$$D^{k+\frac{1}{2}}_{x_{i+\frac{1}{2}j}} = \frac{1}{2}\left(D^{k}_{x_{ij}} + D^{k}_{x_{i+1,j}}\right) \quad D^{k+\frac{1}{2}}_{x_{i-\frac{1}{2}j}} = \frac{1}{2}\left(D^{k}_{x_{ij}} + D^{k}_{x_{i-1,j}}\right), \tag{19}$$

$$D^{k+\frac{1}{2}}_{y_{i,j+\frac{1}{2}}} = \frac{1}{2}\left(D^{k}_{y_{ij}} + D^{k}_{y_{i,j+1}}\right) \quad D^{k+\frac{1}{2}}_{y_{i,j-\frac{1}{2}}} = \frac{1}{2}\left(D^{k}_{y_{ij}} + D^{k}_{y_{i,j-1}}\right) \tag{20}$$

Substituting **Eqs. 19–20** into **Eq. 18**, moving the unknown item of the k+1/2 layer to the one side and the known item of the k layer on the other in the equation, marking $r = \Delta t/h^2$, and by rewriting into matrix form, a linear equation system in the X direction can be obtained. Its expression is

$$[A]\left\{C^{k+\frac{1}{2}}_{j}\right\} = [B]\left\{C^{k}_{j-1}\right\} + [C]\left\{C^{k}_{j+1}\right\} + [D]\left\{C^{k}_{j}\right\} + \{e\} \tag{21}$$

The initial $C^{1}_{i,j}$ of the first layer can be obtained according to the boundary conditions, and $C^{k}_{i,j}$ of the k layer can be obtained by using the catch-up method for each step. According to the above equations, the concentration value of the k+1/2 layer ($C^{k+\frac{1}{2}}$) was obtained, so the first step of solving the ADI has been completed.

Second, the explicit format and implicit format are used in the X direction and the Y direction from the k+1/2 to k+1 layer, respectively. In other words, $\partial C/\partial x$ and $\partial^2 C/\partial x^2$ are substituted by the difference quotient of the k+1/2 layer; $\partial C/\partial y$ and $\partial^2 C/\partial y^2$ are substituted by the difference quotient of the k+1 layer. The calculation process is the same as the first step. So far, the ADI has been used to completely solve the 2D diffusion equation with variable coefficient of chloride.

VALIDATION OF THE CHLORIDE TRANSPORT MODEL

Generally, the validation of the chloride transport model under loading is to directly test the results of the transport coefficient, but some literature works give the results of chloride concentration distribution [30, 31], so this section gives the comparison of their validation results.

Validation of Chloride Diffusion Coefficient

In the 2D experiment of chloride diffusion, a nonstandard sample with the size of 100 mm × 100 mm×300 mm was used. Ordinary Portland cement (referred to as cement hereafter) with a strength grade of 42.5R I and Blaine fineness of 369 m^2/kg was produced by China United Cement Group. The chemical compositions of the cement and slag were measured with the German S4 EXPLORER X-ray fluorescence spectrometer and are shown in **Table 3**. It is alkaline with the basicity coefficient [K_b = (CaO + MgO)/(SiO_2 + Al_2O_3)] of 1.07, as can be seen from **Table 3**.

The sample group C1, C2, and C3 represented the w/c of 0.4, 0.5, and 0.6, respectively, and the mix proportion is shown in **Table 4**. The test temperature and humidity are 25°C and 95%, respectively. The NaCl concentration is wt. 5% (850 mol/m^3). The sample predicted with loading and without loading was placed in NaCl solution for 30 days, and the whole diffusion test chamber was placed in the curing chamber. The loading mode of concrete is the same as that of Zhang et al. [30, 31].

The chloride diffusion coefficient of the sample is detected by the chloride diffusion coefficient tester of concrete. The samples are cut into a cylinder with a diameter of 100 mm and a height of 50 mm, and put it into the bottom of the rubber bucket, in which there is 300 ml KOH solution, so that both the anode plate and the sample surface are immersed in the solution. Finally, it is placed in KOH + NaCl solution. The schematic diagram of the RCM test device is shown in **Figure 7**.

Based on the chloride diffusion model determined in **Figure 4**, the initial parameters such as curing time, immersed time, water binder ratio, loading, and aggregate content are input into **Eqs. 2–11** to obtain the diffusion coefficient of chloride. All experimental data are measured from three samples and averaged. The experimental results are compared with the simulation results, and the results are shown in **Figure 8**.

Figure 8 shows the test and model comparison of chloride diffusion coefficients at different water binder ratios. The results show that the chloride diffusion coefficient of concrete predicted under loading (compressive stress) is lower than that of concrete predicted under without loading, and the maximum error of test is 14.5%. The variation trend of chloride diffusion coefficient between the model value and the test value is consistent and that increases with the increase of the water binder ratio. The difference is that

TABLE 3 | Chemical composition of cement (%).

Composition	SiO_2	Al_2O_3	Fe_2O_3	CaO	MgO	SO_3	NaO_{equi}	Loss on ignition
OPC	18.79	4.69	2.70	60.16	2.19	3.54	0.75	3.83

TABLE 4 | Mix proportion of concrete.

Test number	W/c	Cement/(kg/m^3)	Water/(kg/m^3)	Sand/(kg/m^3)	Stone/(kg/m^3)	Compressive strength for 28 days/(MPa)
C1	0.4	380	170	861	1239	38.4
C2	0.5	350	170	870	1305	32.7
C3	0.6	320	170	860	1344	30.3

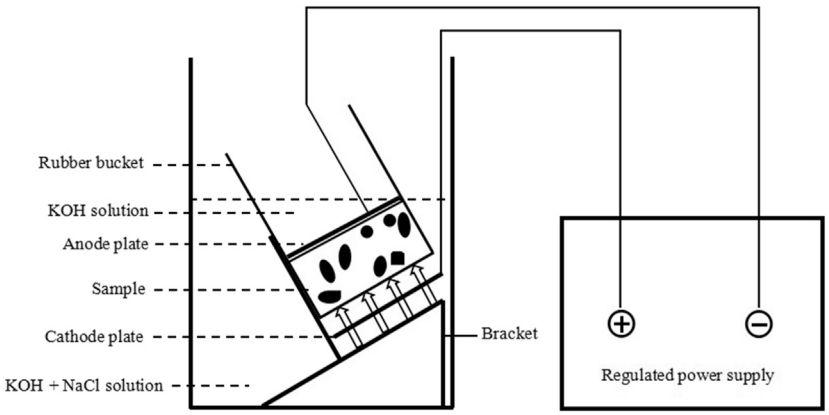

FIGURE 7 | Schematic diagram of the RCM test device.

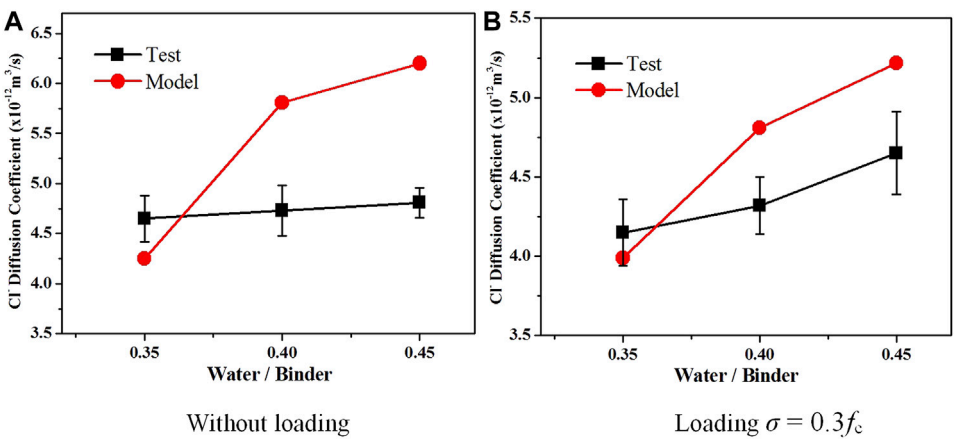

FIGURE 8 | Chloride diffusion coefficient of concrete immersed for 30 days.

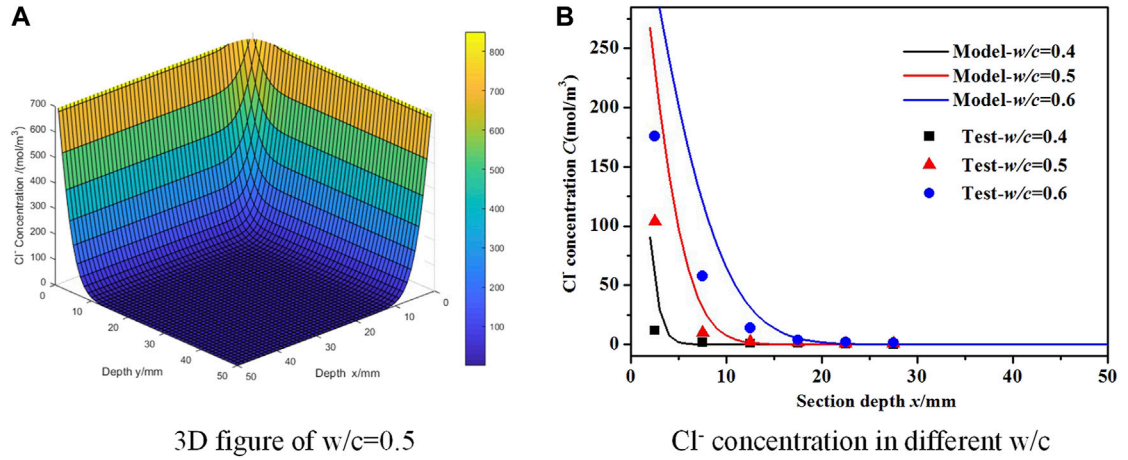

FIGURE 9 | Comparison between experimental and theoretical Cl^- concentration.

when the water binder ratio is low, the test value is higher than the model value, but when it is higher than 0.4, the result is opposite. Under the same water binder ratio, the maximum error between the test and the model is 28.7%, and the numerical fitting is in good agreement with the experimental results. The chloride diffusion variable coefficient model established is more reasonable.

The chloride diffusion coefficient depends on the change of concrete microstructure under loading and without loading in concrete, such as the amount of hydration products, ITZ volume fraction, pore structure distribution, and cracks. This article also systematically predicted the key microstructure parameters that affect the transport of concrete. Second, the accuracy of predicting chloride diffusion was improved by solving the constitutive relation of diffusion with the variable coefficient. It can be seen from **Figure 8** that the overall prediction accuracy of diffusion coefficient is high under loading and without loading. In **Figure 8A**, there is a large error when w/b = 0.45. This is because the concrete is a heterogeneous material. According to the research of Care [22], Yang [32], and Sun [33] et al., the prediction accuracy of diffusion coefficient is within 30% for concrete, which is considered reasonable.

Verification of the Chloride Concentration Distribution Model

The verification methods of chloride diffusion coefficient are different, so it is necessary to verify the chloride concentration distribution in concrete. The verification of the 2D chloride concentration is more meaningful in practical engineering.

The two different diffusion directions for each of the samples were taken, and holes from the outside to the inside for sampling were drilled. The range was 2.5–27.5 mm, the distance interval was 5 mm, and the number of sampling points was 5. The powder obtained from the sampling points was mixed, and the Cl^- concentration test was performed by using a portable chloride tester.

The experimental data and simulation results were compared when the loading σ is $0.3f_c$ and the results are as follows:

(a) 3D figure of w/c=0.5
(b) Cl- concentration in different w/c

Figure 9A shows the 3D distribution of Cl^- concentration of concrete with the w/c of 0.5 under the action of loading σ is $0.3f_c$ after 30 days diffusion in two different directions. **Figure 9B** shows the comparison between the test value and the model value of the w/c of 0.4, 0.5, and 0.6 when the σ is $0.3f_c$. It can be seen from the figure that the distribution trend of Cl^- concentration of the test value agrees with the model value. Due to the limitation of the simulation conditions and the measurement error, there is an error between the model value and test value, but it is basically within 40% when $x < 10$ mm. Therefore, the model with the diffusion variable coefficient of chloride established can predict the distribution of Cl^- concentration in concrete scientifically.

Zhang [30, 31] carried out 2D diffusion test of chloride in concrete under loading and without loading. In the test, the w/c is 0.35, and the sample size without loading and bending load is 100 mm × 100 mm×100 mm and 70 mm × 70 mm × 250 mm, respectively. The stress ratio is 0.35, the NaCl concentration in the environment is 350 g/L (5.98×10^3 mol/m^3), and the distribution of Cl^- concentration is measured after soaking for 365 days in NaCl solution. The above parameters are introduced into the diffusion model (**Eqs. 2–12**) established to simulate the distribution of Cl^- concentration after 365 days, and the results are shown in **Figure 10A**. The theoretical values are basically the same as the experimental results, and the maximum error is 20%, indicating that the numerical fitting of the model is highly consistent with the experimental results, and the model established has high reliability in this article.

In addition, Wu et al. [34] have also conducted a host of experiments to characterize the distribution of Cl^- concentration in 2D direction. In the test, the w/c is 0.54; the size of the sample is 100 mm × 100 mm×400 mm, the NaCl concentration is 3.5% in the environment, and the distribution of Cl^- concentration is measured after soaking for 180 days in concrete. The above test parameters are introduced into the diffusion model in this article, and the simulation results are shown in **Figure 10B**. The

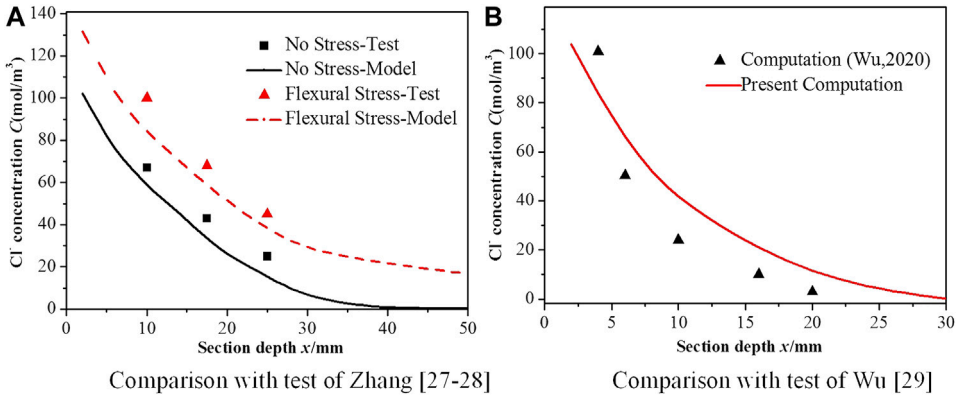

FIGURE 10 | Experimental verification of 2D diffusion variable coefficient of chloride.

theoretical values are basically the same as the experimental results, and the maximum error is 18%, further indicating that the model established is more reliable in this article.

INFLUENCE OF LOADING ON CHLORIDE CONCENTRATION DISTRIBUTION

Model parameters are w/c = 0.45, σ = 0, 0.3f_c and −0.3f_c, L = 100 mm, C_0 = 20 mol/m^3, T = 200 days, and the step length of depth and time is 2 mm and 1 day, respectively. The selected point is as follows: A (5 mm, 5 mm), B (15 mm, 15 mm), C (25 mm, 25 mm), and D (35 mm, 35 mm).

It indicates that the Cl^- concentration at the same depth is the same at different directions in **Figure 11A**, and when the depth is greater than 30 mm, there is a concentration-level surface. Among (a), (b), and (c), the concentration level of (b) is larger and the concentration level of (c) is smaller, and the smaller the concentration level, the greater the Cl^- concentration in **Figure 11**.

In **Figure 11D**, the Cl^- concentration in concrete under different loading decreases with the increase of depth. At the same depth, the Cl^- concentration is smaller in the compression zone, while that in the tension zone is larger, and that in the without loading zone is between the two. For example, when x = 10 mm and σ = 0.3f_c, 0, and −0.3f_c, the Cl^- concentration is 5.7 mol/m^3, 7.4 mol/m^3, and 9.2 mol/m^3, respectively. It is because the loading will affect the change of the porosity in the concrete. For example, under the bending load, the porosity p in the tension zone of the concrete increases (see **Eq. 7a**), resulting in a larger diffusion coefficient (D_{cp}) in cement matrix (see **Eq. 3a**), and the final effective diffusion coefficient (D_{eff}) will also be greater (see **Eq. 2**).

It indicates that the distribution trend of Cl^- concentration is the same under different loading, but the diffusion rate is different in **Figure 11E**. For example, when T = 0–100 days, the diffusion rate is about 0.15, while when T = 100–200 days, the diffusion rate is about 0.01, which is a huge difference. Compared with no stress, the results of chloride diffusion are quite different in the tension zone and the compression zone. For example, when T = 150 days and σ = 0.3f_c, 0, and −0.3f_c, the Cl^- concentration is 16.4 mol/m^3, 17.1 mol/m^3, and 17.6 mol/m^3, respectively.

Compared with (f) and (e) in **Figure 11**, the diffusion rate of chloride is stable after 50 days, and the relationship between Cl^- concentration and diffusion time is approximately linear. In **Figure 11**, the distribution trend of Cl^- concentration in (g) and (h) is the same as that in (f), but the difference is the occurrence time and rate of diffusion. The diffusion of point C and point D occurs at T = 75 days and 100 days, and the diffusion rate of the two gradually increases, which is different from the diffusion rate of point B that is approximately fixed, and point A gradually decreases. Because the greater the depth x, the greater the number of cycles at the same depth step, that is, the greater the M value (see **Eq. 13**). The chloride concentration under σ = -0.3f_c is 42.1% higher than that under σ = 0.3f_c when the diffusion time is 200 days and the concrete depth is 15 mm. When chloride is continuously diffusing into the concrete, there will be chloride accumulation at the place where x is smaller. In the 2D diffusion progress of chloride, the diffusion rate of chloride is different at the intersection point with the same distance from the adjacent diffusion surface. The smaller the depth x, the higher the increasing rate of Cl^- concentration. The trend of Cl^- concentration under different loading is the same as that under without loading, but the Cl^- concentration in the tension zone is significantly higher than that in the compression zone.

CONCLUSION

1) Based on micromechanics theory and porous medium theory, the effective diffusion coefficient model of chloride was established in concrete, considering the significant factors such as the w/c, hydration degree, ITZ volume fraction, porosity, and diffusion coefficient. The quantitative relationship among p, p_0, and σ was determined, and the 2D diffusion equation of chloride was solved in concrete based on the theory of elasticity and material mechanics. The 2D diffusion model of chloride with a variable coefficient was proposed based on Fick's second law.
2) Based on the 2D parabolic partial differential equation formed by Fick's second law, the 2D diffusion variable coefficient of chloride was systematically solved. The ADI of numerical

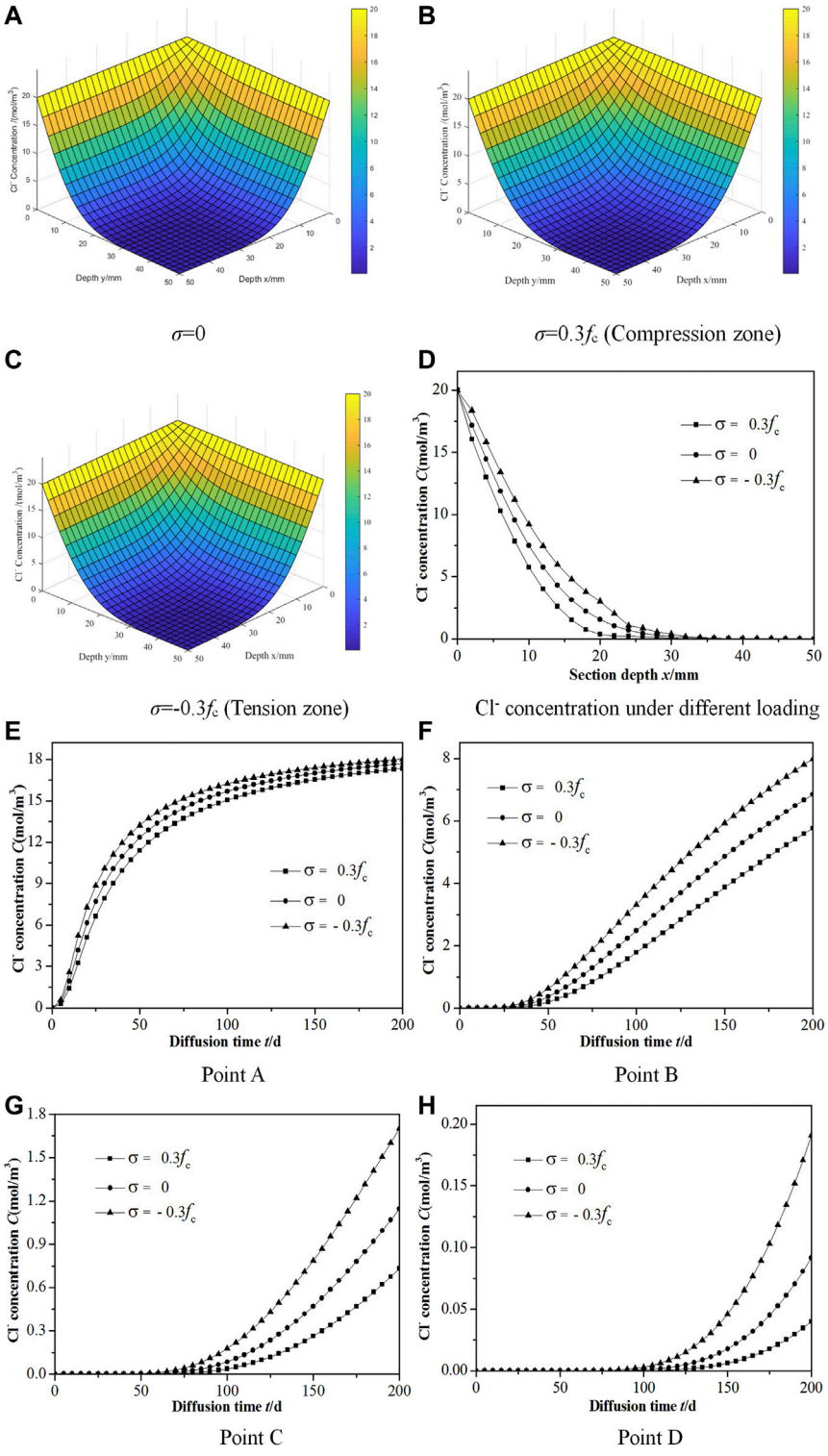

FIGURE 11 | Distribution of Cl^- concentration in concrete under different loading.

analysis was used to deduce the numerical solution of the 2D diffusion equation of chloride. The distribution of Cl^- concentration was obtained by programming in concrete. The model reliability was verified by the experiments and literatures. The simulation results were basically consistent with the experimental results.

3) The results of variable coefficient showed that the concrete eroded by chloride and the distribution of Cl^- concentration

was stepwise, which was decreasing from outside to inside along the concrete surface. The bending load affected the porosity of the cement matrix, and then the diffusion coefficient of chloride was changed in concrete. The compression zone and tension zone were formed in the concrete, and the Cl^- concentration under tension zone was 42.1% higher than that under compression zone when the diffusion time was 200 days and the concrete depth was 15 mm.

DATA AVAILABILITY STATEMENT

The original contributions presented in the study are included in the article/Supplementary Material; further inquiries can be directed to the corresponding author.

AUTHOR CONTRIBUTIONS

LZ have made contributions to the conception or design of the work; or the acquisition, analysis, or interpretation of data for the work. JZ have contributed to the building of the model. GS have drafted the substantial work or revised it for important intellectual content. ZL have made an important contribution to the theoretical calculation of the article.

FUNDING

This work was supported by the Fundamental Research Funds for the Central Universities and the National Natural Science Foundations of China (No. 51778378).

REFERENCES

1. Zhang W-M., Ba H-J., and Chen S-J. Effect of Fly Ash and Repeated Loading on Diffusion Coefficient in Chloride Migration Test. *Construction Building Mater* (2011) 25(5):2269–74. doi:10.1016/j.conbuildmat.2010.11.016
2. Yang L, Ma Q, and Yu B. Analytical Solution and Experimental Validation for Dual Time-dependent Chloride Diffusion in Concrete. *Construction Building Mater* (2018) 161:676–86. doi:10.1016/j.conbuildmat.2017.11.176
3. Jin WL, Yan YD, and Wang HL. Research Progress on the Chloride Transportation in Stressed Concrete[J]. *Chin Silicate Soc* (2010) 38(11): 2217–24. doi:10.14062/j.issn.0454-5648.2010.11.035
4. Tegguer AD, Bonnet S, Khelidj A, and Bouny VB. Effect of Uniaxial Compressive Loading on Gas Permeability and Chloride Diffusion Coefficient of Concrete and Their Relationship[J]. *Cement Concrete Res* (2013) 52:131–9. doi:10.1016/j.cemconres.2013.05.013
5. Wang H, Lu C, Jin W, and Bai Y. Effect of External Loads on Chloride Transport in Concrete. *J Mater Civ Eng* (2011) 23(7):1043–9. doi:10.1061/(asce)mt.1943-5533.0000265
6. Gowripalan N, Sirivivatnanon V, and Lim CC. Chloride Diffusivity of Concrete Cracked in Flexure. *Cement Concrete Res* (2000) 30(5):725–30. doi:10.1016/s0008-8846(00)00216-7
7. Xi Y, and Bažant ZP. Modeling Chloride Penetration in Saturated Concrete. *J Mater Civil Eng* (1999) 11(1):58–65. doi:10.1061/(asce)0899-1561(1999)11:1(58)
8. Liu Q-f., Feng G-l., Xia J, Yang J, and Li L-y.. Ionic Transport Features in Concrete Composites Containing Various Shaped Aggregates: a Numerical Study. *Compos Structures* (2018) 183(1):371–80. doi:10.1016/j.compstruct.2017.03.088
9. Cao TN, Zhang LJ, Sun GW, Wang CH, Zhang Y, Wang PS, et al.Simulation of Chloride Ion Transport in Concrete under the Coupled Effects of a Bending Load and Drying–Wetting Cycles[J]. *Construction Building Mater* (2020) 241: 118045. doi:10.1016/j.conbuildmat.2020.118045
10. Garboczi EJ, and Bentz DP. Computer Simulation of the Diffusivity of Cement-Based Materials. *J Mater Sci* (1992) 27(8):2083–92. doi:10.1007/bf01117921
11. Zhang Y, Liu C, Liu Z, Liu G, and Yang L. Modelling of Diffusion Behavior of Ions in Low-Density and High-Density Calcium Silicate Hydrate. *Construction Building Mater* (2017) 155(30):965–80. doi:10.1016/j.conbuildmat.2017.08.128
12. Sun G, Zhang J, Zhang L, Cao T, Wang P, Zhang Y, et al.M-T Scheme for Predicting Effective Diffusion Coefficient of Chloride Ions in Cement-Based Materials. *J Wuhan Univ Technol.-Mat Sci Edit* (2020) 35(3):520–7. doi:10.1007/s11595-020-2288-3
13. Xu J, and Li FM. Analytical Model for Load Dependence of Chloride Penetration into Concrete[J]. *J Mater Civil Eng ASCE* (2017) 29(5): 04016279. doi:10.1061/(asce)mt.1943-5533.0001823
14. Xu J, and Li F. A Meso-Scale Model for Analyzing the Chloride Diffusion of Concrete Subjected to External Stress. *Construction Building Mater* (2017) 130(1):11–21. doi:10.1016/j.conbuildmat.2016.11.054
15. Xu J, Li F, Zhao J, and Huang L. Model of Time-dependent and Stress-dependent Chloride Penetration of Concrete under Sustained Axial Pressure in the Marine Environment. *Construction Building Mater* (2018) 170(3):207–16. doi:10.1016/j.conbuildmat.2018.03.077
16. Li W, and Guo L. A Mechanical-Diffusive Peridynamics Coupling Model for Meso-Scale Simulation of Chloride Penetration in Concrete under Loadings. *Construction Building Mater* (2020) 241:118021. doi:10.1016/j.conbuildmat.2020.118021
17. Jin L, Du X, and Ma G. Macroscopic Effective Moduli and Tensile Strength of Saturated Concrete. *Cement Concrete Res* (2012) 42(12):1590–600. doi:10.1016/j.cemconres.2012.09.012
18. Xu W, Zhang Y, Jiang J, Liu Z, and Jiao Y. Thermal Conductivity and Elastic Modulus of 3D Porous/fractured Media Considering Percolation. *Int J Eng Sci* (2021) 161:103456. doi:10.1016/j.ijengsci.2021.103456
19. Liu Z, Xu D, Gao S, Zhang Y, and Jiang J. Assessing the Adsorption and Diffusion Behavior of Multicomponent Ions in Saturated Calcium Silicate Hydrate Gel Pores Using Molecular Dynamics. *ACS Sustain Chem. Eng.* (2020) 8:3718–27. doi:10.1021/acssuschemeng.9b06817
20. Zhang J, Zhang L, Sun G, and Wang C. Modeling and Software Development of the Interfacial Transition Zone of Ellipsoidal Aggregate in Cement-Based Composites. *J Wuhan Univ Technol.-Mat Sci Edit* (2019) 34(3):648–55. doi:10.1007/s11595-019-2099-6
21. Liu C, Liu Z, and Zhang Y. A Multi-Scale Framework for Modelling Effective Gas Diffusivity in Dry Cement Paste: Combined Effects of Surface, Knudsen and Molecular Diffusion. *Cement Concrete Res* (2020) 131:106035. doi:10.1016/j.cemconres.2020.106035
22. Caré S. Influence of Aggregates on Chloride Diffusion Coefficient into Mortar. *Cement Concrete Res* (2003) 33(7):1021–8. doi:10.1016/s0008-8846(03)00009-7
23. Zhang JJ, and Zhou XZ. Analytical Solution for the Chloride Diffusivity of Hardened Cement Paste[J]. *J Mater Civil Eng ASCE* (2008) 20(5):384–91. doi:10.1061/(ASCE)0899-1561(2008)20:5(384)
24. Zuo XB, Sun W, Li H, and Zhou WJ. Calculation of Ion Diffusion Coefficient Related to Concrete Deterioration Based on Debye-Huckel-Onsager Theory [J]. *J Southeast University(English Edition)* (2010) 26(4):569–73. doi:10.14062/j.issn.1003-7985.2010.4.026
25. Sun GW, Sun W, Zhang YS, and Liu ZY. Prediction of the Effective Diffusion Coefficient of Chloride Ions in Cement-Based Composite Materials. *J Mater Civ Eng* (2012) 24(9):1245–53. doi:10.1061/(asce)mt.1943-5533.0000477
26. Garboczi EJ, and Bentz DP. Multiscale Analytical/Numerical Theory of the Diffusivity of Concrete. *Adv Cement Based Mater* (1998) 8(2):77–88. doi:10.1016/s1065-7355(98)00010-8

27. Garboczi EJ, and Bentz DP. Analytical Formulas for Interfacial Transition Zone Properties [J]. *Adv Cement Based Mater* (1997) 6(3-4):99–108. doi:10.1016/s1065-7355(97)90016-x
28. Du X, Jin L, and Ma G. A Meso-Scale Numerical Method for the Simulation of Chloride Diffusivity in Concrete. *Finite Elem Anal Des* (2014) 85(8):87–100. doi:10.1016/j.finel.2014.03.002
29. Guo A, Li H, Ba X, Guan X, and Li H. Experimental Investigation on the Cyclic Performance of Reinforced Concrete Piers with Chloride-Induced Corrosion in Marine Environment. *Eng Structures* (2015) 105(11):1–11. doi:10.1016/j.engstruct.2015.09.031
30. Zhang Y, Sun W, Chen S, and Guo F. Two- and Three-Dimensional Chloride Ingress into Fly Ash Concrete. *J Wuhan Univ Technol.-Mat Sci Edit* (2011) 26(5):978–82. doi:10.1007/s11595-011-0348-4
31. Zhang Y-s., Sun W, Liu Z-y., and Chen S-d. One and Two Dimensional Chloride Ion Diffusion of Fly Ash Concrete under Flexural Stress. *J Zhejiang Univ Sci A* (2011) 12(9):692–701. doi:10.1631/jzus.a1100006
32. Yang CC, and Su JK. Approximate Migration Coefficient of Interfacial Transition Zone and the Effect of Aggregate Content on the Migration Coefficient of Mortar. *Cement Concrete Res* (2002) 32(10):1559–65. doi:10.1016/s0008-8846(02)00832-3
33. Sun G, Zhang Y, Sun W, Liu Z, and Wang C. Multi-scale Prediction of the Effective Chloride Diffusion Coefficient of Concrete. *Construction Building Mater* (2011) 25(10):3820–31. doi:10.1016/j.conbuildmat.2011.03.041
34. Wu L, Wang Y, Wang Y, Ju X, and Li Q. Modelling of Two-Dimensional Chloride Diffusion Concentrations Considering the Heterogeneity of Concrete Materials. *Construction Building Mater* (2020) 243:118213. doi:10.1016/j.conbuildmat.2020.118213

Conflict of Interest: The authors declare that the research was conducted in the absence of any commercial or financial relationships that could be construed as a potential conflict of interest.

frontiers in Physics

ORIGINAL RESEARCH
published: 29 July 2021
doi: 10.3389/fphy.2021.711959

Robust Optical Frequency Comb Generation by Using a Three-Stage Optical Nonlinear Dynamic

*Yali Zhang *, Shuxu Liao, Guan Wang, Ke Yang, Zhiyao Zhang, Shangjian Zhang and Yong Liu*

State Key Laboratory of Electronic Thin Films and Integrated Devices, School of Optoelectronic Science and Engineering, University of Electronic Science and Technology of China, Chengdu, China

In this article, we propose and investigate a novel scheme to generate optical frequency combs (OFCs) by using a three-stage generator, which is based on optical injection–induced dynamics cascaded by subharmonic electro-optic modulation and the four-wave mixing (FWM) effect. A primary seed OFC is rooted from the nonlinear dynamics in the optically injected semiconductor laser, and its performance is improved using a two-stage booster based on subharmonic electro-optic modulation and the FWM effect. The comb spacing can be easily tuned by adjusting that of the primary seed OFC or through electro-optic modulation by the use of subharmonics with different orders. Moreover, it becomes stabilized because the phase relationship between the comb teeth can be fixed in the process of subharmonic electro-optic modulation. Its optical spectrum continues to be broadened in the following FWM process. Finally, robust OFCs with a comb spacing of 4 GHz and a comb teeth number of 23 and a comb spacing of 5 GHz and a comb teeth number of 21 are experimentally demonstrated.

Keywords: optical frequency comb, optical injection, subharmonic electro-optic modulation, four-wave mixing, nonlinear dynamics

OPEN ACCESS

Edited by:
Jinjin Li,
Shanghai Jiao Tong University, China

Reviewed by:
Xihua Zou,
Southwest Jiaotong University, China
Yu Liu,
Institute of Semiconductors (CAS), China

****Correspondence:***
Yali Zhang
ylzhang@uestc.edu.cn

Specialty section:
This article was submitted to Optics and Photonics, a section of the journal Frontiers in Physics

Received: *19 May 2021*
Accepted: *15 June 2021*
Published: *29 July 2021*

Citation:
Zhang Y, Liao S, Wang G, Yang K, Zhang Z, Zhang S and Liu Y (2021) Robust Optical Frequency Comb Generation by Using a Three-Stage Optical Nonlinear Dynamic. Front. Phys. 9:711959. doi: 10.3389/fphy.2021.711959

INTRODUCTION

As a special kind of ultrashort optical pulse, optical frequency combs (OFCs) have important applications in various fields, ranging from examining the theory of quantum electro-dynamics [1, 2], space and time variations of fundamental constants [3–5], optical frequency synthesis [6], optical communications [7], and precise optical metrology [8] to optical arbitrary waveform generation [9] and so on. For example, it can realize high-precision measurement of optical frequency. The core of such high-precision optical spectroscopy is due to high frequency stabilities and accuracies of ultranarrow light sources at the desired wavelengths provided by the OFC [10].

Over the past decades, to meet the preference demand on OFCs in various application scenarios, various kinds of generation techniques for OFCs have been proposed, which have demonstrated their own distinct characteristics. These generation techniques can be generally categorized into six main types. The two classical ones are based on mode-locked lasers (MLLs) [11, 12] and on cyclic frequency shift structures [13, 14]. The four others can all be classified into the microwave photonic domain, namely, based on modulators [15, 16], based on optoelectronic oscillators (OEOs) [17, 18], based on nonlinear optical fibers [19, 20], and based on optically injected semiconductor lasers [21, 22]. For OFCs based on modulators, the phase relationship between the comb teeth is fixed due to the known electro-optic effect, the frequency stability is robust, and comb spacing can be flexibly adjusted by changing the frequency of the modulation signal. However, the number of comb teeth is

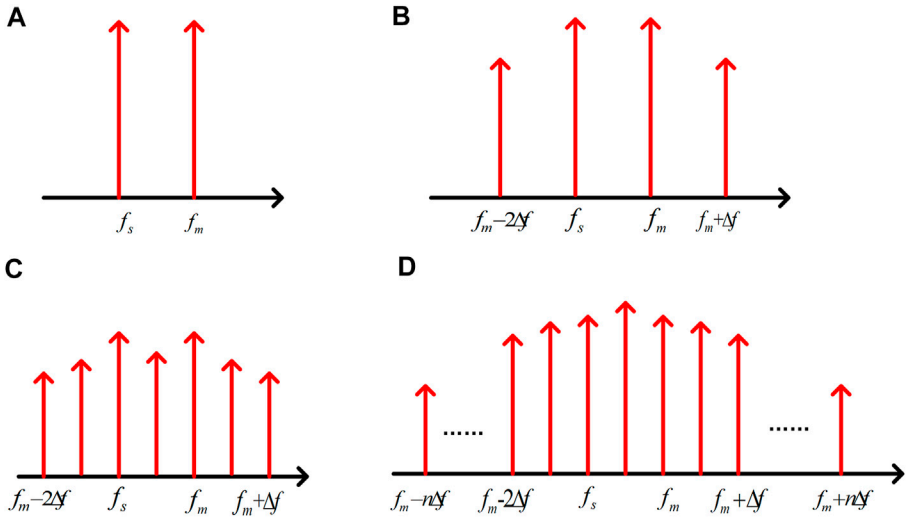

FIGURE 1 | Principle diagram of the proposed generation system of the OFC. Spectra diagram of **(A)** free-running ML and SL lasers, **(B)** primary seed OFC, **(C)** subharmonic-locked OFC, and **(D)** FMW-broadened OFC.

small and the flatness is poor, both of which are limited by the power of the modulation signal and the bandwidth of the used modulators. The comb spacing of OFCs based on MLLs can also be adjustable, for the wavelength tuning range of MLLs is large and its repetition frequency can be adjusted in a certain range. Yet its flexibility is poor, for the repetition frequency of MLLs can only be tuned in a small range. The OFC based on cyclic frequency shift structures has numbers of comb teeth and good flatness, whereas it has disadvantages such as an unclear phase relationship between comb teeth and high carrier noise. The OFC generated by the self-oscillation in the optoelectronic oscillation loop does not need an external microwave source, which can help avoid the additional phase noise caused by the external microwave source. At the same time, OEOs can provide a stable microwave signal with stable ultralow noise to reduce the phase noise of the generated OFC. However, not only is the system structure of the scheme complex and expensive but also the number of comb teeth is relatively small and the comb spacing cannot be changed due to the limited narrow bandwidth of the electronic filter in the OEO loop. The OFC based on nonlinear effects in optical fibers has numbers of comb teeth, but the flatness is poor. What is worse is that the number of comb teeth cannot be controlled because it is difficult to quantitatively control nonlinear effects. Interestingly, the optical spectrum of the period-one oscillation state induced in the optically injected semiconductor laser has several frequency modes, and the frequency spacing between these modes is strictly equal, which is exactly an embryonic form of OFCs. Therefore, it has the potential to generate OFCs based on optical injection technology. It has been found that the nonlinear period-one dynamic can successfully provide seed OFCs. The process of optical injection in the resonance cavity of the laser can ensure coherence among the comb teeth, and it can realize the flexile adjustment of comb spacing in principle. In addition, the optical injection technology is simple in structure, rich in theoretical analysis, and mature in technology. However, such primary seed OFCs are quite sparse in number and uneven in flatness with respect to comb teeth, and the phase relationship between the comb teeth may become unstable due to the fluctuation noise originating in the resonance cavity of the laser.

In this study, we employ the primary OFC that originated from the process of optical injection as the seed OFC. We propose and demonstrate that improved OFCs with adjustable comb spacing and excellent frequency stability can be obtained with cascaded subharmonic electro-optic modulation and the four-wave mixing (FWM) effect. Finally, robust OFCs with a comb spacing of 4 GHz and a comb teeth number of 23 and a comb spacing of 5 GHz and a comb teeth number of 21 are demonstrated in the experiment.

OPERATION PRINCIPLE

The evolution process of the proposed three-stage OFC generator is shown in **Figure 1**. f_m and f_s are the working frequencies of the master laser (ML) and the free-running slave laser (SL), as shown in **Figure 1A**. The SL that is optically injected by the ML can be piloted to enter the period-one oscillation state under appropriate injection conditions, and a primary seed OFC with a comb spacing of Δf ($\Delta f = f_m - f_s$) is generated in the first stage, which has sparse comb teeth, as shown in **Figure 1B**. This primary seed OFC is then sent into a phase modulator (PM) and modulated by the external RF signal at the frequencies of subharmonics of the oscillation period. The primary seed OFC teeth are locked by the subharmonic electro-optic modulation sidebands in the second stage, which will fix the phase relationship of the comb teeth through electro-optic modulation. Interestingly, similar to the dynamic process that is the optical injection locking being able to occur in a certain range of the detuning frequency between the ML and the SL, this

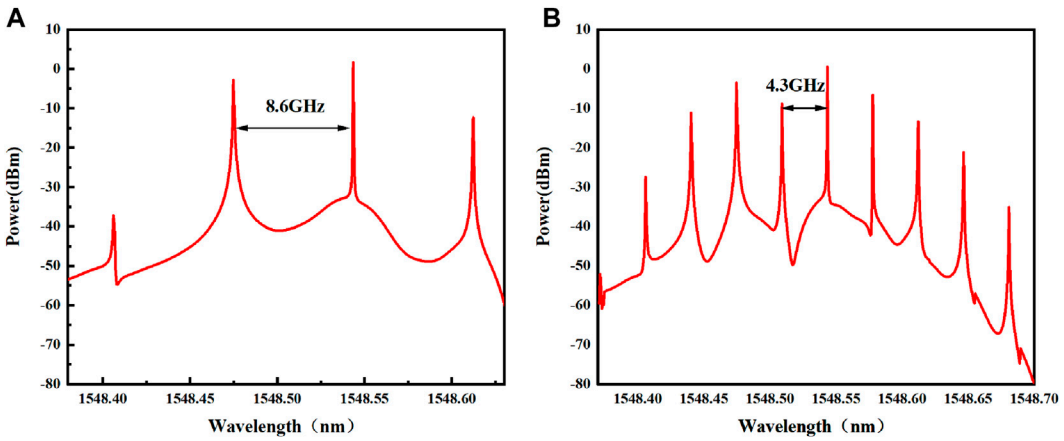

FIGURE 2 | (A) Primary seed OFC. **(B)** Subharmonic-locked OFC obtained by simulation.

subharmonic locking behavior stays robust in a certain frequency deviation between the period-one frequency and the subharmonic frequency. In addition, the number of comb teeth of this subharmonic-locked OFC increases, and the comb spacing is now $\Delta f/N$(at $1/N$ subharmonic electro-optic modulation, N = 1, 2, 3 ...), as shown in **Figure 1C** at 1/2 subharmonic electro-optic modulation. Then the subharmonic-locked OFC with the locked phase relationship between the comb teeth is sent into a semiconductor optical amplifier (SOA).

In the SOA, if the comb teeth at frequencies of $f_m - 1.5\Delta f, f_m - 2\Delta f, f_m - 2.5\Delta f$ satisfy the phase matching condition, they will interact with each other and bring out the FWM effect, which leads to the parametric amplification of the frequency mode $f_m - 1.5\Delta f$while generating the signal light with the frequency of $f_m - 3\Delta f$. The generated signal light with the two comb teeth at frequencies of $f_m - 2\Delta f$ and $f_m - 2.5\Delta f$ will continue to bring out the FWM effect under the condition of phase matching, which will lead to another new signal light at the frequency of $f_m - 3.5\Delta f$ being generated and new parametric amplification being carried out at the same time. The comb teeth at frequencies of $f_m - 3\Delta f, f_m - 3.5\Delta f \ldots f_m - n\Delta f$ will be generated in turn. Similarly, the comb teeth at frequencies of $f_m + 2\Delta f$, $f_m + 2.5\Delta f \ldots f_m + n\Delta f$ will be generated at the side of high frequency, and the intensity of the newly generated modes will be increased in these parametric amplification processes. Consequently, the number of comb teeth becomes greater in the third stage, and the newly generated OFC becomes flatter, namely, the FWM-broadened OFC, as shown in **Figure 1D**. In summary, the robust OFC is obtained after experiencing a three-stage evolutionary process, including the period-one oscillation state in the optically injected laser, the electro-optic modulation in the PM, and the FWM effect in the SOA.

SIMULATION RESULTS

To verify the proposed scheme, simulation is conducted using Optisystem. When the detuning frequency is set to 5 GHz and the injected intensity is −17.5 dBm, the SL enters the period-one oscillation state and the primary seed OFC is generated, as shown in **Figure 2A**. Due to the redshift of 3.6 GHz caused by optical injection, the frequency spacing between the comb teeth is 8.6 GHz. The primary seed OFC has few comb teeth, only 4, and is not flat in intensity. In order to increase the number of comb teeth and stabilize the phase relationship between the comb teeth, a PM is used to modulate the seed OFC, and an RF signal is employed, whose frequency is set to 4.3 GHz, which is half of the oscillation period of 8.6 GHz. For the subharmonic-locked OFC, the number of comb teeth is increased to 10, and the comb spacing is equal to the frequency of the modulation RF signal, as shown in **Figure 2B**.

The subharmonic-locked OFC is then sent into the following SOA, and the FWM effect in the SOA is induced to relay the increasing of the number of comb teeth. The corresponding simulation results are shown in **Figure 3**. It can be seen that the FWM effect drives the number of comb teeth increasing in an obvious manner, and the number of comb teeth increases with the increase in the injection current of the SOA. Compared with the primary seed OFC, the number of comb teeth is up to 35 when the injection current of the SOA is 200 mA, 50 when it is 400 mA, 65 when it is 600 mA, 79 when it is 800 mA, and 101 when it is 1000 mA. The cascaded subharmonic electro-optic modulation and the relaying FWM effect can effectively improve the primary seed OFC in terms of the number and flatness of its comb teeth.

EXPERIMENT RESULTS AND DISCUSSION

Experiments based on the scheme in **Figure 4** are performed to verify the proposed scheme and the simulation results above. The light emitted by the ML passes through the optical isolator (OI), the variable optical attenuator (VOA), and the polarization controller (PC1) in sequence and is then sent into the 3-port optical circulator (OC) at the first port. The SL is connected to the second port of this OC. Due to the perturbation by the external coherence light from the ML, the SL can be controlled into the

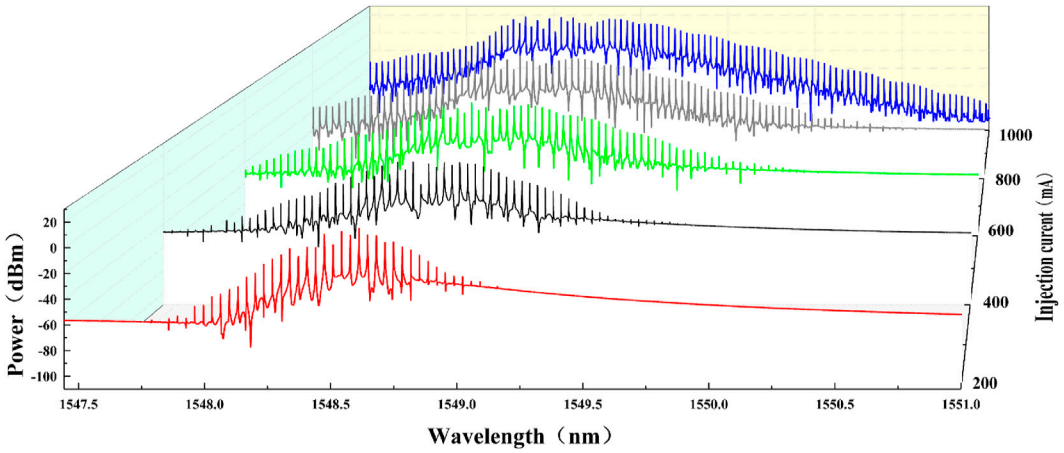

FIGURE 3 | OFCs obtained by simulation under different injection currents of the SOA.

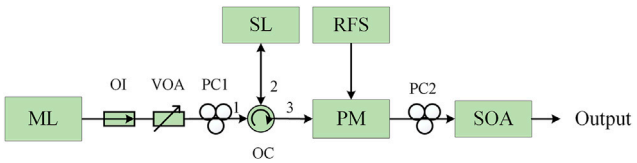

FIGURE 4 | Experimental setup of the proposed system. ML, master laser; SL, slave laser; RFS, RF source; PM, phase modulator; SOA, semiconductor optical amplifier; OI, optical isolator; VOA, variable optical attenuator; PC, polarization controller.

period-one oscillation state, and the primary seed OFC is experimentally generated, which is directly sent into the PM at the third port of the OC. After being modulated in the PM, it is sent into the SOA through the PC2. Finally, the enhanced OFC can be obtained at the output end of the SOA. As analyzed above, the reason for modulating the primary seed OFC from the SL is that the phase stability between the frequency modes of the period-one oscillation state is poor. Such a primary seed OFC is unstable in phase due to carriers in the resonance cavity of the SL. With the use of subharmonic electro-optic modulation, the phase relationship between the comb teeth can be locked and stabilized in the process of the electro-optic modulation, and the original comb teeth are locked to the modulation sidebands at the same frequency. At the same time, subharmonic electro-optic modulation can also make the primary seed OFC teeth become more in number. The function of the PC2 is to control the polarization state of the subharmonic-locked seed OFC because the FWM effect is polarization dependent. By adjusting the PC, the FWM efficiency in the SOA can be maximized.

The bias current of the SL is set to 19.72 mA, the temperature of the laser control system is set to 19.81°C, the working wavelength is 1554.1460 nm, and the output power is −3 dBm for the SL. Adjusting the injection intensity by the VOA and the working wavelength of the ML (i.e., changing the detuning frequency between the ML and the SL), the primary seed OFC with flexible and adjustable comb spacing can be obtained. When the detuning frequency is 6 GHz, a primary seed OFC with a comb spacing of 8 GHz and a comb teeth number of eight is generated, as shown in **Figure 5A**. The reason why the comb spacing is larger than the detuning frequency between the ML and the SL is the redshift of the cavity resonant mode wavelength of the SL due to optical injection. It can be seen that the period-one oscillation state can naturally provide a primary seed OFC with tunable comb spacing, but the number of comb teeth is relatively small and its flatness is poor. When the primary seed OFC is modulated by 1/2 subharmonic at 18 dBm, the comb spacing becomes 4 GHz and the number of comb teeth becomes 16, as shown in **Figure 5B**. The comb spacing of the OFC modulated by the 1/2 subharmonic is halved, the number of comb teeth is doubled, and the envelope of comb teeth becomes flatter as well.

The subharmonic-locked OFC with a comb spacing of 4 GHz is sent into the following SOA. The performance of the experimentally obtained OFCs varies with the injection current of the SOA, as shown in **Figure 6**. Because the phase relationship between the comb teeth is stabilized by subharmonic electro-optic modulation, it is observed that the obtained OFC is very stable when the FWM effect occurs in the SOA. With the increase in the injection current of the SOA, the FWM efficiency increases, which leads to the number of comb teeth increasing in an obvious manner, as expected by the simulation.

For the proposed system, when the intensity of the modulation signal is set to 18 dBm and the injection current of the SOA is set to 300 mA, the quality of the primary seed OFC is obviously improved, and we finally get the FWM-broadened OFC with a comb teeth number of 23 and a comb spacing of 4 GHz, as shown in **Figure 7A**. The system can also generate OFCs with different comb spacing. By adjusting the injection parameters, we obtain a primary seed OFC with a comb spacing of 10 GHz and modulate it with the use of the 1/2 subharmonic before sending it into the SOA with an injection current of 300 mA, and then another OFC with a comb spacing of 5 GHz and a comb teeth number of 21 is obtained, as shown in **Figure 7B**. While in the SOA, the smaller the comb spacing, the higher the FWM efficiency. Moreover, the higher the injection current of the SOA, the higher the FWM efficiency. Here, the authors would like to mention that the injection current of the

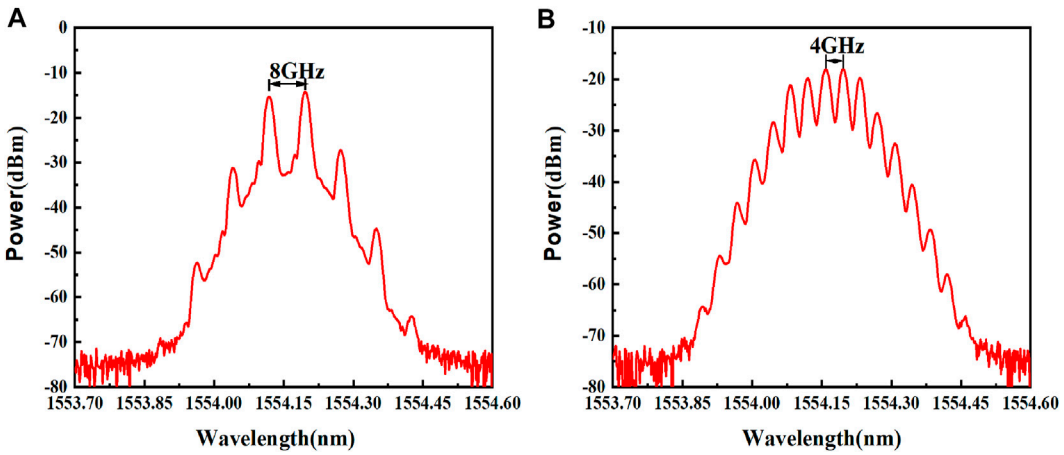

FIGURE 5 | (A) Primary seed OFC. **(B)** Subharmonic-locked OFC generated in the experiment.

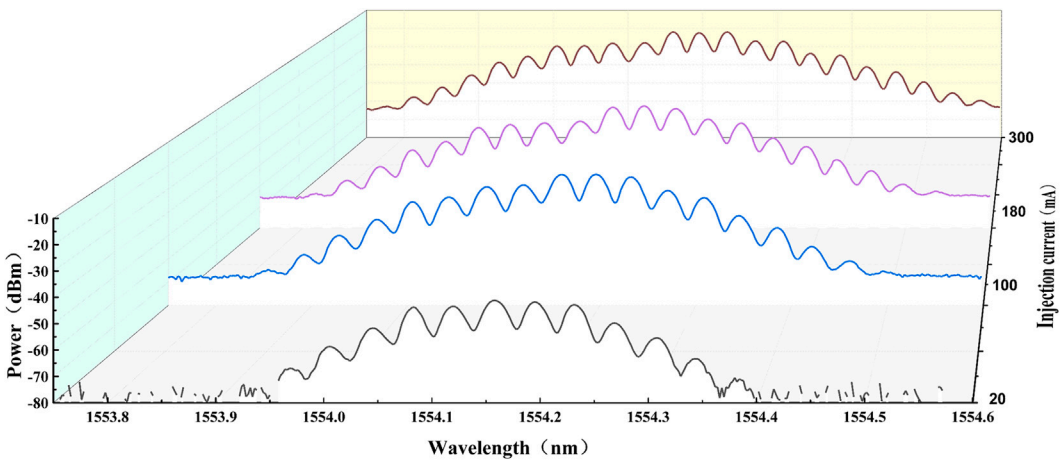

FIGURE 6 | Experimentally obtained FWM-broadened OFCs under different injection currents of the SOA.

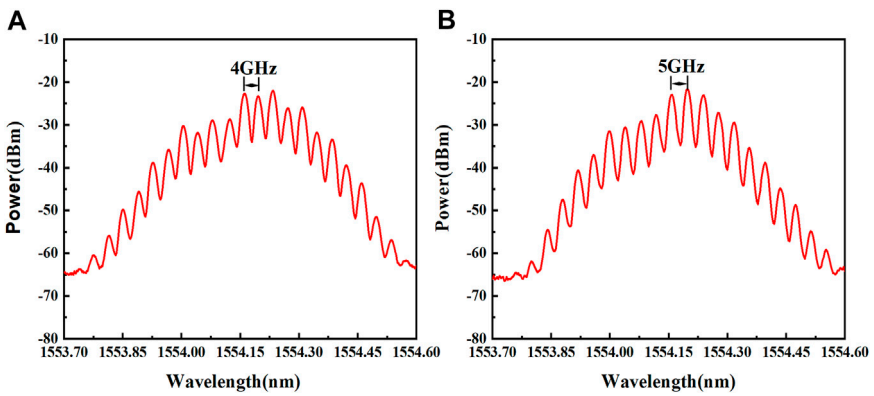

FIGURE 7 | OFCs from the SOA with a comb spacing of **(A)** 4 GHz and **(B)** 5 GHz.

SOA in our laboratory is limited to less than 300 mA, which greatly limits the performance enhancement for the proposed OFC.

CONCLUSIONS

In this article, we have proposed and demonstrated a novel scheme to produce robust OFCs using a three-stage generator, which is based on optical injection and improved by cascaded subharmonic electro-optic modulation and the FWM effect. The obtained OFC features high stability, thanks to the stable phase relationship between the primary seed OFC teeth and the subharmonic electro-optic modulation sidebands through the subharmonic locking. Moreover, it can be flexibly tuned by adjusting the injection parameters of the slaver laser. Finally, robust OFCs with a comb spacing of 4 GHz and a comb teeth number of 23 and a comb spacing of 5 GHz and a comb teeth number of 21 are experimentally obtained and demonstrated. If the injection current of the SOA in the experiment can be higher than 300 mA, the maximum value in our laboratory, the proposed OFC generator can be expected to behave like the simulation situation.

DATA AVAILABILITY STATEMENT

The raw data supporting the conclusions of this article will be made available by the authors, without undue reservation.

AUTHOR CONTRIBUTIONS

SL and YZ designed the research and discussed it with ZZ, SZ, and YL. SL, KY, and GW completed the experiment together. ZZ, SZ, and YL participated in the analysis and discussion of the experimental results. SL drafted the content of the manuscript. YZ was the corresponding author and guided and revised the manuscript.

FUNDING

This work was supported by the National Key R & D Program of China (2018YFE0201900) and the National Natural Science Foundation of China (NSFC) (61927821).

REFERENCES

1. Altmann RK, Dreissen LS, Salumbides EJ, Ubachs W, and Eikema KSE. Deep-ultraviolet Frequency Metrology of H2 for Tests of Molecular Quantum Theory. *Phys Rev Lett* (2018) 120(4):1–6. doi:10.1103/physrevlett.120.043204
2. Biesheuvel J, Karr JP, Hilico L, Eikema KSE, Ubachs WG, and Koelemeij JCJ. Probing QED and Fundamental Constants through Laser Spectroscopy of Vibrational Transitions in HD. *Nat Commun* (2016) 7(1):10385. doi:10.1038/ncomms10385
3. Webb JK, King JA, Murphy MT, Flambaum VV, Carswell RF, and Bainbridge MB. Indications of a Spatial Variation of the fine Structure Constant. *Phys Rev Lett* (2011) 107(19):191101. doi:10.1103/physrevlett.107.191101
4. Huntemann N, Lipphardt B, Tamm C, Gerginov V, Weyers S, and Peik E. Improved Limit on a Temporal Variation of Mp/me from Comparisons of Yb+ and Cs Atomic Clocks. *Phys Rev Lett* (2014) 113(21):210802. doi:10.1103/physrevlett.113.210802
5. Godun RM, Nisbet-Jones PBR, Jones JM, King SA, Johnson LAM, Margolis HS, et al. Frequency Ratio of Two Optical Clock Transitions in 171Yb+ and Constraints on the Time Variation of Fundamental Constants. *Phys Rev Lett* (2014) 113(21):210801. doi:10.1103/physrevlett.113.210801
6. Jones DJ, Diddams SA, Ranka JK, Stentz AS, Windeler RS, Hall JL, et al. Carrier-envelope Phase Control of Femtosecond Mode-Locked Lasers and Direct Optical Frequency Synthesis. *Science* (2000) 288(5466):635–9. doi:10.1126/science.288.5466.635
7. Yu JJ, Dong Z, Zhang JW, Xiao X, Chien H-C, and Chi N. Generation of Coherent and Frequency-Locked Multi-Carriers Using Cascaded Phase Modulators for 10 Tb/s Optical Transmission System. *J Lightwave Technol* (2012) 30(4):458–65. doi:10.1109/jlt.2011.2173460
8. Coddington I, Swann WC, and Newbury NR. Coherent Dual-Comb Spectroscopy at High Signal-To-Noise Ratio. *Phys Rev Lett* (2010) 82(4):043817. doi:10.1103/physreva.82.043817
9. Zhang FZ, Wu J, Li Y, and Lin JT. Flat Optical Frequency Comb Generation and its Application for Optical Waveform Generation. *Opt Commun* (2013) 290(1):37–42. doi:10.1016/j.optcom.2012.10.051
10. Chae E, Nakashima K, Ikeda T, Sugiyama K, and Yoshioka K. Direct Phase-Locking of a Ti:Sapphire Optical Frequency Comb to a Remote Optical Frequency Standard. *Opt Express* (2019) 27(11):15649–61. doi:10.1364/oe.27.015649
11. Davila-Rodriguez J, Bagnell K, and Delfyett PJ. Frequency Stability of a 10GHz Optical Frequency Comb from a Semiconductor-Based Mode-Locked Laser with an Intracavity 10,000 Finesse Etalon. *Opt Lett* (2013) 38(18):3665–8. doi:10.1364/OL.38.003665
12. Hellwig T, Rieger S, and Fallnich C. An All-Optically Stabilized Frequency Comb Based on a Mode-Locked Fiber Laser. *Opt Lett* (2014) 39(3):525–7. doi:10.1364/OL.39.000525
13. Li JP, Zhang XG, and Xi LX. Generation of Stable and High-Quality Frequency-Locked Carriers Based on Improved Re-circulating Frequency Shifter. *Opt Commun* (2012) 285(20):4072–5. doi:10.1016/j.optcom.2012.06.014
14. Li JP, and Li ZH. Frequency-locked Multicarrier Generator Based on a Complementary Frequency Shifter with Double Recirculating Frequency-Shifting Loops. *Opt Lett* (2013) 38(3):359–61. doi:10.1364/ol.38.000359
15. Wang Q, Huo L, Xing YF, and Zhou BK. Ultra-flat Optical Frequency Comb Generator Using a Single-Driven Dual-Parallel Mach-Zehnder Modulator. *Opt Lett* (2014) 39(10):3050–3. doi:10.1364/ol.39.003050
16. Qu K, Zhao SH, Li X, Zhu ZH, Liang D, and Liang DY. Ultra-flat and Broadband Optical Frequency Comb Generator *via* a Single Mach-Zehnder Modulator. *IEEE Photon Technol Lett* (2017) 29(2):255–8. doi:10.1109/lpt.2016.2640276
17. Dai J, Xu XY, Wu ZL, Dai YT, Yin FF, Zhou Y, et al. Self-oscillating Optical Frequency Comb Generator Based on an Optoelectronic Oscillator Employing Cascaded Modulators. *Opt Express* (2015) 23(23):30014–9. doi:10.1364/oe.23.030014
18. Plascak ME, Bustos Ramirez R, Bagnell K, and Delfyett PJ. Tunable Broadband Electro-Optic Comb Generation Using an Optically Filtered Optoelectronic Oscillator. *Photon Technol Lett* (2018) 30(4):335–8. doi:10.1109/lpt.2017.2788361
19. Yang X, Richardson DJ, and Petropoulos P. Broadband, Flat Frequency Comb Generated Using Pulse Shaping-Assisted Nonlinear Spectral Broadening. *IEEE Photon Technol Lett* (2013) 25(6):543–5. doi:10.1109/lpt.2013.2242882
20. Yu SY, Bao FD, and Hu H. Broadband Optical Frequency Comb Generation with Flexible Frequency Spacing and center Wavelength. *IEEE Photon J.* (2018) 10(2):1–7. doi:10.1109/jphot.2018.2832842
21. Ge MF, Zhang YL, Xia Y, Zhang ZY, Zhang SJ, and Liu Y. Optical-injection-seeded Optical Frequency Comb Generation Promoted by the Sub-harmonic Modulation. In: The 18th International Conference on Optical Communications and Networks; 2019 Aug 05–08; Huangshan, China (2019). doi:10.1109/icocn.2019.8933971
22. Zhang YL, Ge MF, Zhang ZY, Zhang SJ, and Liu Y. Self-recirculating Modulation-Enhanced Optical Frequency Comb Generation Pumped by

Optical Injection. In: SPIE/COS Photonics Asia; 2019 Oct 20–23; Hangzhou, China (2019). doi:10.1117/12.2538935

Conflict of Interest: The authors declare that the research was conducted in the absence of any commercial or financial relationships that could be construed as a potential conflict of interest.

Publisher's Note: All claims expressed in this article are solely those of the authors and do not necessarily represent those of their affiliated organizations, or those of the publisher, the editors and the reviewers. Any product that may be evaluated in this article, or claim that may be made by its manufacturer, is not guaranteed or endorsed by the publisher.

frontiers in Physics

ORIGINAL RESEARCH
published: 17 September 2021
doi: 10.3389/fphy.2021.730761

Equivalence of Dissipative and Dissipationless Dynamics of Interacting Quantum Systems With Its Application to the Unitary Fermi Gas

Masaaki Tokieda[1,2]* *and Shimpei Endo*[1,3]*

[1]Department of Physics, Tohoku University, Sendai, Japan, [2]Strangeness Nuclear Physics Laboratory, RIKEN Nishina Center, Wako, Japan, [3]Frontier Research Institute for Interdisciplinary Science, Tohoku University, Sendai, Japan

We analytically study quantum dissipative dynamics described by the Caldirola-Kanai model with inter-particle interactions. We have found that the dissipative quantum dynamics of the Caldirola-Kanai model can be exactly mapped to a dissipationless quantum dynamics under a negative external harmonic potential, even when the particles are strongly interacting. In particular, we show that the mapping is valid for the unitary Fermi gas, which is relevant for cold atoms and nuclear matters.

Keywords: dissipative quantum system, Caldirola-Kanai model, cold atoms, unitary fermi gas, nuclear dynamics

OPEN ACCESS

Edited by:
Jinjin Li,
Shanghai Jiao Tong University, China

Reviewed by:
Ignazio Licata,
Institute for Scientific Methodology (ISEM), Italy
Joaquin Drut,
University of North Carolina at Chapel Hill, United States

***Correspondence:**
Masaaki Tokieda
masaaki.tokieda@inria.fr
Shimpei Endo
shimpei.endo@nucl.phys.tohoku.ac.jp

Specialty section:
This article was submitted to Nuclear Physics, a section of the journal Frontiers in Physics

Received: *25 June 2021*
Accepted: *31 August 2021*
Published: *17 September 2021*

Citation:
Tokieda M and Endo S (2021) Equivalence of Dissipative and Dissipationless Dynamics of Interacting Quantum Systems With Its Application to the Unitary Fermi Gas. Front. Phys. 9:730761. doi: 10.3389/fphy.2021.730761

1 INTRODUCTION

Dissipation plays essential roles in the non-equilibrium dynamics of quantum matters. There has been rapid growth of research interests in the dissipative quantum dynamics as it is relevant to macroscopic quantum tunneling [1], low-energy nuclear reactions [2–4], dynamics of cold atoms [5–7], and quantum information processings [8, 9]. Milestones in this research field is the Caldeira-Leggett model [1] and the Lindblad type equations [10, 11], where dissipation in the quantum system originates from the coupling of the system with the environment.

While these approaches to the quantum dissipative dynamics have been widely and successfully used, it is rather difficult to obtain an exact result in an analytical manner for most practical problems. To deal with the quantum dissipative dynamics in a more analytically feasible manner, we can alternatively resort to a simpler quantum equation of motion. One of the elementary models describing such a dissipative quantum motion is the Caldirola-Kanai model [12, 13] characterized by the Lagrangian

$$L_{\mathrm{CK}}\left(\{\mathbf{x}_i\},\{\dot{\mathbf{x}}_i\},t\right)=e^{\gamma t}\left[\sum_{i=1}^{N}\frac{m_i}{2}\dot{\mathbf{x}}_i^2-U\left(\mathbf{x}_1,\ldots,\mathbf{x}_N,t\right)\right], \tag{1}$$

and its semi-classical equation of motion.

$$\ddot{\mathbf{x}}_i\left(t\right)+\gamma\dot{\mathbf{x}}_i\left(t\right)+\frac{1}{m_i}\frac{\partial U}{\partial\mathbf{x}_i}\left(\mathbf{x}_1\left(t\right),\ldots,\mathbf{x}_N\left(t\right),t\right)=0, \tag{2}$$

where m_i, $\mathbf{x}_i$ and $\dot{\mathbf{x}}_i=(d/dt)\mathbf{x}_i$ are the mass, the position, and the velocity of the i-th particle respectively. U denotes an interaction or an external potential, and γ is the dissipation rate (see **Equation 26** for the Schrödinger equation and the Hamiltonian for the Caldirola-Kanai model). Taking advantage of its simplicity, the Caldirola-Kanai model has been applied to various dissipative quantum phenomena, including damping of electromagnetic fields in a plasma medium [14],

dissipative quantum tunneling in low-energy nuclear fusion reactions [15], dynamics of a damped charged oscillator in the presence of the Aharanov-Bohm effect [16], and so on. While the Caldirola-Kanai model has usually been applied to a single-particle motion regarding U as an external potential as in the original setting [12, 13], we can also consider the dynamics of interacting quantum particles under the dissipation regarding U as inter-particle interactions.

In this paper, we analytically study the quantum dissipative motion of interacting particles with the Caldirola-Kanai model. We show that this dissipative system can be exactly mapped to a dissipationless system with an inverted harmonic potential. Similar mappings have been discussed for single-particle systems in the literature [17–19]. In this paper, we extend the mapping to many-particle systems, particularly to a strongly interacting system with a divergently large s-wave scattering length, i.e., unitary interaction. Such a system has attracted increasing interests in terms of the unitary Fermi gas in cold atoms. Furthermore, as neutron matters are well described by the unitary Fermi gas [20–26], our exact mapping should be useful for understanding non-equilibrium dynamics of nuclear matters.

The paper is organized as follows: in **Section 2**, we introduce the Caldirola-Kanai model and its Hamiltonian, and then show the formal mapping procedure from the Caldirola-Kanai model to a dissipationless Hamiltonian with an inverted harmonic barrier. In **Section 3**, we study the exact mapping for interacting systems. In particular, we consider the Caldirola-Kanai model with the zero-range interaction, and show that it can be mapped to the dissipationless Hamiltonian with an inverted harmonic barrier when the particles are interacting via the unitary interaction. We conclude and discuss physical implications of our exact mapping in **Section 4**.

2 MAPPING THE CALDIROLA-KANAI MODEL TO A DISSIPATIONLESS MOTION WITH AN INVERTED HARMONIC BARRIER

In this section, we show the exact mapping from the Caldirola-Kanai model to a dissipationless Hamiltonian with an inverted harmonic potential. To make it self-contained, we reformulate the arguments in Refs. [17–19] and begin our discussion with a single-particle system in a one-dimensional space for classical mechanics in **Section 2.1** and for quantum mechanics in **Section 2.2**. We see that the mapping between the dissipative and dissipationless dynamics can be understood as a transformation of the coordinate from one system to the other. We then extend this idea to a many-particle system in a d-dimensional space in **Section 2.3**. We find that the mapping can formally remain true even in the presence of inter-particle interactions.

2.1 Transformation of the Classical Coordinates

To see the mapping heuristically, let us first consider the classical dynamics of a damped harmonic oscillator in one spacial dimension. The equation of motion reads

$$\ddot{x}(t) + \gamma\dot{x}(t) + \omega^2 x(t) = 0, \tag{3}$$

with the frequency ω and the dissipation rate γ. Its analytical solution can be obtained easily. For example, for an under-damped case, it reads

$$x(t) = e^{-\frac{\gamma t}{2}}\left[x(0)\cos(\Omega t) + \frac{\dot{x}(0) + (\gamma/2)x(0)}{\Omega}\sin(\Omega t)\right], \tag{4}$$

with $\Omega = \sqrt{\omega^2 - (\gamma/2)^2}$.

Notice that the solution is similar to that of a simple harmonic oscillator. This similarity can be understood in the following way. We first introduce a new variable $y(t)$,

$$x(t) = e^{-\gamma t/2}y(t). \tag{5}$$

Substituting this relation into the equation of motion for $x(t)$, **Eq. 3**, one finds that $y(t)$ satisfies the equation of motion of a simple harmonic oscillator,

$$\ddot{y}(t) + \Omega^2 y(t) = 0. \tag{6}$$

The general solution is given by

$$y(t) = y(0)\cos(\Omega t) + \frac{\dot{y}(0)}{\Omega}\sin(\Omega t). \tag{7}$$

From the relation **Eq. 5**, one finds

$$\begin{aligned} y(0) &= x(0), \\ \dot{y}(0) &= \dot{x}(0) + \frac{\gamma}{2}x(0). \end{aligned} \tag{8}$$

Substituting **Eqs. 7** and **8** into **Eq. 5** leads to the solution of the damped harmonic oscillator **Eq. 4**.

In the above discussion, we observe that the transformation **Eq. 5** replaces the damping term $\gamma\dot{x}(t)$ with the $-(\gamma^2/4)y(t)$ term. This replacement remains true even in the presence of an arbitrary external potential: suppose that $x(t)$ describes a dissipative motion with an arbitrary external potential $V(x, t)$, that is, $x(t)$ satisfies the following equation of motion,

$$\ddot{x}(t) + \gamma\dot{x}(t) + \frac{1}{m}\frac{dV}{dx}(x(t), t) = 0. \tag{9}$$

By the transformation **Eq. 5**, the equation of motion for $y(t)$ is given as

$$\ddot{y}(t) + \frac{1}{m}e^{\gamma t/2}\frac{dV}{dz}(z = y(t)e^{-\gamma t/2}, t) - \frac{\gamma^2}{4}y(t) = 0. \tag{10}$$

This equation of motion is derived from the following Lagrangian,

$$L_y(y, \dot{y}, t) = \frac{m}{2}\dot{y}^2 - \left[e^{\gamma t}V(ye^{-\gamma t/2}, t) - \frac{m\gamma^2}{8}y^2\right]. \tag{11}$$

This means that the transformation **Eq. 5** maps a dissipative system to a system with the rescaled potential $e^{\gamma t}V(ye^{-\gamma t/2}, t)$ together with the inverted harmonic potential $-m\gamma^2y^2/8$. The damped harmonic oscillator discussed above is a special example where the potential is given by $V(x, t) = m\omega^2x^2/2$ and the time-dependence of the rescaled potential disappears because of $e^{\gamma t}V(ye^{-\gamma t/2}) = \frac{m\omega^2}{2}y^2$.

With the transformation **Eq. 5**, one can find an effective Lagrangian for a dissipative motion described by **Eq. 9**:

$$L_x(x,\dot{x},t) = L_y(y(x),\dot{y}(x,\dot{x}),t) = e^{\gamma t}\left[\frac{m}{2}\dot{x}^2 - V(x,t)\right] + \frac{m\gamma}{4}\frac{d}{dt}\left(xe^{\gamma t/2}\right)^2. \tag{12}$$

Neglecting the last term which does not affect the equation of motion, one obtains the Lagrangian of the Caldirola-Kanai model under an arbitrary time-dependent external potential

$$L_{\mathrm{CK}}(x,\dot{x},t) = e^{\gamma t}\left[\frac{m}{2}\dot{x}^2 - V(x,t)\right]. \tag{13}$$

From these Lagrangians, we can derive the Hamiltonians for the motions of $x(t)$ and $y(t)$. For a dissipative system described by the Caldirola-Kanai model, $x(t)$, it should be noted that the canonical momentum, $\pi_x(t)$, is different from the kinetic momentum, $m\dot{x}(t)$,

$$\pi_x(t) = \frac{\partial L_{\mathrm{CK}}}{\partial \dot{x}} = m\dot{x}(t)e^{\gamma t}. \tag{14}$$

One then obtains the Caldirola-Kanai Hamiltonian

$$H_{\mathrm{CK}}(x,\pi_x,t) = \frac{\pi_x^2}{2m}e^{-\gamma t} + V(x,t)e^{\gamma t}. \tag{15}$$

For a system described by $y(t)$, on the other hand, the canonical momentum is equal to the kinetic momentum,

$$\pi_y(t) = \frac{\partial L_y}{\partial \dot{y}} = m\dot{y}(t), \tag{16}$$

and the Hamiltonian is given by

$$H_y(y,\pi_y,t) = \frac{\pi_y^2}{2m} + e^{\gamma t}V\left(ye^{-\gamma t/2},t\right) - \frac{m\gamma^2}{8}y^2. \tag{17}$$

We note that the essence of this mapping between the dissipative motion of $x(t)$ and the dissipationless motion of $y(t)$ is the scale transformation **Eq. 5**. The slowing-down effect of the damping γ is captured by the $e^{\frac{\gamma t}{2}}$ scale factor when relating the dissipative motion of $x(t)$ and dissipationless motion of $y(t)$ [17–19].

2.2 Mapping in Quantum Mechanics

Let us extend the mapping discussed in the previous subsection to quantum mechanics [17–19]. From the Hamiltonians **Eqs 15** and **17**, one can derive the corresponding Schrödinger equations. For the Caldirola-Kanai model, **Eq. 15**, the Schrödinger equation reads

$$i\hbar\frac{\partial}{\partial t}\phi(x,t) = \left[-\frac{\hbar^2}{2m}e^{-\gamma t}\frac{\partial^2}{\partial x^2} + e^{\gamma t}V(x,t)\right]\phi(x,t), \tag{18}$$

while for the other Hamiltonian without dissipation, one obtains

$$i\hbar\frac{\partial}{\partial t}\psi(x,t) = \left[-\frac{\hbar^2}{2m}\frac{\partial^2}{\partial x^2} + e^{\gamma t}V\left(xe^{-\gamma t/2},t\right) - \frac{m\gamma^2}{8}x^2\right]\psi(x,t). \tag{19}$$

The Schrödinger equation **Eq. 18** for $\phi(x, t)$ serves as a phenomenological modeling of quantum dissipative systems [12, 13]. Indeed, one can show that the Heisenberg equation of motion with **Eq. 18** has the same form as **Eq. 9**. The equivalence of **Eq. 18** and **Eq. 19** can be understood clearly by showing that the wavefunctions ϕ and ψ are related by a scale transformation as follows: we recall that the two models' solutions in the classical cases can be mapped to each other by the following transformation

$$x(t) = y(t)e^{-\gamma t/2}, \qquad \pi_x(t) = \left(\pi_y(t) - \frac{m\gamma}{2}y(t)\right)e^{\gamma t/2}. \tag{20}$$

In quantum mechanics, these relations should be satisfied as operators, not merely as expectation values. In other words, $\phi(x, t)$ and $\psi(x, t)$ should satisfy

$$\int_{-\infty}^{\infty} dz\,\phi^*(z,t)z^n\phi(z,t) = \int_{-\infty}^{\infty} dz\,\psi^*(z,t)\left(ze^{-\gamma t/2}\right)^n\psi(z,t), \tag{21}$$

and

$$\int_{-\infty}^{\infty} dz\,\phi^*(z,t)\left(\frac{\hbar}{i}\frac{\partial}{\partial z}\right)^n\phi(z,t) = \int_{-\infty}^{\infty} dz\,\psi^*(z,t)\left\{\left(\frac{\hbar}{i}\frac{\partial}{\partial z} - \frac{m\gamma}{2}z\right)e^{\gamma t/2}\right\}^n\psi(z,t), \tag{22}$$

for any natural number n. From these conditions, we can find a relation between $\phi(x, t)$ and $\psi(x, t)$ up to a time-dependent phase, which should be determined to be consistent with the Schrödinger equations **Eqs. 18**, **19**. This consideration leads to the following relation between $\phi(x, t)$ and $\psi(x, t)$,

$$\phi(x,t) = \exp\left(-i\frac{m\gamma}{4\hbar}e^{\gamma t}x^2 + \frac{\gamma t}{4}\right)\psi\left(xe^{\gamma t/2},t\right). \tag{23}$$

Indeed, one can directly show that $\phi(x, t)$ defined by **Eq. 23** satisfies the Schrödinger equation with the Caldirola-Kanai Hamiltonian **Eq. 18** if $\psi(x, t)$ is a solution of **Eq. 19**. Therefore, if the initial conditions are related by

$$\phi(x,0) = \exp\left(-i\frac{m\gamma}{4\hbar}x^2\right)\psi(x,0), \tag{24}$$

one can find $\phi(x, t)$ from $\psi(x, t)$ through the equivalence **Eq. 23**, and vice verse.

The mapping dictates that the dissipative and dissipationless models obey essentially the same quantum dynamics through **Eq. 23** and thus physically equivalent, as pointed out in the previous literature [19]. The effect of the dissipation in **Eq. 18** is represented as a scale transformation between $x(t)$ and $y(t)$, and as the inverted harmonic barrier $-m\gamma^2x^2/8$. In particular, the time-dependent scale transformation of the coordinate captures the slowing-down effect of the damping γ. This can be understood more directly by taking $V = 0$: the dissipative quantum motion in free space of **Eqs. 9** and **18** are equivalent to the dissipationless quantum motion under an inverted harmonic barrier $-m\gamma^2x^2/8$ in **Eqs. 10** and **19**. Another important example is the harmonic oscillator potential $V(x, t) = m\omega^2x^2/2$, which was discussed in the previous subsection. In this case, **Eq. 19** reads

$$i\hbar\frac{\partial}{\partial t}\psi(x,t) = \left[-\frac{\hbar^2}{2m}\frac{\partial^2}{\partial x^2} + \frac{m\Omega^2}{2}x^2\right]\psi(x,t). \tag{25}$$

On the other hand, the corresponding Caldirola-Kanai model describes a quantum damped harmonic oscillator. Therefore, one can map the quantum dynamics of a simple harmonic oscillator to that of a damped harmonic oscillator, as was found in Refs. [17–19].

2.3 Extension to Many-Particle Systems

Let us extend the results in the previous subsections and in Refs. [17–19] for a single particle to an N-particle system in d-spacial dimensions in the presence of inter-particle interactions. Our starting point is the dissipative equation of motion given by **Eq. 2**. Instead of **Eq. 5**, we now consider the transformation $\mathbf{x}_i(t) = e^{-\gamma t/2}\mathbf{y}_i(t)$ for $i = 1, \ldots, N$ (note that all particles feel the same damping force, see **Eq. 2**). As we derive **Eq. 13** in **Section 2.1**, the transformation leads to the Lagrangian given by **Eq. 1**. Therefore, the Schrödinger equation for the dissipative motion reads

$$i\hbar\frac{\partial}{\partial t}\phi(\mathbf{x}_1,\ldots,\mathbf{x}_N,t) = \left[-e^{-\gamma t}\sum_{i=1}^{N}\frac{\hbar^2\nabla_{\mathbf{x}_i}^2}{2m_i} + e^{\gamma t}U(\mathbf{x}_1,\ldots,\mathbf{x}_N)\right]\phi(\mathbf{x}_1,\ldots,\mathbf{x}_N,t). \tag{26}$$

On the other hand, the Schrödinger equation corresponding to **Eq. 19** reads

$$\begin{aligned} &i\hbar\frac{\partial}{\partial t}\psi(\mathbf{x}_1,\ldots,\mathbf{x}_N,t) \\ &= \left[-\sum_{i=1}^{N}\frac{\hbar^2\nabla_{\mathbf{x}_i}^2}{2m_i} + e^{\gamma t}U(\mathbf{x}_1e^{-\gamma t/2},\ldots,\mathbf{x}_Ne^{-\gamma t/2},t) - \sum_{i=1}^{N}\frac{m_i\gamma^2}{8}\mathbf{x}_i^2\right]\psi(\mathbf{x}_1,\ldots,\mathbf{x}_N,t). \end{aligned} \tag{27}$$

As in the derivation of **Eq. 23**, we can find the relation between ϕ and ψ,

$$\phi(\mathbf{x}_1,\ldots,\mathbf{x}_N,t) = \exp\left(-ie^{\gamma t}\sum_{i=1}^{N}\frac{m_i\gamma}{4\hbar}\mathbf{x}_i^2 + \frac{dN\gamma t}{4}\right)\psi(\mathbf{x}_1e^{\gamma t/2},\ldots,\mathbf{x}_Ne^{\gamma t/2},t). \tag{28}$$

This mapping for many-body quantum systems is a natural extension of what was studied for a single-particle motion in the previous literatures [17–19]. The single-particle case in one dimension in **Eq. 23** is indeed contained as $N = 1$, $d = 1$. When $U(\mathbf{x}_1,\ldots,\mathbf{x}_N,t) = \sum_{i=1}^{N}V(\mathbf{x}_i,t)$ and hence each particle moves independently, we can regard them as a collection of non-interacting particles, each obeying the Schrödinger equations **Eqs. 18**, **19**. When the potential U cannot be represented as such a sum of one-body potentials, on the other hand, **Eq. 26** describes interacting N quantum particles moving under the dissipation, while **Eq. 27** describes dissipationless motions of interacting quantum particles in the presence of the inverted harmonic barrier $-m\gamma^2x_i^2/8$.

3 APPLICATION TO STRONGLY INTERACTING QUANTUM SYSTEMS

We show in this section that the exact mapping formulated in the previous section can be utilized for a physical problem of a strongly interacting quantum system, namely the unitary Fermi gas [20–22, 27–33]. The unitary Fermi gas is a system of spin-1/2 fermions interacting with an infinitely large s-wave scattering length. It has been recently realized with ultracold atoms [27–32], and it has been extensively studied because it is important for understanding nuclear matters and neutron star physics [20–26]. The exact mapping between the dissipative and dissipationless motions should therefore be useful for understanding not only the dynamics of the unitary Fermi gas in ultracold atoms, but also for nuclear phenomena.

In **Section 3.1**, we explain the interaction between the particles to model the unitary two-body interaction. In **Section 3.2**, we show that the exact mapping holds for a quantum system with the unitary interaction. In **Section 3.3**, we discuss the effects of dimensions and statistics of the particles. We argue that our exact mapping is non-trivial and useful for a three-dimensional system of fermions, while it is either trivial or breaks down for low-dimensional systems and for bosonic systems.

3.1 Zero-Range Interaction

Solutions of interacting quantum systems in general sensitively depends on details of the interaction potentials. However, for low-energy quantum systems, details of the interaction become irrelevant, so that any Hamiltonian can be universally described by a so-called pseudo-potential. This universality originates from the fact that the scattering between the particles at low energy are dominated by the s-wave scattering, which is universally characterized solely by the s-wave scattering length a for non-relativistic low-energy quantum systems interacting via short-range interactions. As long as this condition holds, the interaction potential between the i-th and j-th particles V_{ij} can be legitimately replaced by the following pseudo potential introduced by Huang and Yang in three spacial dimension [34].

$$V_{ij}(\mathbf{r}_{ij}) = \frac{2\pi a_{ij}\hbar^2}{\mu_{ij}}\delta^{(3)}(\mathbf{r}_{ij})\frac{\partial}{\partial r_{ij}}r_{ij}, \tag{29}$$

where $r_{ij} = |\mathbf{r}_i - \mathbf{r}_j|$, and a_{ij} and $\mu_{ij} = m_im_j/(m_i + m_j)$ are the s-wave scattering length and the reduced mass of the i-th and j-th particles, respectively. The Hamiltonian can then be wrriten as the sum of the independent-particle Hamiltonian H_0 and the interaction term U, $H = H_0 + U$ with

$$U(\mathbf{x}_1,\ldots,\mathbf{x}_N,t) = \sum_{i<j}V_{ij}(\mathbf{r}_{ij}). \tag{30}$$

An alternative low-energy universal approach can be found by noting that the solution of the Huang and Yang pseudo-potential has the following asymptotic form when the particles get close together

$$\begin{aligned} &\lim_{r_{ij}\to 0}\Psi(\mathbf{r}_1,\mathbf{r}_2,\ldots,\mathbf{r}_N) \\ &= \left(\frac{1}{r_{ij}} - \frac{1}{a_{ij}}\right)A(\mathbf{R}_{ij},\mathbf{r}_1,\ldots,\mathbf{r}_{i-1},\mathbf{r}_{i+1}\ldots,\mathbf{r}_N), \end{aligned} \tag{31}$$

where $\mathbf{R}_{ij} = (m_i\mathbf{r}_i + m_j\mathbf{r}_j)/(m_i + m_j)$ is the center of mass between the i-th and j-th particles, and A is the regular part of the wavefunction Ψ when the limit $r_{ij} \to 0$ is taken. The singular

term $1/r_{ij} - 1/a_{ij}$ represents the universal *s*-wave scattering behavior of the two-body scattering. Therefore, we can simply replace the effect of the interaction term V_{ij} with this boundary condition: we solve the free particles' equation of motion of $H = H_0$ supplemented with the boundary condition **Eq. 31**

The above two approaches, the Huang-Yang pseudo-potential **Eq. 29** and the Bethe-Peierls boundary condition **Eq. 31**, are equivalent, and have both been widely used for low-energy dilute systems where *s*-wave interaction is predominantly large. In particular, they have been successfully used to study ultracold atoms close to the unitary limit $|a_{ij}| \to \infty$ [21, 22, 24, 25, 35, 36]. It has also been used in low-energy nuclear physics as the *s*-wave scattering length between the nucleons are very large [20, 23, 26]. We note however that **Eqs. 29** and **31** are only valid in three spacial dimension: they need to be modified in the other spacial dimension, as will be discussed in **Section 3.3**. We also note that it is required that three- and higher-body interactions are negligibly small to legitimately use the pseudo-potential and the boundary condition methods, as will also be discussed in more details in **Section 3.3**.

3.2 Exact Mapping for the Unitary Interacting System

Let us first consider *N*-particle system where the inter-particle interactions are modeled by the Bethe-Peierls boundary condition **Eq. 31**. As the boundary condition method deals with the non-interacting Hamiltonian $U = 0$, the Schrödinger equations for the Caldirola-Kanai model and the corresponding dissipationless model are the same as **Eqs. 26**, **27** with $U = 0$. Thus, we can naturally expect that the mapping **Eq. 28** should also relate these two problems. This turns out to be true if the *s*-wave scattering length of the two systems satisfy a certain relation (see **Eq. 34**).

To show this, let us consider the Bethe-Peierls boundary condition for the Caldirola-Kanai model under the unitary interaction

$$\phi(\mathbf{x}_1, \mathbf{x}_2, \ldots, \mathbf{x}_N, t) \propto \left(\frac{1}{x_{ij}} - \frac{1}{a_{ij}^{(\mathrm{CK})}(t)} \right). \tag{32}$$

Here $a_{ij}^{(\mathrm{CK})}(t)$ is the *s*-wave scattering length between the *ij* particles, which is now allowed to vary with time for later purposes. Note that the Caldirola-Kanai model with $U = 0$ describes the motion of non-interacting particles under the influence of a damping force (see **Eq. 2** with $U = 0$). With the boundary condition **Eq. 32**, those damped particles interact through the *s*-wave scattering length $a_{ij}^{(\mathrm{CK})}(t)$ once two particles come to the same position. Assuming that the mapping **Eq. 28** holds and noting that the exponential phase factor does not affect the singular short-distance behavior of the wavefunction, we obtain the following boundary condition of the corresponding dissipationless system

$$\psi(\mathbf{y}_1, \mathbf{y}_2, \ldots, \mathbf{y}_N, t) \propto \left(\frac{1}{y_{ij}} - \frac{1}{e^{\frac{\gamma t}{2}} a_{ij}^{(\mathrm{CK})}(t)} \right). \tag{33}$$

Therefore, we find that the *s*-wave scattering length of the ψ system, $a_{ij}^{(\mathrm{H})}(t)$, must be given by

$$a_{ij}^{(\mathrm{H})}(t) = e^{\frac{\gamma t}{2}} a_{ij}^{(\mathrm{CK})}(t). \tag{34}$$

While we have used above the Bethe-Peierls boundary condition to derive the condition **Eq. 34** for the equivalence of the two systems, we can alternatively derive it with the Huang-Yang pseudo-potential **Eq. 29**. Indeed, **Eqs. 26**, **27** with the Huang-Yang interaction read

$$\begin{aligned} &i\hbar \frac{\partial}{\partial t} \phi(\mathbf{x}_1, \ldots, \mathbf{x}_N, t) \\ &= \left[-e^{-\gamma t} \sum_{i=1}^{N} \frac{\hbar^2 \nabla_{\mathbf{x}_i}^2}{2m_i} + e^{\gamma t} \sum_{i<j} \frac{2\pi a_{ij}(t) \hbar^2}{\mu_{ij}} \delta^{(3)}(\mathbf{x}_{ij}) \frac{\partial}{\partial x_{ij}} x_{ij} \right] \phi(\mathbf{x}_1, \ldots, \mathbf{x}_N, t). \end{aligned} \tag{35}$$

$$\begin{aligned} &i\hbar \frac{\partial}{\partial t} \psi(\mathbf{x}_1, \ldots, \mathbf{x}_N, t) \\ &= \left[-\sum_{i=1}^{N} \frac{\hbar^2 \nabla_{\mathbf{x}_i}^2}{2m_i} + e^{\frac{5\gamma}{2} t} \sum_{i<j} \frac{2\pi a_{ij}(t) \hbar^2}{\mu_{ij}} \delta^{(3)}(\mathbf{x}_{ij}) \frac{\partial}{\partial x_{ij}} x_{ij} - \sum_{i=1}^{N} \frac{m_i \gamma^2 x_i^2}{8} \right] \\ &\psi(\mathbf{x}_1, \ldots, \mathbf{x}_N, t). \end{aligned} \tag{36}$$

We then need to relate $a_{ij}(t)$ with the *s*-wave scattering lengths of the two systems $a_{ij}^{(\mathrm{CK})}(t)$, $a_{ij}^{(\mathrm{H})}(t)$. This can be done by substituting the **Eqs. 32**, **33** to the right-hand sides of **Eq. 35** and **Eq. 36**, respectively. We then find

$$a_{ij}^{(\mathrm{CK})}(t) = e^{2\gamma t} a_{ij}(t), \qquad a_{ij}^{(\mathrm{H})}(t) = e^{\frac{5}{2}\gamma t} a_{ij}(t), \tag{37}$$

from which we arrive at **Eq. 34**.

As the condition **Eq. 34** must be satisfied for all pairs of particles *ij* at any time, our exact mapping is difficult to hold true in general. However, there are two special cases where **Eq. 34** is easily satisfied. The first case is the non-interacting system $a_{ij}^{(\mathrm{H})} = a_{ij}^{(\mathrm{CK})} = 0$. This corresponds to the system considered in the previous section and in Refs. [17–19]. The other more interesting case is the unitary gas $a_{ij}^{(\mathrm{H})} = a_{ij}^{(\mathrm{CK})} = \pm\infty$. We thus arrive at the following non-trivial conclusion for the two strongly interacting quantum dynamics: a dissipative quantum motion of the unitary gas described by **Eq. 35** is equivalent to the dissipationless quantum dynamics of the unitary gas under an inverted harmonic potential in **Eq. 36** *via* the mapping **Eq. 28**.

The physical reason for the two seemingly opposite conditions, the non-interacting system and the unitary system, can be ascribed to the scale invariance. The mapping between the Caldirola-Kanai system and the dissipationless inverted harmonic system can be regarded as a sort of scale transformation in **Eq. 5**. With this transformation, the interaction term is transformed as (see **Eqs. 26**, **27**)

$$U(\mathbf{x}_1, \ldots, \mathbf{x}_N) \to e^{\gamma t} U(\mathbf{x}_1 e^{-\gamma t/2}, \ldots, \mathbf{x}_N e^{-\gamma t/2}, t). \tag{38}$$

In general, they show rather different Hamiltonian dynamics. However, if the interaction term satisfies the scale invariance

$$e^{\gamma t} U(\mathbf{x}_1 e^{-\gamma t/2}, \ldots, \mathbf{x}_N e^{-\gamma t/2}, t) = f(t) U(\mathbf{x}_1, \ldots, \mathbf{x}_N, t) \tag{39}$$

with $f(t)$ an arbitrary time-dependent function, the Hamiltonian keeps its form with this scale transformation, showing essentially

the same dynamics. Indeed, the non-interacting system and the unitary system are known to be scale invariant because the length scale characterizing the interaction, the *s*-wave scattering length, disappears. In addition to the zero-range type interaction, we can also consider more general classes of scale-invariant interactions as will be discussed in the **Supplementary Appendix A**. We can indeed show that the exact mapping holds true for various classes of scale-invariant interactions as long as the interaction strength satisfies a similar relation as **Eq. 34** (see **Supplementary Appendix A**). We also note that our mapping for the unitary system can be alternatively proved using the scaling solution of the unitary Fermi gas in the time-dependent harmonic trap [37, 38] (see **Supplementary Appendix B**).

3.3 Effects of Dimensions, Quantum Statistics of the Particles, and Higher-Body Interactions

We note that the Huang and Yang pseudo-potential **Eq. 29** and the Bethe-Peierls boundary condition **Eq. 31** are only valid in three spacial dimensions. For low-dimensional systems, the Bethe-Peierls boundary condition should be modified as [22, 36, 37, 39].

$$\lim_{r_{ij}\to 0}\Psi(\mathbf{r}_1,\mathbf{r}_2,\ldots,\mathbf{r}_N) = \ln\left(\frac{r_{ij}}{a_{ij}^{(2D)}}\right)A(\mathbf{R}_{ij},\mathbf{r}_1,\ldots,\mathbf{r}_{i-1},\mathbf{r}_{i+1}\ldots,\mathbf{r}_N) \tag{40}$$

for a two-dimensional system, and

$$\lim_{r_{ij}\to 0}\Psi(\mathbf{r}_1,\mathbf{r}_2,\ldots,\mathbf{r}_N) = \left(|x_{ij}| - a_{ij}^{(1D)}\right)A(\mathbf{R}_{ij},\mathbf{r}_1,\ldots,\mathbf{r}_{i-1},\mathbf{r}_{i+1}\ldots,\mathbf{r}_N) \tag{41}$$

for a one-dimensional system, respectively. Here, $a_{ij}^{(2D)}$ and $a_{ij}^{(1D)}$ are two-dimensional and one-dimensional scattering lengths, respectively. By using these boundary conditions, we can follow almost the same argument as in **Section 3.2**. We then arrive at the same conclusion: the two-dimensional and one-dimensional systems of the Caldirola-Kanai model **Eq. 26** and the corresponding inverted harmonic model **Eq. 27** are equivalent via the mapping **Eq. 28** if and only if the *s*-wave scattering lengths of the two systems satisfy **Eq. 34** for any *ij* particles at any time. This can be also shown by using the Huang-Yang pseudo potential in two and one dimension [40, 41].

$$V_{ij}(\mathbf{r}_{ij}) = -\frac{\pi\hbar^2\delta^{(2)}(\mathbf{r}_{ij})}{\mu_{ij}\ln(q\Lambda a_{ij}^{(2D)})}\times\left[1-\ln(q\Lambda r_{ij})r_{ij}\frac{\partial}{\partial r_{ij}}\right]\ \text{(2D)}, \tag{42}$$

$$V_{ij}(x_{ij}) = -\frac{\hbar^2}{\mu_{ij}a_{ij}^{(1D)}}\delta(x_{ij})\quad\text{(1D)}, \tag{43}$$

where $q=\frac{1}{2}e^C$ with $C=0.577\ldots$ is the Euler gamma, and Λ is an arbitrary momentum scale.

It is then tempting to conclude that our exact mapping is also valid for the strongly interacting two-dimensional and one-dimensional systems. However, this is not the case: our mapping for the unitary interacting system should be non-trivial only for three-dimensional system. Indeed, the unitary system $a=\pm\infty$ is known to be non-interacting and thus trivial in two and one dimensions, which is in stark contrast to the three dimensional system where it is genuine strongly interacting system [21, 22, 37, 42]. This well-known fact can be easily understood from **Eqs. 42** and **43**, where the interaction becomes non-interacting $V_{ij}=0$ when $a=\pm\infty$. This is in contrast to **Eq. 29** in three dimension where $V_{ij}\neq 0$ when $a=\pm\infty$. Therefore, our mapping for low dimensional quantum systems is trivial and has limited range of applications.

We note that we have solely considered two-body interaction, neglecting three- and higher-body interactions. In most interacting quantum systems, the two-body interaction is much more relevant than the three- and higher-body interactions, even when it is present. Thus, our assumption seems plausible. We should remark however that the unitary interacting system may essentially require the three- and higher-body interactions. A prime example is a system of identical bosons interacting via the unitary interaction $a=\pm\infty$, where the Efimov effect occurs [35, 36, 43, 44]. When the Efimov effect occurs, the Hamiltonian with only the unitary two-body interaction in **Eq. 29** becomes singular, and one needs to introduce the three-body boundary condition to make the Hamiltonian well-defined [35, 36, 45, 46]. As this three-body boundary condition is generally not scale invariant, our exact mapping breaks down. The Efimov effect generally occurs for three-dimensional unitary interacting bosonic systems, and thus our result is not applicable. On the other hand, the Efimov effect does not tend to occur for fermionic system due to the Pauli exclusion principle. In particular, it is shown that the spin-1/2 identical fermions with the unitary interaction **Eq. 29**, i.e., the unitary Fermi gas, is well-defined as there is no three-body nor higher-body Efimov effect [36, 47–52]. Our result should therefore be useful for the unitary Fermi gas. Furthermore, as the mass-imbalanced Fermi system does not show the Efimov effect either when the mass imbalance is $M/m\lesssim 13$ [36, 47, 48, 52, 53], we can state that we can readily apply our exact mapping to such mass-imbalanced two-component unitary Fermi gas systems [54, 55].

We also note that the Efimov effect does not occur for two-dimensional and one-dimensional systems [35–37, 42, 56]. The Hamiltonian with the two-body interaction **Eqs. 42**, **43** are thus well-defined even without the higher-body interaction, and our argument on the two- and one-dimensional systems above are valid regardless of the quantum statistics of the particles. We repeat however that the two-dimensional and one-dimensional unitary systems correspond to non-interacting systems, so that the mapping would not be so useful.

4 CONCLUSION AND DISCUSSIONS

We have studied a quantum dissipative dynamics of the Caldirola-Kanai model (see **Eqs. 2** and **26**), and shown that it can be rigorously mapped to a dissipationless quantum dynamics under an inverted-harmonic potential (see **Eq. 27**). While this mapping has been known for a single-particle and non-interacting systems [17–19], we have shown that it also holds true for strongly interacting systems. In particular, we have found that the dissipative dynamics of the unitary Fermi gas can be

exactly mapped to a dissipationless dynamics of the unitary Fermi gas under an inverted harmonic potential.

The unitary Fermi gas has been recently realized in cold atom experiments [6, 7, 27–32]. It has attracted a lot of research interests, because unveiling the properties of the unitary Fermi gas is important for understanding nuclear matters and neutron star physics [20–26]. Our work therefore should be particularly useful for cold atoms and nuclear systems. The external potential can be well-controlled in cold atom experiments with laser and magnetic field, and it is possible to engineer the harmonic or inverted-harmonic potential [21, 22] and observe its quantum dynamics. It is thus a promising system where our mapping would be useful. We also note that we can control the *s*-wave scattering length in a time-dependent manner in cold atoms [57]. It is thus possible to realize a situation where our condition in **Eq. 34** holds, so that our exact mapping is valid for systems with finite scattering length or low-dimensional systems.

A more challenging but interesting system to apply our result is nuclear physics. Nuclear systems composed of protons and neutrons can be approximately regarded as the unitary Fermi system as the *s*-wave scattering lengths between the nucleons are large. With recent studies on nuclear reactions, it has been pointed out that the dissipative quantum tunneling may play an important role in low-energy fusion reactions [58–60]. It is also suggested that quantum dissipations of the nuclear matters are indispensable for understanding the dynamics of the neutron stars [61, 62]. Although we should remark that the Caldirola-Kanai model is a rather simple toy model and that the range corrections and three-body interaction neglected in our study often turns out to be relevant in the nuclear systems [46, 63, 64], our analytical mapping between the dissipative and dissipationless systems can provide us with novel qualitative perspective to understand those nuclear phenomena.

DATA AVAILABILITY STATEMENT

The original contributions presented in the study are included in the article/**Supplementary Material**, further inquiries can be directed to the corresponding authors.

AUTHOR CONTRIBUTIONS

The contribution of each of the authors has been significant and the manuscript is the result of an even effort of both the authors. They share the first authorship.

FUNDING

This work was supported by Tohoku University Graduate Program on Physics for the Universe (GP-PU), and JSPS KAKENHI Grant Numbers JP18J20565 and 21H00116.

ACKNOWLEDGMENTS

We thank Kouchi Hagino, Yvan Castin, Hajime Togashi, and Yusuke Tanimura for fruitful discussions. In particular, some discussions in the **Supplementary Appendix B** are inspired by private communication with Yvan Castin.

SUPPLEMENTARY MATERIAL

The Supplementary Material for this article can be found online at: https://www.frontiersin.org/articles/10.3389/fphy.2021.730761/full#supplementary-material

REFERENCES

1. Caldeira AO, and Leggett AJ. Influence of Dissipation on Quantum Tunneling in Macroscopic Systems. *Phys Rev Lett* (1981) 46:211–4. doi:10.1103/PhysRevLett.46.211
2. Diaz-Torres A, Hinde DJ, Dasgupta M, Milburn GJ, and Tostevin JA. Dissipative Quantum Dynamics in Low-Energy Collisions of Complex Nuclei. *Phys Rev C* (2008) 78:064604. doi:10.1103/PhysRevC.78.064604
3. Tokieda M, and Hagino K. Time-dependent Approaches to Open Quantum Systems. *Front Phys* (2020) 8:8. doi:10.3389/fphy.2020.00008
4. Jeung DY, Hinde DJ, Williams E, Dasgupta M, Simpson EC, du Rietz R, et al. Energy Dissipation and Suppression of Capture Cross Sections in Heavy Ion Reactions. *Phys Rev C* (2021) 103:034603. doi:10.1103/PhysRevC.103.034603
5. Diehl S, Micheli A, Kantian A, Kraus B, Büchler HP, and Zoller P. Quantum States and Phases in Driven Open Quantum Systems with Cold Atoms. *Nat Phys* (2008) 4:878–83. doi:10.1038/nphys1073
6. Bardon AB, Beattie S, Luciuk C, Cairncross W, Fine D, Cheng NS, et al. Transverse Demagnetization Dynamics of a Unitary Fermi Gas. *Science* (2014) 344:722–4. doi:10.1126/science.1247425
7. Cao C, Elliott E, Joseph J, Wu H, Petricka J, Schäfer T, et al. Universal Quantum Viscosity in a Unitary Fermi Gas. *Science* (2011) 331:58–61. doi:10.1126/science.1195219
8. Azouit R, Chittaro F, Sarlette A, and Rouchon P. Towards Generic Adiabatic Elimination for Bipartite Open Quantum Systems. *Quan Sci Technol* (2017) 2:044011. doi:10.1088/2058-9565/aa7f3f
9. Blais A, Grimsmo AL, Girvin SM, and Wallraff A. Circuit Quantum Electrodynamics. *Rev Mod Phys* (2021) 93:025005. doi:10.1103/RevModPhys.93.025005
10. Gorini V, Kossakowski A, and Sudarshan ECG. Completely Positive Dynamical Semigroups of N-Level Systems. *J Math Phys* (1976) 17:821. doi:10.1063/1.522979
11. Lindblad G. On the Generators of Quantum Dynamical Semigroups. *Commun Math Phys* (1976) 48:119–30. doi:10.1007/bf01608499
12. Caldirola P. Forze Non Conservative Nella Meccanica Quantistica. *Nuovo Cim* (1941) 18:393–400. doi:10.1007/BF02960144
13. Kanai E. On the Quantization of the Dissipative Systems. *Prog Theor Phys* (1948) 3:440–2. doi:10.1143/ptp/3.4.440
14. Choi JR, Lakehal S, Maamache M, and Menouar S. Quantum Analysis of a Modified Caldirola-Kanai Oscillator Model for Electromagnetic Fields in Time-Varying Plasma. *PIER Lett* (2014) 44:71–9. doi:10.2528/PIERL13061601
15. Tokieda M, and Hagino K. Quantum Tunneling with Friction. *Phys Rev C* (2017) 95:054604. doi:10.1103/PhysRevC.95.054604
16. Nascimento JPG, Aguiar V, Cortez DS, and Guedes I. Dissipative Dynamics and Uncertainty Measures of a Charged Oscillator in the Presence of the Aharonov-Bohm Effect. *Revista Brasileira de Ensino de Fisica* (2021) 43: e20200464. doi:10.1590/1806-9126-rbef-2020-0464

17. Kerner EH. Note on the Forced and Damped Oscillator in Quantum Mechanics. *Can J Phys* (1958) 36:371–7. doi:10.1139/p58-038
18. Baskoutas S, Jannussis A, and Mignani R. Dissipative Tunnelling of the Inverted Caldirola-Kanai Oscillator. *J Phys A Math Gen* (1994) 27:2189–96. doi:10.1088/0305-4470/27/6/039
19. Huang MC, and Wu MC. The Caldirola-Kanai Model and its Equivalent Theories for a Damped Oscillator. *Chin J Phys* (1998) 36:566–87.
20. George A, and Baker jr. Neutron Matter Model. *Phys Rev C* (1999) 60:054311. doi:10.1103/PhysRevC.60.054311
21. Zwerger W. *The BCS-BEC Crossover and the Unitary Fermi Gas*, Vol. 836. Springer Science & Business Media (2011).
22. Giorgini S, Pitaevskii LP, and Stringari S. Theory of Ultracold Atomic Fermi Gases. *Rev Mod Phys* (2008) 80:1215–74. doi:10.1103/RevModPhys.80.1215
23. Horikoshi M, and Kuwata-Gonokami M. Cold Atom Quantum Simulator for Dilute Neutron Matter. *Int J Mod Phys E* (2019) 28:1930001. doi:10.1142/s0218301319300017
24. van Wyk P, Tajima H, Inotani D, Ohnishi A, and Ohashi Y. Superfluid Fermi Atomic Gas as a Quantum Simulator for the Study of the Neutron-star Equation of State in the Low-Density Region. *Phys Rev A* (2018) 97: 013601. doi:10.1103/PhysRevA.97.013601
25. Endo S. Virial Expansion Coefficients in the Unitary Fermi Gas. *Scipost Phys Proc* (2020) 3:049. doi:10.21468/SciPostPhysProc.3.049
26. Shen G, Horowitz CJ, and Teige S. Equation of State of Nuclear Matter in a Virial Expansion of Nucleons and Nuclei. *Phys Rev C* (2010) 82:045802. doi:10.1103/PhysRevC.82.045802
27. Bourdel T, Khaykovich L, Cubizolles J, Zhang J, Chevy F, Teichmann M, et al. Experimental Study of the Bec-Bcs Crossover Region in Lithium 6. *Phys Rev Lett* (2004) 93:050401. doi:10.1103/PhysRevLett.93.050401
28. Nascimbène S, Navon N, Jiang KJ, Chevy F, and Salomon C. Exploring the Thermodynamics of a Universal Fermi Gas. *Nature* (2010) 463:1057–60. doi:10.1038/nature08814
29. Horikoshi M, Nakajima S, Ueda M, and Mukaiyama T. Measurement of Universal Thermodynamic Functions for a Unitary Fermi Gas. *Science* (2010) 327:442–5. doi:10.1126/science.1183012
30. Ku MJH, Sommer AT, Cheuk LW, and Zwierlein MW. Revealing the Superfluid Lambda Transition in the Universal Thermodynamics of a Unitary Fermi Gas. *Science* (2012) 335:563–7. doi:10.1126/science.1214987
31. Gaebler JP, Stewart JT, Drake TE, Jin DS, Perali A, Pieri P, et al. Observation of Pseudogap Behaviour in a Strongly Interacting Fermi Gas. *Nat Phys* (2010) 6: 569–73. doi:10.1038/nphys1709
32. Carcy C, Hoinka S, Lingham MG, Dyke P, Kuhn CCN, Hu H, et al. Contact and Sum Rules in a Near-Uniform Fermi Gas at Unitarity. *Phys Rev Lett* (2019) 122:203401. doi:10.1103/PhysRevLett.122.203401
33. Levinsen J, Massignan P, Endo S, and Parish MM. Universality of the Unitary Fermi Gas: a Few-Body Perspective. *J Phys B: Mol Opt Phys* (2017) 50:072001. doi:10.1088/1361-6455/aa5a1e
34. Huang K, and Yang CN. Quantum-mechanical many-body Problem with Hard-Sphere Interaction. *Phys Rev* (1957) 105:767–75. doi:10.1103/physrev.105.767
35. Nielsen E, Fedorov DV, Jensen AS, and Garrido E. The Three-Body Problem with Short-Range Interactions. *Phys Rep* (2001) 347:373–459. doi:10.1016/s0370-1573(00)00107-1
36. Naidon P, and Endo S. Efimov Physics: a Review. *Rep Prog Phys* (2017) 80: 056001. doi:10.1088/1361-6633/aa50e8
37. Werner F, and Castin Y. General Relations for Quantum Gases in Two and Three Dimensions: Two-Component Fermions. *Phys Rev A* (2012) 86:013626. doi:10.1103/PhysRevA.86.013626
38. Werner F, and Castin Y. Unitary Gas in an Isotropic Harmonic Trap: Symmetry Properties and Applications. *Phys Rev A* (2006) 74:053604. doi:10.1103/PhysRevA.74.053604
39. Olshanii M. Atomic Scattering in the Presence of an External Confinement and a Gas of Impenetrable Bosons. *Phys Rev Lett* (1998) 81:938–41. doi:10.1103/PhysRevLett.81.938
40. Olshanii M, and Pricoupenko L. Rigorous Approach to the Problem of Ultraviolet Divergencies in Dilute Bose Gases. *Phys Rev Lett* (2001) 88: 010402. doi:10.1103/PhysRevLett.88.010402
41. Rontani M, Eriksson G, Åberg S, and Reimann SM. On the Renormalization of Contact Interactions for the Configuration-Interaction Method in Two-Dimensions. *J Phys B Mol Opt Phys* (2017) 50:065301. doi:10.1088/1361-6455/aa606a
42. Werner F, and Castin Y. General Relations for Quantum Gases in Two and Three Dimensions. Ii. Bosons and Mixtures. *Phys Rev A* (2012) 86:053633. doi:10.1103/PhysRevA.86.053633
43. Efimov V. Energy Levels Arising from Resonant Two-Body Forces in a Three-Body System. *Phys Lett B* (1970) 33:563–4. doi:10.1016/0370-2693(70)90349-7
44. Kraemer T, Mark M, Waldburger P, Danzl JG, Chin C, Engeser B, et al. Evidence for Efimov Quantum States in an Ultracold Gas of Caesium Atoms. *Nature* (2006) 440:315–8. doi:10.1038/nature04626
45. Thomas LH. The Interaction between a Neutron and a Proton and the Structure ofH3. *Phys Rev* (1935) 47:903–9. doi:10.1103/PhysRev.47.903
46. Naidon P, Endo S, and Ueda M. Microscopic Origin and Universality Classes of the Efimov Three-Body Parameter. *Phys Rev Lett* (2014) 112:105301. doi:10.1103/PhysRevLett.112.105301
47. Efimov V. Energy Levels of Three Resonantly Interacting Particles. *Nucl Phys A* (1973) 210:157–88. doi:10.1016/0375-9474(73)90510-1
48. Petrov DS. Three-body Problem in Fermi Gases with Short-Range Interparticle Interaction. *Phys Rev A* (2003) 67:010703. doi:10.1103/PhysRevA.67.010703
49. Endo S, Naidon P, and Ueda M. Universal Physics of 2+1 Particles with Non-zero Angular Momentum. *Few-body Syst* (2011) 51:207–17. doi:10.1007/s00601-011-0229-6
50. Endo S, Naidon P, and Ueda M. Crossover Trimers Connecting Continuous and Discrete Scaling Regimes. *Phys Rev A* (2012) 86:062703. doi:10.1103/physreva.86.062703
51. Endo S, and Castin Y. Absence of a Four-Body Efimov Effect in The2+2fermionic Problem. *Phys Rev A* (2015) 92:053624. doi:10.1103/PhysRevA.92.053624
52. Bazak B, and Petrov DS. Five-body Efimov Effect and Universal Pentamer in Fermionic Mixtures. *Phys Rev Lett* (2017) 118:083002. doi:10.1103/PhysRevLett.118.083002
53. Castin Y, Mora C, and Pricoupenko L. Four-body Efimov Effect for Three Fermions and a Lighter Particle. *Phys Rev Lett* (2010) 105:223201. doi:10.1103/PhysRevLett.105.223201
54. Jag M, Zaccanti M, Cetina M, Lous RS, Schreck F, Grimm R, et al. Observation of a strong Atom-Dimer Attraction in a Mass-Imbalanced Fermi-Fermi Mixture. *Phys Rev Lett* (2014) 112:075302. doi:10.1103/PhysRevLett.112.075302
55. Endo S, García-García AM, and Naidon P. Universal Clusters as Building Blocks of Stable Quantum Matter. *Phys Rev A* (2016) 93:053611. doi:10.1103/PhysRevA.93.053611
56. Bruch LW, and Tjon JA. Binding of Three Identical Bosons in Two Dimensions. *Phys Rev A* (1979) 19:425–32. doi:10.1103/PhysRevA.19.425
57. Clark LW, Gaj A, Feng L, and Chin C. Collective Emission of Matter-Wave Jets from Driven Bose-Einstein Condensates. *Nature* (2017) 551:356–9. doi:10.1038/nature24272
58. Dasgupta M, Hinde DJ, Diaz-Torres A, Bouriquet B, Low CI, Milburn GJ, et al. Beyond the Coherent Coupled Channels Description of Nuclear Fusion. *Phys Rev Lett* (2007) 99:192701. doi:10.1103/PhysRevLett.99.192701
59. Hagino K, and Takigawa N. Subbarrier Fusion Reactions and many-particle Quantum Tunneling. *Prog Theor Phys* (2012) 128:1061–106. doi:10.1143/ptp.128.1061
60. Rafferty DC, Dasgupta M, Hinde DJ, Simenel C, Simpson EC, Williams E, et al. Multinucleon Transfer inO16,18,F19+Pb208reactions at Energies Near the Fusion Barrier. *Phys Rev C* (2016) 94:024607. doi:10.1103/PhysRevC.94.024607
61. Cutler C, and Lindblom L. The Effect of Viscosity on Neutron star Oscillations. *ApJ* (1987) 314:234–41. doi:10.1086/165052
62. Alford MG, Bovard L, Hanauske M, Rezzolla L, and Schwenzer K. Viscous Dissipation and Heat Conduction in Binary Neutron-star Mergers. *Phys Rev Lett* (2018) 120:041101. doi:10.1103/PhysRevLett.120.041101
63. Epelbaum E, Nogga A, Glöckle W, Kamada H, Meißner U-G, and Witała H. Three-nucleon Forces from Chiral Effective Field Theory. *Phys Rev C* (2002) 66:064001. doi:10.1103/PhysRevC.66.064001

64. Hammer H-W, Nogga A, and Schwenk A. Colloquium: Three-Body Forces: From Cold Atoms to Nuclei. *Rev Mod Phys* (2013) 85:197–217. doi:10.1103/RevModPhys.85.197

Conflict of Interest: The authors declare that the research was conducted in the absence of any commercial or financial relationships that could be construed as a potential conflict of interest.

Publisher's Note: All claims expressed in this article are solely those of the authors and do not necessarily represent those of their affiliated organizations, or those of the publisher, the editors and the reviewers. Any product that may be evaluated in this article, or claim that may be made by its manufacturer, is not guaranteed or endorsed by the publisher.

frontiers in Physics

ORIGINAL RESEARCH
published: 30 September 2021
doi: 10.3389/fphy.2021.755253

Rational Design of Pepsin for Enhanced Thermostability via Exploiting the Guide of Structural Weakness on Stability

Yue Zhao[1], Yulu Miao[1], Fengdong Zhi[1], Yue Pan[1], Jianguo Zhang[2], Xuepeng Yang[3], John Z. H. Zhang[1,4,5] and Lujia Zhang[1,4]**

[1]Shanghai Engineering Research Center of Molecular Therapeutics & New Drug Development, School of Chemistry and Molecular Engineering, East China Normal University, Shanghai, China, [2]Institute of Food Science and Engineering, School of Medical Instrument and Food Engineering, University of Shanghai for Science and Technology, Shanghai, China, [3]School of Food and Biological Engineering, Zhengzhou University of Light Industry, Zhengzhou, China, [4]NYU-ECNU Center for Computational Chemistry at NYU Shanghai, Shanghai, China, [5]Department of Chemistry, New York University, New York, NY, United States

OPEN ACCESS

Edited by:
Jinjin Li,
Shanghai Jiao Tong University, China

Reviewed by:
Zhi Yang,
California Institute of Technology, United States
Xinqing Zhao,
Shanghai Jiao Tong University, China

***Correspondence:**
John Z. H. Zhang
John.zhang@nyu.edu
Lujia Zhang
ljzhang@chem.ecnu.edu.cn

Specialty section:
This article was submitted to Physical Chemistry and Chemical Physics, a section of the journal Frontiers in Physics

Received: *08 August 2021*
Accepted: *20 September 2021*
Published: *30 September 2021*

Citation:
Zhao Y, Miao Y, Zhi F, Pan Y, Zhang J, Yang X, Zhang JZH and Zhang L (2021) Rational Design of Pepsin for Enhanced Thermostability via Exploiting the Guide of Structural Weakness on Stability. Front. Phys. 9:755253. doi: 10.3389/fphy.2021.755253

Enzyme thermostability is an important parameter for estimating its industrial value. However, most naturally produced enzymes are incapable of meeting the industrial thermostability requirements. Software programs can be utilized to predict protein thermostability. Despite the fast-growing number of programs designed for this purpose; few provide reliable applicability because they do not account for thermodynamic weaknesses. Aspartic proteases are widely used in industrial processing; however, their thermostability is not able to meet the large-scale production requirements. In this study, through analyzing structural characteristics and modifying thermostability using prediction software programs, we improved the thermostability of pepsin, a representative aspartic protease. Based on the structural characteristics of pepsin and the experimental results of mutations predicted by several energy-based prediction software programs, it was found that the majority of pepsin's thermodynamic weaknesses lie on its flexible regions on the surface. Using computational design, mutations were made based on the predicted sites of thermodynamic weakness. As a result, the half-lives of mutants D52N and S129A at 70°C were increased by 200.0 and 66.3%, respectively. Our work demonstrated that in the effort of improving protein thermostability, identification of structural weaknesses with the help of computational design, could efficiently improve the accuracy of protein rational design.

Keywords: thermostability, aspartic protease, prediction software programs, structural weakness, site-specific mutagenesis

INTRODUCTION

Enzymes, as catalytic biological macromolecules, have the advantages of high efficiency and low pollution. They are competitive alternatives to chemical catalysts and are widely used in food, medicine, biofuel, and other industries [1–3]. Industrial processes usually need to be performed in extreme environments. For example, processing at high temperatures accelerates reactions, increases substrate utilization, and reduces the risk of microbial contamination [4]. However, high temperatures can easily destroy the enzyme structure, resulting in a loss of its catalytic activity.

Therefore, thermostability is an important parameter for measuring the industrial value of enzymes. Traditional methods for enzyme thermostability modification include directed evolution, ancestral stabilization, and site-directed mutagenesis based on structure prediction. However, owing to their unpredictability and long-range effects, mutants with improved thermostability are not readily obtained [5, 6]. With the development of structural and computational biology, protein structures can be obtained efficiently through experimental determination and computational prediction [7–10]. In recent years, based on protein structure and energy function, the prediction of mutations stabilizing the folded protein structure has improved considerably. Several methods based on structures, sequences, and other characteristics have been developed to predict protein stability, including machine learning, and physical, statistical, and empirical potentials [11–16]. These methods provide a clear ranking of mutations, but are not widely used in the design of enzymes for enhanced thermostability. This is primarily due to the optimization of prediction software programs based on a specific potential or structural feature, i.e., if these characteristics are not the weakest points responsible for poor stability, thermostability improvement due to mutagenesis may not be significant, and may result in the destruction of protein structure and lead to contradictory results. Therefore, it is necessary to analyze the structural characteristics of enzymes and consider thermodynamic structural weaknesses as a guide for rapid screening. Here, we selected an important enzyme, pepsin, to conduct a systematic test of conventional stability prediction software programs.

Aspartic proteases are a large class of proteases widely used in food, fermentation, pharmaceutical, and other industries [17, 18]. However, the poor thermostability of most natural aspartic proteases hinders their large-scale industrial applications, making the improvement of their thermostability crucial. Traditional methods, such as site-directed mutagenesis based on comparison of the amino acid sequence with a more thermostable, homologous counterpart, have achieved good results in the modification of other proteases [19–21]. However, these methods are not suitable for aspartic proteases due to their low sequence identity across different species [22]. Improving thermostability by enhancing resistance to autocatalysis was successful in aspartic protease, but the result of single point mutation increased by only 53.0% [23]. Therefore, the feasibility of improving the thermostability of aspartic proteases using traditional methods is fairly low. Aspartic proteases have the advantages of having a clear structure and catalytic mechanism, making it more suitable to adopt a computational design strategy. However, few studies have been conducted on improving the thermostability of aspartic proteases using prediction software programs. This is primarily owing to a lack of a thermodynamic structural weakness guide, as it is difficult to predict mutations with improved thermostability quickly and accurately by relying solely on the energy function.

In this study, we first performed an in-depth analysis of the structural characteristics of pepsin, a typical aspartic protease, and predicted possible thermodynamic weaknesses. By systematically testing a variety of software programs, we found that mutations with good prediction scores were not associated with thermodynamic weakness and performed poorly during experimental verification. The major structural area of weakness in pepsin was determined to be the flexible regions on its surface. Several mutations were identified based on this structural weakness. Among them, two excellent mutants, D52N and S129A, were obtained, and their half-lives at 70°C were found to increase by 200.0 and 66.3%, respectively. Our analysis showed that the guide of thermodynamic structural weakness promotes fast and accurate thermostability design using prediction software programs.

MATERIALS AND METHODS

Strains, Reagents, and Chemicals

The pPIC9K plasmid and *Pichia pastoris* GS115 (Invitrogen, Carlsbad, CA, United States) were used for subcloning and overexpression. *Escherichia coli* DH5α (Weidi Biotechnology Co., Ltd., Shanghai, China) was used for gene cloning and DNA sequencing. Plasmid pPIC9K-pepsinogen was previously constructed and stored in our laboratory. Primers for mutation construction were synthesized by Ruimian Biotech Co., Ltd. (Shanghai, China). Plasmid Extraction and Gel/PCR Purification Kits were purchased from TOROIVD (BVI, United Kingdom). The Seamless Cloning Kit was purchased from Beyotime Biotechnology (Shanghai, China). All enzymes used in the experiments were supplied by Thermo Scientific (Waltham, MA, United States). The bovine hemoglobin substrate was purchased from Maokang Biotech Co., Ltd. (Shanghai, China). All other chemicals were of analytical grade and are commercially available.

Site-Directed Mutagenesis

Site-directed mutagenesis was performed using the Seamless Cloning Kit according to the manufacturer's instructions, with the plasmid pPIC9K-pepsinogen (with a C-terminal His-tag) as the template. The primers used for mutagenesis are listed in **Supplementary Table S1**. Subsequently, the seamless cloning products were transformed into *E. coli* DH5α cells. Recombinant plasmid construction was confirmed by DNA sequencing. They were then linearized with *Sal*I, and transformed into *P. pastoris* GS115 competent cells through electroporation. Positive clones were screened using minimal dextrose (MD) plates, their activity was demonstrated using skim milk plates, and confirmed by DNA sequencing.

Heterologous Expression and Purification

Positive clones were fermented as previously described [24]. Cultures were centrifuged at 8000 ×*g* for 10 min at 4°C and crudely purified by the slow addition of ammonium sulfate until 80% saturation was achieved. After overnight dialysis against TE buffer (20 mM Tris-HCl, 500 mM NaCl, pH 7.5) at 4°C, the crude samples were purified using a HisTrap HP affinity column (General Electric Company, Boston, MA, United States). The fractions containing pepsinogen were pooled and dialyzed against

the TE buffer, then activated by adding 0.9 M HCl to adjust the pH to ~2 and subsequently incubated at 25°C for 10 min. The prosegment was removed using Centricon filtration units with a 10 kDa molecular mass cutoff (Millipore, Boston, MA, United States). All samples were stored in 20 mM sodium acetate (pH 5.3) and analyzed using 12% sodium dodecyl sulfate-polyacrylamide gel electrophoresis (SDS-PAGE, Coomassie Brilliant Blue R250-stained). Finally, the concentration of recombinant pepsin was measured using a BCA protein quantificationkit (Yeasen Biotech Co., Ltd., Shanghai, China).

Enzymatic Activity and Kinetic Assays

The proteolytic activities of pepsin and its variants were determined by measuring the amount of exposed tyrosine residues during hydrolysis in 100 mM sodium citrate buffer (pH 2.0), with 1% bovine hemoglobin as the substrate. A mixture containing 0.5 ml of 1% bovine hemoglobin and 0.5 ml of appropriately diluted recombinant proteins was incubated at 60°C for 10 min. The reactions were terminated by adding 1.0 ml of 0.4 M trichloroacetic acid (TCA). Exposed tyrosine residues were quantified by incubating reactions containing 0.5 ml of the filtered supernatant, 2.5 ml of 0.4 M sodium carbonate solution, and 0.5 ml of Folin's phenol reagent at 40°C for 20 min and then measuring absorbance at 680 nm. Control samples were treated in a similar manner, but TCA was added before adding the enzyme.

The initial reaction rates of recombinant proteins were also determined at 60°C and a pH of 2.0, using 0.5–10.0 mg ml^{-1} bovine hemoglobin as the substrate. Kinetic parameters (K_m, k_{cat}, and V_{max}) were obtained by fitting the initial data to the Michaelis–Menten nonlinear regression equation in the Origin 9.0 software (Origin Lab Corporation).

Half-Life Analysis

To evaluate thermostability, the half-lives ($t_{1/2}$) of pepsin and its mutants were measured at 65°C and 70°C. Recombinant proteins were appropriately diluted with 100 mM sodium citrate buffer (pH 2.0) and pre-incubated at 65°C and 70°C. Samples were taken at regular intervals, and the residual activities measured at 60°C and pH 2.0, as described in *Enzymatic Activity and Kinetic Assays*. Initial activity, before pre-incubation, was set to 100%.

Molecular Dynamics Simulation

The crystal structure of pepsin was obtained from the Protein Data Bank (PDB: 4PEP), and all the crystal waters were removed. The structures of the mutants were prepared using Discovery Studio 2019. The Leap module of AMBER18 was used to fill the missing atoms. The parameters were generated using the AMBER14SB force field. The protein was placed in a TIP3P water box with 12 Å buffer, and counter ions were added to neutralize the system. The steepest descent and conjugate gradient methods were used to optimize the structure. The entire system was subsequently heated to 310 K and the protein was constrained to 10 kcal/(mol $Å^2$). The SHAKE algorithm was employed to constrain chemical bonds involving hydrogen atoms [25]. Finally, simulations were run for 100 ns.

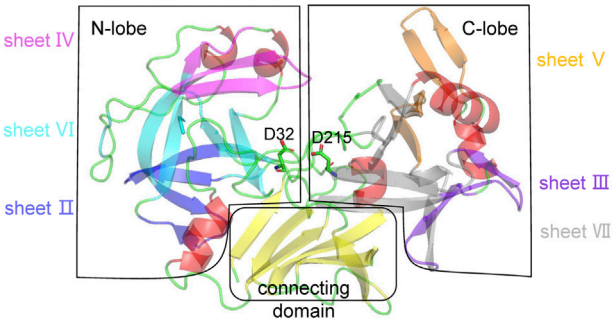

FIGURE 1 | Structural analysis of pepsin. Pepsin is divided into three regions: N-lobe, C-lobe, and connecting domain. In the N-lobe, *ß*-strands can be divided into three layers: sheets IV (magenta), VI (cyan), and II (blue) that are orthogonally packed. In the C-lobe, *ß*-strands can be divided into two orthogonal packing sheets, VII (grey) and III (purpleblue), and a rather separate sheet V (orange). The connecting domain is composed of a six-stranded antiparallel interdomain *ß*-sheet (yellow). Other secondary structures, *a*-helices and loops are shown in red and green. The catalytic dyad is represented by sticks.

Statistical Analyses

All statistical analyses were performed using Origin 9.0 software, with values expressed as the mean ± standard error of the mean. A one-sample Student's *t*-test was used to compare the mutant and wild-type means. Statistical significance was set at $p < 0.05$. For comparisons between the wild-type and mutants, *represents $p < 0.05$, **represents $p < 0.01$, and ***represents $p < 0.001$.

RESULTS

Analysis of Catalytic Mechanism, Structural Characteristics, and Stability Weaknesses of Pepsin

Members of the aspartic protease family have a similar catalytic mechanism. A nucleophile is formed from a water general-base activated by Asp215, which subsequently attacks the carbonyl oxygen of the scissile bond to form a *gem* diol of a tetrahedral intermediate with Asp32. The proton transfer from Asp215 to the leaving group is coupled with the regeneration of the proton of Asp32 [26]. Finally, the peptide bond is broken. Thus, the catalytic dyad composed of Asp32 and Asp215 is crucial for the catalysis of pepsin. Two key points need to be avoided in the thermostability design.

Many aspartic proteases have been reported to have similar three-dimensional structures. For simplicity, the pepsin structure can be divided into three regions: N-lobe, C-lobe, and connecting domain (**Figure 1**). The N-lobe is made up of a series of *ß*-strands that are folded into three layers of orthogonal packing: sheets IV, VI, andII.The C-lobe has two orthogonal packing sheets, VII and III, and a rather separate sheet V [27]. Several *a*-helices and loops

are also present in both lobes. The connecting domain is comprised mainly of a six-stranded antiparallel interdomain ß-sheet connecting the N-lobe and the C-lobe to form the catalytic dyad.

Structural analysis revealed that the three ß-sheets in the N-lobe form a continuous hydrophobic region, and the *a*-helix near the connecting domain and adjacent loops cap the hydrophobic core, further stabilizing the structure. Similarly, a hydrophobic core is formed in the C-lobe, and the connecting domain simultaneously interacts internally with the N- and C-lobes [27]. The loops in pepsin are mainly ß-turns or ß-hairpins that connect ß-strands. We speculated that pepsin may possess two thermodynamic structural weaknesses: the relatively loose internal hydrophobic packing and the high flexibility of the surface *a*-helices and loops that are not part of the hydrophobic cores. Therefore, there are two strategies for improving the thermostability of pepsin: 1) designing ß-strands that directly improve the interaction between ß-sheets or ß-strands, and 2) designing *a*-helices or loops on the surface to reduce local disorder.

Selection of Thermostability Predicting Software Programs and Mutation Screening Principles

To investigate correlations between computational design software programs and structural characteristics, we selected several thermostability prediction software programs with successful cases and with varying principles. PoPMuSiC is a web server that predicts folding free energy changes ($\Delta\Delta G$) caused by single-site mutations in proteins. $\Delta\Delta G$ is a linear combination of statistical potentials, considering the amino acid type, torsion angles defining the backbone conformation, and solvent accessibility. $\Delta\Delta G < 0$ indicates that the mutant is more stable than the wild-type. The thermostability of multiple proteins has been improved using the PoPMuSiC algorithm [9, 28, 29]. HoTMuSiC is a computational tool that uses an artificial neural network to predict the change in melting temperature ΔT_m, upon the introduction of single-point mutations, based on the imperfect correlation of thermodynamics and thermal stabilities [30]. $\Delta T_m > 0$ indicates that the mutants are more stable than the wild-type. Enzyme thermal stability system (ETSS) is an enzyme redesign protocol that improves stability based on the TK-SA model calculation and surface charge–charge interaction analysis protocol [31, 32]. Charged amino acids are computed using the ETSS and residues with $\Delta G_{qq} > 0$ are deemed unstable for the given protein and considered to be uncharged or oppositely charged amino acid mutations. ETSS is effective at improving the thermostability of many enzymes [33, 34]. DeepDDG is a neural network-based method used to predict changes in protein stability resulting from single-point mutations. $\Delta\Delta G > 0$ indicates that the mutant is more stable than the wild-type. The neural network was trained on the largest dataset of experimentally determined stability data from various sources, and it predicted stability changes based on the three-dimensional structure of a protein. This algorithm gave Pearson correlation coefficients of 0.48–0.56 for three independent test sets, outperforming 11 other methods [35]. Fireprot is a web server developed by Musil et al., which integrates 16 computing tools, including Clustal ω, Rosetta, and FoldX [36]. The algorithm combines energy- and evolution-based approaches to predict stable mutations. Prior to virtual mutation, correlation and conserved analyses are performed to exclude important residues. Surprisingly, the phylogenetic analysis enabled the identification of mutations stabilized by entropy, which could not be predicted by force field calculations [36].

We chose the above-mentioned representative and unique software programs. By analyzing the successful cases of these software programs, mutations were found in *a*-helices, ß-strands, and loops distributed in the interior and surface of proteins, thus meeting the requirements of our analysis of thermodynamic weaknesses. Among these software programs, PoPMuSiC, HoTMuSiC, ETSS, and DeepDDG provided mutation rankings. Based on the highest-ranking batch and the principle of scattered mutation points, we selected four mutations predicted by each software program for follow-up experimental verification. The top 20 mutations predicted by PoPMuSiC, HoTMuSiC, ETSS, and DeepDDG are shown in **Supplementary Tables S2–S5** to assist with explaining the screening principles. The number of mutations given by Fireprot was limited; thus all mutations were selected for further experiments.

Thermostability Detection of Mutations Designed Based on Energy From Multiple Software Programs

Based on the screening described above, 34 single-site mutants were constructed and transformed into *P. pastoris* for expression, using the pPIC9K-pepsinogen plasmid as the template. The mutants predicted based on energy (from PoPMuSiC, HoTMuSiC, ETSS, DeepDDG, and Fireprot-Energy) were tested as a set. To rapidly screen the mutants, we used crude enzyme to measure thermostability. One unit of enzyme activity was defined as the amount of enzyme required to hydrolyze bovine hemoglobin toproduce 1 μg tyrosine per minute at 60°C and pH 2.0. HCl (0.9 M) was added to the fermentation broth supernatants and the pH was adjusted to 2.0, to convert pepsinogen into pepsin. The acidified fermentation broths were incubated at 65°C for 3 min and then cooled on ice. Changes in enzyme activity before and after incubation were measured to reflect the thermostability of recombinant proteins. Enzyme activity before incubation was plotted at 100%. The results are shown in **Figure 2A**. Apart from the mutations selected by energy-based Fireprot, some mutants predicted by PoPMuSiC, HoTMuSiC, ETSS, and DeepDDG resulted in complete loss of enzyme activity before incubation. These occurred mainly at Gly85, Asp87, Gly102, and Arg315. The remaining mutants did not improve pepsin thermostability. These results indicate that the energy-based mutants were not associated with the thermodynamic weakness of pepsin, and some were located on critical

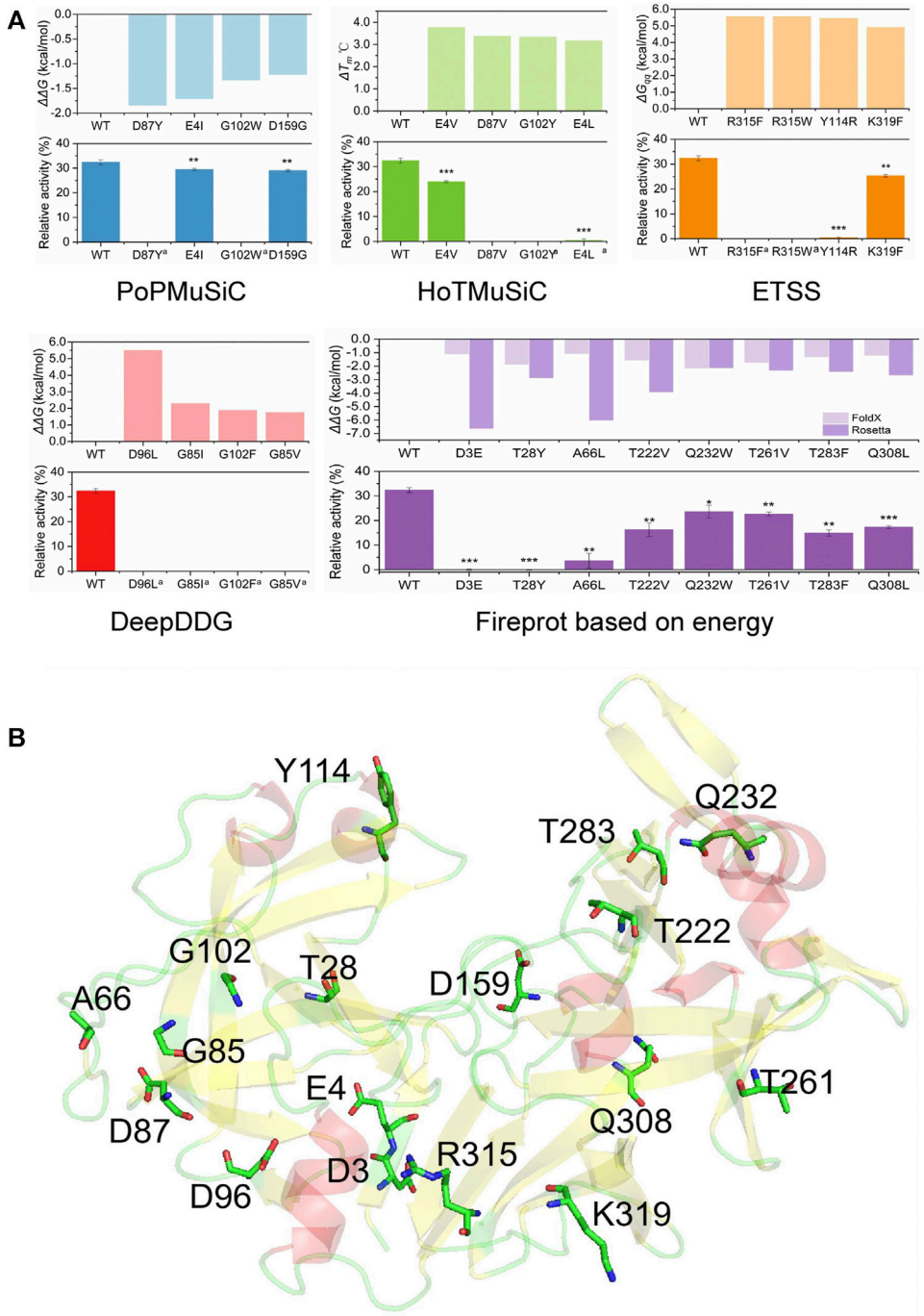

FIGURE 2 | Thermostability results and analyses of positions of the set of mutations predicted using various energy-based software programs. **(A)** Software programs' parameters and relative activities of single-point mutations after incubation at 65°C for 3 min. Data are mean ± s.e.m. ***$p < 0.001$, **$p < 0.01$, *$p < 0.05$. Data are from three independent experiments. **(B)** Positions of mutations on the pepsin structure. [a] indicates that the activity of the original crude enzyme is too low to be measured.

pepsin residues, resulting in the collapse of the hydrophobic cores.

To guide the follow-up design, we analyzed the positions of the above mutations to confirm the structural weakness of pepsin. As shown in **Figure 2B**, Ala66 and Asp159 are on loops, Tyr114 and Gln232 are on *a*-helices, and the remaining mutation sites are on *ß*-strands. Thr28, Gly85, Asp87, Asp96, and Gly102 are located on the three *ß*-sheets of the N-lobe, which are stacked orthogonally to form hydrophobic cores; Asp3, Glu4, Arg315, and Lys319 are located on the closely packed *ß*-sheet in the

TABLE 1 | Single-point mutations predicted by Fireprot based on evolution.

Mutation by Fireprot based on evolution	BTC by majority	BTC by ratio	FoldX kcal/mol
A24P	Y	N	−1.34
D52N	Y	Y	−0.92
Q55R	Y	Y	−0.97
E65Q	N	Y	−0.19
S129A	Y	N	−0.43
L140M	T	N	−0.48
W141M	Y	N	−0.70
L167F	Y	N	−1.36
D200N	Y	Y	−0.54
S270P	Y	Y	−2.16

BTC is the abbreviation of Back-to-consensus analysis. BTC by majority means the mutations on the positions where the consensus residue frequency is at least 50%. BTC by ratio means the mutations on the positions where the consensus residue frequency is more than 40% and is at least five times more than the wild-type residue. Y means yes, N means no.

connecting domain; Thr222, Thr261, Thr283, and Tyr309 are located in the orthogonally packed ß-sheets in the C-lobe. The *a*-helices where Tyr114 and Gln232 are located are also close to hydrophobic cores; the Gln232 side chain is oriented towards the protein, and Tyr114 is an aromatic amino acid. Thus, most of the mutations are located on or near hydrophobic cores, and changes in hydrophobic cores can easily cause enzyme inactivation [37]. The results showed that pepsin's hydrophobic cores were tightly packed, and were not the major thermodynamic structural weakness of the enzyme. Mutations in the compact region can have long-range effects. Therefore, when further strengthening the internal packing, mutations in the ß-strands and *a*-helices involving hydrophobic cores lead to enzyme inactivation. Although the computational design results showed that the overall energy of these mutants was greatly reduced, the probability of protein structure destruction was very high. Thus, mutations on ß-strands or inside *a*-helices are not suitable and mutations guided by the real structural weaknesses—flexible regions on the surface of pepsin—need to be selected.

Detection of Thermostable Mutants Predicted by Fireprot Based on Evolution

Fireprot also identified 10 mutations based on evolution (**Table 1**). As mentioned above, mutations on tightly packed sheets and *a*-helices are less feasible, and surface *a*-helices and loops are the main thermodynamic weakness points of pepsin. Thus, we initially analyzed the positions of these 10 mutations. As shown in **Figure 3A**, E65Q is on the orthogonally packed ß-sheet of the N-lobe, L167F is on the tightly packed ß-sheet of the connecting domain, D200N is on the ß-turn of the C-lobe, L140M and W141M are on the *a*-helix, which is part of the hydrophobic core, and the other five mutations are on the loops or *a*-helices on the surface of pepsin. Thus, A24P, D52N, Q55R, S129A, and S270P mutants were set as the experimental group, and E65Q, L140M, W141M, L167F, and D200N were set as the control group. As described above, we measured the thermostability of the crude enzymes, the results of which are shown in **Figure 3B**. The wild-type pepsin retained 32.4% of its original activity after incubation for 3 min at 65°C. Among the mutants in the experimental group, the thermostabilities of A24P, D52N, E65Q, and S129A were significantly improved, with D52N and S129A retaining 75.4 and 63.5% of their initial activity, respectively. Only S270P showed a slight decrease in thermostability. The thermostability of mutants in the control group decreased, particularly L140M and W141M. The results indicate that the above strategy of being guided by the thermodynamic weakness of pepsin can rapidly and effortlessly guide mutant design.

Mutants A24P, D52N, E65Q, and S129A, which had improved thermostability, were purified (**Supplementary Figure S1**). The thick band around 35 kDa is unglycosylated pepsin, and the fuzzy fine band above it is O-glycosylated pepsin, both of which are consistent with previous reports. Glycosylation is used to enhance the thermostability of proteins, and Yoshimasu et al. confirmed that the thermostability of O-glycosylated pepsin was improved

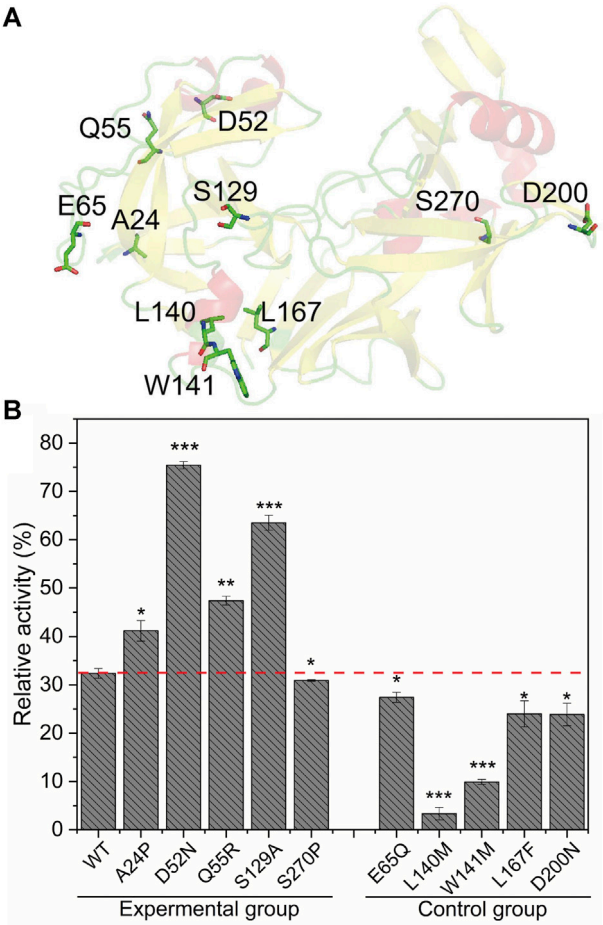

FIGURE 3 | Analysis of the positions and thermostability results of mutations predicted using Fireprot based on evolution. **(A)** Positions of mutations on the pepsin structure. **(B)** Relative activities of mutants after incubation at 65°C for 3 min. Data are mean ± s.e.m. ***$p < 0.001$, **$p < 0.01$, *$p < 0.05$. Data are from three independent experiments.

TABLE 2 | Half-life ($t_{1/2}$) values of wild-type (WT) and mutant pepsin.

Enzyme	$t_{1/2}$ (min)	
	65°C	70°C
WT	3.20 ± 0.09	0.80 ± 0.03
A24P	3.42 ± 0.01*	1.14 ± 0.08*
D52N	13.06 ± 0.27***	2.40 ± 0.03***
Q55R	3.42 ± 0.05*	1.10 ± 0.04*
S129A	4.98 ± 0.21*	1.33 ± 0.02**

*Data are mean ± s.e.m. ***p < 0.001, **p < 0.01, *p < 0.05. Data are from three independent experiments.*

[24]. Therefore, it was retained in the experiment. The half-lives ($t_{1/2}$) at 65°C and 70°C were measured and 1% bovine hemoglobin was used as the substrate to determine changes in thermostability (**Table 2**). The $t_{1/2}$ values of A24P and Q55R at 65°C and 70°C were slightly improved. The $t_{1/2}$ of S129A at 65°C and 70°C increased by 55.6 and 66.3%, respectively, while that of D52N at 65°C and 70°C increased by 308.1 and 200.0%, respectively.

The activities of the mutants D52N and S129A were determined at pH 2.0 and 60°C, using 1% bovine hemoglobin as the substrate. The kinetic parameters were also measured under these conditions using gradient concentrations of bovine hemoglobin (**Supplementary Figure S3**). As shown in **Table 3**, compared with the wild-type, the activities of the D52N and S129A mutants decreased by 31.8 and 23.3%, respectively. The K_m values of D52N and S129A were 2.12 ± 0.05 and 1.40 ± 0.09 mg ml^{-1}, 130.4 and 52.2% lower than that of the wild-type, respectively. Thus, although k_{cat} values improved, the k_{cat} and k_{cat}/K_m values of D52N and S129A mutants decreased by 37.0 and 27.0%, respectively.

Structural and Mechanistic Analysis of Mutations

Dynamic simulation analysis was performed to explore the mechanism of the effect of mutations on the thermostability of pepsin and its mutants. Single-point mutations D52N and S129A were introduced into the crystal structure of pepsin using Discovery Studio 2019, and a stable structure was obtained through a 100 ns MD simulation. The root mean squared deviations (RMSDs) of the protein backbones are shown in **Supplementary Figure S2**. The RMSD of the wild-type and the D52N and S129A substituted structures were approximately 2.5 Å, 1.5 Å, and 1.5 Å, respectively, indicating that the three systemsare stable, and that D52N and S129A are more stable than the wild-type. A snapshot was extracted from each of the three stable structures for structural analysis (**Figure 4**). The D52N substitution was located on the *a*-helix on the protein surface, and formed hydrogen bonds with Leu48 and Ala49, making the *a*-helix more stable and improving structural rigidity. The S129A substitution was located in a loop on the protein surface. The replacement of Ser with Ala promoted the hydrophobic packing of Pro126, Gly132, Ala133, and Pro135, making this region more stable.

Furthermore, isotropic temperature factors (B-factors) of the three systems in the last 10 ns of the simulation were calculated to measure the residue fluctuations relative to their mean positions. As shown in **Figure 4**, we found that the D52N substitution reduced the flexibility of position 52, and the flexibility of Leu48 and Ala49 also decreased, but to varying degrees. After S129A substitution, the flexibility of position 129 decreased, and the flexibility of Pro126, Gly132, and Pro135 of the residues forming the hydrophobic packing decreased by different degrees, with the biggest decrease being noted in Pro126 and Pro135.

DISCUSSION

Numerous breakthroughs have recently been made in the study of enzyme thermostability. The structural rigidity of proteins has been associated with their thermostability through the comparison of mesophilic and thermophilic variants [38]. Protein engineering, which includes the introduction of hydrogen bonds, salt bridges, and disulfide bonds to enhance local rigidity and improve enzyme thermostability, further confirmed this finding [39–41]. Rigidifying flexible sites is a common strategy that seems to be similar to that employed in our study, which involved improving the thermostability of proteins by analyzing the flexible regions of proteins and then rigidifying these sites. However, this strategy is associated with some difficulties when it comes to determining the flexible regions, for example, the crystal structure does not perfectly reflect the flexibility of the protein in the solution, the molecular dynamics is complex and time-consuming, and choosing possible positions to be rigidified [42]. Therefore, as a non-regular secondary structure with high flexibility, loops are often chosen as potential sites for rigidification. Rigidifying loops combined with saturation mutagenesis, proline substitutions, and $\Delta\Delta G$ calculations in Rosetta have been applied to the thermostability modifications of lipase, luciferase, and transketolase, with the qualitative prediction accuracy of the Rosetta program reaching 65.3% [43–45]. However, the flexibility of some sites is critical to the catalytic activity of the

TABLE 3 | Kinetic analysis of wild-type pepsin and its mutants.

	Specific activity U mg^{-1}	K_m mg mL^{-1}	V_{max} μM s^{-1} mg^{-1}	k_{cat} s^{-1}	k_{cat}/k_m mL mg^{-1} s^{-1}
WT	3173 ± 73	0.92 ± 0.03	2369.97 ± 31.63	16589.81 ± 221.44	18071.43 ± 316.46
D52N	2164 ± 5***	2.12 ± 0.03***	3441.65 ± 66.06**	24091.55 ± 462.45**	11383.44 ± 364.13**
S129A	2433 ± 14***	1.40 ± 0.09*	2607.35 ± 1.99***	18265.42 ± 13.94***	13193.22 ± 847.37*

*Data are mean ± s.e.m. ***p < 0.001, **p < 0.01, *p < 0.05. Data are from three independent experiments.*

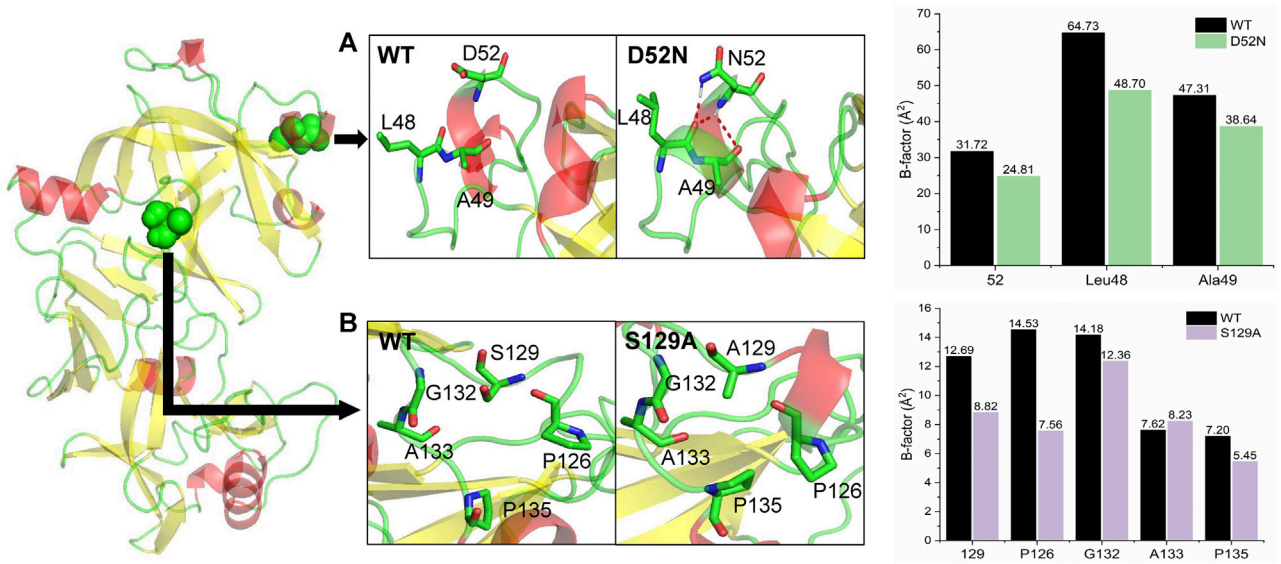

FIGURE 4 | Conformational analysis of wild-type (WT) and mutant pepsin. **(A)** Mutant D52N formed new hydrogen bonds with Leu48 and Ala49. The B-factors of these residues decreased compared with the wild-type. **(B)** Mutant S129A promoted hydrophobic packing in the loop. The B-factors of most these residues decreased compared with the wild-type.

enzyme, and rigidifying will cause significant damage [46, 47]. In our study, the loop regions were not focused on in advance. Instead, the major thermodynamic weakness points were determined through in-depth structural analysis and were subsequently used as the targets to guide thermostability design. Qualitative prediction accuracy of the computational design with the assistance of thermodynamic weakness reached 80.0%. Structural weaknesses, not limited to loop regions with high flexibility, provide a more comprehensive perspective and more potential sites. In our study, we designed the mutant D52N, which is located on an *a*-helix, which may be ignored when rigidifying flexible sites.

The conformational fluctuation of a protein increases when it is exposed to high temperatures. High fluctuation yields reversible or irreversible protein unfolding, leading to loss of function [48]. Therefore, regions that have fewer contacts with the surrounding residues fluctuate significantly and can easily trigger protein unfolding. This is why loops are often chosen as mutation sites [45]. However, the results of agarase AgWH50C from *Agarivorans gilvus WH0801* and glucose oxidase from *Aspergillus niger* showed that modification of other secondary structures within the protein can significantly enhance thermostability, and modification of loops is not the only option [33, 49]. Therefore, based on its high-resolution crystal structure, pepsin is divided into hydrophobic cores and surface covering areas. At high temperatures, the solvation of hydrophobic cores caused by surface fluctuations and the collapse of hydrophobic cores can result in thermodynamic weaknesses. The surface flexible regions were confirmed as the major points of thermodynamic weakness and subsequently used in computational design. The results also showed that mutants on the surface flexible regions enhanced the thermostability of pepsin by reducing local fluctuation. We also found that the enzyme's reaction temperature can reflect its structural rigidity, to a certain extent, providing some guidance for follow-up mutation design. Pepsin is mainly composed of orthogonally packed antiparallel *ß*-sheets, which are stable enough to form hydrophobic cores, while most of the flexible regions are located on the protein surface. The optimum reaction temperature for pepsin was determined to be 60°C, and after incubation at 60°C for 30 min, the enzyme still retained more than 50% of its peak activity, indicating the rigidity of the pepsin structure. The results of the set of mutations provided by energy-based prediction software programs confirmed this result. Therefore, pepsin's rigidity implies that the flexible regions on the surface are the major thermodynamic weakness point, and its design is more feasible. Compared with our results, Guo et al. generated a mutation on the surface *ß*-strand to increase the thermostability of *Bs*APA at an optimum temperature of 75°C [23]. Chen et al. generated a mutation on the surface *a*-helix to improve the thermostability of L-rhamnose isomerase at an optimum temperature of 85°C [50]. Mu et al. generated an interior mutant to improve the thermostability of glucoseoxidase via enhancing internal hydrophobic packing at an optimum temperature of 40°C [51]. The results of these studies are consistent with our finding that the reaction temperature reflects structural rigidity, to a certain extent, which assists in modifications.

The prediction software programs utilized in this study also have a cross-linked application in enzyme thermostability. In a study on improving the thermostability of agarase AgWH50C, Zhang et al. used a cross-linked protocol combining PoPMuSiC, HoTMuSiC, and ETSS, and successfully screened three mutations with improved thermostability from seven potential mutations [49]. This showed that combining multiple software programs

TABLE 4 | Mutations with improved thermostability predicted using PoPMuSiC, HoTMuSiC, ETSS and DeepDDG software programs.

Mutation	PoPMuSiC $\Delta\Delta G$ (kcal/mol)	HoTMuSiC ΔT_m (°C)	ETSS ΔG_{qq} (kcal/mol)	DeepDDG $\Delta\Delta G$ (kcal/mol)
A24P	0.35	−0.83	–	0.951
D52N	0.04	−0.15	−6.63	0.161
Q55R	0.22	−0.61	–	0.13
S129A	0.79	−0.88	–	0.058

can effectively reduce the scope of mutations for experimentation. However, in our study, the four mutations with improved thermostability performed poorly in PoPMuSiC, HoTMuSiC, and ETSS, only exhibiting positive performance in DeepDDG, and the best mutations (D52N and S129A) were not at the top of the list (**Table 4**). The linear combination of the statistical potentials used by PoPMuSiC depends on the volume of the wild-type and mutant amino acids [13]. The volume terms were also considered in the standard and temperature-dependent statistical potentials of HoTMuSiC [30]. Therefore, partial consistency in the results is expected. However, PoPMuSiC only considers the torsion angles defining the backbone conformation, whereas HoTMuSiC does not consider local structural rearrangements upon residue substitutions in the hydrophobic cores. ETSS does not consider the pH of the enzymatic reaction. Under the optimal pH for pepsin (2.0), the charge of the residue changes significantly, possibly causing errors [34]. Thus, each software program has its own limitations, and considering the structural weaknesses of the enzyme will be a highly appropriate choice.

Thermostability modification is an important method for improving the industrial value of enzymes. Apart from quite blind and inefficient directed evolution, there have been many successful cases in the past decade involving local minor modifications such as introducing non-covalent or covalent interactions, increasing proline levels, or deleting glycine through protein engineering [52]. However, it is still difficult to accurately determine the regions and residues to be modified. Although thermostability prediction software programs can identify a clear mutation, their accuracy and effectiveness are poor and they therefore have low applicability [53]. By improving the thermostability of pepsin, we showed that thermodynamic weakness combined with rational design guided by prediction software programs can solve the difficulties involved in identifying the regions and the replacement residues, thus improving the accuracy of rational thermostable protein design. However, we must recognize that while we effectively and accurately obtained mutants with improved thermostability, assisted by the thermodynamic weakness of pepsin, in-depth structural analysis was based on high-resolution protein structure, which is a challenge for structure determination and prediction. The types and structures of enzymes vary, and the identification of thermodynamic weaknesses in different enzyme families requires comprehensive research. It is also necessary to develop systematic testing methods and trial-and-error experiments. Decreased activity of mutants with improved thermostability is the common activity-stability trade-off in enzyme design [54]. This needs to be addressed through additional research. Nevertheless, our research provides an effective method for modifying enzyme thermostability.

DATA AVAILABILITY STATEMENT

The original contributions presented in the study are included in the article/**Supplementary Material**, further inquiries can be directed to the corresponding authors.

AUTHOR CONTRIBUTIONS

YZ: performed the experiments, processed and analysed the data, and wrote the article; YM: performed the virtual calculation and dynamics simulation and interpreted the results; FZ: performed part of the experiments; YP: reviewed the paper and provided technical assistance; JZ and XY: reviewed the paper; JZ and LZ: acquired funding and provided project supervision, conceived and designed the study, and reviewed the article. All authors approved the final version of the article.

FUNDING

This work was supported by the National Key R&D Program of China (grant no. 2019YFA0905200), the National Natural Science Foundation of China (grant nos. U1805235, 31571786), and the NYU-ECNU Center for Computational Chemistry at NYU, Shanghai.

SUPPLEMENTARY MATERIAL

The Supplementary Material for this article can be found online at: https://www.frontiersin.org/articles/10.3389/fphy.2021.755253/full#supplementary-material

REFERENCES

1. Guo Y, Tu T, Yuan P, Wang Y, Ren Y, Yao B, et al. High-level Expression and Characterization of a Novel Aspartic Protease from Talaromyces leycettanus JCM12802 and its Potential Application in Juice Clarification. *Food Chem* (2019) 281:197–203. doi:10.1016/j.foodchem.2018.12.096
2. Li X, Cong Y, Ma M, You Z-N, Gao B, Zhang JZH, et al. An Energy Optimization Strategy Based on the Perfect Conformation of Prolyl Endopeptidase for Improving Catalytic Efficiency. *J Agric Food Chem* (2020) 68(18):5129–37. doi:10.1021/acs.jafc.0c00731
3. Polgár L. The Catalytic Triad of Serine Peptidases. *Cell. Mol Life Sci* (2005) 62(19-20):2161–72. doi:10.1007/s00018-005-5160-x

4. Gomes J, and Steiner W. The Biocatalytic Potential of Extremophiles and Extremozymes. *Food Technol Biotechnol* (2004) 42(4):223–35. doi:10.1016/j.fm.2003.12.003
5. Lehmann M, Pasamontes L, Lassen SF, and Wyss M. The Consensus Concept for Thermostability Engineering of Proteins. *Biochim Biophys Acta (Bba) - Protein Struct Mol Enzymol* (2000) 1543(2):408–15. doi:10.1016/S0167-4838(00)00238-7
6. Wijma HJ, Floor RJ, and Janssen DB. Structure- and Sequence-Analysis Inspired Engineering of Proteins for Enhanced Thermostability. *Curr Opin Struct Biol* (2013) 23(4):588–94. doi:10.1016/j.sbi.2013.04.008
7. Baek M, DiMaio F, Anishchenko I, Dauparas J, Ovchinnikov S, Lee GR, et al. Accurate Prediction of Protein Structures and Interactions Using a Three-Track Neural Network. *Science* (2021) 373:871–6. doi:10.1126/science.abj8754
8. Hao L, Zhang R, and Lohman TM. Heterogeneity in *E. coli* RecBCD Helicase-DNA Binding and Base Pair Melting. *J Mol Biol* (2021) 433(18):167147. doi:10.1016/j.jmb.2021.167147
9. Jones JC, Banerjee R, Shi K, Semonis MM, Aihara H, Pomerantz WCK, et al. Soluble Methane Monooxygenase Component Interactions Monitored by 19F NMR. *Biochemistry* (2021) 60(25):1995–2010. doi:10.1021/acs.biochem.1c00293
10. Jumper J, Evans R, Pritzel A, Green T, Figurnov M, Ronneberger O, et al. Highly Accurate Protein Structure Prediction with AlphaFold. *Nature* (2021) 596(7873):583–9. doi:10.1038/s41586-021-03819-2
11. Adzhubei IA, Schmidt S, Peshkin L, Ramensky VE, Gerasimova A, Bork P, et al. A Method and Server for Predicting Damaging Missense Mutations. *Nat Methods* (2010) 7(4):248–9. doi:10.1038/nmeth0410-248
12. Cheng J, Randall A, and Baldi P. Prediction of Protein Stability Changes for Single-Site Mutations Using Support Vector Machines. *Proteins* (2006) 62(4): 1125–32. doi:10.1002/prot.20810
13. Dehouck Y, Kwasigroch JM, Gilis D, and Rooman M. PoPMuSiC 2.1: a Web Server for the Estimation of Protein Stability Changes upon Mutation and Sequence Optimality. *BMC Bioinformatics* (2011) 12(1):151. doi:10.1186/1471-2105-12-151
14. Masso M, and Vaisman II. AUTO-MUTE 2.0: A Portable Framework with Enhanced Capabilities for Predicting Protein Functional Consequences upon Mutation. *Adv Bioinformatics* (2014) 2014:1–7. doi:10.1155/2014/278385
15. Parthiban V, Gromiha MM, and Schomburg D. CUPSAT: Prediction of Protein Stability upon point Mutations. *Nucleic Acids Res* (2006) 34: W239–W242. doi:10.1093/nar/gkl190
16. Topham CM, Srinivasan N, and Blundell TL. Prediction of the Stability of Protein Mutants Based on Structural Environment-dependent Amino Acid Substitution and Propensity Tables. *Protein Eng Des Selection* (1997) 10(1): 7–21. doi:10.1093/protein/10.1.7
17. Landbo A-KR, Pinelo M, Vikbjerg AF, Let MB, and Meyer AS. Protease-Assisted Clarification of Black Currant Juice: Synergy with Other Clarifying Agents and Effects on the Phenol Content. *J Agric Food Chem* (2006) 54(18): 6554–63. doi:10.1021/jf060008d
18. Quintieri L, Caputo L, Monaci L, Deserio D, Morea M, and Baruzzi F. Antimicrobial Efficacy of Pepsin-Digested Bovine Lactoferrin on Spoilage Bacteria Contaminating Traditional Mozzarella Cheese. *Food Microbiol* (2012) 31(1):64–71. doi:10.1016/j.fm.2012.02.015
19. Osire T, Yang T, Xu M, Zhang X, Li X, Niyomukiza S, et al. Lys-Arg Mutation Improved the Thermostability of Bacillus Cereus Neutral Protease through Increased Residue Interactions. *World J Microbiol Biotechnol* (2019) 35(11):173. doi:10.1007/s11274-019-2751-5
20. Xu B-L, Dai M, Chen Y, Meng D, Wang Y, Fang N, et al. Improving the Thermostability and Activity of a Thermophilic Subtilase by Incorporating Structural Elements of its Psychrophilic Counterpart. *Appl Environ Microbiol* (2015) 81(18):6302–13. doi:10.1128/AEM.01478-15
21. Zhao H-Y, Wu L-Y, Liu G, and Feng H. Single-site Substitutions Improve Cold Activity and Increase Thermostability of the Dehairing Alkaline Protease (DHAP). *Biosci Biotechnol Biochem* (2016) 80(12):2480–5. doi:10.1080/09168451.2016.1230005
22. Rawlings ND, and Barrett AJ. Introduction. In: ND Rawlings and S Guy, editors. *Handbook of Proteolytic Enzymes*. Cambridge: Academic Press (2013) p. 3–19. doi:10.1016/b978-0-12-382219-2.00001-6
23. Guo Y, Tu T, Zheng J, Bai Y, Huang H, Su X, et al. Improvement of BsAPA Aspartic Protease Thermostability via Autocatalysis-Resistant Mutation. *J Agric Food Chem* (2019) 67(37):10505–12. doi:10.1021/acs.jafc.9b03959
24. Yoshimasu MA, Ahn J-K, Tanaka T, and Yada RY. Soluble Expression and Purification of Porcine Pepsinogen from Pichia pastoris. *Protein Expr Purif* (2002) 25(2):229–36. doi:10.1016/s1046-5928(02)00003-1
25. Ryckaert J-P, Ciccotti G, and Berendsen HJC. Numerical Integration of the Cartesian Equations of Motion of a System with Constraints: Molecular Dynamics of N-Alkanes. *J Comput Phys* (1977) 23(3):327–41. doi:10.1016/0021-9991(77)90098-5
26. Bizzozero SA, and Dutler H. Stereochemical Aspects of Peptide Hydrolysis Catalyzed by Serine Proteases of the Chymotrypsin Type. *Bioorg Chem* (1981) 10(1):46–62. doi:10.1016/0045-2068(81)90042-0
27. Sielecki AR, Fedorov AA, Boodhoo A, Andreeva NS, and James MNG. Molecular and crystal Structures of Monoclinic Porcine Pepsin Refined at 1.8A° resolution. *J Mol Biol* (1990) 214(1):143–70. doi:10.1016/0022-2836(90)90153-d
28. Guo J, Rao Z, Yang T, Man Z, Xu M, Zhang X, et al. Enhancement of the Thermostability of Streptomyces Kathirae SC-1 Tyrosinase by Rational Design and Empirical Mutation. *Enzyme Microb Tech* (2015) 77:54–60. doi:10.1016/j.enzmictec.2015.06.002
29. Liao H, Gong JY, Yang Y, Jiang ZD, Zhu YB, Li LJ, et al. Enhancement of the Thermostability of Aspergillus niger α- L -rhamnosidase Based on PoPMuSiC Algorithm. *J Food Biochem* (2019) 43(8):e12945. doi:10.1111/jfbc.12945
30. Pucci F, Bourgeas R, and Rooman M. Predicting Protein thermal Stability Changes upon point Mutations Using Statistical Potentials: Introducing HoTMuSiC. *Sci Rep* (2016) 6:23257. doi:10.1038/srep23257
31. Richmond TJ. Solvent Accessible Surface Area and Excluded Volume in Proteins. *J Mol Biol* (1984) 178(1):63–89. doi:10.1016/0022-2836(84)90231-6
32. Tanford C, and Kirkwood JG. Theory of Protein Titration Curves. I. General Equations for Impenetrable Spheres. *J Am Chem Soc* (1957) 79(20):5333–9. doi:10.1021/ja01577a001
33. Tu T, Wang Y, Huang H, Wang Y, Jiang X, Wang Z, et al. Improving the Thermostability and Catalytic Efficiency of Glucose Oxidase from Aspergillus niger by Molecular Evolution. *Food Chem* (2019) 281:163–70. doi:10.1016/j.foodchem.2018.12.099
34. Zhang L, Tang X, Cui D, Yao Z, Gao B, Jiang S, et al. A Method to Rationally Increase Protein Stability Based on the Charge-Charge Interaction, with Application to Lipase LipK107. *Protein Sci* (2014) 23(1):110–6. doi:10.1002/pro.2388
35. Cao H, Wang J, He L, Qi Y, and Zhang JZ. DeepDDG: Predicting the Stability Change of Protein Point Mutations Using Neural Networks. *J Chem Inf Model* (2019) 59(4):1508–14. doi:10.1021/acs.jcim.8b00697
36. Musil M, Stourac J, Bendl J, Brezovsky J, Prokop Z, Zendulka J, et al. FireProt: Web Server for Automated Design of Thermostable Proteins. *Nucleic Acids Res* (2017) 45(W1):W393–W399. doi:10.1093/nar/gkx285
37. Banach M, Fabian P, Stapor K, Konieczny L, and Roterman a. I. Structure of the Hydrophobic Core Determines the 3D Protein Structure-Verification by Single Mutation Proteins. *Biomolecules* (2020) 10(5):767. doi:10.3390/biom10050767
38. Paul M, Hazra M, Barman A, and Hazra S. Comparative Molecular Dynamics Simulation Studies for Determining Factors Contributing to the Thermostability of Chemotaxis Protein "CheY". *J Biomol Struct Dyn* (2014) 32(6):928–49. doi:10.1080/07391102.2013.799438
39. Akbulut N, Tuzlakoğlu Öztürk M, Pijning T, İşsever Öztürk S, and Gümüşel F. Improved Activity and Thermostability of Bacillus Pumilus Lipase by Directed Evolution. *J Biotechnol* (2013) 164(1):123–9. doi:10.1016/j.jbiotec.2012.12.016
40. Veno J, Ahmad Kamarudin N, Mohamad Ali M, Masomian M, and Raja Abd. Rahman R. Directed Evolution of Recombinant C-Terminal Truncated Staphylococcus Epidermidis Lipase AT2 for the Enhancement of Thermostability. *Ijms* (2017) 18(11):2202. doi:10.3390/ijms18112202
41. Xie Y, An J, Yang G, Wu G, Zhang Y, Cui L, et al. Enhanced Enzyme Kinetic Stability by Increasing Rigidity within the Active Site. *J Biol Chem* (2014) 289(11):7994–8006. doi:10.1074/jbc.M113.536045
42. Yu H, and Huang H. Engineering Proteins for Thermostability through Rigidifying Flexible Sites. *Biotechnol Adv* (2014) 32(2):308–15. doi:10.1016/j.biotechadv.2013.10.012

43. Yedavalli P, and Madhusudhana Rao N. Engineering the Loops in a Lipase for Stability in DMSO. *Protein Eng Des Sel* (2013) 26(4):317–24. doi:10.1093/protein/gzt002
44. Yu H, Zhao Y, Guo C, Gan Y, and Huang H. The Role of Proline Substitutions within Flexible Regions on Thermostability of Luciferase. *Biochim Biophys Acta (Bba) - Proteins Proteomics* (2015) 1854(1):65–72. doi:10.1016/j.bbapap.2014.10.017
45. Yu H, Yan Y, Zhang C, and Dalby PA. Two Strategies to Engineer Flexible Loops for Improved Enzyme Thermostability. *Sci Rep* (2017) 7:41212. doi:10.1038/srep41212
46. Okoniewska M, Tanaka T, and Yada RY. The Pepsin Residue Glycine-76 Contributes to Active-Site Loop Flexibility and Participates in Catalysis. *Biochem J* (2000) 349(Pt 1):169–77. doi:10.1042/0264-6021:3490169
47. Malabanan MM, Amyes TL, and Richard JP. A Role for Flexible Loops in Enzyme Catalysis. *Curr Opin Struct Biol* (2010) 20(6):702–10. doi:10.1016/j.sbi.2010.09.005
48. Wintrode PL, Zhang D, Vaidehi N, Arnold FH, and Goddard WA. Protein Dynamics in a Family of Laboratory Evolved Thermophilic Enzymes. *J Mol Biol* (2003) 327(3):745–57. doi:10.1016/S0022-2836(03)00147-5
49. Zhang P, Zhang J, Zhang L, Sun J, Li Y, Wu L, et al. Structure-based Design of Agarase AgWH50C from Agarivorans Gilvus WH0801 to Enhance Thermostability. *Appl Microbiol Biotechnol* (2019) 103(3):1289–98. doi:10.1007/s00253-018-9540-1
50. Chen Z, Chen J, Zhang W, Zhang T, Guang C, and Mu W. Improving Thermostability and Catalytic Behavior of L-Rhamnose Isomerase from Caldicellulosiruptor Obsidiansis OB47 toward D-Allulose by Site-Directed Mutagenesis. *J Agric Food Chem* (2018) 66(45):12017–24. doi:10.1021/acs.jafc.8b05107
51. Mu Q, Cui Y, Tian Ye., Hu M, Tao Y, and Wu B. Thermostability Improvement of the Glucose Oxidase from Aspergillus niger for Efficient Gluconic Acid Production via Computational Design. *Int J Biol Macromolecules* (2019) 136:1060–8. doi:10.1016/j.ijbiomac.2019.06.094
52. Xu Z, Cen Y-K, Zou S-P, Xue Y-P, and Zheng Y-G. Recent Advances in the Improvement of Enzyme Thermostability by Structure Modification. *Crit Rev Biotechnol* (2020) 40(1):83–98. doi:10.1080/07388551.2019.1682963
53. Pucci F, Bernaerts KV, Kwasigroch JM, and Rooman M. Quantification of Biases in Predictions of Protein Stability Changes upon Mutations. *Bioinformatics* (2018) 34(21):3659–65. doi:10.1093/bioinformatics/bty348
54. Stimple SD, Smith MD, and Tessier PM. Directed Evolution Methods for Overcoming Trade-Offs between Protein Activity and Stability. *AICHE J* (2020) 66(3). doi:10.1002/aic.168149

Conflict of Interest: The authors declare that the research was conducted in the absence of any commercial or financial relationships that could be construed as a potential conflict of interest.

Publisher's Note: All claims expressed in this article are solely those of the authors and do not necessarily represent those of their affiliated organizations, or those of the publisher, the editors and the reviewers. Any product that may be evaluated in this article, or claim that may be made by its manufacturer, is not guaranteed or endorsed by the publisher.

frontiers in Physics

ORIGINAL RESEARCH
published: 04 October 2021
doi: 10.3389/fphy.2021.740627

Confined Monolayer Ice Between CaF_2 (111) and Graphene: Structure and Stability

*Shi-Qi Li, Shi Qiu, Hongsheng Liu, Maodu Chen and Junfeng Gao**

Key Laboratory of Materials Modification by Laser, Ion and Electron Beams, Dalian University of Technology, Ministry of Education, Dalian, China

Water monolayer can form in layered confined systems. Here, CaF_2 (111) and graphene are chosen as modeling systems to explore the structure and stability of confined monolayer water. First, water molecules tend to intercalate into a confined space between graphene and CaF_2, rather than on a bare surface of graphene. Water molecules can move fast in the confined space due to a low diffusion barrier. These water molecules are likely to aggregate together, forming monolayer ice. Four ice phases including ice II, ice III, ice IV, and ice Ih are compared in this confined system. Intriguingly, all the ice phases undergo very small deformation, indicating the 2D monolayer ice can be stable in the CaF_2–graphene–confined system. Beyond, projected band structures are also plotted to understand the electronic behavior of these confined ice phases. Nearly all the bands originated from confined ices are flat and locate about 2–3 eV below the Fermi level. Binding energy calculations suggest that the stability sequence in this confined system as follows: Ih-up ≈ Ih-down ≈ II < IV < III. Our results bring new insights into the formation of water monolayer production in such a confined condition.

Keywords: structure and stability, confined water, graphene, ice phases, first-principle calculations

OPEN ACCESS

Edited by:
Wenxiang Xu,
Hohai University, China

Reviewed by:
Haifei Zhan,
Zhejiang University, China
Dengfeng Li,
Chongqing University of Posts and Telecommunications, China

****Correspondence:***
Junfeng Gao
gaojf@dlut.edu.cn

Specialty section:
This article was submitted to Condensed Matter Physics, a section of the journal Frontiers in Physics

Received: *13 July 2021*
Accepted: *30 August 2021*
Published: *04 October 2021*

Citation:
Li S-Q, Qiu S, Liu H, Chen M and Gao J (2021) Confined Monolayer Ice Between CaF_2 (111) and Graphene: Structure and Stability. Front. Phys. 9:740627. doi: 10.3389/fphy.2021.740627

INTRODUCTION

The behavior of water at surfaces and a nanoconfined space [1] in two, three, or one dimensions is significantly different from that in bulk ice [2–4]. Understanding the structural tendencies of nanoconfined water is of great interest in biology [5], material science [6–8], nanofluidics [9], tribology, and, most recently, electronics [10, 11]. Because of various possible hydrogen bond networks, the structure of water is notoriously perplexed [12], rising as one of the most challenging issues in the 21st century [13]. The subtle interplay between the water–substrate and water–water interactions brings about many new distinctive ice configurations on different substrates [14–18]. In vacuum and on weakly interacting substrates, Xu et al. [14] found a helical ice monolayer with every six water molecules helically arranged along the normal of the basal plane by performing an intensive structural search based on ab initio calculations. On Au(111), a two-dimensional (2D) interlocked ice consisting of two flat hexagonal water layers in which the hexagons in two sheets are in registry is imaged by non-contact atomic force microscopy and identified by density functional calculations [15].

Except for various types of monolayer ice formed on surfaces, 2D monolayer-confined ice also has drawn much attention due to its relevance to a series of processes in nature and industry [19]. Nevertheless, the structures of 2D monolayer ice under distinct confinements are still under debate.

Recently, by performing scanning probe microscopy (SPM), graphene ultrathin coatings are utilized to assist the visualization of interfacial water adlayers. This made remarkable progress on interfacial water. Xu et al. [20] observed water adlayers on mica coated by monolayer graphene at room temperature by using atomic force microscopy. The graphene coating can stably "fix" the water adlayer structures, thus permitting the detection of the structure of the first water adlayers under ambient conditions [21]. Therefore, the presence of ambient water adlayers between graphene [19] and various substrates, including mica [11, 21–24], SiO_2 [25, 26], BaF_2 [27], SiC [28], sapphire [29], Ni [30], Ru, Cu [31], and Si [32], has been widely studied by experimental probing techniques. Taking mica as an example, the structure of the first wetting adlayer confined between graphene and mica is unique, quite different from ice Ih, due to strong mica–water interaction [21]. The structural characteristics of intercalated water adlayers between graphene and mica under a thermal treatment were also investigated by Ochedowski et al [22]. They showed that the intercalated water adlayers are partially removed under mild heating (200°C), and the defect density increases, leading to "nanoblister" formation at a temperature of 600°C, causing a transition from the p-type to n-type for graphene layers [22].

CaF_2 (111)/graphene is an excellent platform to trap water molecules and generate confined ice layers. Recently, the formation of a several monolayer thick hydration layer on a graphene-coated hydrophilic substrate CaF_2 (111) was revealed [33]. The first layer is so stable that it cannot be removed upon heating. After this, hydration layers confined between graphene and the CaF_2 substrate were found to electronically modify graphene as the material's electron density transfers from graphene to the hydration layer [34]. However, the structure and stability of monolayer ice confined between CaF_2 (111) and graphene remain unclear. In an experiment, many factors can influence the hydration layers and properties of graphene [35], such as the types of adhesive tapes [23], other adsorbents [22], and additives. So a theoretical study on structural information and stability of water confined between graphene and CaF_2 at the atomic level is urgently needed.

In this study, the structure and stability of monolayer ice confined between CaF_2 (111) and graphene are investigated systematically based on first-principles calculations. Water molecules tend to aggregate together to form monolayer ice. A water molecule will automatically move to the "edge" of the top surface of the ice layer, promoting monolayer ice growth and prohibiting multilayer nucleation. Beyond, the energy barrier for water diffusion between CaF_2 (111) and graphene is very low. Thus, water molecule can move freely and connect with each other into a monolayer ice between CaF_2 (111) and graphene. Four probable ice phase structures including ice II, ice III, ice IV, and ice Ih are studied in our confined system. All the ice phases are maintained with only small deformations in the CaF_2–graphene–confined system. Binding energy suggests that the most stable monolayer ice confined between CaF_2 (111) and graphene is phase-III. Confined ice III is thermodynamically stable under a wide temperature and pressure span according to the calculated phase diagram. Furthermore, the band structures of these systems are plotted to explore the electronic properties of confined ice phases. The bands originated from confined ice are flat and locate about 2–3 eV below the Fermi level.

METHODS

All the first-principles calculations are based on the DFT, which is implanted in the Vienna ab initio simulation package code (VASP) [36]. The Perdew–Burke–Ernzerhof version of the generalized gradient approximation (GGA-PBE) was chosen as the exchange-correlation functional [37] along with the dispersion correction introduced by Grimme (PBE + D3) [38]. In this work, all atoms were fully relaxed using DFT with vdW correction to obtain the equilibrium distance. The electron wave functions are solved with plane wave basis set in conjunction with pseudo potentials by the projector augmented wave (PAW) method [39]. The K points in the first Brillouin zone (BZ) are generated in the form of a Monkhorst–Pack $4 \times 4 \times 1$ grid [40]. A 500 eV kinetic cutoff energy was used for the plane wave basis. The structure of water confined between CaF_2 (111) and graphene were optimized using standard local optimization algorithms with convergence criteria of 10^{-4} eV for both electronic and ionic relaxation. In our CaF_2 surface slab, there is a net dipole along the Z direction, which will introduce an artificial electric field in calculations with periodic boundary conditions (PBC), and the dipole correction scheme introduced by Neugebauer and Scheffler is applied in all calculations [41, 42]. To avoid spurious interactions between neighboring structures in the tetragonal supercell, a vacuum layer of 25 Å was included in all non-periodic directions.

The surface lattice of CaF_2 (111) is 3.86 Å, which is in good agreement with prior studies, and the CaF_2 (111) surface slab is terminated with fluorine atoms and composed by two F-Ca-F triple layers. The lattice of graphene is 2.46 Å. All the ice structures including ice II, ice III, and ice IV are from MD simulations [43], which will be intercalated between CaF_2 (111) and graphene. We choose 4×4 CaF_2 (111)/3×3 ice II/6×6 graphene, 3×3 CaF_2 (111)/2×2 ice III/5×5 graphene, 4×4 CaF_2 (111)/$1 \times \sqrt{3}$ ice IV/6×6 graphene, and 4×4 CaF_2 (111)/3×3 ice Ih/6×6 graphene to construct the confined systems. The lattice mismatch of these supercells is 4.4, 5.9, 8.1, and 8.1% for CaF_2 (111)/ice II/graphene, CaF_2 (111)/ice III/graphene, CaF_2 (111)/ice IV/graphene, and CaF_2 (111)/ice Ih/graphene, respectively.

Water molecule diffusion barriers are calculated *via* the climbing image–nudged elastic band (CI-NEB) [44] method. This technique can efficiently map the minimum energy path and find the saddle points between two given local minima for the system. Six intermediate images are used in CI-NEB calculations. Each image was relaxed until the forces on the atom were less than 0.02 eV/Å.

The binding energies of monolayer ice phases between the CaF_2 and the graphene system are calculated as follows:

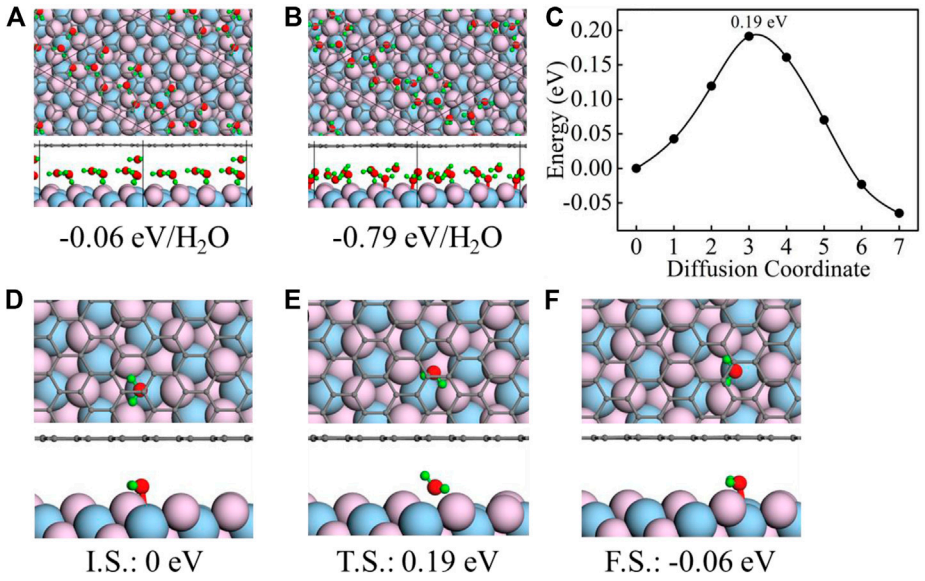

FIGURE 1 | Initial **(A)** and final **(B)** geometric structures for the stratification test along with their corresponding binding energies. **(C)** Calculated energy barriers for water molecule diffusion between CaF_2 (111) and graphene. **(D–F)** Top- and side-view geometric structures of the initial state (I.S.) **(D)**, transition state (T.S.) **(E)**, and final state (F.S.) **(F)** of water molecule diffusion between CaF_2 (111) and graphene. The total energies for I.S., T.S., and F.S. are all denoted in the bottom as a reference of I.S. In all panels, the black, red, green, flesh pink, and light blue spheres represent the C, O, H, F, and Ca atoms, respectively.

$$E_b = [\mathrm{E(Total)} - \mathrm{E}(CaF_2) - \mathrm{E(Graphene)} - \mathrm{N}(H_2O) * \mathrm{E}(H_2O)]/\mathrm{N}(H_2O), \quad (1)$$

where E(Total), E(CaF_2), E(Graphene), and E(H_2O) is total energy of the CaF_2/H_2O/graphene system, a clean CaF_2(111), graphene sheet, and an isolated water molecule, respectively.

RESULTS AND DISCUSSION

Stratification Test and NEB Calculations

CaF_2 (111)–graphene is an excellent platform to trap water [33, 34]. These water molecules are likely to aggregate together forming monolayer connecting with each other by hydrogen bonding. We perform stratification test to make certain the confined ice is monolayer or not. As shown in **Figure 1A**, we put a water molecule on top of the monolayer water structure confined between CaF_2 (111) and graphene. After optimization, the water molecule move to the edge of the existing water structure forming a new monolayer (**Figure 1B**). This process is barrierless, during which the binding energy decrease by 0.73 eV/H_2O. Therefore, the confined ice between CaF_2 (111) and graphene must be monolayer.

Furthermore, the water molecule diffusion between CaF_2 (111) and graphene is investigated using the CI-NEB method. As shown in **Figure 1C**, the water diffusion energy barrier is 0.19 eV from initial adsorption local minima (I.S., **Figure 1D**) to final adsorption local minima (F.S., **Figure 1F**). During this process, the water molecule is first locates on the top of Ca atom (**Figure 1D**), then moves to the hollow site (**Figure 1E**), and finally locates on the top of the neighboring Ca atom (**Figure 1F**). Choosing the total energy of the I.S. system as a reference, the energy of F.S. and T.S. are all listed in the **Figures 1E,F** (0.19 eV and −0.06 eV). The speed of water diffusion can be characterized by the water diffusion coefficient D_{H_2O} which can be estimated from the diffusion barriers by the following formula:

$$D_{H_2O} = a^2 \nu exp\left(\frac{-\Delta E}{K_B T}\right), \quad (2)$$

where a is the distance of the hop along the diffusion pathway and ν is the attempt frequency, about 10^{13} Hz, which is generally in the range of phonon frequencies [45, 46]. ΔE is the diffusion energy barrier [45]. K_B is the Boltzmann constant and T represents the temperature. According to the diffusion results, at room temperature (T = 300 K), the water diffusion coefficient D_{H_2O} is calculated as 8.35×10^{-6} cm^2/s. The low diffusion energy barrier and high diffusion speed of water molecule provide strong evidence for monolayer ice formation between CaF_2 (111) and graphene.

Structure and Stability of Confined Ice

Four monolayer ice phases including Ice II [43], III [43], IV [43], and Ih are intercalated between CaF_2 (111) and graphene. All the free-standing structures of the four ice phases are depicted in the **Supplementary Figure S1** in Supporting Information. For ice I_h, two cases in which H atoms pointing to CaF_2 (Ih-down) or graphene (Ih-up) are all considered. The optimized results are shown in the **Figures 2A–E**.

The monolayer ice II has a planar hexagonal morphology, and it is made up of two kinds of water molecules with different orientations. The plane of every water molecule is perpendicular to the planes of three nearest-neighbor molecules. Besides, the

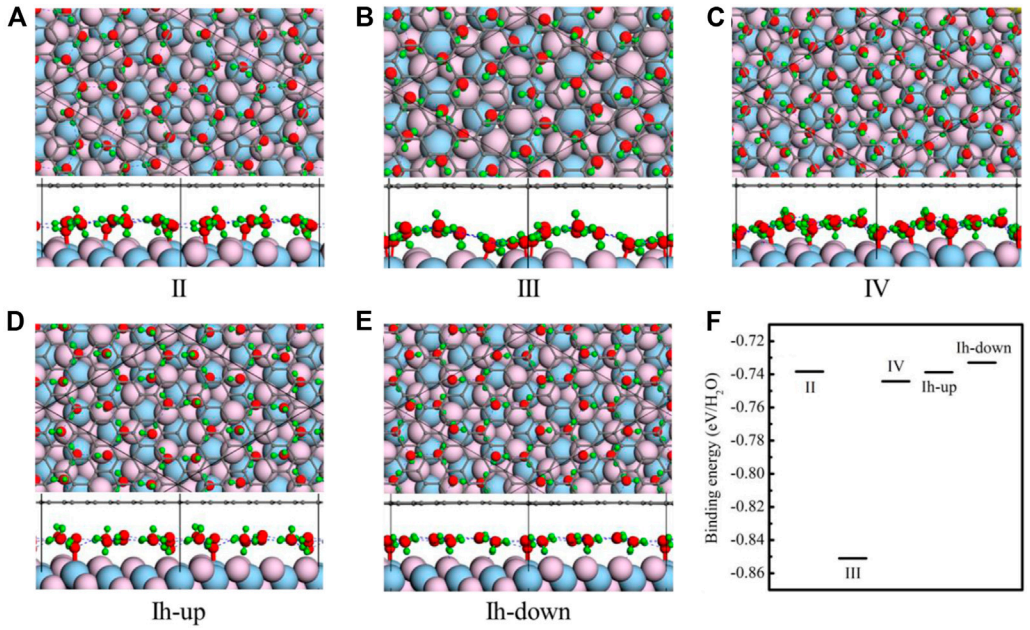

FIGURE 2 | Structures of five ice phases including ice II **(A)**, III **(B)**, IV **(C)**, and Ih **(D,E)** confined between CaF_2(111) and graphene. According to the different orientations of OH, ice Ih can be classified into two kinds. In all panels, the black, red, green, flesh pink, and light blue spheres represent the C, O, H, F, and Ca atoms, respectively. **(F)** The binding energies of monolayer ice phases between the CaF_2 and the graphene system. Light blue spheres represent the C, O, H, F, and Ca atoms, respectively.

monolayer ice II displays considerable net polarization because all the dipole vectors of water molecules are parallel to the longest diagonal of a hexagon. As shown in **Figure 2A**, under confinement of graphene and CaF_2 (111), the structural motifs of ice II change slightly. The location and orientation of water molecule whose plane is parallel with the CaF_2 (111) is nearly unchanged. Nevertheless, those water molecules whose plane is vertical with CaF_2 (111) rotates slightly to form hydrogen bonds with F atoms. The unit cell is still the six-numbered planar ring, and the hydrogen bond network is the same with ice II which satisfy the ice rule.

Different from ice II, monolayer ice III is composed of planar rhombic rings and all the water molecules tilt with respect to the plane of oxygen. When intercalated into CaF_2 (111) and graphene, it distorts slightly. The four-membered unit cell almost remains unchanged, but the orientations of water molecules become disorganized and delamination appears. Unlike ice II-III, oxygen atoms of ice IV are in alternative ridges with different height in the normal direction. Under confinement, the unit cell of ice IV also changes from rhombic to four-and five-membered rings (**Figure 2C**).

Ice Ih is also intercalated into the CaF_2 (111) and graphene. Two cases of ice Ih are tried as shown in **Figures 2D,E**. In the **Figure 2D**, all the hydrogen atoms are pointing to the graphene coating, while in the **Figure 2E**, all the hydrogen atoms are pointing to the CaF_2(111). These two ice configurations are called "Ih-up" and "Ih-down," respectively. In the two cases, the ice structure nearly remains unchanged. The hydrogen atoms tend to point to the CaF_2 (111), so in the structure of "Ih-up," some water molecules rotate to point to the CaF_2 (111).

To further determine the stability of these monolayer ice phases when they are confined between CaF_2 (111) and the graphene system, the binding energies of monolayer ice phases between the CaF_2 and the graphene system are calculated *via* **Eq. 1**. The results are shown in **Figure 2F**. Clearly, the stability sequence is: III (−0.851 eV/H_2O) > IV (−0.744 eV/H_2O) > II (−0.738 eV/H_2O) ≈ Ih-up (−0.739 eV/H_2O) ≈ Ih-down (−0.733 eV/H_2O). Intriguingly, ice III possesses largest binding energy (−0.85 eV/H_2O), demonstrating its high stability confined between CaF_2 (111) and graphene. Moreover, we have also tried several amorphous water structures in this confined system by random distributing the water molecules. As shown in **Supplementary Figure S2**, the amorphous water layers retain a monolayer character. But these two amorphous structures are less stable than ordered ice phases. The stability sequence is: III (−0.851 eV/H_2O) > IV (−0.744 eV/H_2O) > II (−0.738 eV/H_2O) ≈ Ih-up (−0.739 eV/H_2O) ≈ Ih-down (−0.733 eV/H_2O) > Amor-1 (**Supplementary Figure S2A**) (−0.65 eV/H_2O) > Amor-2 (**Supplementary Figure S2B**) (−0.55 eV/H_2O).

To understand the stability and structural properties through electronic properties, the band structures of the CaF_2/graphene system and five ice phases confined between CaF_2 (111) and graphene are presented in **Figures 3A–F**, respectively. Due to the different size of the graphene's supercell, the location of Dirac cone is distinct. The contribution from graphene and CaF_2 (111) is plotted in **Figure 3A**. Before ice intercalation, the gap of CaF_2 (111) bands is about 6.35 eV; while in the ice confined systems, the gap changes slightly, in the range of (5.5, 6.18) eV. Additionally, in CaF_2 (111)/II/graphene and CaF_2 (111)/Ih-down/graphene, the CaF_2 (111) bands both move downward probably because most H atoms point to the CaF_2 (111) surface. The contribution to each band from ice phases

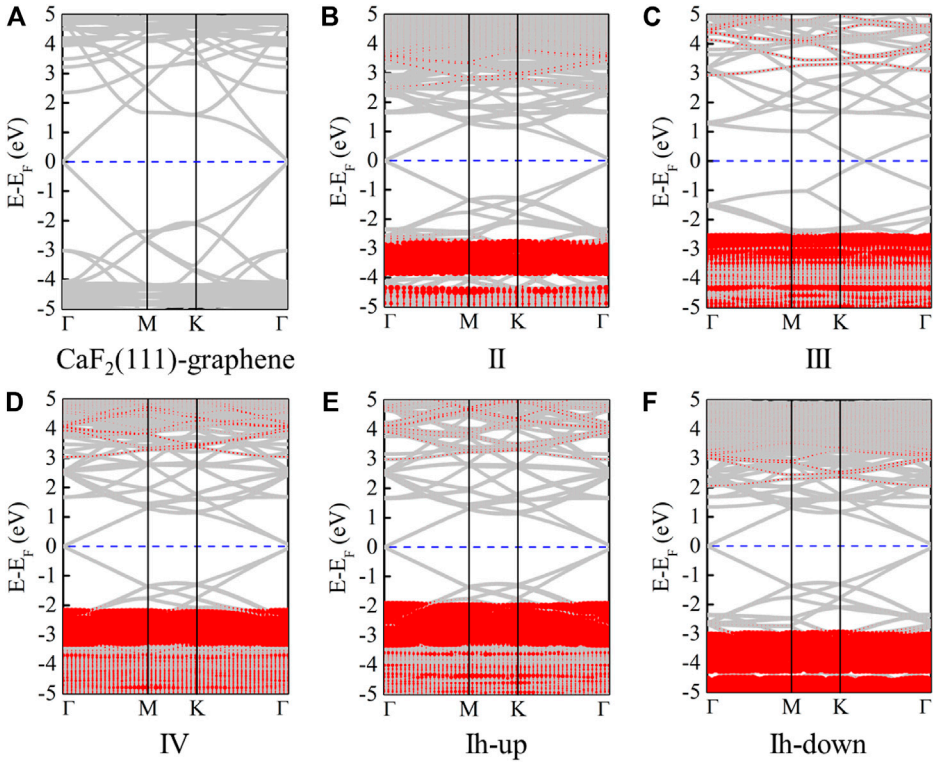

FIGURE 3 | Band structures of CaF_2 (111)/graphene **(A)**, CaF_2 (111)/II/graphene **(B)**, CaF_2 (111)/III/graphene **(C)**, CaF_2 (111)/IV/graphene **(D)**, CaF_2 (111)/Ih-up/graphene **(E)**, and CaF_2 (111)/Ih-down/graphene **(F)**, respectively. Here, the red parts represent the contribution from monolayer ice. The Fermi levels are set to zero and indicated by the blue line.

are all depicted in **Figures 3B–F**. For these five ice phases, band dispersion is very flat along the high symmetry directions in the Brillouin zone. Besides, the ice bands are all located at the deep energy level at least 2–3 eV lower than the Fermi level. Similarly, due to the orientation of H atoms, the locations of bands originated from ice II and ice Ih-down are the deepest among these five ice phases [(−3.79, −2.93) (−5.36, −3.02) eV].

Phase Diagram

Binding energy results demonstrate the highly kinetic stability of ice III; nevertheless, under real environment, the water pressure and temperature must be considered. Based on first-principles thermodynamic calculations [47–50], the free Gibbs energy change ΔG of the CaF_2 (111)/ice III/graphene confined system is defined as:

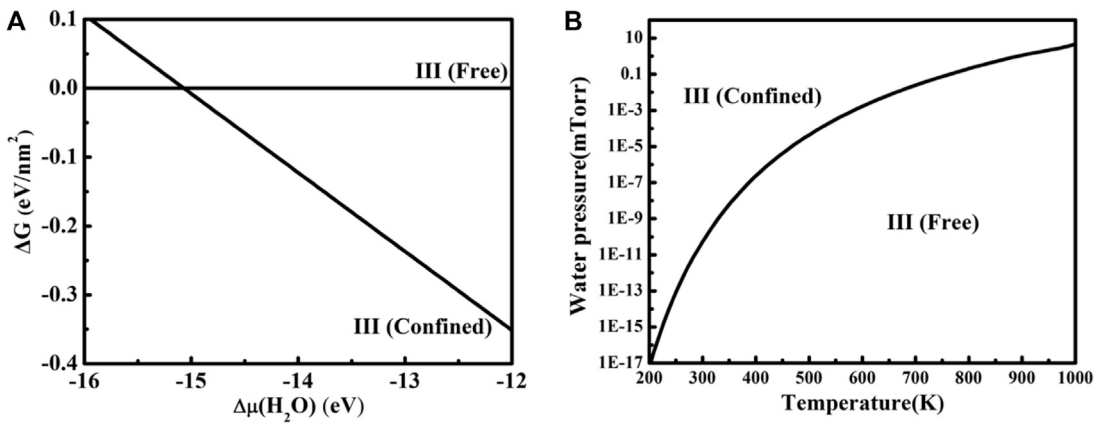

FIGURE 4 | (A) Gibbs free energy change ΔG for freestanding ice III and the CaF_2 (111)/ice III/graphene system *versus* the chemical potential change of the gas water molecule. **(B)** The phase diagram for free standing ice III and the CaF_2 (111)/ice III/graphene system under different P and T.

$$\Delta G = \left[E(\text{Total}) - E(CaF_2) - E(\text{Graphene}) - N(H_2O) * \Delta\mu(H_2O)\right]/A, \quad (3)$$

where $E(\text{Total})$, $E(CaF_2)$, $E(\text{Graphene})$, and $E(H_2O)$ is total energy of the CaF_2/H_2O/graphene system, clean CaF_2 (111), graphene sheet, and isolated water molecule, respectively. A is the surface area and $N(H_2O)$ is the number of the water molecules included in the ice phases. $\Delta\mu(H_2O)$ is the chemical potentials of water in gas phase, which can be associated with the DFT results and experimental thermodynamic data, as follows:

$$\Delta\mu(H_2O) = E(H_2O) + \mu_g(P^0, T) - K_b T ln\left[P_g(H_2O)/P^0\right], \quad (4)$$

where P^0 = 1 bar and the $\mu_g(P_0, T)$ represents the standard chemical potential of gas water, which can be obtained from standard thermodynamic tables [51].

The free Gibbs energy change ΔG of freestanding ice III [III(free)] and the CaF_2(111)/ice III/graphene [III(confined)] system is depicted in **Figure 4A** using **Eq. 3**. When $\Delta\mu(H_2O)$ is lower than −15.07 eV, ice III is not likely to be confined between CaF_2(111) and graphene. On the contrary, the confined system will be more favorable. According to **Eq. 4** and the phase transition value of $\Delta\mu(H_2O)$ obtained from **Figure 4B**, a two-dimensional (*T, P*) phase diagram is further plotted. Ice III tends to be confined between CaF_2 (111) and graphene under a wide T and P span. For example, at room temperature, confined ice III is more thermodynamically favorable when the water pressure is larger than 10^{-10} mTorr. However, the condition for freestanding ice III is harsh, often under ultra-high vacuum. Noted that all our configurations were obtained without compression, applying the compression to reduce the layer distance between graphene and CaF_2 could further tune the structure and stability of water layer, which deserves comprehensive study in the future.

CONCLUSION

In conclusion, we have theoretically studied the structure and stability of monolayer ice phases confined between CaF_2 (111) and graphene. The stratification test and CI-NEB calculations demonstrate the possibility of monolayer ice formation in the CaF_2 (111) and graphene system. Therefore, five systems including monolayer ice II, III, IV, I_h-up, and I_h-down confined between CaF_2(111) and graphene are considered. After optimization, all the ice phases undergo very small deformation, indicating that the 2D monolayer ice can be stable in the CaF_2–graphene–confined system. The electronic properties of these five systems are calculated. Nearly all the bands originated from confined ice are flat and locate about 2–3 eV below the Fermi level. By comparing the binding energy of five systems, the stability sequence is identified as: III > IV > II ≈ Ih-up ≈ Ih-down. Beyond, based on first-principles thermodynamic calculations, a two-dimensional (*T*, *P*) phase diagram for III(free) and III(confined) is further plotted. Ice III tends to be confined between CaF_2 (111) and graphene under a wide T and P range.

DATA AVAILABILITY STATEMENT

The raw data supporting the conclusions of this article will be made available by the authors, without undue reservation.

AUTHOR CONTRIBUTIONS

JG and S-QL proposed this study. S-QL and SQ performed simulation. JG, HL, and MC conducted the studies and discussed the result. All authors wrote and revised this paper.

FUNDING

This work was financially supported by the National Natural Science Foundation of China (Nos. 12074053, 91961204, and 11664028) and by Xin Liao Ying Cai Project of the Liaoning Province, China (XLYC1907163). JG thanks the Start-Up grant of DUT (DUT20RC(5)026).

ACKNOWLEDGMENTS

We also acknowledge the computers supporting from the Shanghai Supercomputer Center, the DUT supercomputing Center, and Tianhe supercomputer of Tianjin Center.

SUPPLEMENTARY MATERIAL

The Supplementary Material for this article can be found online at: https://www.frontiersin.org/articles/10.3389/fphy.2021.740627/full#supplementary-material

REFERENCES

1. Soper AK. THERMODYNAMICS: Enhanced: Water and Ice. *Science* (2002) 297:1288–9. doi:10.1126/science.297.5585.1288
2. Zangi R, and Mark AE. Monolayer Ice. *Phys Rev Lett* (2003) 91:025502. doi:10.1103/PhysRevLett.91.025502
3. Qiu H, and Guo W. Electromelting of Confined Monolayer Ice. *Phys Rev Lett* (2013) 110:195701. doi:10.1103/physrevlett.110.195701
4. Chen J, Schusteritsch G, Pickard CJ, Salzmann CG, and Michaelides A. Two Dimensional Ice from First Principles: Structures and Phase Transitions. *Phys Rev Lett* (2016) 116:025501. doi:10.1103/PhysRevLett.116.025501
5. Rasaiah JC, Garde S, and Hummer G. Water in Nonpolar Confinement: from Nanotubes to Proteins and beyond. *Annu Rev Phys Chem* (2008) 59:713–40. doi:10.1146/annurev.physchem.59.032607.093815
6. Asay DB, and Kim SH. Evolution of the Adsorbed Water Layer Structure on Silicon Oxide at Room Temperature. *J Phys Chem B* (2005) 109(35):16760–3. doi:10.1021/jp053042o

7. Zhang Y, Nappini S, Sankar R, Bondino F, Gao J, and Politano A. Assessing the Stability of Cd3As2 Dirac Semimetal in Humid Environments: the Influence of Defects, Steps and Surface Oxidation. *J Mater Chem C* (2021) 9:1235–44. doi:10.1039/d0tc04883f
8. Centi G. Smart Catalytic Materials for Energy Transition. *SmartMat* (2020) 1: e1005. doi:10.1002/smm2.1005
9. Giovambattista N, Rossky PJ, and Debenedetti PG. Effect of Pressure on the Phase Behavior and Structure of Water Confined between Nanoscale Hydrophobic and Hydrophilic Plates. *Phys Rev E Stat Nonlin Soft Matter Phys* (2006) 73:041604. doi:10.1103/PhysRevE.73.041604
10. Jang C, Adam S, Chen J-H, Williams ED, Das Sarma S, and Fuhrer MS. Tuning the Effective fine Structure Constant in Graphene: Opposing Effects of Dielectric Screening on Short- and Long-Range Potential Scattering. *Phys Rev Lett* (2008) 101:146805. doi:10.1103/physrevlett.101.146805
11. Shim J, Lui CH, Ko TY, Yu Y-J, Kim P, Heinz TF, et al. Water-gated Charge Doping of Graphene Induced by Mica Substrates. *Nano Lett* (2012) 12:648–54. doi:10.1021/nl2034317
12. Li S-Q, Chang Y, Zhang Z, Liu H, Chen M, Han Y, et al. Evolution of Water Layer Adsorption on the GaN(0001) Surface and its Influence on Electronic Properties. *J Phys Chem C* (2021) 125:667–74. doi:10.1021/acs.jpcc.0c10256
13. So Much More to Know. *Science*. (2005) 309: 78–102. doi:10.1126/science.309.5731.78b
14. Xu Y, Xuan X, Zhang Z, and Guo W. A Helical Monolayer Ice. *J Phys Chem Lett* (2020) 11:3860–5. doi:10.1021/acs.jpclett.0c01129
15. Ma R, Cao D, Zhu C, Tian Y, Peng J, Guo J, et al. Atomic Imaging of the Edge Structure and Growth of a Two-Dimensional Hexagonal Ice. *Nature* (2020) 577:60–3. doi:10.1038/s41586-019-1853-4
16. Chen J, Guo J, Meng X, Peng J, Sheng J, Xu L, et al. An Unconventional Bilayer Ice Structure on a NaCl(001) Film. *Nat Commun* (2014) 5:4056. doi:10.1038/ncomms5056
17. Nie S, Feibelman PJ, Bartelt NC, and Thürmer K. Pentagons and Heptagons in the First Water Layer on Pt(111). *Phys Rev Lett* (2010) 105:026102. doi:10.1103/PhysRevLett.105.026102
18. Yang J, Meng S, Xu LF, and Wang EG. Ice Tessellation on a Hydroxylated Silica Surface. *Phys Rev Lett* (2004) 92:146102. doi:10.1103/physrevlett.92.146102
19. Algara-Siller G, Lehtinen O, Wang FC, Nair RR, Kaiser U, Wu HA, et al. Square Ice in Graphene Nanocapillaries. *Nature* (2015) 519:443–5. doi:10.1038/nature14295
20. Xu K, Cao P, and Heath JR. Graphene Visualizes the First Water Adlayers on Mica at Ambient Conditions. *Science* (2010) 329:1188–91. doi:10.1126/science.1192907
21. Matheswaran P, Gokul B, Abhirami KM, and Sathyamoorthy R. Thickness Dependent Structural and Optical Properties of In/Te Bilayer Thin Films. *Mater Sci Semiconductor Process* (2012) 15:486–91. doi:10.1016/j.mssp.2012.03.006
22. Ochedowski O, Bussmann BK, and Schleberger M. Graphene on Mica - Intercalated Water Trapped for Life. *Sci Rep* (2014) 4:6003. doi:10.1038/srep06003
23. Rezania B, Dorn M, Severin N, and Rabe JP. Influence of Graphene Exfoliation on the Properties of Water-Containing Adlayers Visualized by Graphenes and Scanning Force Microscopy. *J Colloid Interf Sci* (2013) 407:500–4. doi:10.1016/j.jcis.2013.06.034
24. Severin N, Lange P, Sokolov IM, and Rabe JP. Reversible Dewetting of a Molecularly Thin Fluid Water Film in a Soft Graphene-Mica Slit Pore. *Nano Lett* (2012) 12:774–9. doi:10.1021/nl2037358
25. Lee D, Ahn G, and Ryu S. Two-Dimensional Water Diffusion at a Graphene-Silica Interface. *J Am Chem Soc* (2014) 136:6634–42. doi:10.1021/ja4121988
26. Lee MJ, Choi JS, Kim J-S, Byun I-S, Lee DH, Ryu S, et al. Characteristics and Effects of Diffused Water between Graphene and a SiO2 Substrate. *Nano Res* (2012) 5:710–7. doi:10.1007/s12274-012-0255-9
27. Verdaguer A, Segura JJ, López-Mir L, Sauthier G, and Fraxedas J. Communication: Growing Room Temperature Ice with Graphene. *J Chem Phys* (2013) 138:121101. doi:10.1063/1.4798941
28. Kazakova O, Panchal V, and Burnett T. Epitaxial Graphene and Graphene-Based Devices Studied by Electrical Scanning Probe Microscopy. *Crystals* (2013) 3:191–233. doi:10.3390/cryst3010191
29. Komurasaki H, Tsukamoto T, Yamazaki K, and Ogino T. Layered Structures of Interfacial Water and Their Effects on Raman Spectra in Graphene-On-Sapphire Systems. *J Phys Chem C* (2012) 116:10084–9. doi:10.1021/jp301402u
30. Xu Z, Ao Z, Chu D, Younis A, Li CM, and Li S. Reversible Hydrophobic to Hydrophilic Transition in Graphene *via* Water Splitting Induced by UV Irradiation. *Sci Rep* (2014) 4:6450. doi:10.1038/srep06450
31. Feng X, Maier S, and Salmeron M. Water Splits Epitaxial Graphene and Intercalates. *J Am Chem Soc* (2012) 134:5662–8. doi:10.1021/ja3003809
32. Ochedowski O, Begall G, Scheuschner N, El Kharrazi M, Maultzsch J, and Schleberger M. Graphene on Si(111)7×7. *Nanotechnology* (2012) 23:405708. doi:10.1088/0957-4484/23/40/405708
33. Temmen M, Ochedowski O, Schleberger M, Reichling M, and Bollmann TRJ. Hydration Layers Trapped between Graphene and a Hydrophilic Substrate. *New J Phys* (2014) 16:053039. doi:10.1088/1367-2630/16/5/053039
34. Bollmann TRJ, Antipina LY, Temmen M, Reichling M, and Sorokin PB. Hole-doping of Mechanically Exfoliated Graphene by Confined Hydration Layers. *Nano Res* (2015) 8:3020–6. doi:10.1007/s12274-015-0807-x
35. Xu J, Cui X, Liu N, Chen Y, and Wang HW. Structural Engineering of Graphene for High-resolution Cryo-electron Microscopy. *SmartMat* (2021) 2: 202–12. doi:10.1002/smm2.1045
36. Kresse G, and Furthmüller J. Efficient Iterative Schemes Forab Initiottotal-Energy Calculations Using a Plane-Wave Basis Set. *Phys Rev B* (1996) 54: 11169–86. doi:10.1103/physrevb.54.11169
37. Perdew JP, Burke K, and Ernzerhof M. Generalized Gradient Approximation Made Simple. *Phys Rev Lett* (1996) 77:3865–8. doi:10.1103/PhysRevLett.77.3865
38. Grimme S, Antony J, Ehrlich S, and Krieg H. A Consistent and Accurate Ab Initio Parametrization of Density Functional Dispersion Correction (DFT-D) for the 94 Elements H-Pu. *J Chem Phys* (2010) 132:154104. doi:10.1063/1.3382344
39. Kresse G, and Joubert D. From Ultrasoft Pseudopotentials to the Projector Augmented-Wave Method. *Phys Rev B* (1999) 59:1758–75. doi:10.1103/physrevb.59.1758
40. Monkhorst HJ, and Pack JD. Special Points for Brillouin-Zone Integrations. *Phys Rev B* (1976) 13:5188–92. doi:10.1103/physrevb.13.5188
41. Neugebauer J, and Scheffler M. Adsorbate-substrate and Adsorbate-Adsorbate Interactions of Na and K Adlayers on Al(111). *Phys Rev B* (1992) 46:16067–80. doi:10.1103/physrevb.46.16067
42. Krukowski S, Kempisty P, and Strąk P. Electrostatic Condition for the Termination of the Opposite Face of the Slab in Density Functional Theory Simulations of Semiconductor Surfaces. *J Appl Phys* (2009) 105: 113701. doi:10.1063/1.3130156
43. Zhao W-H, Wang L, Bai J, Yuan L-F, Yang J, and Zeng XC. Highly Confined Water: Two-Dimensional Ice, Amorphous Ice, and Clathrate Hydrates. *Acc Chem Res* (2014) 47:2505–13. doi:10.1021/ar5001549
44. Henkelman G, Uberuaga BP, and Jónsson H. A Climbing Image Nudged Elastic Band Method for Finding Saddle Points and Minimum Energy Paths. *J Chem Phys* (2000) 113:9901–4. doi:10.1063/1.1329672
45. Kang K, Morgan D, and Ceder G. First Principles Study of Li Diffusion in I-Li_2NiO_2 Structure. *Phys Rev B* (2009) 79:014305. doi:10.1103/physrevb.79.014305
46. Morgan D, Van der Ven A, and Ceder G. Li Conductivity in Li[sub x]MPO[sub 4] (M = Mn, Fe, Co, Ni) Olivine Materials. *Electrochem Solid-state Lett* (2004) 7:A30. doi:10.1149/1.1633511
47. Kowalski PM, Meyer B, and Marx D. Composition, Structure, and Stability of the rutileTiO2(110)surface: Oxygen Depletion, Hydroxylation, Hydrogen Migration, and Water Adsorption. *Phys Rev B* (2009) 79:115410. doi:10.1103/physrevb.79.115410
48. Li W, Zhao J, Zhu Q, and Wang D. Insight into the Initial Oxidation of 4H-SiC from First-Principles Thermodynamics. *Phy Rev B* (2013) 87:085320. doi:10.1103/physrevb.87.085320
49. Reuter K, and Scheffler M. First-principles Atomistic Thermodynamics for Oxidation Catalysis: Surface Phase Diagrams and Catalytically Interesting Regions. *Phys Rev Lett* (2003) 90:046103. doi:10.1103/PhysRevLett.90.046103
50. Zhang W, Wu P, Li Z, and Yang J. First-principles Thermodynamics of Graphene Growth on Cu Surfaces. *J Phys Chem C* (2011) 115:17782–7. doi:10.1021/jp2006827

51. Chase JMW. *NIST-JANAF Thermochemical Tables*. 4th ed. New York: American Institute of Physics (1998).

Conflict of Interest: The authors declare that the research was conducted in the absence of any commercial or financial relationships that could be construed as a potential conflict of interest.

Publisher's Note: All claims expressed in this article are solely those of the authors and do not necessarily represent those of their affiliated organizations, or those of the publisher, the editors, and the reviewers. Any product that may be evaluated in this article, or claim that may be made by its manufacturer, is not guaranteed or endorsed by the publisher.

frontiers in Physics

MINI REVIEW
published: 29 November 2021
doi: 10.3389/fphy.2021.755597

Physical Intuition to Improve Electronic Properties of Thermoelectrics

Wei Yang Samuel Lim[1], *Danwei Zhang*[1], *Solco Samantha Faye Duran*[1], *Xian Yi Tan*[1], *Chee Kiang Ivan Tan*[1], *Jianwei Xu*[1] *and Ady Suwardi*[1,2]*

[1]*Institute of Materials Research and Engineering, Agency for Science, Technology and Research, Singapore, Singapore,* [2]*Department of Materials Science and Engineering, National University of Singapore, Singapore, Singapore*

Thermoelectrics convert heat to electricity and vice versa. They are of technological importance in cooling and energy harvesting. Their performances are defined by figure of merit, *zT*. Decades of studies have largely focused on the development of novel and advanced materials reaching higher performance in devices. To date, the lack of sufficiently high-performance thermoelectrics, especially among Earth-abundant and lightweight materials, is one of the reasons why there is no broad commercial application of thermoelectric devices yet. This challenge is due to the complex correlations of parameters that make up the *zT*. Theoretical estimation can reveal the optimal charge carrier concentration, which can provide a good idea of doping compositions. Depending on the material characteristics, decoupling these intercorrelated parameters could be viable. Broadly speaking, increasing carrier mobility, inducing a large fluctuation in density of states (DOS) at the Fermi level, and lowering the lattice thermal conductivity lead to better thermoelectric performance. In this mini review, we provide a broad picture of electronic property optimization for thermoelectric materials. This work will be a useful guide to quickly take readers to the forefront of thermoelectric research.

Keywords: thermoelectrics, thermal transport, electronic transport, semiconductor, energy harvesting

OPEN ACCESS

Edited by:
Wenxiang Xu,
Hohai University, China

Reviewed by:
Bhuvanesh Srinivasan,
National Institute for Materials Science, Japan
Yun Zheng,
Jianghan University, China

***Correspondence:**
Ady Suwardi
ady_suwardi@imre.a-star.edu.sg

Specialty section:
This article was submitted to Condensed Matter Physics, a section of the journal Frontiers in Physics

Received: *09 August 2021*
Accepted: *29 October 2021*
Published: *29 November 2021*

Citation:
Lim WYS, Zhang D, Duran SSF, Tan XY, Tan CKI, Xu J and Suwardi A (2021) Physical Intuition to Improve Electronic Properties of Thermoelectrics. Front. Phys. 9:755597. doi: 10.3389/fphy.2021.755597

INTRODUCTION

In this era of rapid technological developments, more can be done to combat the climate change due to overconsumption of energy. As one of the potential alternative energy technologies, thermoelectric (TE) materials, which convert waste heat to electricity, are gaining increasing attention [1–8]. In general, a TE module is made of n- and p-type materials that are electrically connected in a series circuit, while the heat gradients applied are parallel to the device.

TE generators have been used for decades in space and automotive applications, especially high-temperature TEs [9–16], and recently in wearable electronic devices [17]. However, the efficiency of TE generators needs to be improved for commercialization. To date, the highest module efficiency achieved is ~12% with Bi_2Te_3-based materials of at least $zT \sim 1.5$ [18–22]. **Figure 1A** shows a progressive overview of research based on thermoelectric performance since the year 1960, as well as the main physical driving force behind the developments. In addition, low-dimensional TEs such as thin films and 2D materials are also popular [23]. **Figure 1B** illustrates the complexity of components that influences the dimensionless figure of merit, *zT*. The parameters that can be experimentally measured are highlighted as green in the figure, whereas experimentally measurable but only in single crystals is highlighted in yellow. It is evident that measuring fundamental properties such as elastic

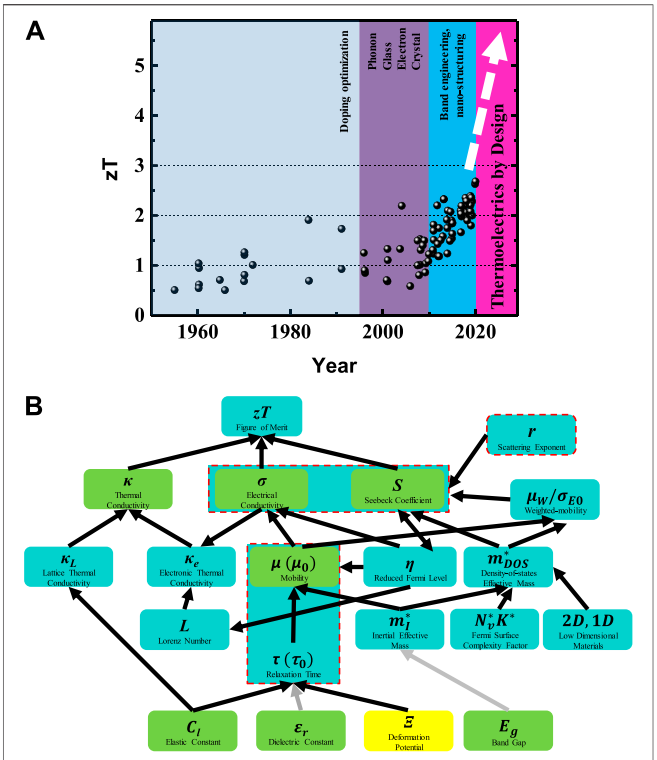

FIGURE 1 | (A) Progressive overview of thermoelectric performance as a function to the timeline in years and correlations of *zT* components. **(B)** Tree diagram showing the complex web of interdependencies between electronic transport parameters that make up *zT*.

constant, dielectric constant, and band gaps are important to complement and accurately determine the other derived TE parameters. In addition, it is crucial to note that the viability for commercialization is dependent on thermoelectric performance for a range of working temperatures as well as processing methods. Hence, the application space is limited by the materials' mechanical and chemical properties.

The overall TE device performance depends on two factors: materials performance and Carnot efficiency, which is temperature dependent. Materials wise, thermoelectric performance is typically expressed in terms of figure of merit *zT*, which is defined as $zT = S^2\sigma T/\kappa$, with *S*, σ, and κ denoting the Seebeck coefficient, electrical, and thermal conductivity, respectively. The overall power conversion efficiency depends on both *zT* and ΔT (temperature gradient) and can be expressed as follows:

$$\eta = \frac{\Delta T}{T_h}\frac{\sqrt{1+ZT_{ave}}-1}{\sqrt{1+ZT_{ave}}+T_c/T_h} \quad (1)$$

The first term of the equation, $\Delta T/T_h$, represents the Carnot efficiency, which is the theoretical maximum efficiency limit in any energy conversion process. Mathematically, higher ΔT favors higher conversion efficiency and vice versa. The second term of the equation represents the relative efficiency of the TE, which is proportional to zT_{ave} (average *zT* over a temperature range). In addition, a more subtle interpretation from the above equation is the importance to keep the cold side temperature (T_c) low (i.e., through effective heat dissipation) in order to maximize the efficiency.

To date, the majority of efforts in thermoelectric materials research have been focused on maximizing the materials figure of merit *zT*. However, although it sounds simple, *zT* is not a trivial parameter to optimize or improve on. This is due to the complex interdependencies between the parameters that make up *zT* as summarized in **Figure 1B**. This is not considering the many interrelated parameters making up the lattice thermal conductivity, k_L. It is evident that these interdependencies and compromises exist even at the level of fundamental material properties. It has been a grand challenge with decades of research from the TE, physics, and chemistry communities to arrive at the current understanding.

In general, the strategies around enhancing thermoelectric performances can be categorized into two broad classes: Seebeck coefficient enhancement and mobility enhancement. Both aspects will be discussed in turn in the subsequent sections. More importantly, the discussion around these parameters will focus on the importance of taking grain boundaries resistance into account, which is an important topic that has been gaining prominence of late.

SEEBECK COEFFICIENT ENHANCEMENT

Based on postulates by Cutler and Mott [24], the value of *S* for degenerate semiconductors or metals can be written by the following formula [25]:

$$S = \frac{\pi^2}{3}\frac{k_B}{e}(k_BT)\left[\frac{1}{n(E)}\frac{dn(E)}{dE}+\frac{1}{\mu(E)}\frac{d\mu(E)}{dE}\right] \quad (2)$$

where *S* is the Seebeck coefficient, k_B is Boltzmann's constant, *T* is the temperature in Kelvin, *e* is the electron mass, *n* is the charge carrier concentration, and μ is the charge carrier mobility. Enhanced *S* can be achieved through degenerate band convergence for Fermi level shifts towards the valence band maxima (VBM) or conduction band minima (CBM), or through enhancement of the density of states (DOS). Based on **Eq. 2**, *S* can be enhanced through the variation of both *n*(E) and μ(E) at E_F. The *n* and E_F have a significant influence on the energy-dependent electrical conductivity, σ. The *n* at energy E is equivalent to the $g(E)$. See **Figure 2** also. Variation of μ and *n* can be achieved by varying the effective mass of DOS (m'_{dos}) together with band engineering. In other words, the Seebeck coefficient depends on the symmetry breaking of both the DOS at the Fermi level and the energy-dependent mobility. In addition to these effects, phonon drag has also been widely reported to contribute to the Seebeck coefficient at low temperatures [26, 27]. It is worthy to mention the significant breakthroughs by Dresselhaus et al. in the field of TE to enhance *zT* with the modification of the electronic properties of some materials when prepared in the form of quantum-well superlattices or nanowires. This concept of quantum confinement offers additional degrees of freedom for enhancing the TE performance because of the strong dependence between electronic DOS and dimensionality [28, 29].

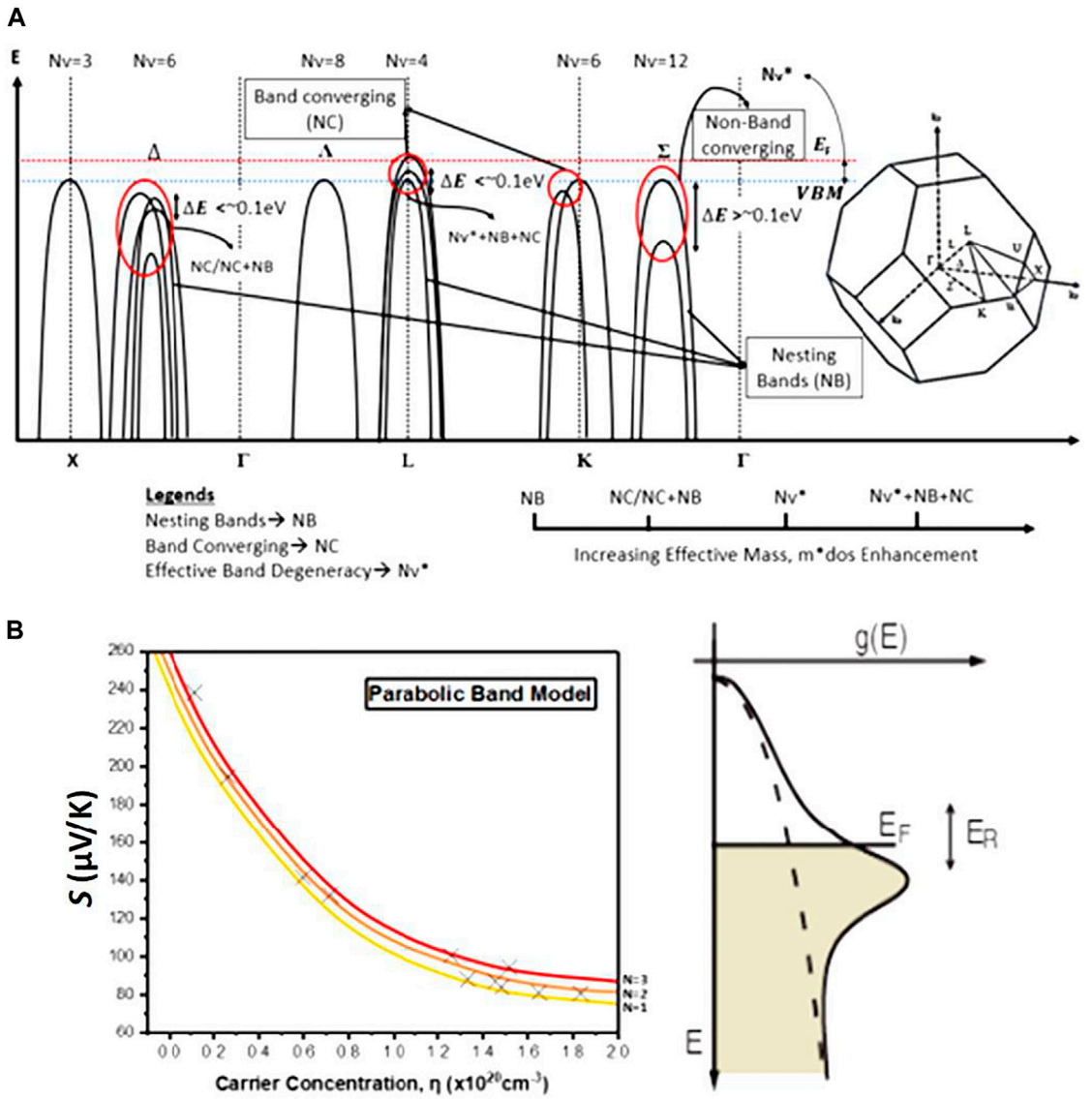

FIGURE 2 | (A) An illustration of the band structure consisting of examples of converging, non-converging, and nesting bands, and the Brillouin zone of face-centered cubic (FCC) lattice. **(B)** An illustration of the Pisarenko plot based on single parabolic band (SPB) model calculations with a density of states (DOS) profile of 3D bulk material relative to energy.

To date, strategies to enhance the Seebeck coefficients at room temperature and above have been mainly *via* the first term of **Eq. 2**, $dn(E)/dE$ (i.e., the slope of DOS vs. energy). This can be achieved *via* either band convergence or resonant doping. In addition, the second term of **Eq. 2**, $d\mu(E)/dE$, is closely associated with energy filtering, which manifests in scattering exponent r. Lastly, size effects in low-dimensional materials have been known to provide such symmetry breaking in DOS, as well elucidated in a recent review [30].

Band Convergence

For effective transport, the DOS effective mass (m^*_{DOS}) must be asymmetric around the Fermi level. This means that symmetry breaking is desired (sharp peak in DOS) to achieve a high Seebeck coefficient.

The effective mass of the DOS, m^*_{DOS}, is expressed as

$$m^*_{DOS} = m^*_{Band} N_V^{\frac{2}{3}} \tag{3}$$

where m_{band} is the effective mass for the band and N_V is the band degeneracy.

There are many ways of achieving band convergence [31, 32]. In p-type PbTe, the L and Σ band convergence happens at high temperatures due to the higher downward shift of L band compared with Σ band [33]. Such convergence is due to thermal expansion. On the other hand, with the addition of group 2 elements such as Mg or transition metal, Mn can also cause band convergence in PbTe due to the absence of s^2 lone pair in Mg/Mn, which replaces Pb [34, 35]. The absence of lone pairs

in Mg/Mn weakens the quenching of lone pairs in PbTe, resulting in lower *L* band energy [36]. In addition, band convergence in PbTe and SnTe can be achieved by doping of Zn, Cd, Mg, Mn, or Ca, all of which are without s^2 lone pair [37–44]. A very useful reference for designing band convergence and resonant doping in binary chalcogenides can be found in Ref. [45]. To understand more about the role of lone pairs in the electronic band structure, Ref. [36] is a useful guide.

The face-centered cubic (FCC) lattice band structure consists of Γ, *L*, and *K* points in the reciprocal space representing the center, corners, and edges of the cubic lattice in real space, respectively. The illustration in **Figure 2** summarizes the examples of nesting, converging, and non-converging bands.

FCC lattice has eight corners; thus, an electronic band on the *L* symmetry line in the band structure corresponds to eight energetically similar Fermi surfaces of the Brillouin zone as shown on the right side of **Figure 2**. These are degenerate bands, and the number or multiplicity of degenerate bands is defined by Nv. Further represented in **Eq. 3**, the higher the Nv, the larger the effective mass DOS. Hence, identifying the symmetry points with high Nv is crucial for enhancing Seebeck. The ideal band modulation doping is to have band converging and band nesting within the effective band degeneracy, Nv*, close to the valence band. See **Figure 2**.

In certain cases, band convergence can be achieved at structural phase-transition, just like in the case of GeTe. At low temperature, the s^2 lone pair is stereochemically expressed due to the light ligand field in GeTe compared with SnTe and PbTe. The stereochemical expression of the s^2 lone pair leads to rhombohedral structure, with Σ band as the VBM. However, at high temperatures, the cubic structure prevails, leading to *L* band as the VBM. Therefore, at the phase transition temperature, both *L* and Σ bands converge, leading to a high thermoelectric performance in GeTe. Consequently, manipulating phase transition temperature in GeTe becomes a versatile tool to control its peak performance at a particular temperature [22, 46–78].

Resonant Doping

In addition to band convergence, resonant doping and energy filtering are also popular in enhancing Seebeck. Resonant doping differs from the usual doping states such that the energy states of the resonant dopant lie within the valence band or conduction band, yet away from the VBM or the CBM. Resonant dopants normally have similar electronic configurations as the host atoms, and they are usually selected from the neighboring main group elements. Resonant doping is achieved when the dopant energy level coincides with the host energy level to form two extended states. These developed extended states have similar energy levels again with host energy states and resonate to form more energy states resulting in the increase in DOS. These new energy states introduce distortion to the existing DOS within the material. See **Figure 2**. When the dopant states lie near the band edge where the Fermi level is, the resonant level becomes beneficial in enhancing Seebeck. It is noteworthy that although fostering resonance levels can enhance the Seebeck, it can adversely affect the carrier mobility. Therefore, it is crucial to have a minimal doping level to achieve a resonance state (unlike band convergence, where the doping level can be much higher). Equation [4] postulates that increased DOS results in enhanced Seebeck. The Pisarenko plot in **Figure 2** further illustrates this relationship between the Seebeck and DOS. One of the landmark papers on resonant doping was reported in 2008 by Heremans *et al.* on Tl-doped PbTe [79].

$$S = \frac{8\pi^2 k_B^2 T}{3eh^2} m^*_{DOS} \left(\frac{\pi}{3n}\right)^{2/3} \tag{4}$$

Energy Filtering

On the other hand, the idea behind energy filtering lies in symmetry breaking of carrier energy. Due to the nature that carriers of lower and higher energy than Fermi level contribute oppositely to the total Seebeck coefficient, the presence of potential barriers to selectively block out lower energy carriers may be beneficial for the Seebeck coefficient while only sacrificing a little bit of electrical conductivity. Mathematically, energy filtering is described by $d\mu(E)/dE$ (see **Eq. 2**). A more rigorous mathematical treatment and derivation of energy filtering can be found in the literature [80]. Experimentally, such a large energy-dependent mobility, which gives rise to enhanced Seebeck coefficient, has been reported in the work by Xie *et al.* [81].

ENHANCING ELECTRICAL CONDUCTIVITY *VIA* MOBILITY

Electrical conductivity written as σ defines the capacity of a medium to transfer current in direct proportion to n and μ as shown below:

$$\sigma = q\left(\mu_n n + \mu_p p\right) \tag{5}$$

where σ is the electrical conductivity, q is the electronic charge, μ_n and μ_p refer to mobilities of electrons and holes, and n/p is the carrier concentration of each type.

From this equation, enhancing *s* requires that the values of n and μ are maintained at high levels. Usually, enhancing the value of n is achieved by the introduction of a dopant. In general, the optimal carrier concentration, n, ranges between 10^{19} and 10^{21} cm^3 with considerable μ. The reduction of μ results from the enhanced scattering of ionized impurities. This calls for a midpoint between the two parameters n and μ. In order to achieve this midpoint, modulation doping is used for discretizing charge carriers from ionized dopants in a bid to reduce the scattering of ionized impurities to achieve high values of μ while enhancing the value of n in the thermoelectric material.

Owing to the variance in the value of E_f in the undoped and uniformly doped, the carriers found within the modulation-doped material overflow across the boundaries of the equitably doped region to the undoped region. This results in carriers eluding the scattering effect of ionized impurities, and therefore, μ is enhanced. The most recent application of modulation doping was in BiCuSeO where high values of PF and ZT were obtained, 5.4 $\mu W \cdot cm^{-1} \cdot K^{-2}$ and 0.99 at 873 K, respectively, compared with

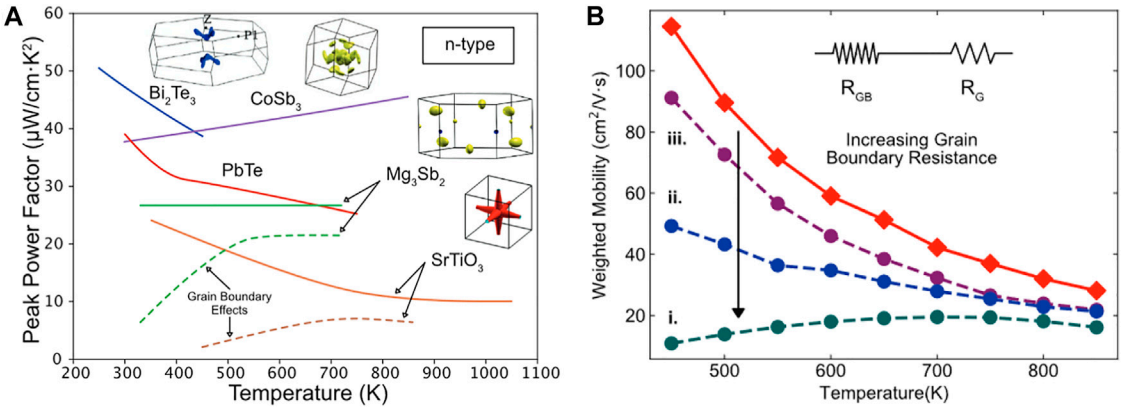

FIGURE 3 | (A) The modelled peak power factor for different thermoelectric materials showing higher values when grain boundary resistance is not considered (solid lines) compared with when they are considered (dashed lines). **(B)** Influence of grain boundaries on weighted mobility vs. temperature trend. Smaller grain (more grain boundaries) lowers the low temperature weighted mobility. Figure reproduced with permission from [86]. Copyright Wiley 2019.

the lower values obtained from uniformly and highly doped BiCuSeO. Moreover, this method is known to enhance the carrier concentration, n, and reduce the carrier mobility, μ, due to intervalley scattering in PbTe quantum well. That said, as discussed in the previous section on band convergence, degenerate band convergence leads to an increase in effective mass, m*, which in this case outweighs the loss of carrier mobility. Hence, the overall zT is enhanced [82].

Just like enhancing Seebeck coefficients, there are a few reliable strategies to independently enhance carrier mobility without sacrificing the Seebeck coefficient (i.e., without changing carrier concentration or reduced Fermi level). These strategies can be broadly categorized into tuning inertial effective mass, tuning the deformation potential, tuning carrier scattering, and, in certain cases, even tuning dielectric constant, elastic constant, or band gaps.

In addition to the popular acoustic and ionized impurities scattering, grain boundary scattering, and alloy scattering are also prevalent, especially in polycrystalline materials. Physically, different scattering mechanisms mainly manifest in the temperature and energy (carrier concentration) dependency of carrier mobility. The temperature dependence of some common scattering mechanisms such as acoustic phonon (AP), ionized impurity (II), alloy (AL), and grain boundaries (GB) are as follows:

$$\mu_{AP} \propto T^{-3/2}\eta^{-1/2} \tag{6}$$

$$\mu_{II} \propto T^{3/2}\eta^{3/2} \tag{7}$$

$$\mu_{AL} \propto T^{-1/2}\eta^{-1/2} \tag{8}$$

$$\mu_{GB} \propto T^{-\frac{1}{2}}\exp\left(-CT^{-1}\right) \tag{9}$$

In fact, grain boundary scattering recently gained popularity among TE communities, driven by rigorous work from Kuo *et al.*, who propose that in a system with mixed acoustic phonon and ionized impurities scattering, Matthiessen's rule does not adequately reconcile with the sharp transition in temperature dependence between these two scattering mechanisms [83]. This is later verified in NbFeSb system too [84]. The importance of taking grain boundaries into account can also affect the conclusion of other physical mechanisms, as illustrated in **Figure 3**. **Figure 3A** shows the lower peak power factor in polycrystalline materials where grain boundaries effects are considered (dashed lines) as compared with single crystals (solid line). **Figure 3B** shows the effect on weighted mobility vs. temperature, showing acoustic phonon-dominated behavior in single crystals (red curve) and gradually shifting to mixed scattering with increasing grain boundaries (dark green curve). Furthermore, overestimation of lattice thermal conductivity has also been reported when grain boundaries were not taken into account [85].

SUMMARY AND OUTLOOK

In summary, although the existing physical understanding of the electronic properties of TEs is quite comprehensive, caution must still be taken when trying to draw conclusions from analyzing these properties. For instance, although it sounds trivial, the consideration of grain boundaries electrical resistance may lead to over/underestimation of lattice thermal conductivity and wrong conclusions about the predominant scattering mechanisms in a material. This is especially prevalent in polycrystalline materials, where grain boundaries are present in abundance.

Moving forward, this importance of grain boundaries can be a useful guide towards materials performance optimization especially in 3D-printed TEs, which has been gaining traction recently. By designing printing parameters to optimize the grain boundaries, there is much more performance that can be gained from 3D-printed TEs for power harvesting and cooling applications.

AUTHOR CONTRIBUTIONS

WL wrote the paper. DZ helped with writing and literature review. SD helped with writing and literature review. XT

helped with writing and literature review. CT helped with writing and literature review. JX helped with writing and literature review. AS supervised the writing and gave technical advice.

FUNDING

This research is supported by a funding from A*STAR "Brain-inspired Vision Sensors": C210112022.

REFERENCES

1. Hamid Elsheikh M, Shnawah DA, Sabri MFM, Said SBM, Haji Hassan M, Ali Bashir MB, et al. A Review on Thermoelectric Renewable Energy: Principle Parameters that Affect Their Performance. *Renew Sustain Energ Rev* (2014) 30:337–55. doi:10.1016/j.rser.2013.10.027
2. Ul Haq B, Ahmed R, AlFaify S, Butt FK, Shaari A, Laref A. Exploring Thermoelectric Materials for Renewable Energy Applications: The Case of Highly Mismatched Alloys Based on AlBi1-xSbx and InBi1-xSbx. *Intermetallics* (2018) 93:235–43. doi:10.1016/j.intermet.2017.09.017
3. Suwardi A, Lim SH, Zheng Y, Wang X, Chien SW, Tan XY, et al. Effective Enhancement of Thermoelectric and Mechanical Properties of Germanium telluride via Rhenium-Doping. *J Mater Chem C* (2020) 8(47):16940–8. doi:10.1039/d0tc04903d
4. Suwardi A, Bash D, Ng HK, Gomez JR, Repaka DVM, Kumar P, et al. Inertial Effective Mass as an Effective Descriptor for Thermoelectrics via Data-Driven Evaluation. *J Mater Chem A* (2019) 7(41):23762–9. doi:10.1039/c9ta05967a
5. Tan LP, Sun T, Fan S, Ng LY, Suwardi A, Yan Q, et al. Facile Synthesis of Cu7Te4 Nanorods and the Enhanced Thermoelectric Properties of Cu7Te4-Bi0.4Sb1.6Te3 Nanocomposites. *Nano Energy* (2013) 2(1):4–11. doi:10.1016/j.nanoen.2012.07.004
6. Zhu Q, Wang S, Wang X, Suwardi A, Chua MH, Soo XYD, et al. Bottom-Up Engineering Strategies for High-Performance Thermoelectric Materials. *Nano-micro Lett* (2021) 13(1):119. doi:10.1007/s40820-021-00637-z
7. Zheng Y, Slade TJ, Hu L, Tan XY, Luo Y, Luo Z-Z, et al. Defect Engineering in Thermoelectric Materials: what Have We Learned?. *Chem Soc Rev* (2021) 50(16):9022–54. doi:10.1039/d1cs00347j
8. Zhao Y, Zheng M, Wu J, Guan X, Suwardi A, Li Y, et al. Modification of thermal Transport in Few-Layer MoS2 by Atomic-Level Defect Engineering. *Nanoscale* (2021) 13(26):11561–7. doi:10.1039/d1nr01832a
9. Yang J, Caillat T. Thermoelectric Materials for Space and Automotive Power Generation. *MRS Bull* (2006) 31(3):224–9. doi:10.1557/mrs2006.49
10. LeBlanc S. Thermoelectric Generators: Linking Material Properties and Systems Engineering for Waste Heat Recovery Applications. *Sustain Mater Tech* (2014) 1-2:26–35. doi:10.1016/j.susmat.2014.11.002
11. Qin F, Nikolaev SA, Suwardi A, Wood M, Zhu Y, Tan X, et al. Crystal Structure and Atomic Vacancy Optimized Thermoelectric Properties in Gadolinium Selenides. *Chem Mater* (2020) 32(23):10130–9. doi:10.1021/acs.chemmater.0c03581
12. Jia N, Cao J, Tan XY, Zheng J, Chien SW, Yang L, et al. Suppressing Ge-Vacancies to Achieve High Single-Leg Efficiency in GeTe with an Ultra-high Room Temperature Power Factor. *J Mater Chem A* (2021) 9(41):23335–44. doi:10.1039/d1ta05866e
13. Jia N, Cao J, Tan XY, Dong J, Liu H, Tan CKI, et al. Thermoelectric Materials and Transport Physics. *Mater Today Phys* (2021) 21:100519. doi:10.1016/j.mtphys.2021.100519
14. Bourgès C, Srinivasan B, Fontaine B, Sauerschnig P, Minard A, Halet J-F, et al. Tailoring the Thermoelectric and Structural Properties of Cu-Sn Based Thiospinel Compounds [CuM1+xSn1−xS4 (M = Ti, V, Cr, Co)]. *J Mater Chem C* (2020) 8(46):16368–83. doi:10.1039/d0tc04393a
15. Virtudazo RVR, Srinivasan B, Guo Q, Wu R, Takei T, Shimasaki Y, et al. Improvement in the Thermoelectric Properties of Porous Networked Al-Doped ZnO Nanostructured Materials Synthesized via an Alternative Interfacial Reaction and Low-Pressure SPS Processing. *Inorg Chem Front* (2020) 7(21):4118–32. doi:10.1039/d0qi00888e
16. Srinivasan B, Cui S, Prestipino C, Gellé A, Boussard-Pledel C, Ababou-Girard S, et al. Possible Mechanism for Hole Conductivity in Cu-As-Te Thermoelectric Glasses: A XANES and EXAFS Study. *J Phys Chem C* (2017) 121(26):14045–50. doi:10.1021/acs.jpcc.7b04555
17. Hong S, Gu Y, Seo JK, Wang J, Liu P, Meng YS, et al. Wearable Thermoelectrics for Personalized Thermoregulation. *Sci Adv* (2019) 5(5):eaaw0536. doi:10.1126/sciadv.aaw0536
18. Zhang Q, Liao J, Tang Y, Gu M, Ming C, Qiu P, et al. Realizing a Thermoelectric Conversion Efficiency of 12% in Bismuth telluride/skutterudite Segmented Modules through Full-Parameter Optimization and Energy-Loss Minimized Integration. *Energ Environ Sci* (2017) 10(4):956–63.
19. Recatala-Gomez J, Kumar P, Suwardi A, Abutaha A, Nandhakumar I, Hippalgaonkar K. Direct Measurement of the Thermoelectric Properties of Electrochemically Deposited Bi2Te3 Thin Films. *Sci Rep* (2020) 10(1):17922–10. doi:10.1038/s41598-020-74887-z
20. Hu L, Luo Y, Fang YW, Qin F, Cao X, Xie H, et al. High Thermoelectric Performance through Crystal Symmetry Enhancement in Triply Doped Diamondoid Compound Cu 2 SnSe 3. *Adv Energ Mater.* (2021) 2100661. doi:10.1002/aenm.202100661
21. Hu L, Fang Y-W, Qin F, Cao X, Zhao X, Luo Y, et al. High Thermoelectric Performance Enabled by Convergence of Nested Conduction Bands in Pb7Bi4Se13 with Low thermal Conductivity. *Nat Commun* (2021) 12(1):4793. doi:10.1038/s41467-021-25119-z
22. Hong M, Zheng K, Lyv W, Li M, Qu X, Sun Q, et al. Computer-aided Design of High-Efficiency GeTe-Based Thermoelectric Devices. *Energy Environ. Sci.* (2020) 13(6):1856–64. doi:10.1039/d0ee01004a
23. Dresselhaus MS, Chen G, Tang MY, Yang RG, Lee H, Wang DZ, et al. New Directions for Low-Dimensional Thermoelectric Materials. *Adv Mater* (2007) 19(8):1043–53. doi:10.1002/adma.200600527
24. Cutler M, Mott NF. Observation of Anderson Localization in an Electron Gas. *Phys Rev* (1969) 181(3):1336–40. doi:10.1103/physrev.181.1336
25. Wei S-H. Overcoming the Doping Bottleneck in Semiconductors. *Comput Mater Sci* (2004) 30(3):337–48. doi:10.1016/j.commatsci.2004.02.024
26. Vavro J, Llaguno MC, Fischer JE, Ramesh S, Saini RK, Ericson LM, et al. Thermoelectric Power of P-Doped Single-wall Carbon Nanotubes and the Role of Phonon Drag. *Phys Rev Lett* (2003) 90(6):065503. doi:10.1103/PhysRevLett.90.065503
27. Zhou J, Liao B, Qiu B, Huberman S, Esfarjani K, Dresselhaus MS, et al. Ab Initio optimization of Phonon Drag Effect for Lower-Temperature Thermoelectric Energy Conversion. *Proc Natl Acad Sci USA* (2015) 112(48):14777–82. doi:10.1073/pnas.1512328112
28. Hicks LD, Dresselhaus MS. Effect of Quantum-Well Structures on the Thermoelectric Figure of merit. *Phys Rev B* (1993) 47(19):12727–31. doi:10.1103/physrevb.47.12727
29. Hicks LD, Dresselhaus MS. Thermoelectric Figure of merit of a One-Dimensional Conductor. *Phys Rev B* (1993) 47(24):16631–4. doi:10.1103/physrevb.47.16631
30. Mao J, Liu Z, Ren Z. Size Effect in Thermoelectric Materials. *Npj Quant Mater* (2016) 1(1):16028. doi:10.1038/npjquantmats.2016.28
31. Fu C, Zhu T, Pei Y, Xie H, Wang H, Snyder GJ, et al. High Band Degeneracy Contributes to High Thermoelectric Performance in P-type Half-Heusler Compounds. *Adv Energ Mater.* (2014) 4(18):1400600. doi:10.1002/aenm.201400600
32. Srinivasan B, Fontaine B, Gucci F, Dorcet V, Saunders TG, Yu M, et al. Effect of the Processing Route on the Thermoelectric Performance of Nanostructured CuPb18SbTe20. *Inorg Chem* (2018) 57(20):12976–86. doi:10.1021/acs.inorgchem.8b02248
33. Pei Y, Shi X, LaLonde A, Wang H, Chen L, Snyder GJ. Convergence of Electronic Bands for High Performance Bulk Thermoelectrics. *Nature* (2011) 473(7345):66–9. doi:10.1038/nature09996
34. Zhao LD, Wu HJ, Hao SQ, Wu CI, Zhou XY, Biswas K, et al. All-scale Hierarchical Thermoelectrics: MgTe in PbTe Facilitates Valence Band Convergence and Suppresses Bipolar thermal Transport for High Performance. *Energ Environ. Sci.* (2013) 6(11):3346–55. doi:10.1039/c3ee42187b

35. Pei Y, Wang H, Gibbs ZM, LaLonde AD, Snyder GJ. Thermopower Enhancement in Pb1−xMnxTe Alloys and its Effect on Thermoelectric Efficiency. *NPG Asia Mater* (2012) 4(9):e28. doi:10.1038/am.2012.52
36. Zeier WG, Zevalkink A, Gibbs ZM, Hautier G, Kanatzidis MG, Snyder GJ. Thinking like a Chemist: Intuition in Thermoelectric Materials. *Angew Chem Int Ed* (2016) 55(24):6826–41. doi:10.1002/anie.201508381
37. Pei Y, LaLonde AD, Heinz NA, Shi X, Iwanaga S, Wang H, et al. Stabilizing the Optimal Carrier Concentration for High Thermoelectric Efficiency. *Adv Mater* (2011) 23(47):5674–8. doi:10.1002/adma.201103153
38. Biswas K, He J, Wang G, Lo S-H, Uher C, Dravid VP, et al. High Thermoelectric Figure of merit in Nanostructured P-type PbTe-MTe (M = Ca, Ba). *Energ Environ. Sci.* (2011) 4(11):4675–84. doi:10.1039/c1ee02297k
39. Pei Y, LaLonde AD, Heinz NA, Snyder GJ. High Thermoelectric Figure of Merit in PbTe Alloys Demonstrated in PbTe-CdTe. *Adv Energ Mater.* (2012) 2(6):670–5. doi:10.1002/aenm.201100770
40. Al Rahal Al Orabi R, Mecholsky NA, Hwang J, Kim W, Rhyee J-S, Wee D, et al. Band Degeneracy, Low Thermal Conductivity, and High Thermoelectric Figure of Merit in SnTe-CaTe Alloys. *Chem Mater* (2016) 28(1):376–84. doi:10.1021/acs.chemmater.5b04365
41. He J, Xu J, Liu G-Q, Shao H, Tan X, Liu Z, et al. Enhanced Thermopower in Rock-Salt SnTe-CdTe from Band Convergence. *RSC Adv* (2016) 6(38): 32189–92. doi:10.1039/c6ra02658c
42. Bhat DK, Shenoy US. Zn: a Versatile Resonant Dopant for SnTe Thermoelectrics. *Mater Today Phys* (2019) 11:100158. doi:10.1016/j.mtphys.2019.100158
43. Srinivasan B, Gellé A, Gucci F, Boussard-Pledel C, Fontaine B, Gautier R, et al. Realizing a Stable High Thermoelectric zT ~ 2 over a Broad Temperature Range in Ge1−x−yGaxSbyTe via Band Engineering and Hybrid Flash-SPS Processing. *Inorg Chem Front* (2019) 6(1):63–73. doi:10.1039/c8qi00703a
44. Muchtar AR, Srinivasan B, Tonquesse SL, Singh S, Soelami N, Yuliarto B, et al. Physical Insights on the Lattice Softening Driven Mid-Temperature Range Thermoelectrics of Ti/Zr-Inserted SnTe-An Outlook beyond the Horizons of Conventional Phonon Scattering and Excavation of Heikes' Equation for Estimating Carrier Properties. *Adv Energ Mater.* (2021) 11:2101122. doi:10.1002/aenm.202101122
45. Tan X, Wang H, Liu G, Noudem JG, Hu H, Xu J, et al. Designing Band Engineering for Thermoelectrics Starting from the Periodic Table of Elements. *Mater Today Phys* (2018) 7:35–44. doi:10.1016/j.mtphys.2018.10.004
46. Suwardi A, Cao J, Hu L, Wei F, Wu J, Zhao Y, et al. Tailoring the Phase Transition Temperature to Achieve High-Performance Cubic GeTe-Based Thermoelectrics. *J Mater Chem A* (2020) 8(36):18880–90. doi:10.1039/d0ta06013e
47. Jin Y, Xiao Y, Wang D, Huang Z, Qiu Y, Zhao L-D. Realizing High Thermoelectric Performance in GeTe through Optimizing Ge Vacancies and Manipulating Ge Precipitates. *ACS Appl Energ Mater.* (2019) 2(10): 7594–601. doi:10.1021/acsaem.9b01585
48. Liu WD, Wang DZ, Liu Q, Zhou W, Shao Z, Chen Z-G. *High-Performance GeTe-Based Thermoelectrics: From Materials to Devices*. *Adv. Energy Mater.* (2020) 10(19):2000367.
49. Li P, Ding T, Li J, Zhang C, Dou Y, Li Y, et al. Positive Effect of Ge Vacancies on Facilitating Band Convergence and Suppressing Bipolar Transport in GeTe-Based Alloys for High Thermoelectric Performance. *Adv Funct Mater* (2020) 30(15):1910059. doi:10.1002/adfm.201910059
50. Suwardi A, Bash D, Ng HK, Gomez JR, Repaka DVM, Kumar P, et al. Inertial Effective Mass as an Effective Descriptor for Thermoelectrics via Data-Driven Evaluation. *J Mater Chem A* (2019) 7(41):23762–9. doi:10.1039/c9ta05967a
51. Tsai YF, Wei PC, Chang L, Wang KK, Yang CC, Lai YC, et al. Compositional Fluctuations Locked by Athermal Transformation Yielding High Thermoelectric Performance in GeTe. *Adv Mater* (2021) 33(1):2005612. doi:10.1002/adma.202005612
52. Xing T, Zhu C, Song Q, Huang H, Xiao J, Ren D, et al. Ultralow Lattice Thermal Conductivity and Superhigh Thermoelectric Figure-of-Merit in (Mg, Bi) Co-Doped GeTe. *Adv Mater* (2021) 33(17):2008773. doi:10.1002/adma.202008773
53. Cao J, Chien SW, Tan XY, Tan CKI, Zhu Q, Wu J, et al. Realizing zT Values of 2.0 in Cubic GeTe. *ChemNanoMat* (2021) 7(4):476–82. doi:10.1002/cnma.202100033
54. Srinivasan B, Berthebaud D, Mori T. Is Lii a Potential Dopant Candidate to Enhance the Thermoelectric Performance in Sb-free Gete Systems? A Prelusive Study. *Energies* (2020) 13(3):643. doi:10.3390/en13030643
55. Xing T, Song Q, Qiu P, Zhang Q, Gu M, Xia X, et al. High Efficiency GeTe-Based Materials and Modules for Thermoelectric Power Generation. *Energ Environ. Sci.* (2021) 14(2):995–1003. doi:10.1039/d0ee02791j
56. Dong J, Sun F-H, Tang H, Pei J, Zhuang H-L, Hu H-H, et al. Medium-temperature Thermoelectric GeTe: Vacancy Suppression and Band Structure Engineering Leading to High Performance. *Energ Environ. Sci.* (2019) 12(4): 1396–403. doi:10.1039/c9ee00317g
57. Hong M, Zheng K, Lyv W, Li M, Qu X, Sun Q, et al. Computer-aided Design of High-Efficiency GeTe-Based Thermoelectric Devices. *Energ Environ. Sci.* (2020) 13(6):1856–64. doi:10.1039/d0ee01004a
58. Li J, Zhang X, Chen Z, Lin S, Li W, Shen J, et al. Low-Symmetry Rhombohedral GeTe Thermoelectrics. *Joule* (2018) 2(5):976–87. doi:10.1016/j.joule.2018.02.016
59. Perumal S, Samanta M, Ghosh T, Shenoy US, Bohra AK, Bhattacharya S, et al. Realization of High Thermoelectric Figure of Merit in GeTe by Complementary Co-doping of Bi and in. *Joule* (2019) 3(10):2565–80. doi:10.1016/j.joule.2019.08.017
60. Zhang X, Bu Z, Lin S, Chen Z, Li W, Pei Y. GeTe Thermoelectrics. *Joule* (2020) 4(5):986–1003. doi:10.1016/j.joule.2020.03.004
61. Bayikadi KS, Wu CT, Chen L-C, Chen K-H, Chou F-C, Sankar R. Synergistic Optimization of Thermoelectric Performance of Sb Doped GeTe with a Strained Domain and Domain Boundaries. *J Mater Chem A* (2020) 8(10): 5332–41. doi:10.1039/d0ta00628a
62. Feng Y, Li J, Li Y, Ding T, Zhang C, Hu L, et al. Band Convergence and Carrier-Density fine-tuning as the Electronic Origin of High-Average Thermoelectric Performance in Pb-Doped GeTe-Based Alloys. *J Mater Chem A* (2020) 8(22): 11370–80. doi:10.1039/d0ta02758h
63. Nshimyimana E, Hao S, Su X, Zhang C, Liu W, Yan Y, et al. Discordant Nature of Cd in GeTe Enhances Phonon Scattering and Improves Band Convergence for High Thermoelectric Performance. *J Mater Chem A* (2020) 8(3):1193–204. doi:10.1039/c9ta10436d
64. Qiu Y, Jin Y, Wang D, Guan M, He W, Peng S, et al. Realizing High Thermoelectric Performance in GeTe through Decreasing the Phase Transition Temperature via Entropy Engineering. *J Mater Chem A* (2019) 7(46):26393–401. doi:10.1039/c9ta10963c
65. Srinivasan B, Le Tonquesse S, Gellé A, Bourgès C, Monier L, Ohkubo I, et al. Screening of Transition (Y, Zr, Hf, V, Nb, Mo, and Ru) and Rare-Earth (La and Pr) Elements as Potential Effective Dopants for Thermoelectric GeTe - an Experimental and Theoretical Appraisal. *J Mater Chem A* (2020) 8(38): 19805–21. doi:10.1039/d0ta06710e
66. Wang L, Li J, Zhang C, Ding T, Xie Y, Li Y, et al. Discovery of Low-Temperature GeTe-Based Thermoelectric Alloys with High Performance Competing with Bi2Te3. *J Mater Chem A* (2020) 8(4):1660–7. doi:10.1039/c9ta11901a
67. Samanta M, Ghosh T, Arora R, Waghmare UV, Biswas K. Realization of Both N- and P-type GeTe Thermoelectrics: Electronic Structure Modulation by AgBiSe2 Alloying. *J Am Chem Soc* (2019) 141(49):19505–12. doi:10.1021/jacs.9b11405
68. Shuai J, Tan XJ, Guo Q, Xu JT, Gellé A, Gautier R, et al. Enhanced Thermoelectric Performance through crystal Field Engineering in Transition Metal-Doped GeTe. *Mater Today Phys* (2019) 9:100094. doi:10.1016/j.mtphys.2019.100094
69. Li M, Hong M, Tang X, Sun Q, Lyu W-Y, Xu S-D, et al. Crystal Symmetry Induced Structure and Bonding Manipulation Boosting Thermoelectric Performance of GeTe. *Nano Energy* (2020) 73:104740. doi:10.1016/j.nanoen.2020.104740
70. Xing T, Song Q, Qiu P, Zhang Q, Xia X, Liao J, et al. Superior Performance and High Service Stability for GeTe-Based Thermoelectric Compounds. *Natl Sci Rev* (2019) 6(5):944–54. doi:10.1093/nsr/nwz052
71. Bu Z, Zhang X, Shan B, Tang J, Liu H, Chen Z, et al. Realizing a 14% Single-Leg Thermoelectric Efficiency in GeTe Alloys. *Sci Adv* (2021) 7(19):eabf2738. doi:10.1126/sciadv.abf2738
72. Shuai J, Sun Y, Tan X, Mori T. Manipulating the Ge Vacancies and Ge Precipitates through Cr Doping for Realizing the High-Performance GeTe Thermoelectric Material. *Small* (2020) 16(13):1906921. doi:10.1002/smll.201906921

73. Suwardi A, Hu L, Wang X, Tan XY, Repaka DVM, Wong L-M, et al. Origin of High Thermoelectric Performance in Earth-Abundant Phosphide-Tetrahedrite. *ACS Appl Mater Inter* (2020) 12(8):9150–7. doi:10.1021/acsami.9b17269
74. Yang F, Wu J, Suwardi A, Zhao Y, Liang B, Jiang J, et al. Gate-Tunable Polar Optical Phonon to Piezoelectric Scattering in Few-Layer Bi 2 O 2 Se for High-Performance Thermoelectrics. *Adv Mater* (2021) 33(4):2004786. doi:10.1002/adma.202004786
75. Suwardi A, Lim SH, Zheng Y, Wang X, Chien SW, Tan XY, et al. Effective Enhancement of Thermoelectric and Mechanical Properties of Germanium telluride via Rhenium-Doping. *J Mater Chem C* (2020) 8(47):16940–8. doi:10.1039/d0tc04903d
76. Wang X, Suwardi A, Lim SL, Wei F, Xu J. Transparent Flexible Thin-Film P–N junction Thermoelectric Module. *Npj Flexible Electron* (2020) 4(1):1–9. doi:10.1038/s41528-020-00082-9
77. Dinh KN, Sun Y, Pei Z, Yuan Z, Suwardi A, Huang Q, et al. Electronic Modulation of Nickel Disulfide toward Efficient Water Electrolysis. *Small* (2020) 16(17):1905885. doi:10.1002/smll.201905885
78. Suwardi A, Prasad B, Lee S, Choi E-M, Lu P, Zhang W, et al. Turning Antiferromagnetic Sm0.34Sr0.66MnO3 into a 140 K Ferromagnet Using a Nanocomposite Strain Tuning Approach. *Nanoscale* (2016) 8(15):8083–90. doi:10.1039/c6nr01037g
79. Heremans JP, Jovovic V, Toberer ES, Saramat A, Kurosaki K, Charoenphakdee A, et al. Enhancement of Thermoelectric Efficiency in PbTe by Distortion of the Electronic Density of States. *Science* (2008) 321(5888):554–7. doi:10.1126/science.1159725
80. Narducci D, Selezneva E, Cerofolini G, Frabboni S, Ottaviani G. Impact of Energy Filtering and Carrier Localization on the Thermoelectric Properties of Granular Semiconductors. *J Solid State Chem* (2012) 193:19–25. doi:10.1016/j.jssc.2012.03.032
81. Xie H, Su X, Bailey TP, Zhang C, Liu W, Uher C, et al. Anomalously Large Seebeck Coefficient of CuFeS2 Derives from Large Asymmetry in the Energy Dependence of Carrier Relaxation Time. *Chem Mater* (2020) 32(6):2639–46. doi:10.1021/acs.chemmater.0c00388
82. Xiao Y, Zhao L-D. Charge and Phonon Transport in PbTe-Based Thermoelectric Materials. *Npj Quant Mater* (2018) 3(1):55. doi:10.1038/s41535-018-0127-y
83. Kuo JJ, Kang SD, Imasato K, Tamaki H, Ohno S, Kanno T, et al. Grain Boundary Dominated Charge Transport in Mg3Sb2-Based Compounds. *Energ Environ. Sci.* (2018) 11(2):429–34. doi:10.1039/c7ee03326e
84. Shen J, Fan L, Hu C, Zhu T, Xin J, Fu T, et al. Enhanced Thermoelectric Performance in the N-type NbFeSb Half-Heusler Compound with Heavy Element Ir Doping. *Mater Today Phys* (2019) 8:62–70. doi:10.1016/j.mtphys.2019.01.004
85. Kuo JJ, Wood M, Slade TJ, Kanatzidis MG, Snyder GJ. Systematic Over-estimation of Lattice thermal Conductivity in Materials with Electrically-Resistive Grain Boundaries. *Energ Environ. Sci.* (2020) 13(4):1250–8. doi:10.1039/c9ee03921j
86. Dylla MT, Kuo JJ, Witting I, Snyder GJ. Grain Boundary Engineering Nanostructured SrTiO 3 for Thermoelectric Applications. *Adv Mater Inter* (2019) 6(15):1900222. doi:10.1002/admi.201900222

Conflict of Interest: The authors declare that the research was conducted in the absence of any commercial or financial relationships that could be construed as a potential conflict of interest.

Publisher's Note: All claims expressed in this article are solely those of the authors and do not necessarily represent those of their affiliated organizations, or those of the publisher, the editors, and the reviewers. Any product that may be evaluated in this article, or claim that may be made by its manufacturer, is not guaranteed or endorsed by the publisher.

frontiers in Physics

BRIEF RESEARCH REPORT
published: 24 December 2021
doi: 10.3389/fphy.2021.785801

The Transport Properties of Quasi–One-Dimensional $Ba_3Co_2O_6(CO_3)_{0.7}$

*Minnan Chen[1], Jiangtao Wu[1], Qing Huang[2], Jinlong Jiao[1], Zhiling Dun[3], Guohua Wang[1], Zhiwei Chen[4], Gaoting Lin[1], Vasudevan Rathinam[1], Cangjin Li[5], Yanzhong Pei[5], Feng Ye[6], Haidong Zhou[2] and Jie Ma[1,7]**

[1]Key Laboratory of Artificial Structures and Quantum Control, School of Physics and Astronomy, Shanghai Jiao Tong University, Shanghai, China, [2]Department of Physics and Astronomy, University of Tennessee, Knoxville, TN, United States, [3]School of Physics, Georgia Institute of Technology, Atlanta, GA, United States, [4]Center for Phononics and Thermal Energy Science, Shanghai Key Laboratory of Special Artificial Microstructure Materials and Technology, School of Physics Science and Engineering, Tongji University, Shanghai, China, [5]Interdisciplinary Materials Research Center, School of Materials Science and Engineering, Tongji University, Shanghai, China, [6]Neutron Scattering Division, Oak Ridge National Laboratory, Oak Ridge, TN, United States, [7]Wuhan National High Magnetic Field Center, Huazhong University of Science and Technology, Wuhan, China*

We have performed combined elastic neutron diffuse, electrical transport, specific heat, and thermal conductivity measurements on the quasi–one-dimensional $Ba_3Co_2O_6(CO_3)_{0.7}$ single crystal to characterize its transport properties. A modulated superstructure of polyatomic CO_3^{2-} is formed, which not only interferes the electronic properties of this compound, but also reduces the thermal conductivity along the c-axis. Furthermore, a large magnetic entropy is observed to be contributed to the heat conduction. Our investigations reveal the influence of both structural and magnetic effects on its transport properties and suggest a theoretical improvement on the thermoelectric materials by building up superlattice with conducting ionic group.

Keywords: cobalt oxide, neutron diffuse, spin entropy, carrier mobility, thermal conductivity, scattering mechanism

OPEN ACCESS

Edited by:
Gang Zhang,
*Technology and Research (A*STAR), Singapore*

Reviewed by:
Ke-Qiu Chen,
Hunan University, China
Zhi Zeng,
Hefei Institutes of Physical Science (CAS), China

****Correspondence:***
Jie Ma
jma3@sjtu.edu.cn

Specialty section:
This article was submitted to Condensed Matter Physics, a section of the journal Frontiers in Physics

Received: *29 September 2021*
Accepted: *19 November 2021*
Published: *24 December 2021*

Citation:
Chen M, Wu J, Huang Q, Jiao J, Dun Z, Wang G, Chen Z, Lin G, Rathinam V, Li C, Pei Y, Ye F, Zhou H and Ma J (2021) The Transport Properties of Quasi–One-Dimensional $Ba_3Co_2O_6(CO_3)_{0.7}$. Front. Phys. 9:785801. doi: 10.3389/fphy.2021.785801

INTRODUCTION

Thermoelectric (TE) materials can recycle waste heat into usable electricity based on the Seebeck effect and are believed to play a significant role in efficient use of energy [1]. As the energy conversion performance of TE materials is evaluated by the dimensionless figure of merit zT, $zT = S^2\sigma T/(\kappa_{ele} + \kappa_{latt})$, where T is operating temperature, σ is electrical conductivity, S is Seebeck coefficient, κ_{ele} is electronic thermal conductivity, and κ_{latt} is lattice thermal conductivity, the research on the TE material is usually focused on two main approaches: (1) increasing the power factor $S^2\sigma$ through electronic structure or energy band engineering [2–4] and (2) reducing the lattice thermal conductivity κ_{latt} by introducing additional phonon scattering and manipulating phonon structure [5–9]. Actually, those approaches are very complex. For example, the electrical transport ($\sigma = n\mu e$) could be regulated by the carrier concentration n, the carrier mobility μ, and the electron charge e, whereas the acoustic phonon scattering introduces a $\mu \propto T^{-1.5}$ dependence, and the ionized impurity scattering gives a $\mu \propto T^{1.5}$ relationship [10]. Furthermore, the lattice thermal conductivity, κ_{latt}, could be decreased by the grain boundary scattering, point defect scattering, disorder scattering, and Umklapp scattering [11, 12]. Therefore, if the scattering mechanisms of both the electrical and thermal transport could be well understood, the energy conversion performance of TE materials can be better optimized.

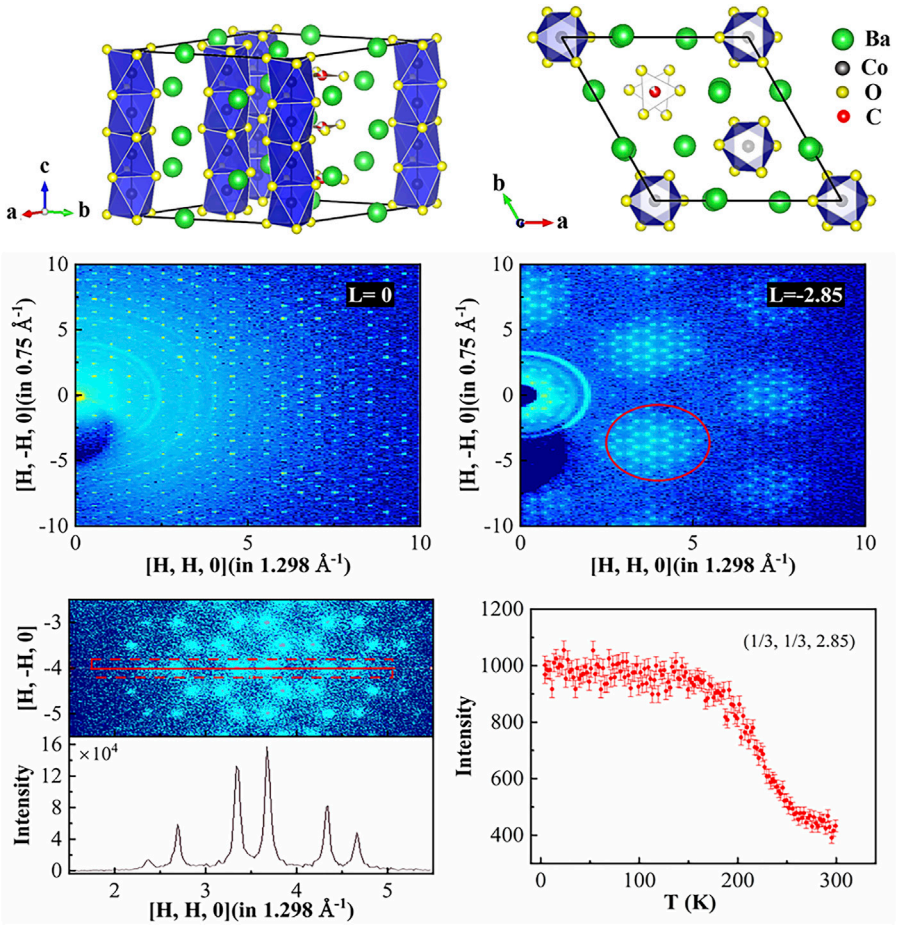

FIGURE 1 | (A) Crystal structure of $Ba_3Co_2O_6(CO_3)_{0.7}$ consisting of chains of CoO_6 and carbonate CO_3 along the c-axis in the standard orientation [space group: P-6]. **(B)** The c-axis projected crystal structure. 2D slice of diffuse neutron scattering patterns of $Ba_3Co_2O_6(CO_3)_{0.7}$ single crystal at 50 K. **(C)** $L = 0$, **(D)** $L = -2.85$, and **(E)** enlarged view of a section of **(D)** obtained on CORELLI. **(F)** Cuts along the [H, H, 0] direction of the Bragg peak marked by red solid line in panel **(E)**. **(G)** Temperature dependence of the peak intensity of the (1/3 1/3 2.85).

At present, alloy TE materials have been widely applied as a TE compound. Although the performance has been continuously improved, there are some unavoidable limitations on the environment, expenses, oxidization stability, and so on [13–15]. Therefore, the investigation of oxide TE materials has been proposed. Because of its special crystal structure and magnetic effect, the cobalt oxide has good electronic properties and low lattice thermal conductivity [16–21]. For example, the power factor ($S^2\sigma$) of $NaCo_2O_4$ is 5×10^{-3} W · m^{-1} · K^{-2}, even higher than that of Bi_2Te_3 [22]. Among them, $NaCo_2O_4$, $Ca_3Co_4O_9$, and $Bi_2Sr_2Co_2O_x$ have received much attention, and their TE performance is also continuously improved and even higher than some alloys [17, 23–26].

Recently, a quasi–one-dimensional cobaltate $Ba_3Co_2O_6(CO_3)_{0.7}$ has been reported as a new excellent potential TE material [27]. This compound comprised face-sharing CoO_6 octahedra and carbonate CO_3^{2-} molecular chains along its c-axis with the space group of P-6, $a = 9.683$ Å and $c = 9.518$ Å [28], **Figures 1A, B**. The average occupancy of the polyatomic CO_3^{2-} molecule is 0.7. Although z of $Ba_3Co_2O_6(CO_3)_{0.7}$ was reported as 5.1×10^{-5} K^{-1}, which is comparable to NaxCoO$_2$-y at 300 K, and it was considered as a promising cobalt oxide TE material [24], the thermal conductivity, transport properties, and the physics remain unknown.

In this article, we report neutron diffuse scattering, electrical conductivity, Hall effect, specific heat, and thermal conductivity of $Ba_3Co_2O_6(CO_3)_{0.7}$ single crystal. Moreover, the magnetic effect of the Co ions is discussed.

EXPERIMENTAL DETAILS

Single crystal of $Ba_3Co_2O_6(CO_3)_{0.7}$ was grown by a flux method using a mixture of Co_3O_4, $BaCO_3$, K_2CO_3, and $BaCl_2$ [27]. These single crystals have the shape of short hexagonal rods. The c-axis was determined using the X-ray Laue method to be along the rod direction.

A single crystal with dimension of $2 \times 2 \times 6$ mm^3 was aligned in the (H, K, 0) horizontal scattering plane for the diffuse

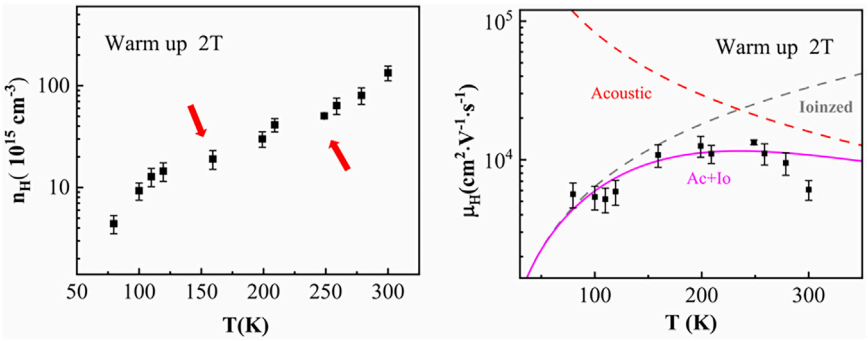

FIGURE 2 | Temperature dependence of **(A)** carrier concentration n_H and **(B)** Hall mobility μ_H along the c-axis for $Ba_3Co_2O_6(CO_3)_{0.7}$. **(B)** Calculated carrier mobility (magenta solid line) took into account the ionized impurity scattering (gray dashed line) and acoustic phonon scattering (red dashed line) contributions.

scattering studies using the elastic single crystal diffuse scattering spectrometer CORELLI at the Spallation Neutron Source (SNS), Oak Ridge Nation Laboratory [29]. Based on the Hall effect, the carrier concentration of $Ba_3Co_2O_6(CO_3)_{0.7}$ in the temperature range of 80 to 300 K was measured by the van der Pauw technique at a reversible magnetic field of 2 T. And the conductivity along the c-direction was obtained by Physical Property Measurement System (PPMS, Quantum Design) with resistivity option, using the four-probe method. The specific heat measurement was applied on PPMS's heat capacity option in two steps. First, the background specific heat was measured by an empty puck with a small amount of N-grease in the temperature range from 2 to 250 K at zero field. Then, a $Ba_3Co_2O_6$ $(CO_3)_{0.7}$ sample (approximately 4.71 mg) was placed in the measured N-grease, and the total specific heat was measured at same conditions. Finally, we gained the specific heat of the sample by subtracting the background specific heat from the total specific heat. The thermal conductivity along the c-axis was characterized using PPMS with thermal transport options, and the four-probe lead configuration method was used. During the measurement, the matching gold-plated copper bar in PPMS was used as leads. More detail for the measurement of carrier concentration, specific heat and thermal conductivity can be find in **Supplementary Material**. The diffuse scattering studies, carrier concentration, electrical conductivity, and thermal conductivity, were carried out on the same crystal, and the sample for the measurement of the specific heat was cut from this crystal too.

RESULTS AND DISCUSSION

Elastic Diffuse Scattering

To further understand the structural details of $Ba_3Co_2O_6(CO_3)_{0.7}$, we study the elastic diffuse scattering behavior of it. **Figures 1C, D** show the contour plot of neutron intensity at 50 K in the (H, K, 0) plane of $Ba_3Co_2O_6(CO_3)_{0.7}$ with $L = 0$ and $L = -2.85$. The sharp spots in **Figure 1C** demonstrate the good crystallinity of the single crystal. The signals of strong diffuse scattering are clearly observed at $L = -2.85$. **Figure 1F**, corresponding to the red solid line in **Figure 1E**, shows the elastic intensity along the [H, H, 0] direction and the relative diffuse intensity of each diffuse spot. Morgan et al. [30] have analyzed the short-range diffuse scattering using reverse Monte Carlo method and concluded that the diffuse scattering has short-range correlation between the disorder vibrations of polyatomic CO_3^{2-}.

Figure 1G shows the temperature dependence of the superlattice (1/3, 1/3, 2.85) reflection. Upon warming, the intensity starts to decrease at 150 K and approaches a T-independent constant greater than 250 K. Thus, the vibrations of polyatomic CO_3^{2-} should be affected by the thermal effect, and the localization of the CO_3^{2-} cluster should be relaxed.

Electrical Transport Properties

To obtain the electrical transport properties of $Ba_3Co_2O_6(CO_3)_{0.7}$ single crystal, Hall carrier concentration n_H was collected at a reversible magnetic field of 2 T, and Hall mobility μ_H was determined with zero-field resistivity, as shown in **Figure 2**. The exponential increase of carrier concentration with rising temperature indicates the thermal excitation of carriers. The charge polarity is dominated by holes in the measured temperature range, which is consistent with the positive Seebeck coefficients reported by Igarashi et al. [31]. The low carrier concentrations suggest that the further acceptor doping is required for TE applications. As marked in **Figure 2A**, there are two anomalies at 150 and 250 K, which agrees very well with the diffuse data and confirmed that CO_3^{2-} ion is a conductor in the system.

The temperature versus μ_H of $Ba_3Co_2O_6(CO_3)_{0.7}$ single crystal is nonmonotonic, as shown in **Figure 2B**. The calculated mobility involving both the ionized impurity scattering and acoustic phonon scattering can well match the experimental values over a wide temperature range. μ_H follows a temperature dependence closing to $T^{1.5}$ at low temperature range, implying that ionized impurity scattering dominates at low temperature in $Ba_3Co_2O_6(CO_3)_{0.7}$ single crystal. We believe that the ionized impurity scattering relates to polyatomic CO_3^{2-}. As the temperature increases, the localized ordering of CO_3^{2-} weakens, and the scattering of ionized impurity also diminishes. On the other hand, the lattice vibrations become

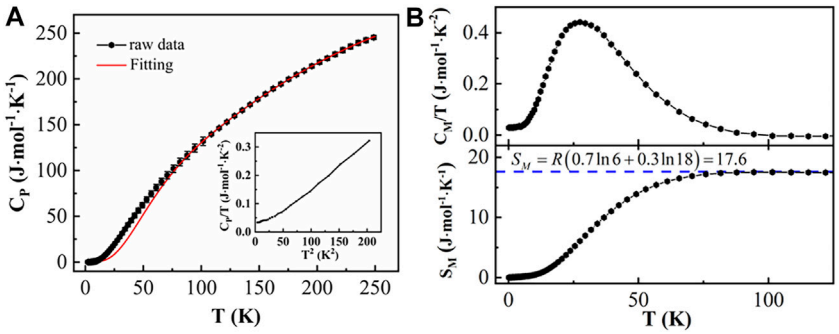

FIGURE 3 | (A) The total specific heat C_P of $Ba_3Co_2O_6(CO_3)_{0.7}$ measured at zero field. The red line represents the lattice contribution by **Eq. 1**. The inset shows the C_P/T vs T^2 **(B)** The magnetic specific heat is obtained by subtracting the lattice contribution C_p from the raw data. **(C)** Magnetic entropy obtained by integrating C_M/T over the entire measured temperature range.

stronger with increasing temperature. These two factors together lead to the acoustic phonon scattering, gradually overshadowing the ionized impurity scattering and becoming the dominant scattering mechanism in the material, which causes a negative temperature-dependence slope of μ_H greater than 250 K. The CO_3^{2-} is delocalized when $T > 250$ K, which might introduce other scattering mechanisms affecting the carriers transports and make the carrier mobility lower than the theoretical value.

Results of $C_P(T)$

To investigate the thermal effect in $Ba_3Co_2O_6(CO_3)_{0.7}$, the specific heat C_P was measured in the temperature range from 2 to 250 K at zero field. As shown in **Figure 3A**, the profile of data is very smooth, and no obvious peak is detected, indicating the absence of structure and magnetic transitions. The inset of **Figure 3A** displays the data as a C_P/T versus T^2. According to the Debye model, the lattice term of the total specific heat C_P/T is linear with T^2 at low T, but the data demonstrate a deviation from the linear relationship at low temperature and a nonzero intercept (approximately 0.29 J · mol^{-1} · K^{-2}) at 0 K. The nonzero intercept is an order of magnitude larger than that for $NaCo_2O_4$, which is a strongly correlated electronic cobalt system [32], and suggests $Ba_3Co_2O_6(CO_3)_{0.7}$ as also a strongly correlated electronic system.

In order to further study the specific heat of $Ba_3Co_2O_6(CO_3)_{0.7}$, a fitting was gained by using the Debye–Einstein model, which can fit the lattice specific heat data well at both low and high temperature. The model is written as follows [33]:

$$C_p(T) = C_D\left[9R\left(\frac{T}{\theta_D}\right)^3\int_0^{x_D}\frac{x^4e^x}{(e^x-1)^2}dx\right] + \sum_i C_{E_i}\left[3R\left(\frac{\theta_{E_i}}{T}\right)^2\frac{\exp\left(\frac{\theta_{E_i}}{T}\right)}{\left[\exp\left(\frac{\theta_{E_i}}{T}\right)-1\right]^2}\right], \quad (1)$$

where the first term is the contribution from the acoustic branch (Debye term), and the remaining terms are related to the contribution of the optical branch (Einstein terms). C_D and C_{Ei} are the relative weights of the Debye and Einstein terms,

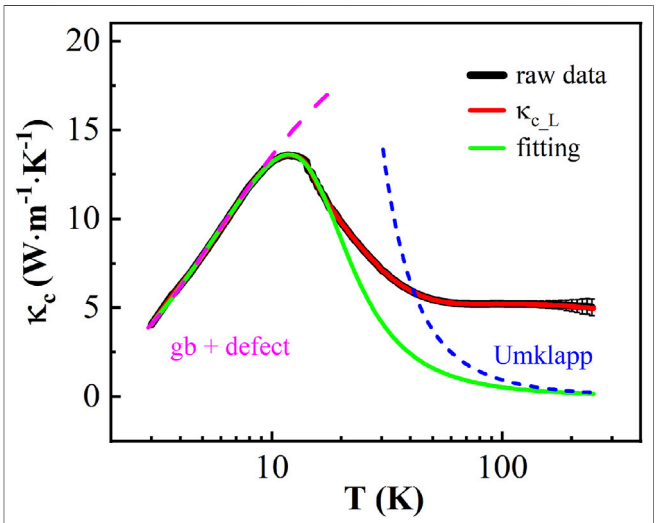

FIGURE 4 | The temperature dependence of the thermal conductivity κ_c and the lattice thermal conductivity (κ_{c_L}) along the c-axis of $Ba_3Co_2O_6(CO_3)_{0.7}$ at zero field. The black line is experimental data of the thermal conductivity; the red line is κ_{c_L}, and the green one represents the result of fitting by **Eq. 2**. The magenta dashed line is the contribution of the grain boundary and the point defect scattering, and the blue one is Umklapp process scattering.

respectively. R is the universal gas constant. θ_D and θ_{Ei} represent Debye and Einstein temperatures. There are 13.8 atoms per formula in our system. The best fitting for our data results is one Debye term and three E terms with a ratio 1:6:2.8:4 for C_D: C_{E1}:C_{E2}:C_{E3} and $\theta_D = 163$ K, $\theta_{E1} = 816$ K, $\theta_{E2} = 179$ K, and $\theta_{E3} = 290$ K, respectively.

As there is no distinct phase transition in the specific heat data, and the magnetic long-range order was not observed down to 2 K [34], the deviation of the experimental data from the fitted values indicates the presence of short-range magnetic fluctuations. **Figures 3B, C** display the magnetic specific heat, C_M, by subtracting the fitted lattice contribution from raw data, and the related magnetic entropy S_M, respectively. The S_M enhances with increasing temperature, and almost 100% recovered the theoretical value 17.6 J · mol^{-1} · K^{-1} at

approximately 100 K. Both contributions of spin and orbital degrees of freedom are suggested to be considered [35]: Co^{4+} has high-spin state with $S = 1/2$ ($3d^5$), and Co^{3+} has intermediate-spin state with $S = 1$ ($3d^6$), leading to $S_M = R(0.7 \ln 6 + 0.3 \ln 18) = 17.6\ J \cdot mol^{-1} \cdot K^{-1}$, as shown by the blue dotted line in **Figure 3C**. There may be spin-phonon scattering in the huge magnetic entropy regimen that interferes with the thermal conductivity.

Thermal Transport Properties

Figure 4 shows the temperature dependence of the total thermal conductivity κ_c and the lattice thermal conductivity κ_{c_L} of $Ba_3Co_2O_6(CO_3)_{0.7}$ parallel to the c-axis from 3 to 250 K κ_c consists of κ_{c_L} and the electronic thermal conductivity κ_{c_e}, where the electronic thermal conductivity can be determined by the Wiedemann–Franz law ($\kappa_e = \sigma L_n T$, where the Lorenz number $L_n = 2.45 \times 10^{-8}\ W \cdot \Omega \cdot K^{-2}$) and subtracted. At low temperatures, κ_c and κ_{c_L} almost completely overlap due to the very small electronic thermal conductivity. As the temperature increases, κ_c and κ_{c_L} begin to separate because of the exponential increase in conductivity. Although κ_{c_e} is maximum at 250 K, it is only a few percent of κ_{c_L}. The contribution of phonon to κ_c is domain. κ_{c_L} increases rapidly at low temperature with the dominant boundary scattering, which displays a $\kappa_{c\_L} \propto T^3$ dependence. A maximum with a value of $13.5\ W \cdot m^{-1} \cdot K^{-1}$ appears at approximately 12 K, where the Umklapp processes with exp (θ_D/bT) dependence become frequent and enough to compare with boundary scattering. One notes that the peak of κ_{c_L} is an order of magnitude smaller than that of other cobalt oxides, such as $Ca_3Co_2O_6$ [36]. This difference may be caused by the superlattice in $Ba_3Co_2O_6(CO_3)_{0.7}$, which can enhance the scatting of κ_{c_L}. As temperature increases further, κ_{c_L} drops very quickly and reflects that the Umklapp process scattering gradually becomes the main scattering mechanism. When the temperature is higher than 60 K, the trend of the curve gets flat. At approximately 250 K, the lattice thermal conductivity of $Ba_3Co_2O_6(CO_3)_{0.7}$ along the c-axis is $5.02\ W \cdot m^{-1} \cdot K^{-1}$.

The data of κ_{c_L} were fitted to the formula given by the Debye model of phonon thermal conductivity[37].

$$\kappa_{c\_L} = \frac{k_B}{2\pi^2 \nu_p}\left(\frac{k_B}{\hbar}\right)^3 T^3 \int_0^{\theta_D/T} \frac{x^4 e^x}{(e^x - 1)^2}\tau(\omega, T)dx, \quad (2)$$

where k_B is the Boltzmann's constant, ν_p is the average sound velocity, $\hbar$ is the Planck constant, $x = \hbar\omega/k_B T$, ω is frequency, and τ is the mean lifetime of phonon. The phonon relaxation is usually defined as follows:

$$\tau^{-1} = \nu_p/L + A\omega^4 + BT\omega^3 \exp(-\theta_D/bT). \quad (3)$$

These three items correspond with phonon boundary scattering, phonon point defect scattering, and the phonon–phonon Umklapp processes, respectively. L, A, B, and b are the fitting parameters. ν_p can be calculated by the Debye temperature $\theta_D = 163$ K obtained by the fitting above and **Eq. 4**:

$$\theta_D = \frac{\hbar\nu_p}{k_B}\left(\frac{6\pi^2 N}{V}\right)^{\frac{1}{3}} \quad (4)$$

where N is the number of atoms in crystal, and V is the volume of crystal, and then we obtain the average sound velocity of the sample $\nu_p \approx 1{,}343\ m \cdot s^{-1}$.

The best fitting is shown in **Figure 4** as green solid line with $L = 1.6 \times 10^{-5}$ m, $A = 1.7 \times 10^{-41}\ s^3$, $B = 7.4 \times 10^{-29}\ K^{-1}\ s^2$, and $b = 2.7$. The lattice thermal conductivity is mainly the contribution of phonons below approximately 18 K. As the temperature increases, the fitted values gradually deviate from the raw data. An extra contribution of the thermal conductivity has also been observed in $Ca_3Co_2O_6$ [38]. In combination with the heat capacity, the deviation of thermal conductivity might be due to the overestimation of the lattice thermal conductivity, because of the magnetic contribution to the total thermal conductivity: (1) The magnetic entropy increases rapidly after 18 K; in the meantime, κ_{c_L} starts to be higher than the theoretical value. (2) After the magnetic entropy reaches saturation at approximately 100 K, the κ_{c_L} also decreases slowly with growing temperature at the same rate as the theoretical one. As the electron concentration is very low, the electron–phonon scattering is not dominant in the system, and the CO_3^{2-} affects grain boundary and defect.

CONCLUSION

In summary, we have studied the structural, electrical, and thermal transport properties of quasi–one-dimensional $Ba_3Co_2O_6(CO_3)_{0.7}$ single crystal and the connection between the lattice structure, magnetism, and its transport properties. Neutron diffuse reveals that a modulated superstructure of CO_3^{2-} is formed in $Ba_3Co_2O_6(CO_3)_{0.7}$. The main hole carriers in the systems are continuously excited with increasing temperature and scattered not only by short-range ordered polyatomic CO_3^{2-} at low temperature, but also by acoustic phonon and nonlocalized CO_3^{2-} at high temperature. No lattice and magnetic phase transition are observed by the specific heat measurement, and the magnetic entropy is consistent with mixed Co^{3+} and Co^{4+} valence. The thermal conductivity of $Ba_3Co_2O_6(CO_3)_{0.7}$ shows an enhancement at higher temperatures over classic phonon heat transfer due to the contribution of the itinerant magnetism. The unique lattice and transport properties in $Ba_3Co_2O_6(CO_3)_{0.7}$ suggest a potential superlattice designs for regulating the TE properties.

DATA AVAILABILITY STATEMENT

The original contributions presented in the study are included in the article/**Supplementary Material**, further inquiries can be directed to the corresponding author.

AUTHOR CONTRIBUTIONS

MC and JM conceived the project. QH and HZ provided single crystals used in this study. FY and ZD performed neutron scattering experiments and analyzed the data with the help

from JM JW and VR. ZC, CL and YP performed carrier concentration measurement. MC performed specific heat and conductivity measurements and analyzed the data with the help with GW, GL and JJ. GW carried out the thermal property measurements. All authors discussed the results and contributed to the writing of the manuscript.

FUNDING

MC, JW, JJ, GW, GL, and JM thank the financial support from the National Science Foundation of China (Nos. 11774223, and U2032213), the interdisciplinary program Wuhan National High Magnetic Field Center (Grant No. WHMFC 202122), Huazhong University of Science and Technology, and the National Key Research and Development Program of China (Grant Nos. 2016YFA0300501 and 2018YFA0704300). GL thanks the project funded by China Postdoctoral Science Foundation (Grant No. 2019M661474). JM thanks a Shanghai talent program. QH and HZ thank the support from NSF-DMR- 2003117. The ND experiment was performed at CORELLI of SNS. VR thanks the project funded by Natural Science Foundation of China (Grant No. QN20200009030). A portion of this research used resources at the Spallation Neutron Source, a DOE Office of Science User Facility operated by the Oak Ridge National Laboratory.

SUPPLEMENTARY MATERIAL

The Supplementary Material for this article can be found online at: https://www.frontiersin.org/articles/10.3389/fphy.2021.785801/full#supplementary-material

REFERENCES

1. Tritt TM. Holey and Unholey Semiconductors. *Science* (1999) 283:804–5. doi:10.1126/science.283.5403.804
2. Pei Y, Shi X, LaLonde A, Wang H, Chen L, Snyder GJ. Convergence of Electronic Bands for High Performance Bulk Thermoelectrics. *Nature* (2011) 473:66–9. doi:10.1038/nature09996
3. Kim K, Kim G, Lee H, Lee KH, Lee W. Band Engineering and Tuning Thermoelectric Transport Properties of P-type Bi0.52Sb1.48Te3 by Pb Doping for Low-Temperature Power Generation. *Scripta Materialia* (2018) 145:41–4. doi:10.1016/j.scriptamat.2017.10.009
4. Fu C, Yao M, Chen X, Maulana LZ, Li X, Yang J, et al. Revealing the Intrinsic Electronic Structure of 3D Half-Heusler Thermoelectric Materials by Angle-Resolved Photoemission Spectroscopy. *Adv Sci* (2020) 7:1902409. doi:10.1002/advs.201902409
5. Liu Y, Xie H, Fu C, Snyder GJ, Zhao X, Zhu T. Demonstration of a Phonon-Glass Electron-crystal Strategy in (Hf,Zr)NiSn Half-Heusler Thermoelectric Materials by Alloying. *J Mater Chem A* (2015) 3:22716–22. doi:10.1039/c5ta04418a
6. Shen J, Fu C, Liu Y, Zhao X, Zhu T. Enhancing Thermoelectric Performance of FeNbSb Half-Heusler Compound by Hf-Ti Dual-Doping. *Energ Storage Mater* (2018) 10:69–74. doi:10.1016/j.ensm.2017.07.014
7. Yang Y-X, Wu Y-H, Zhang Q, Cao G-S, Zhu T-J, Zhao X-B. Enhanced Thermoelectric Performance of Bi_2Se_3/TiO_2 Composite. *Rare Met* (2020) 39:887–94. doi:10.1007/s12598-020-01414-4
8. Chen X-K, Pang M, Chen T, Du D, Chen K-Q. Thermal Rectification in Asymmetric Graphene/Hexagonal Boron Nitride van der Waals Heterostructures. *ACS Appl Mater Inter* (2020) 12:15517–26. doi:10.1021/acsami.9b22498
9. Zeng Y-J, Feng Y-X, Tang L-M, Chen K-Q. Effect of Out-Of-Plane Strain on the Phonon Structures and Anharmonicity of Twisted Multilayer Graphene. *Appl Phys Lett* (2021) 118:183103. doi:10.1063/5.0047539
10. Chattopadhyay D, Queisser HJ. Electron Scattering by Ionized Impurities in Semiconductors. *Rev Mod Phys* (1981) 53:745–68. doi:10.1103/RevModPhys.53.745
11. Vandersande JW, Wood C. The thermal Conductivity of Insulators and Semiconductors. *Contemp Phys* (1986) 27:117–44. doi:10.1080/00107518608211003
12. Chen X-K, Chen K-Q. Thermal Transport of Carbon Nanomaterials. *J Phys Condens Matter* (2020) 32:153002. doi:10.1088/1361-648X/ab5e57
13. Perumal S, Roychowdhury S, Biswas K. High Performance Thermoelectric Materials and Devices Based on GeTe. *J Mater Chem C* (2016) 4:7520–36. doi:10.1039/c6tc02501c
14. Xiao Y, Zhao L-D. Charge and Phonon Transport in PbTe-Based Thermoelectric Materials. *Npj Quant Mater* (2018) 3:55. doi:10.1038/s41535-018-0127-y
15. Murugasami R, Vivekanandhan P, Kumaran S, Suresh Kumar R, John Tharakan T. Simultaneous Enhancement in Thermoelectric Performance and Mechanical Stability of P-type SiGe alloy Doped with Boron Prepared by Mechanical Alloying and Spark Plasma Sintering. *J Alloys Compd* (2019) 773:752–61. doi:10.1016/j.jallcom.2018.09.029
16. Masset AC, Michel C, Maignan A, Hervieu M, Toulemonde O, Studer F, et al. Misfit-layered Cobaltite with an Anisotropic Giant Magnetoresistance: $Ca_3Co_4O_9$. *Phys Rev B* (2000) 62:166–75. doi:10.1103/PhysRevB.62.166
17. Yang G, Ramasse Q, Klie RF. Direct Measurement of Charge Transfer in thermoelectricCa3Co4O9. *Phys Rev B* (2008) 78:153109. doi:10.1103/PhysRevB.78.153109
18. Fan M, Zhang Y, Hu Q, Zhang Y, Li X-J, Song H. Enhanced Thermoelectric Properties of Bi2Sr2Co2Oy by Alkali Metal Element Doping and SiC Dispersion. *Ceramics Int* (2019) 45:17723–8. doi:10.1016/j.ceramint.2019.05.341
19. Sakabayashi H, Okazaki R. Crossover from Itinerant to Localized States in the Thermoelectric Oxide $[Ca_2CoO_3]_{(0.62)}[CoO_2]$. *Phys Rev B* (2021) 103:125119. doi:10.1103/PhysRevB.103.125119
20. Naruse K, Kawamata T, Ohno M, Matsuoka Y, Hase M, Kuroe H, et al. Magnetic State of the Geometrically Frustrated Quasi-One-Dimensional Spin System Cu3Mo2O9 Studied by Thermal Conductivity. *J Phys Soc Jpn* (2015) 84:124601. doi:10.7566/jpsj.84.124601
21. Wu Z. Thermal Conductivity Anomaly in Spin-Crossover Ferropericlase under Lower Mantle Conditions and Implications for Heat Flow across the Core-Mantle Boundary. *Am Mineral* (2018) 103:1953–8. doi:10.2138/am-2018-6690
22. Terasaki I, Sasago Y, Uchinokura K. Large Thermoelectric Power in $NaCo_2O_4$ Single Crystals. *Phys Rev B* (1997) 56:R12685–R12687. doi:10.1103/PhysRevB.56.R12685
23. Kurosaki K, Muta H, Uno M, Yamanaka S. Thermoelectric Properties of NaCo2O4. *J Alloys Compd* (2001) 315:234–6. doi:10.1016/s0925-8388(00)01277-9
24. Fujita K., Mochida T., Nakamura K.. High-Temperature Thermoelectric Properties of Na_xCoO_2-Delta Single Crystals. (2001) 40:4644–47. doi:10.1143/jjap.40.4644
25. Jakubczyk EM, Mapp A, Chung CC, Sansom CL, Jones JL, Dorey RA. Enhancing Thermoelectric Properties of NaCo2O4 Ceramics through Na Pre-treatment Induced Nano-Decoration. *J Alloys Compd* (2019) 788:91–101. doi:10.1016/j.jallcom.2019.02.199
26. Zhang L, Liu Y, Tan TT, Liu Y, Zheng J, Yang Y, et al. Thermoelectric Performance Enhancement by Manipulation of Sr/Ti Doping in Two Sublayers of Ca3Co4O9. *J Adv Ceram* (2020) 9:769–81. doi:10.1007/s40145-020-0413-6
27. Iwasaki K, Yamamoto T, Yamane H, Takeda T, Arai S, Miyazaki H, et al. Thermoelectric Properties of Ba3Co2O6(CO3)0.7 Containing One-

Dimensional CoO6 Octahedral Columns. *J Appl Phys* (2009) 106:034905. doi:10.1063/1.3174428
28. Boulahya K, Amador U, Parras M, González-Calbet JM. The Oxycarbonate Ba3Co2O6(CO3)0.60 with a 2H−ABO3-Related Structure. *Chem Mater* (2000) 12:966–72. doi:10.1021/cm991122x
29. Ye F, Liu Y, Whitfield R, Osborn R, Rosenkranz S. Implementation of Cross Correlation for Energy Discrimination on the Time-Of-Flight Spectrometer CORELLI. *J Appl Cryst* (2018) 51:315–22. doi:10.1107/S160057671800403X
30. Morgan Z, Zhou HD, Chakoumakosa B, Ye F. RMC-DISCORD. Reverse Monte Carlo Refinement of DIffuse Scattering and CORrelated Disorder from Single Crystals. *J Appl Crystallogr* (2021) 77:A77–A87. doi:10.1107/s0108767321099128
31. Igarashi H, Shimizu Y, Kobayashi Y, Itoh M. Spin Disorder in an Ising Honeycomb Chain Cobaltate. *Phys Rev B* (2014) 89:054431. doi:10.1103/PhysRevB.89.054431
32. Ando Y, Miyamoto N, Segawa K, Kawata T, Terasaki I. Specific-heat Evidence for strong Electron Correlations in the Thermoelectric material(Na,Ca)Co2O4. *Phys Rev B* (1999) 60:10580–3. doi:10.1103/PhysRevB.60.10580
33. Lu Z, Ge L, Wang G, Russina M, Günther G, dela Cruz CR, et al. Lattice Distortion Effects on the Frustrated Spin-1 Triangular-Antiferromagnet $A_3NiNb_2O_9$ (A=Ba, Sr, and Ca). *Phys Rev B* (2018) 98:094412. doi:10.1103/PhysRevB.98.094412
34. Igarashi K, Shimizu Y, Satomi E, Kobayashi Y, Takami T, Itoh M. Absence of Magnetic Order in Ising Honeycomb-Lattice $Ba_3Co_2O_6(CO_3)_{0.7}$. *J Phys Conf Ser* (2012) 400:032024. doi:10.1088/1742-6596/400/3/032024
35. Koshibae W, Tsutsui K, Maekawa S. Thermopower in Cobalt Oxides. *Phys Rev B* (2000) 62:6869–72. doi:10.1103/PhysRevB.62.6869
36. Che HL, Shi J, Wu JC, Rao X, Liu XG, Zhao X, et al. Thermal Conductivity of Ca3Co2O6 Single Crystals. *AIP Adv* (2018) 8:055811. doi:10.1063/1.5005992
37. Song JD, Wang XM, Zhao ZY, Wu JC, Zhao JY, Liu XG, et al. Low-temperature Heat Transport of $CuFe_{1-x}Ga_xO_2$ (x=0-0.12) Single Crystals. *Phys Rev B* (2017) 95:224419. doi:10.1103/PhysRevB.95.224419
38. Cheng J-G, Zhou J-S, Goodenough JB. Thermal Conductivity, Electron Transport, and Magnetic Properties of Single-crystalCa3Co2O6. *Phys Rev B* (2009) 79:184414. doi:10.1103/PhysRevB.79.184414

Conflict of Interest: The authors declare that the research was conducted in the absence of any commercial or financial relationships that could be construed as a potential conflict of interest.

Publisher's Note: All claims expressed in this article are solely those of the authors and do not necessarily represent those of their affiliated organizations, or those of the publisher, the editors and the reviewers. Any product that may be evaluated in this article, or claim that may be made by its manufacturer, is not guaranteed or endorsed by the publisher.

Advantages of publishing in Frontiers

OPEN ACCESS
Articles are free to read for greatest visibility and readership

FAST PUBLICATION
Around 90 days from submission to decision

HIGH QUALITY PEER-REVIEW
Rigorous, collaborative, and constructive peer-review

TRANSPARENT PEER-REVIEW
Editors and reviewers acknowledged by name on published articles

Frontiers
Avenue du Tribunal-Fédéral 34
1005 Lausanne | Switzerland

Visit us: www.frontiersin.org
Contact us: frontiersin.org/about/contact

REPRODUCIBILITY OF RESEARCH
Support open data and methods to enhance research reproducibility

DIGITAL PUBLISHING
Articles designed for optimal readership across devices

FOLLOW US
@frontiersin

IMPACT METRICS
Advanced article metrics track visibility across digital media

EXTENSIVE PROMOTION
Marketing and promotion of impactful research

LOOP RESEARCH NETWORK
Our network increases your article's readership